

Synthesis and Characterisation of Novel Oxovanadium(IV) Schiff Base
Complexes: A study of their Electronic Spectral Properties,
Peroxide Binding Affinities, DFT-calculated Geometries and Spectra,
and Cytotoxicity Towards Human Carcinoma Cells

Submitted in fulfilment of the requirement for the degree of

MASTER OF SCIENCE

By

Malcolm A. Bartlett

BSc. (Hons.) (UKZN)

December 2012

School of Chemistry and Physics,
University of KwaZulu-Natal,
Pietermaritzburg

Declaration

I Malcolm Alan Bartlett declare that:

- (i) The research reported in this dissertation/thesis, except where otherwise indicated, is my original research.
- (ii) This dissertation/thesis has not been submitted for any degree or examination at any other university.
- (iii) This dissertation/thesis does not contain other persons' data, pictures, graphs or other information, unless specifically acknowledged as being sourced from other persons.
- (iv) This dissertation/thesis does not contain other persons' writing, unless specifically acknowledged as being sourced from other researchers. Where other written sources have been quoted, then:
 - a) Their words have been re-written but the general information attributed to them has been referenced;
 - b) Where their exact words have been used, their writing has been placed inside quotation marks, and referenced.
- (v) Where I have reproduced a publication of which I am author, co-author or editor, I have indicated in detail which part of the publication was actually written by myself alone and have fully referenced such publications.
- (vi) This dissertation/thesis does not contain text, graphics or tables copied and pasted from the Internet, unless specifically acknowledged, and the source being detailed in the dissertation/thesis and in the References sections.

Signed: 

Date: 11 December 2012

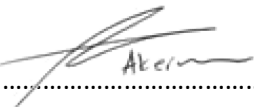
Malcolm A. Bartlett

We hereby certify that this statement is correct to the best of our knowledge:

Signed: 

Date: 11 December 2012

Prof. Orde Q. Munro (Supervisor)

Signed: 

Date: 11 December 2012

Dr. Matthew P. Akerman (Co-Supervisor)

Acknowledgements

I would like to acknowledge the following persons for contributions to this work:

To Prof. Orde Munro, thank you for your willing guidance throughout this project; your enthusiasm for the subject is truly inspiring. Even when pressured from all sides, you still made time to review my work.

To Dr. Matthew Akerman, thank you for “stepping-in” during Prof. Munro’s sabbatical, and for your attention to this project since his return. Your supervision and insight have always been valued.

Craig Grimmer, thank you for your constant willingness to assist me whenever needed in my project, and for your door that was always open. You were always prepared to share your expertise on a subject, and help me through my problems. Also, for reviewing parts of my work, thank you.

To Prof. John Field, you were always ready to give me direction, and highlight the essentials of quality research. Thank you for going out of your way to help me, even though you were meant to be enjoying retirement. I greatly appreciate all you’ve done for me.

I would also like to thank the following persons:

My peers: Savannah Zacharias, Justine dePonte, Thomas “TJ” Theron, Vineet Jeena and Jayd Lawrence, thank you for the years of friendship that have made obtaining this degree an enjoyable and memorable experience.

The technical staff of the chemistry department: Caryl, Shawn, Fazel, Bheki, Prenesha and Prudence, for always offering willing assistance whenever it was needed, and very often “going the extra mile.” It is greatly appreciated.

Allen Mambanda, for his inspiring character during demonstrating sessions, which made even the tedious days, edifying.

MINTEK for their generous financial support to the research expenses incurred during this research.

The NRF, for providing me with the ‘Scarce Skills Scholarship’ that enabled me to complete this degree.

Mr. and Mrs. Bartlett (Mum and Dad), for supporting, encouraging and mentoring me through all of life’s journeys; you are truly two of my best friends.

Cara-Lesley Bartlett (otherwise known as “Sibling”), for her friendship, advice and occasional jokes that always brighten-up my day, no matter what.

Erica Bentley, my beautiful fiancée, who has been my closest friend and greatest supporter. Thank you for being so self-sacrificing while I am studying, and for all the chemistry you’ve learnt for my sake.

God, You’ve given me more to be thankful for than I can ever realise, and Your help through this degree is just one more way that You show Your love for me.

List of Abbreviations and Symbols

A	hyperfine coupling constant
Å	Angstrom
acac	acetylacetonate
AP-1	an endonuclease that repairs AP (apurinic or apyrimidinic) sites on DNA
aq	aqueous
β	Bohr magneton
BMOV	bis(maltolato)oxovanadium(IV)
°C	degree Celsius
^{13}C	Isotope of carbon with atomic weight of 13 amu
CCl_4	carbon tetrachloride
CHCl_3	chloroform
cisplatin	<i>cis</i> -diaminodichloroplatinum(II)
cm^{-1}	reciprocal centimetre
CSC	cancer stem cell
CSD	Cambridge Structural Database
d	doublet
DFT	Density Functional Theory
DMPO	5,5-dimethyl-1-pyrroline-N-oxide
DMSO	dimethyl sulfoxide
DMSO-d6	deuterated dimethyl sulfoxide
DNA	deoxyribonucleic acid
E	electrophile
E°	reduction potential
e.d.g.	electron donating group
EPR	Electron Paramagnetic Resonance
ERK-1	extracellular-signal-regulated-kinase
ESEEM	electron spin echo envelope modulation
ESI	Electro-Spray Ionisation
e.w.g.	electron withdrawing group
FT	fourier transform
G	Gauss
g	gram
<i>g</i>	<i>g</i> -value
GGA	Generalised Gradient Approximation
GHz	gigahertz
GIAO	gauge-including atomic orbital
GSH	glutathione reductase
<i>H</i>	Hamiltonian operator
<i>h</i>	Planck's constant
^1H	proton
H₂L1	4,4'-{benzene-1,2-diylbis[nitrilo(1E)phen-1-yl-1-ylidene]}dibenzene-1,3-diol
H₂L2	4,4'-{ethane-1,2-diylbis[nitrilo(1E)phenyl-1-yl-1-ylidene]}dibenzene-1,3-diol
H₂L3	4,4'-{propane-1,2-diylbis[nitrilo(1E)phen-1-yl-1-ylidene]}dibenzene-1,3-diol

H₂L4	4,4'-{(2-hydroxypropane-1,3-diyl)bis[nitrilo(1E)phen-1-yl-1-ylidene]}dibenzene-1,3-diol
H₂L5	4,4'-{2,2-dimethylpropane-1,3-diyl}bis[nitrilo(1E)phen-1-yl-1-ylidene]}dibenzene-1,3-diolHCl hydrochloric acid
H ₂ O ₂	hydrogen peroxide
HOMO	highest occupied molecular orbital
Hz	hertz
IC ₅₀	inhibitory concentration for 50% of population
IR	Infrared
IUCR	International Union of Crystallography
J	coupling constant
JNK-1	c-Jun N-terminal kinases
K	Kelvin
KOH	potassium hydroxide
λ _{max}	wavelength at maximum absorbance
LiAlH ₄	lithium aluminium hydride
LUMO	lowest unoccupied molecular orbital
M	Molar (concentration)
m	multiplet
M ⁺	positive molecular ion
MAPK	mitogen activated protein kinase
MEK-1	MAP kinase or ERK kinase
MeOH	methanol
MHz	megahertz
ml	millilitre
MLCT	metal-to-ligand charge transfer
μM	microMolar
mmol	millimole
MO	Molecular Orbital
m _s	angular momentum of electron spin
MTS	(3-(4,5-dimethylthiazol-2-yl)-5-(3-carboxymethoxyphenyl)-2-(4-sulfophenyl)-2H tetrazolium
<i>m/z</i>	mass-to-charge ratio
NAD(P)	nicotinamide adenine dinucleotide(phosphate)
NaOH	sodium hydroxide
NBO	Natural Bond Orbital
NCI	national cancer institute
NF-κβ	nuclear transcription factor-κβ
NH ₄ PF ₆	ammonium hexafluorophosphate
NH ₄ VO ₃	ammonium metavanadate
nm	nanometre
nmol	nanomoles
NMR	Nuclear Magnetic Resonance
NPA	Natural Population Analysis
ns	nanosecond
Nu	nucleophile

$O_2^{\bullet-}$	superoxide radical anion
OH^{\bullet}	hydroxyl radical anion
$\pi \rightarrow \pi^*$	electronic transitions from a bonding to an anti-bonding orbital of pi symmetry
p	Pentent
P-gp	P-glyco-protein
pH	the negative log of $[H^+]$
Ph_3SnCl	triphenyl tin(IV)chloride
PI-3K	a kinase of phosphatidyl inositol (PI)
ppm	parts per million
PTPases	phosphotyrosine phosphatases
QM	quantum mechanics
RMSD	root-mean square deviation
ROS	reactive oxygen species
RSA	Republic of South Africa
s	singlet
SA	standard agent
salen	N,N'-disalicylaethylenediamine
SCF	self-consistent field
SOD	superoxide dismutase
T	Tesla
t	triplet
<i>t</i> -BuOOH	<i>tert</i> -butylperoxide
TD	time-dependent
TMS	tetramethyl silane
TNF	tumour necrosis factor
TOF-MS	Time-of-Flight Mass spectrometry
TopoII	Topoisomerase II
TPP	tyrosine phosphorylated protein
UV	Ultra-Violet
vis	visible
μ_B	external magnetic field
V	volt
^{51}V	Isotope of vanadium with atomic weight of 51 amu
[VO(L1)]	2,2'-{benzene-1,2-diylbis[nitrilo(1E)phen-1-yl-1-ylidene]}bis(5-hydroxyphenolate)-vanadyl
[VO(L2)]	2,2'-{ethane-1,2-diylbis[nitrilo(1E)phen-1-yl-1-ylidene]}bis(5-hydroxyphenolate)-vanadyl
[VO(L3)]	2,2'-{propane-1,3-diylbis[nitrilo(1E)phen-1-yl-1-ylidene]}bis(5-hydroxyphenolate)-vanadyl
[VO(L4)]	2,2'-{(2-hydroxypropane-1,3-diyl)bis[nitrilo(1E)phen-1-yl-1-ylidene]}-bis(5-hydroxyphenolate)vanadyl
[VO(L5)]	2,2'-{(2,2-dimethylpropane-1,3-diyl)bis[nitrilo(1E)phen-1-yl-1-ylidene]}bis(5-hydroxyphenolate)-vanadyl
$VOSO_4 \cdot 5H_2O$	vanadylsulfate pentahydrate
XRD	X-ray Diffraction

List of Figures

Page

Chapter 1

Figure 1.1: a) the Norse goddess <i>Vanadis</i> , after whom the element is named, b) tools made from a chrome-vanadium alloy, and c) Italian heavy metal rock band, <i>Vanadium</i> .	1
Figure 1.2: The complex $[\text{VO}(\text{acac})_2]$ showing its square pyramidal coordination geometry and the vacant orbital position for an additional ligand.	3
Figure 1.3: (Left) Structure of amavadine, showing the chiral centres (*) on the ligands, as well as the chiral arrangement of the ligands around the metal. (Right) Mushrooms of the genus <i>Aminita</i> .	5
Figure 1.4: (Left) schematic drawing of the transport protein, Vanabin2. A-helices are represented by the rectangular boxes (picture taken from Ref. 32). (Right) the Blue-Bell tunicate, an ascidian; no other group of organisms on the planet sequester more vanadium from the environment, relative to their body weight, than these ones.	6
Figure 1.5: Two vanadium complexes tested for insulin mimetic properties: (left) bis(maltolato)oxovanadium(IV) (BMOV), one of the most well characterised compounds, is used as a reference for the evaluation of new insulin mimetic candidates; (right) (N,N'-disalicylidineethylenediamine)oxo-vanadium(IV) $[\text{VO}(\text{salen})]$, a Schiff base compound that has shown encouraging results.	8
Figure 1.6: Structure of the vanadocene dichloride, an organometallic vanadium compound, and one of the most promising of the cyclopentadienyl complexes tested against cancer. It forms labile complexes with DNA, rather than covalent ones, as does <i>cis</i> -Platin.	10
Figure 1.7: Examples of hydroxo-bridged vanadium dimmers, a) with two hydroxo anions, and b) with one hydroxo and a non-coordinating anion.	14
Figure 1.8: Hydroxy-salen oxovanadium(IV) complexes able to induce DNA strand breakage. Compound c , with the hydroxyl groups in the <i>para</i> -position, was the most effective in causing DNA strand breakage.	15
Figure 1.9: Proposed structures of Schiff base ligands to be synthesised.	16
Figure 1.10: Proposed structures for the target oxovanadium(IV) complexes.	16
Chapter 2	
Figure 2.1: Diagram of 4,4'-{benzene-1,2-diylbis[nitrilo(1 <i>E</i>)phen-1-yl-1-ylidene]}-dibenzene-1,3-diol ($\text{H}_2\text{L1}$) showing the relevant atom numbering.	17
Figure 2.2: Diagram of 4,4'-{ethane-1,2-diylbis[nitrilo(1 <i>E</i>)phenyl-1-yl-1-ylidene]}-dibenzene-1,3-diol ($\text{H}_2\text{L2}$) showing the relevant atom numbering.	18
Figure 2.3: Diagram of 4,4'-{propane-1,2-diylbis[nitrilo(1 <i>E</i>)phen-1-yl-1-ylidene]}-dibenzene-1,3-diol ($\text{H}_2\text{L3}$), with numbers shown for all non-hydrogen atoms.	19
Figure 2.4: Diagram of the ligand 4,4'-{(2-hydroxypropane-1,3-diyl)bis[nitrilo-(1 <i>E</i>)phen-1-yl-1-ylidene]}di-benzene-1,3-diol ($\text{H}_2\text{L4}$) showing the relevant atom numbering.	19
Figure 2.5: Diagram of 4,4'-{2,2-dimethylpropane-1,3-diyl}bis[nitrilo(1 <i>E</i>)phen-1-yl-1-ylidene]}dibenzene-1,3-diol ($\text{H}_2\text{L5}$).	20
Figure 2.6: Structure of the salen ligand.	21
Figure 2.7: Numbered diagram of the complex 2,2'-{benzene-1,2-diylbis-[nitrilo-(1 <i>E</i>)phen-1-yl-1-ylidene]}bis(5-hydroxyphenolate)-vanadyl ($[\text{VO}(\text{L1})]$).	21
Figure 2.8: Numbered diagram of 2,2'-{ethane-1,2-diylbis[nitrilo(1 <i>E</i>)phen-1-yl-1-ylidene]}bis(5-hydroxyphenolate)-vanadyl, $[\text{VO}(\text{L2})]$.	22
Figure 2.9: Numbered diagram showing the structure of 2,2'-{propane-1,3-diylbis-[nitrilo(1 <i>E</i>)phen-1-yl-1-ylidene]}bis(5-hydroxyphenolate)-vanadyl ($[\text{VO}(\text{L3})]$).	23
Figure 2.10: Numbered diagram for the vanadyl complex, 2,2'-{(2-hydroxypro-	24

pane-1,3-diyl)bis[nitrilo(<i>1E</i>)phen-1-yl-1-ylidene]]-bis(5-hydroxy-phenolate)vanadyl [VO(L4)].	
Figure 2.11: Numbered diagram of 2,2'-{(2,2-dimethylpropane-1,3-diyl)bis[nitrilo- (<i>1E</i>)phen-1-yl-1-ylidene]]bis(5-hydroxy-phenolate)-vanadyl, [VO(L5)].	25
Figure 2.12: Diagram of the structure of the complex [VO(salen)], synthesised as part of this study.	26
Chapter 3	
Figure 3.1: The steps involved in chelating vanadium to one of the tetradentate Schiff base ligands – shown is the procedure for [VO(L3)] synthesis. The steps are as follows: a) an amount of ligand is weighed-out; this is the limiting reactant; b) adding water to the ligand does not dissolve it, the pH must be adjusted to above 10 for dissolution of the ligand c); d) an excess amount of VOSO ₄ (typically 1.3:1) is added to the alkaline solution, turning it brown; e) lowering the pH to just above neutrality causes the complex to precipitate; f) the green precipitate can be isolated by filtration.	30
Figure 3.2: The IR spectra of H ₂ L2 and [VO(L2)] superimposed to show the change in frequencies caused by chelation of the vanadyl cation.	31
Figure 3.3: ¹ H NMR spectrum of H ₂ L3, showing integration, and assignment of peaks. The spectrum was recorded in DMSO-d ₆ at 298 K; the chemical shifts are referenced to the solvent.	32
Figure 3.4: ¹³ C NMR spectrum for H ₂ L3. Assignment of peaks is shown. The spectrum was recorded at 298 K in DMSO-d ₆ . The solvent was used as the reference for the chemical shifts.	33
Figure 3.5: ⁵¹ V NMR spectrum for [VO(L1)], recorded in DMSO-d ₆ at 298 K. NH ₃ VO ₃ is the reference peak that has been set in the acquisition parameters.	34
Figure 3.6: ⁵¹ V NMR spectrum for [VO(L2)] recorded in DMSO-d ₆ at 298 K. NH ₄ VO ₃ is the reference for the chemical shift.	34
Figure 3.7: ⁵¹ V NMR spectrum for [VO(L3)]. The spectrum was recorded in DMSO-d ₆ at 298 K. The reference for the chemical shifts is NH ₄ VO ₃ .	34
Figure 3.8: The ⁵¹ V NMR spectrum for [VO(L4)] measured in DMSO-d ₆ at 298 K. NH ₄ VO ₃ was used to reference the chemical shift of [VO(L4)].	35
Figure 3.9: Two possible geometrical coordination isomers for the complex [VO(L1)] that could give rise to the two ⁵¹ V peaks observed in the NMR spectrum for this compound. (Left) an isomer where the ligand shields the equatorial region of vanadium, and (right) where the ligand distorts to expose the vanadium.	35
Figure 3.10: ORTEP thermal ellipsoid plot of the Schiff base H ₂ L5 showing a 50% probability surface for carbon (black), nitrogen (blue) and oxygen (red). Hydrogen atoms are shown as spheres with an arbitrary covalent bond radius 0.37 Å.	37
Figure 3.11: Diagram of the crystal structure of H ₂ L5 showing the intramolecular hydrogen bonding, and the labelling scheme for the atoms involved.	38
Figure 3.12: Angle formed between the planes bisecting the aromatic rings on each iminium group. For the iminium with the longer N–H ⁺ bond length on the left, the angle formed by the planes is 89.3°, while for that with the shorter N–H ⁺ bond length, the smallest angle between the bisecting planes is 62.6°.	39
Figure 3.13: View of H ₂ L5 showing the gauche conformation about the iminium group with the shortened N–H ⁺ bond (highlighted within the black box).	40
Figure 3.14: View along the b-axis showing the CH–π bonding, responsible for propagating the crystal structure along the c-axis. Insert shows the groups responsible for this CH–π bonding.	41
Figure 3.15: View along the c-axis of the crystal structure, showing the extended crystal structure formed by intermolecular H-bonding.	41

Chapter 4

Figure 4.1: (Left) Electronic structure and transitions as set forth for an aqueous vanadyl ion, $[\text{VO}(\text{H}_2\text{O})_5]^{2+}$, in the Ballhausen-Gray theory. The unpaired electron occupies the b_2 molecular orbital formed by a 3d atomic orbital on vanadium; the d-d transitions on this electron are shown by black arrows. (Right) The location of the unpaired electron in the d orbitals; in its lowest energy state, it is in the non-bonding, d_{xy} orbital.	43
Figure 4.2: The spin state transitions for an electron with spin $S = 1/2$ coupled to a nucleus with $I = 1/2$. The nuclear spin results in two transitions being observed as the electron spin-state changes in the magnetic field.	44
Figure 4.3: The different orientations of ligand and the V–O unit, and how this influences which molecular orbitals interact with the donor atom's p-orbital.	48
Figure 4.4: Vanadyl complexes bearing resemblance to those under investigation, whose EPR and electronic absorption spectra have already been recorded.	48
Figure 4.5: Space group about the vanadyl ion that will be used in the interpretation of the electronic spectra observed for the complexes $[\text{VO}(\text{L1})]$, $[\text{VO}(\text{L2})]$, $[\text{VO}(\text{L3})]$, $[\text{VO}(\text{L4})]$ and $[\text{VO}(\text{L5})]$.	49
Figure 4.6: Powder EPR spectra for the oxovanadium (IV) Schiff base complexes: a) $[\text{VO}(\text{L1})]$, b) $[\text{VO}(\text{L2})]$, c) $[\text{VO}(\text{L3})]$, d) $[\text{VO}(\text{L4})]$ and e) $[\text{VO}(\text{L5})]$ recorded at 298 K. The outermost absorption peaks were used for the calculation of the parallel contribution to the hyperfine coupling constants.	51
Figure 4.7: Solution EPR spectrum of $[\text{VO}(\text{L1})]$ in chloroform (left) and DMSO (right) at room temperature.	54
Figure 4.8: EPR spectrum of $[\text{VO}(\text{L2})]$ in chloroform (left) and DMSO (right).	54
Figure 4.9: Chloroform (left) and DMSO (right) solution EPR spectra of $[\text{VO}(\text{L3})]$, recorded at room temperature.	55
Figure 4.10: EPR spectrum of $[\text{VO}(\text{L4})]$ in a DMSO solution at 298 K. Although the solvent generates a high level of noise, the typical eight-line spectrum for an oxovanadium(IV) species can be seen.	55
Figure 4.11: EPR spectrum of $[\text{VO}(\text{L5})]$ in a room temperature DMSO solution.	55
Figure 4.12: Overlay of the electronic absorption spectra for $[\text{VO}(\text{L1})]$ (green) and $\text{H}_2\text{L1}$ (blue). Labelled peaks correspond to the $\pi \rightarrow \pi^*$ transitions for the ligand and complex. Note how the intensity and of the $\pi \rightarrow \pi^*$ peaks has diminished, and how they have undergone a slight red-shift due to chelation of vanadium.	56
Figure 4.13: An overlay of $[\text{VO}(\text{L2})]$'s (green) and $\text{H}_2\text{L2}$'s (blue) electronic absorption spectra. The $\pi \rightarrow \pi^*$ transitions (peaks labelled A and B) for the aromatic rings can be clearly seen for both the free ligand, and the complex; however both the intensity and energy of the peaks have diminished as a result of complexation.	57
Figure 4.14: The electronic absorption spectra for $\text{H}_2\text{L4}$ (blue) and $[\text{VO}(\text{L4})]$ (green) overlaid on to each other. Peaks A and B correspond to the $\pi \rightarrow \pi^*$ transitions of the aromatic rings. The colour of $[\text{VO}(\text{L4})]$ is notably different from the other complexes, and arises due to lmct , labelled C, which is much stronger in this complex as compared to the others (see above figures and text).	57
Figure 4.15: Electronic absorption spectra over the spectral window where MLCT is observed for the complexes: a) $[\text{VO}(\text{L1})]$, b) $[\text{VO}(\text{L2})]$, c) $[\text{VO}(\text{L3})]$, d) $[\text{VO}(\text{L4})]$ and e) $[\text{VO}(\text{L5})]$. This transition occurs in the visible region of the spectrum, and is responsible for the green or brown colour of the complexes.	58
Figure 4.16: A typical fit of gaussian functions to the experimental data using the fityk software, to determine the position of underlying absorption bands. The example shown is for the region of d-d transitions for the complex, $[\text{VO}(\text{L2})]$.	59
Figure 4.17: The X-ray determined crystal structure of the similar Schiff base complex,	60

$\text{VO}(\text{H}_2\text{O})(\text{C}_{19}\text{H}_{20}\text{N}_2\text{O}_5) \cdot 2\text{C}_2\text{H}_4\text{Cl}_2$; figure modified from Ref. 88. In this complex, the hydroxyl group facilitated the binding of a solvent molecule *via* a hydrogen bond.

Chapter 5

- Figure 5.1:** The coordination geometry of oxoperoxovanadium complexes can be 63 described as (left) pentagonal-bipyramidal, or (right) pentagonal pyramidal. In the latter case, a seventh ligand is usually weakly associated with the axial position.⁷⁸
- Figure 5.2:** V–O bond lengths can vary depending on the position of the bound peroxide 63 relative to other ligands.⁷⁸
- Figure 5.3:** Schiff-base ligands used as chirality inducing oxidation catalysts, in conjunction 65 with hydrogen peroxide and vanadium(IV)/(V). Compound **a**) is one of the early ligands investigated by the Bolm group, while **b**) is a ligand developed by the Maeda group for sulfoxidations.
- Figure 5.4:** Structures of the three samples used as standards when evaluating the ⁵¹V 68 NMR spectra of the oxovanadium(IV) Schiff base complexes: **a**) vanadyl sulfate (VOSO_4), **b**) ammonium metavanadate (NH_4VO_3) and **c**) $[\text{VO}(\text{salen})]$ – a comparable oxovanadium(IV) Schiff base complex.
- Figure 5.5:** Spectral overlay of ⁵¹V NMR spectra for NH_4VO_3 , showing the effects of 69 addition of H_2O_2 . The bottom spectrum, a) is for NH_4VO_3 with no added H_2O_2 , b) when a drop of H_2O_2 has been added, and c) when an excess of H_2O_2 is added so as to completely convert all VO_3^- to the peroxo-species.
- Figure 5.6:** ⁵¹V NMR spectra of VOSO_4 in DMSO-d₆, a) before addition of peroxide, b) after 70 the addition of one drop of H_2O_2 , c) after sufficient peroxide is added to cause the solution colour to change from blue to yellow, and d), the same yellow solution after 15 hours.
- Figure 5.7:** ⁵¹V NMR spectral overlay for the titration of $[\text{VO}(\text{salen})]$ with H_2O_2 (6 % v/v) in 71 DMSO-d₆, having added: a) no H_2O_2 , b) 20 μl, c) 40 μl, d) 60 μl, e) 80 μl, f) 100 μl, g) 140 μl and h) 180 μl of H_2O_2 . All V(IV) species are completely consumed, and two large, sharp peaks form correlating to the peroxo- species.
- Figure 5.8:** Stacked ⁵¹V NMR spectra for the titration of $[\text{VO}(\text{L1})]$ with a solution of H_2O_2 (6 72 % v/v): a) 0 μl, b) 40 μl, c) 60 μl, d) 80 μl and e) 100 μl of H_2O_2 . The single, broad peak due to the V(IV) ion is gradually replaced by two sharper peaks of unequal intensity as the vanadium is oxidised and binds a peroxo-moiety.
- Figure 5.9:** ⁵¹V NMR spectra for the titration of $[\text{VO}(\text{L2})]$ (Ben-en) with an H_2O_2 solution in 73 DMSO: a) spectrum before addition of any H_2O_2 , b-f) 20 μl aliquots of H_2O_2 (6 % v/v) added for each one. Note that the developing peaks are much sharper, and also their intensity is much higher, relative to the one they are replacing.
- Figure 5.10:** Spectral overlay to show what the spectra of $[\text{VO}(\text{L3})]$ looked like after the 74 addition of the same amount of peroxide as had been added for the previous complexes: a) 20 μl, b) 40 μl, c) 60 μl, d) 80 μl, e) 100 μl and f) 140 μl H_2O_2 (6 %, v/v).
- Figure 5.11:** Overlay of all the spectra for the titration of $[\text{VO}(\text{L3})]$ with H_2O_2 (6 %, aq, v/v), 74 after the addition of a) 20 μl, b) 40 μl, c) 60 μl, d) 80 μl, e) 100 μl, f) 140 μl, g) 180 μl, h) 200 μl, i) 240 μl, j) 300 μl and k) 400 μl of the H_2O_2 solution. Interestingly, for this compound, the equilibrium between the two peroxo-species was shifted from one to the other as the concentration was increased. Also, the broad peaks corresponding to the initial vanadyl compound did not disappear, even after excessive amounts of peroxide had been added.
- Figure 5.12:** Overlays of the ⁵¹V NMR for $[\text{VO}(\text{L3})]$ after the addition of a) 200 μl, b) 400 μl 75 and c) 600 μl of H_2O_2 (6 %, aq, v/v) to show the change in intensity of the two ⁵¹V(V) peaks.
- Figure 5.13:** Overlay of ⁵¹V NMR spectra $[\text{VO}(\text{L4})]$ with serial additions of an H_2O_2 (6 %, aq, 75 v/v) solution. The aliquots were as follows: a) no H_2O_2 added, b) 10 μl, c) 20 μl, d) 30 μl, e) 50 μl, f) 70 μl, g) 90 μl, h) 130 μl, i) 230 μl and j) 330 μl H_2O_2 solution added.

Figure 5.14: ^{51}V NMR spectra for the titration of $[\text{VO}(\text{L5})]$ with H_2O_2 (6 %, aq, v/v). Spectra are for: a) no H_2O_2 , b)-f) successive 20 μl aliquots of the H_2O_2 solution.	76
Figure 5.15: The difference in chemical shifts between a DMSO solution, and internal DMSO reference solution caused by the addition of the paramagnetic compound $[\text{VO}(\text{L1})]$.	80
Figure 5.16: Proton resonance positions for (a), sealed internal reference DMSO and (b), DMSO exposed to the oxovanadium complex, $[\text{VO}(\text{L1})]$ after hydrogen peroxide had been added to the solution. The exposed DMSO's resonance has shifted upfield relative the sealed DMSO – contrary to the complex without hydrogen peroxide where a downfield shift was observed.	81
Figure 5.17: The difference in chemical shifts between the internal reference DMSO solution and the exposed DMSO for the solution containing $[\text{VO}(\text{L1})]$ and NaOH, which would oxidise the V(IV) to V(V). Note that the direction and magnitude of the chemical shift for the exposed sample is almost identical to that for the solution containing hydrogen peroxide.	82
Figure 5.18: Stacked spectra for the titration of $[\text{VO}(\text{L1})]$ with 0.02 M NaOH in 0.5 ml DMSO- d_6 : a, 0 ml NaOH, b, 20 μl NaOH, c, 40 μl NaOH, d, 60 μl NaOH, e, 80 μl NaOH, f, 120 μl NaOH, and g, 200 μl NaOH. The chemical shift of this species changes very little in comparison to that for the same compound with hydrogen peroxide. Their line shapes are also very different, which shows that they are not the same species.	83
Chapter 6	
Figure 6.1: The generalised notation used in describing the bond lengths and angles for the various Schiff bases. The choice of left and right when discussing symmetry is made by positioning the molecule so that the benzene rings are directed away from the viewer.	91
Figure 6.2: Optimised geometrical structure for the Schiff base ligand $\text{H}_2\text{L1}$.	91
Figure 6.3: Optimised geometrical structure for the Schiff base ligands $\text{H}_2\text{L2}$ (top), $\text{H}_2\text{L3}$ (middle) and $\text{H}_2\text{L4}$ (bottom).	92
6.4: Optimised geometrical structure for the Schiff base ligand $\text{H}_2\text{L5}$.	93
Figure 6.5: Electronic charge distribution over the Schiff base $\text{H}_2\text{L1}$. Values shown for the charge are fractions, rather than integers, and the charge is correlated to colour – green being positive and red, negative.	94
Figure 6.6: Electronic charge distribution over the Schiff base $\text{H}_2\text{L2}$. Values shown for the charge are fractions, rather than integers, and the charge is correlated to colour – green being positive and red, negative.	94
Figure 6.7: Electronic charge distribution over the Schiff base $\text{H}_2\text{L3}$. Values shown for the charge are fractions, rather than integers, and the charge is correlated to colour – green being positive and red, negative.	95
Figure 6.8: Electronic charge distribution over the Schiff base $\text{H}_2\text{L4}$. Values shown for the charge are fractions, rather than integers, and the charge is correlated to colour – green being positive and red, negative.	95
Figure 6.9: Electronic charge distribution over the Schiff base $\text{H}_2\text{L5}$. Values shown for the charge are fractions, rather than integers, and the charge is correlated to colour – green being positive and red, negative.	96
Figure 6.10: Overlay of the calculated (red) IR spectrum over the experiment (blue) IR spectrum for the ligand $\text{H}_2\text{L2}$.	97
Figure 6.11: Overlay of the calculated (red – in simulated DMSO medium) and experimental (yellow – 298 K in DMSO) electronic absorption spectra for the Schiff base ligand, $\text{H}_2\text{L5}$. The profile of the calculated spectrum matches that of the experimental one reasonable well; however the intensity and wavelength are significantly different.	99
Figure 6.12: DFT-calculated HOMO and LUMO for the ligand $\text{H}_2\text{L1}$ (A).	100

Figure 6.13: DFT-calculated HOMO and LUMO for the Schiff base ligands H₂L2 (B) , H₂L3 (C) , H₂L4 (D) and H₂L5 (E) .	101
Figure 6.14: Numbering/labelling scheme for the Schiff base ligands used for the assignment of the proton NMR spectra.	102
Figure 6.15: Labelling scheme for the ¹³ C chemical shift assignments for the Schiff bases.	104
Figure 6.16: Assignment of terminology for significant bonds and angles in the calculated oxovanadium(IV) Schiff-base complexes. [VO(L2)] is shown as an example complex. Symbols a-d represent the four angles formed between a two donor atoms and vanadium, while symbols e-h represent the angles formed between a donor, vanadium and the vanadyl O atom.	105
Figure 6.17: DFT-calculated geometry optimised structure for [VO(L1)] (right); the pseudo-squarepyramidal geometry of vanadium and its displacement from the basal plane are highlighted (left).	107
Figure 6.18: Calculated structures showing the optimised geometry for the oxovanadium(IV) Schiff base complexes: b) (l, r) [VO(L2)], c) (l, r) [VO(L3)], d) (l, r) [VO(L4)] and e) (l,r) [VO(L5)], where “l” is “left” and “r” is “right.” The blue plane in the left-hand side figures is the calculated plane connecting the donor atoms; vanadium’s displacement from this plane and its pseudo-squarepyramidal geometry can be seen here.	108
Figure 6.19: RMS fit between the DFT-calculated complexes: a) [VO(L1)], b) [VO(L2)], c) [VO(L3)], d) [VO(L4)] and e) [VO(L5)] and the crystal structures of related compounds MAHVIB, ABUZAY, NECCUT, BEGHEB and HOWVUK, respectively. Crystal structures were obtained from the CSD.	109
Figure 6.20: Atomic charge distribution for the complexes [VO(L1)] (top) and [VO(L2)] (bottom). Charge is displayed fractionally, and correlated to colour – green being positive and red, negative.	111
Figure 6.21: Natural atomic distribution over the complexes [VO(L3)] (top) and [VO(L4)] (bottom). Values shown for the charge are fractions, rather than integers, and the charge is correlated to colour – green being positive and red, negative.	112
Figure 6.22: Natural charge distribution for the complex [VO(L5)]. The colour on each atom is correlated to the charge localised to the nucleus; green represents a positive charge, while red represents a negative charge. Values are given as fractions, rather than integers.	113
Figure 6.23: DFT calculated HOMO and LUMO for the complexes: A , ([VO(L1)]); B , ([VO(L2)]); C , ([VO(L3)]) and D , ([VO(L4)]) The extensive, conjugated π character on each complex can be clearly seen in these diagrams.	116
Figure 6.24: DFT calculated HOMO and LUMO for the oxovanadium(IV) complex [VO(L5)], (E). The conjugated system responsible for the strong π→π* transitions can be clearly seen in this diagram.	117
Figure 6.25: Overlay of the simulated and experimentally determined UV-Visible spectra for [VO(L2)] to show similarities in line shape, and differences in predicted absorption peaks.	117
Chapter 7	
Figure 7.1: Typical growth/inhibition curve for determining the IC ₅₀ value of a compound. Concentration is plotted against the total cell population relative to a control population. The concentration at which 50 % of the cell population has been prevented from growing is determined to be the IC ₅₀ value of the compound in question.	119
Figure 7.2: Bar graph of the tested compounds and their contrasting agents showing the	122

negative logarithm of the concentration of the compounds required to inhibit 50 % of the cell population's growth for the cancer cell lines A549 (blue), TK-10 (green), HT29 (red) and U251 (purple).

Figure 7.3: $-\log(\text{IC}_{50})$ values for selected standard agents for the cancerous cell lines123
A549, HT29, TK-10 and U251. Agents shown are those that displayed cytotoxicity comparable to the oxovanadium(IV) complexes at a final concentration of *ca* 50 μM .

Chapter 8

Figure 8.1: A ligand that should have an electron donating ability similar to the iminium129
donors of the Schiff base ligands studied in this body of work.

List of Tables

Table 3.1: Ranges of decomposition for the ligands H₂L1 , H₂L2 , H₂L3 , H₂L4 and H₂L5 , as well as selected differences between the compounds. The number of carbon atoms between connecting the imine nitrogens appears to play a significant role in the thermal stability of the compounds.	31
Table 3.2: Hydrogen bond geometry.	38
Table 4.1: Frequencies, band-names and magnetic field strengths (in Tesla) of commercially available EPR spectrometers.	45
Table 4.2: Donor groups and the contribution they make to the parallel hyperfine coupling constant, A_{\parallel} . (values stated are in units of $\times 10^{-4} \text{ cm}^{-1}$). Table adapted from Ref. 20.	47
Table 4.3: average, parallel and perpendicular g and A tensors for the oxovanadium(IV) Schiff base complexes.	50
Table 4.4: Isotropic g values and hyperfine coupling constants for the vanadyl complexes in chloroform and DMSO determined from spectra recorded at 298 K.	54
Table 4.5: The approximate wavelength of maximum absorbance for the vanadyl complexes and the absorption intensity associated with each one.	59
Table 5.1: A summary of the ^{51}V chemical shifts for the standard and test samples, and selected distances between them.	72
Table 5.2: Differences in location of chemical shift for DMSO samples that were isolated or exposed to vanadium species in different oxidation states.	80
Table 5.3: Summary of the initial, major and minor peaks formed due to the addition of sodium hydroxide to the oxovanadium(IV) Schiff base complexes in a DMSO-d ₆ solution.	84
Table 6.1: Selected DFT-calculated bond lengths and angles for the intramolecular hydrogen-bonding groups of the Schiff bases, and the experimentally determined values for H₂L5 .	90
Table 6.2: The selected highest positive and negative charge locations for a single atom for the Schiff base ligands, and the charge on the iminium proton.	94
Table 6.3: Selected calculated and experimentally determined values for vibrational frequencies of the Schiff base ligands, and the percentage difference between the two values.	98
Table 6.4: Selected calculated and experimentally determined electronic absorption peaks for the Schiff-base ligands. The orbitals most responsible for this transition, their hybridisation character and oscillator strength are also given.	100
Table 6.5: Selected experimental and calculated proton chemical shifts for the Schiff bases, and the percentage differences between the corresponding values.	103
Table 6.6: Selected experimental and calculation carbon chemical shifts for the ligands, and the percentage differences between corresponding values.	104
Table 6.7 Summary of significant calculated bond lengths and angles of the coordination	107

sphere about the vanadyl centre for the oxovanadium(IV) Schiff-base complexes. [VO(L1)], [VO(L2)], [VO(L3)], [VO(L4)] and [VO(L5)].

Table 6.8: Selected calculated values for charge distribution in the oxovanadium complexes.	111
Table 6.9: Selected calculated and experimental vibrational frequencies for the oxovanadium(IV) Schiff base complexes, and the percentage difference* between the two values.	114
Table 6.10: Selected calculated and experimentally determined electronic absorption peaks for the oxovanadium(IV) Schiff base complexes. The orbitals most responsible for this transition, their hybridisation character and oscillator strength are also given.	115
Table 7.1: Negative logarithms of the IC ₅₀ (M) values for the oxovanadium(IV) complexes and the contrasting agents [Au(dppe) ₂]Cl and cisplatin, on the cancerous cell lines A549, HT29, TK-10 and U251.	121
Table 7.2: Standard anticancer agents that had comparable activity to the vanadyl complexes for the tumour cell lines A549, HT29, TK-10 and U251. The structure of each, and their mode of cytotoxicity are shown (continued on following page).	124

List of Schemes

Scheme 1.1: Catalytic cycle of the vanadium-dependent haloperoxidases; “e” represents the enzyme to which the cofactor is attached.	7
Scheme 1.2: The two possible modes of adduct formation for [VO(salen)] and derivative complexes.	14
Scheme 3.1: Typical reaction pathway for synthesis of Schiff-base ligands. The amine attacks the electron deficient carbonyl carbon, resulting in hemiaminal formation and then dehydration to form the imine.	27
Scheme 3.2: Synthetic procedure for H ₂ L1; the second step is performed by removing solvent from the reaction mixture, and continuing to add heat.	28
Scheme 3.3: Tautomeric forms that are possible with <i>o</i> -hydroxy Schiff base species: (a) keto-amine, (b) phenol-imine and (c) zwitterionic	36
Scheme 4.1: Deprotonation of aromatic hydroxyl groups with the tertiary amine <i>N,N</i> -dimethyloctylamine to facilitate dissolution in chloroform.	52
Scheme 5.1: The two possible binding modes of peroxide are, a) side-on and b) end-on.	62
Scheme 6.1: (left) an oxovanadium(IV) complex whose structure was optimised using DFT at the B3LYP/6-31G(d) level of theory, which achieved a close correlation to the experimentally determined crystal structure. (right) a representation of the polymerisation that can occur with vanadyl Schiff base complexes, and two of the complexes examined. DFT was used to determine the magnetic exchange between the vanadyl units for a number of Schiff base complexes, when in this arrangement, as a means to better predicting their EPR spectra.	88
Scheme 8.1: Alkylation of the hydroxyl group at position 4 of 2,4-dihydroxybenzophenone using potassium hydroxide and an alkyl halide to produce a vanadyl complex with enhanced solubility.	127
Scheme 8.2: Assumed mode of protection for the oxide at position 2 of the substituted benzyl ring is <i>via</i> coordination to potassium.	127
Scheme 8.3: The reactant thianthrene-5-oxide and the two products it can form with a peroxo-metal complex depending on the reaction mechanism.	128

List of Equations

1.1(a).....	4
1.1(b).....	4
1.2.....	6
1.3.....	11
1.4.....	11
1.5.....	12
1.6.....	12
1.7.....	12
1.8.....	12
4.1.....	44
5.1.....	62
5.2.....	62
5.3.....	62
5.4.....	64
5.5.....	79
5.6.....	79
5.7.....	79
5.8.....	81
5.9.....	84
7.1.....	87
7.2.....	87

List of Boxes and Charts

Box 1.1: The regulation of radicals.....	12
Box 5.1: Derivation of bulk magnetic susceptibility from a NMR chemical shifts.....	79
Chart 5.1: Distribution of ^{51}V resonance in ppm. Values are relative to VOCl_3 . Highlighted.....	67
bars show the typical distribution for the species of interest in this study, namely vanadates – formed by oxidation of vanadyl, and peroxovanadium(V). Distribution for other species shown is for comparison.	

Abstract

A series of five, tetradentate Schiff-base ligands were synthesised and chelated to vanadyl to form oxovanadium(IV) complexes. The ligands, 4,4'-{benzene-1,2-diylbis[nitrilo(1E)phen-1-yl-1-ylidene]}-dibenzene-1,3-diol (**H₂L1**), 4,4'-{ethane-1,2-diylbis[nitrilo(1E)phenyl-1-yl-1-ylidene]}dibenzene-1,3-diol (**H₂L2**), 4,4'-{propane-1,2-diylbis[nitrilo(1E)phen-1-yl-1-ylidene]}dibenzene-1,3-diol (**H₂L3**), 4,4'-{(2-hydroxypropane-1,3-diyl)bis[nitrilo(1E)phen-1-yl-1-ylidene]}dibenzene-1,3-diol (**H₂L4**) and 4,4'-{2,2-dimethylpropane-1,3-diyl}bis-[nitrilo(1E)phen-1-yl-1-ylidene]}-dibenzene-1,3-diol (**H₂L5**), characterised by TOF-MS, IR, electronic absorption, ¹H and ¹³C NMR spectroscopy. The ligand **H₂L5** was also characterised by XRD. The ligands were shown to have a bis-zwitterionic structure in the solid state, and possibly also in solution. Complexes were characterised by Elemental Analysis, TOF-MS, IR, electronic absorption spectra, EPR and ⁵¹V NMR spectroscopy. They form mononuclear complexes, with one ligand binding a single vanadyl ion.

EPR spectroscopy was performed on both the powdered form and solutions of the complexes. All the complexes displayed axial symmetry, with increasing distortion from an ideal square pyramidal geometry as the size and bulk of the central chelate ring was increased. Isotropic *g*₀ values suggest solvent interaction with the vanadium ion for the coordinating solvent DMSO. Additional distortion on the coordination geometry, presumably from the benzyl groups of the compounds, causes the isotropic hyperfine coupling constants to be greater than expected.

Furthermore, the ability of the complexes to bind peroxide species was investigated by following the addition of H₂O₂ to the complexes using ⁵¹V NMR spectroscopy to observe shielding changes at the vanadium nucleus, and ¹H NMR spectroscopy to monitor the bulk magnetic susceptibility, *via* a modified Evan's NMR method. Similar experiments were done with sodium hydroxide for comparison. As expected, the oxoperoxovanadium(V) complexes were more stable than their progenitor oxovanadium(IV) complexes. Additionally, increasing the distortion from the ideal pseudo square-pyramidal coordination geometry for the vanadyl ion resulted in a greater increase in the apparent stability of the peroxo-complexes. This latter effect is further enhanced by the addition of a hydrogen-bonding group in close proximity to the vanadium nucleus.

DFT calculations of the optimized geometries, natural bond orbitals, electronic absorption and infra-red frequencies were performed for both the ligands and the complexes; nuclear magnetic resonance calculations were performed for the ligands as well. The B3LYP/6-311G (d,p) and B3LYP/LANL2DZ level of theories were used for the ligands and complexes respectively, except for electronic transitions, which were calculated using TD-SCF methods for both ligands and complexes. Calculated and experimental results were compared where possible, and showed reasonable agreement for all calculations performed. The exception to this was for the NMR calculations for the ligands, which were poorly simulated.

Finally, the *in vitro* biological activity of the complexes was evaluated for cytotoxicity against the human tumour cell lines: A549, U251, TK-10 and HT29, *via* an MTT assay. All complexes showed promising anticancer activity, as evidenced by their low IC₅₀ values for the cell lines A549, U251 and TK-10, which are in general, lower than that observed for cisplatin. They did, however, express negligible activity against the HT29 colon adenocarcinoma cell line; showing an apparent selectivity for certain cell lines. These oxovanadium(IV) complexes, thus warrant further evaluation as chemotherapeutic agents.

Contents

Declaration	ii
Acknowledgements	iii
List of Abbreviations and Symbols	iv
List of Figures	vii
List of Tables	xii
List of Schemes	xiv
List of Equations	xv
List of Boxes and Charts	xv
Abstract	xvi
Chapter 1 <i>Introduction</i>	1
1.1 Vanadium: a metal of beauty and strength	1
1.2 Vanadium coordination chemistry	1
1.2.1 Low oxidation states and organometallics	2
1.2.2 Vanadium(IV) coordination complexes	2
1.2.3 Vanadium(V) coordination complexes	3
1.3 Vanadium in biological systems	4
1.3.1 Biological vanadium complexes	4
1.3.2 Proteins involved in vanadium transport and binding	5
1.3.3 Vanadium-requiring enzymes	6
1.3.3.1 Nitrogenases	6
1.3.3.2 Haloperoxidases	7
1.4 Medicinal features and applications of vanadium complexes	7
1.4.1 Insulin mimic	7
1.4.2 Parasites	8
1.4.3 Cancer	8
1.4.3.1 Vanadium's effect on cell proliferation	9
1.4.3.2 Vanadium's cytotoxic effects –apoptosis	10
1.4.3.3 Anti-proliferative effects	10
1.4.3.4 Effect of vanadium compounds on drug-resistance	11
1.4.3.5 <i>In vivo</i> mechanisms	11
1.5 Oxovanadium(IV) complexes of the salen, and salen like, ligands	13
1.5.1 Chemistry of oxovanadium(IV) Schiff base complexes	13
1.5.2 Biological activity of oxovanadium(IV) Schiff base complexes	14
1.6 Aims of Project	15
Chapter 2 <i>Experimental</i>	17
2.1 General Procedures	17
2.1.1 Materials	17
2.1.2 Characterisation procedures	17
2.2 Synthesis of Schiff base Ligands	17
2.2.1 Synthesis of 4,4'-{benzene-1,2-diylbis[nitrilo(1E)phen-1-yl-1ylidene]}- dibenzene-1,3-diol (H ₂ L1)	17

2.2.2 Synthesis of 4,4'-{ethane-1,2-diylbis[nitrilo(1E)phenyl-1-yl-1-ylidene]}-Dibenzene-1,3-diol (H ₂ L)	18
2.2.3 Synthesis of 4,4'-{propane-1,2-diylbis[nitrilo(1E)phen-1-yl-1-ylidene]}-Dibenzene-1,3-diol (H ₂ L3)	19
2.2.4 Synthesis of 4,4'-{(2-hydroxypropane-1,3-diyl)bis[nitrilo(1E)phen-1-yl-1-ylidene]}dibenzene-1,3-diol (H ₂ L4)	19
2.2.5 Synthesis of 4,4'-{(2,2-dimethylpropane-1,3-diyl)bis[nitrilo(1E)phen-1-yl-1-ylidene]}dibenzene-1,3-diol (H ₂ L5)	20
2.2.6 Synthesis of <i>N,N'</i> -disalicylaethylenediamine (Salen)	21
2.3 Synthesis of Oxovanadium(IV) Schiff base complexes	21
2.3.1 Synthesis of 2,2'-{benzene-1,2-diylbis[nitrilo(1E)phen-1-yl-1-ylidene]}-bis(5-hydroxyphenolate)vanadyl ([VO(L1)])	21
2.3.2 Synthesis of 2,2'-{ethane-1,2-diylbis[nitrilo(1E)phen-1-yl-1-ylidene]}-bis(5-hydroxyphenolate)vanadyl ([VO(L2)])	22
2.3.3 Synthesis of 2,2'-{propane-1,3-diylbis[nitrilo(1E)phen-1-yl-1-ylidene]}-Bis(5-hydroxyphenolate)vanadyl ([VO(L3)]).	23
2.3.4 Synthesis of 2,2'-{(2-hydroxypropane-1,3-diyl)bis[nitrilo(1E)phen-1-yl-1-ylidene]}-bis(5-hydroxyphenolate)vanadyl ([VO(L4)])	24
2.3.5 Synthesis of 2,2'-{(2,2-dimethylpropane-1,3-diyl)bis[nitrilo(1E)phen-1-yl-1-ylidene]}bis(5-hydroxyphenolate)vanadyl ([VO(L5)])	25
2.3.6 Synthesis of <i>N,N'</i> -bis(o-hydroxybenzylidene)ethylenediamine vanadyl ([VO(salen)])	26
Chapter 3 <i>Synthesis and Spectroscopic Characterisation and X-ray Diffraction</i>	27
3.1 Synthesis	27
3.1.1 Ligands	27
3.1.2 Complexes	28
3.2 Characterisation	30
3.2.1 Melting points	30
3.2.2 Infrared spectroscopy	31
3.2.3 NMR spectroscopy	32
3.3 X-ray Diffraction	35
3.3.1 Description of Zwitterion X-ray structures	35
3.3.2 X-ray structure determination of H₂L5	36
3.3.3 Discussion of X-ray structure of H₂L5	36
Chapter 4 <i>Electronic Spectroscopy</i>	43
4.1 Introduction	43
4.1.1. EPR spectroscopy – the technique	44
4.1.2 EPR spectroscopy – application to vanadyl systems	46
4.1.3 Theoretical assumptions	48
4.2 Experimental	49
4.3 EPR spectroscopy	49
4.3.1 Powder EPR spectroscopic study	49
4.3.2 Solution EPR spectroscopic study	51

4.4 Electronic absorption spectroscopy	56
4.4.1 $\pi \rightarrow \pi^*$ transitions	56
4.4.2 Transitions of the unpaired electron – MLCT	58
4.5 Conclusion	61
Chapter 5 <i>Hydrogen peroxide binding studies</i>	62
5.1 Background	62
5.1.1 Hydrogen peroxide – structure and properties	62
5.1.2 Peroxide-vanadium interactions	63
5.1.2.1 Structure of Peroxo-complexes	63
5.1.2.2 Formation of peroxovanadium complexes	64
5.1.3 Oxovanadium Schiff-base complexes and their interaction with peroxide	65
5.1.4 Speciation of oxoperoxovanadium(V) complexes	65
5.1.5 ^{51}V NMR Spectroscopy	66
5.2 H_2O_2 titrations – monitored by ^{51}V NMR spectroscopy	67
5.2.1 General procedure	67
5.2.2 Results and Discussion	68
5.2.2.1 Standard samples	68
5.2.2.2 Oxovanadium(IV) Schiff base complexes	71
5.3 Magnetic susceptibility	78
5.4 Titration with NaOH	82
5.5 Conclusion	84
Chapter 6 <i>Computational Chemistry</i>	87
6.1 Introduction	87
6.1.1 Theoretical aspects of DFT	87
6.1.2 Previous use of DFT for vanadyl complexes	88
6.2 Computational method	89
6.3 Computational results for the Schiff base ligands	89
6.3.1 Geometry optimisation results for the Schiff bases	89
6.3.2 Natural bond orbital analysis for Schiff bases	93
6.3.3 Vibrational frequency analysis for Schiff base ligands	96
6.3.4 Electronic transition calculations for ligands	98
6.3.5 NMR simulations for the Schiff base ligands	102
6.4 Computational results for the oxovanadium(IV) complexes	105
6.4.1 Geometry optimisation results for the oxovanadium(IV) complexes	105
6.4.1.1 General notation	105
6.4.1.2 Coordination geometry–bond distances	106
6.4.1.3 Coordination geometry–bond angles	106
6.4.2 Natural bond orbital analysis for the oxovanadium(IV)Schiff-base complexes	110
6.4.3 Infrared vibrational frequency results	113
6.4.4 Electronic transition calculations for the vanadium(IV) complexes	114
6.5 Summary and Conclusions	118

Chapter 7 In Vitro <i>anticancer activity</i>	119
7.1 Cell lines used	119
7.2 Cell Culture and drug assay method	120
7.3 Results and discussion	120
7.3.1 Activity of oxovanadium(IV) Schiff base complexes	120
7.3.2 Comparable compounds	122
7.4 Conclusions	125
Chapter 8 <i>Conclusions and Future Work</i>	126
8.1 Conclusions	126
8.2 Future work	129
8.2.1 Improving solubility	129
8.2.2 Exploring H ₂ O ₂ -mediated reactions	130
8.2.3 Enhancing understanding of EPR spectra	130
8.2.4 Further evaluation of biological activity	131
References	132
Appendix A <i>IR, UV-vis, NMR and EPR spectra</i>	141
A.1 IR spectra	141
A.1.1 Ligands	141
A.1.2 Complexes	142
A.2 UV-vis spectra	143
A.3 NMR spectra	143
A.3.1 ¹ H NMR spectra	143
A.3.2 ¹³ C NMR spectra	145
A.3.3 ⁵¹ V NMR spectra	148
Appendix B <i>Crystallographic Data Tables</i>	149
B.1 Crystallographic data tables for H₂L5	149
Appendix C <i>Comparisons of Experimental and DFT-calculated spectra</i>	153
C.1 UV-vis spectral overlays	153
C.2 IR spectral overlays	154
Appendix D (on CD)	
D.1 DFT Output files	
D.2 CIF file	

Chapter 1 | Introduction

1.1 Vanadium: a metal of beauty and strength

Vanadium derives its names from the Norse deity *Vanadis* (Figure 1.1a), who was the goddess of beauty and war. This is because vanadium displays a wide range of colours throughout its different oxidation states.¹ Vanadium comprises up to 0.05% of the earth's crust, making it the fifth most abundant transition metal in the earth's crust; estimated total abundance is 0.014%. The element is mainly used in ferrovanadium alloys, which are employed in the manufacture of tough, high speed steels among others (Figure 1.1b).² Major world producers of vanadium are Russia, China and South Africa, and it is thus a highly important economic mineral for the RSA.³ Vanadium was also the name of an Italian, heavy-metal rock band with bad hair-styles – fortunately, they will not be discussed further here (Figure 1.1c).

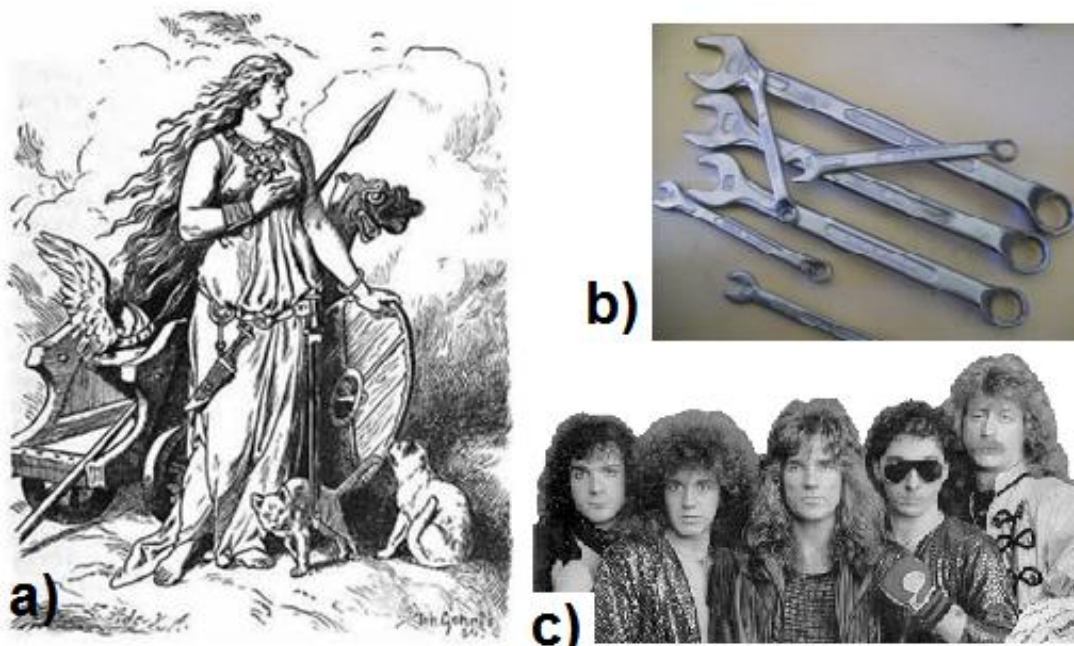


Figure 1.1: a) the Norse goddess, *Vanadis*, after whom the element is named, b) tools made from a chrome-vanadium alloy, and c) Italian heavy metal rock band, *Vanadium*.

The pure metal is silvery-white, malleable and ductile, with a melting point of 1770 °C. It crystallises in the octahedral space group $O_h^9-Im\bar{3}$, with $Z=2$, which is a body-centred cubic lattice.⁴ Up to seven oxidation states are known for the metal, viz. -3, -1, 0, +1, +2, +3, +4 and +5, with the last four states being the most common. Typically, the +4 oxidation state dominates the coordination chemistry of the element.

1.2 Vanadium coordination chemistry

Much of the interest in vanadium coordination chemistry has come about as the result of the discovery of several vanadium-dependent enzymes and complexes.⁵ These are responsible for catalysing a number of crucial organic reactions involving both oxidation and reduction. These will be dealt with in more detail later though. For now, only the general chemistry will be considered.

A wide range of complexes have been synthesised for the oxidation states, +2, +3, +4 and +5. The chemistry of these complexes is characterised by the metal's ability to change oxidation states. Different spectroscopic techniques are applicable for different oxidation states, e.g. NMR spectroscopy is useful for probing the V(V) coordination environment (^{51}V having a high natural abundance of 99.76%),⁶ while EPR spectroscopy can give valuable information on the nature of the ligand coordinated to V(IV) ($[\text{Ar}4\text{d}^1]$) through the single electron that is strongly coupled to the nucleus.⁷

1.2.1 Low oxidation states and organometallics

The low oxidation states are only known with strong-field ligands that can stabilise them.⁸ They are usually formed by complexing vanadium in a higher oxidation state with the suitable ligands, and then reducing it with a strong reducing agent, such as Mg or LiAlH_4 . They decompose readily if exposed to the air or if heated to between 100-200 °C. Organovanadium compounds are somewhat different, however, and have stabilities comparable to those of other early transition metal complexes. Practical applications of organovanadium complexes are in the areas of catalysis, such as Ziegler-Natta catalysis,⁹ to name but one, organic synthesis, for the preparation of alkanes and alkynes,¹⁰ and as potential medical compounds, e.g. vanadocene dichloride shows antitumour activity.¹¹ The alkyne and alkene complexes also serve as functional models in deciphering the activity of nitrogenases.¹²

1.2.2 Vanadium(IV) coordination complexes

While the lower oxidation states are not stable, the higher numbers, being V(III), V(IV) and V(V) are the most commonly encountered in coordination chemistry. Of these, V(IV) is the most stable; V(III) (aq) is readily oxidised to V(IV) by air, and V(V) will revert to V(IV) if even a mild reducing agent is administered.¹³ The oxovanadium cation is thus a very important species, which predominates in aqueous solutions. The chemistry of vanadium(IV) is dominated by the vanadyl ion $[\text{VO}]^{2+}$, and this is of special interest within the scope of this study; it will thus be considered in greater detail. The rest of the coordination chemistry for V(IV) consists of tetradentate halide complexes, VX_4 .

The vanadyl ion is one of the most stable oxometal species known; through most reactions, it will remain unchanged.¹⁴ This stability is postulated to originate from its ground state electronic configuration, $[\text{Ar}]3\text{d}^1$, which is similar to that of the d^9 system of Cu^{2+} .¹⁵ Complexes with highly electronegative atoms, *viz.* F, Cl, O and N, are the most favoured, although S-donors are also known.¹⁶ These are typically green to blue-green in colour, depending on the donor strength. X-ray crystal structures of these complexes show that the V=O bond, at 1.57 to 1.68 Å, is shorter than other V–O bonds, testifying to its double-bond character.¹⁷

There are a number of spectral and physical properties typical for vanadyl complexes that are fairly indifferent to the ligand(s) coordinated. One is the IR stretching frequency of the vanadyl ion, which is located at approximately 980 cm^{-1} for a mononuclear complex; however, note that occasionally, aggregation of vanadyl complexes occurs when the vanadyl ions coordinate to one another in a linear fashion.^{18,19} This has the effect of lowering the stretching frequency for the vanadyl ion to approximately 840 cm^{-1} . The other distinguishing property is their magnetic moment, μ_B , which typically lies within the value of $1.73\ \mu_B$ – correlating to the spin-only value for one electron.²⁰ Magnetic exchange forces are however not generally present, with the orbital contribution between

neighbours being quenched. This affects the EPR spectrum as well in that superhyperfine coupling is not usually observed for vanadyl complexes. The unpaired electron does not couple to the neighbouring nuclei to a significant extent.²⁰ Dimerisation of vanadyl species can have an effect on the magnetic moment.²¹ In these systems, there develops a pairwise magnetic exchange, which results in a greatly lowered value for μ_B ; usually between 0.77 and 1.55 μ_B . The colour of these complexes, depending on whether dimerisation or polymerisation occurs, changes from green to orange-brown.

Structurally, the vanadyl ion tends to form five-coordinate, square pyramidal complexes; trigonal bipyramidal complexes are also known, though.²² The structure is often not strictly square pyramidal, i.e. the L–V=O angle is usually greater than 90°, so that the vanadyl unit lies above the basal plane formed by the other donors. Coordination of a sixth axial ligand *trans* to the V=O bond is dependent on the nature of the hetero-ligand(s) bonded in the equatorial positions. The weaker the donors of this hetero-ligand are, the more likely it will be that an additional ligand can be axially coordinated.²³ However, this coordination is very weak, and the ligand is usually substitutionally very labile. The figure of [VO(acac)₂] (Figure 1.2) demonstrates all the above mentioned principles for vanadium complexes, *viz.* the V=O double bond, the distorted square pyramidal structure and the vacant site for axial coordination.

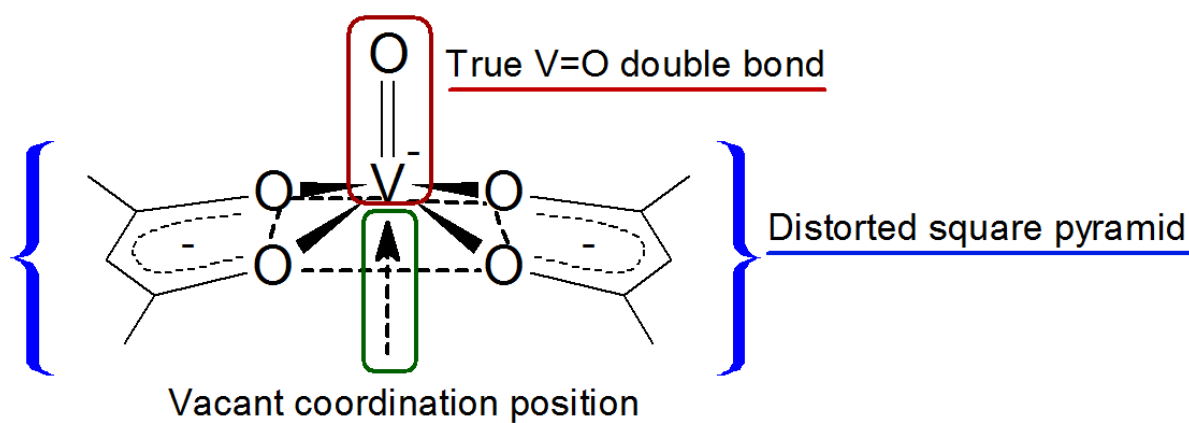


Figure 1.2: The complex [VO(acac)₂] showing its square pyramidal coordination geometry and the vacant orbital position for an additional ligand.

1.2.3 Vanadium(V) coordination complexes

Vanadium(V), although not the principal state of vanadium dealt with in this study, does play a role in the catalytic and biological functioning of vanadium-dependent enzymes, as well being the oxidation state involved with peroxide coordination, the importance of which will be revealed later. It is thus worthwhile to briefly consider this species.

V(V) is the highest possible oxidation state for the metal; its d^0 electronic configuration leads to diamagnetic properties,⁶ making it amenable to NMR spectroscopy. Complexes of V(V) would be colourless, if not for charge-transfer processes between the ligand and metal.¹⁶ A number of halide complexes are known, but the most of the chemistry involves an oxo-species.¹⁷ The VO³⁺ unit is capable of forming bonds with a diverse range of donors, including F, Cl, Br and N-containing heterocycles such as pyridine.²⁵ The VO₂⁺ unit (dioxovanadium(V)) will also form bonds with an

assorted range of donors, including halides, nitrates and N-donor heterocycles.²⁶ This VO_2^+ unit is linear, but the two oxygens have non-identical bond lengths to the vanadium centre, typically 1.60 and 1.56 Å.²⁷ Their IR stretching frequencies also differ, typically falling between 970 and 960 cm^{-1} . Crystallographic evidence points to each of the two oxygens as being doubly bonded to the vanadium, i.e. in an O=V=O conformation. VO_2^+ can be formed by dissolving V_2O_5 in strongly acidic solutions. V_2O_5 is the most common, naturally occurring form of vanadium,¹³ and hence is the most likely form to be encountered by organisms. V_2O_5 is also an acidic oxide, and hence, can be dissolved in alkaline solutions as well to give the $[\text{VO}_4]^{3-}$ (vanadate) ion.

As mentioned above, the most stable oxidation state of vanadium is +4. This can be seen in values for the reduction potentials (E°) for the half-reactions shown below (Equation 1.1a and b).¹³ Here, V(V) reduction to V(IV) is large and positive, at 1.0 V, and the reduction of V(IV) to V(III) is smaller, at 0.34 V. Therefore, neutral or mildly reducing solutions will favour the reduction of VO_2^+ to VO^{2+} , while air is sufficient to cause oxidation of V^{3+} to VO^{2+} .



Equation 1.1: The two half-reactions for the vanadium conversions from +4 to +3 (a) and from +5 to +4 (b). Note that both E° values are positive, indicating that they are favourable reactions as written.

1.3 Vanadium in biological systems

Vanadium is widely spread in the biosphere, with many compounds and proteins that either interact with it or utilise it directly in a structural task. In mammals, it is found in very low concentrations of only 10 nmol L^{-1} on average.^{28,29}

1.3.1 Biological vanadium complexes

Many biological molecules form complexes with vanadium. The siderophores are proteins usually used to sequester iron from the environment, but they also appear to have a secondary role as vanadium binders.²⁹ Vanadate seems to interact with, and inhibit the transport of, the iron-siderophore complex, thus regulating iron transport.

Other metabolites are known to form complexes with vanadium as well, namely carbohydrates, nucleotides, glutathione (GSH), cysteine and ascorbic acid. Of these, GSH has been the most extensively studied.²⁹

Perhaps one of the best known examples of a biological vanadium complex is that of amavadine (Figure 1.3).²⁹ Amavadine occurs in the *Aminita* genus of mushrooms. The complex consists of a vanadium (IV) cation bound to two *N*-hydroxyl-2,2'-iminodipropionic acid ligands in a chiral manner. Also, there are four chiral carbons on the ligands themselves; each with an S configuration.

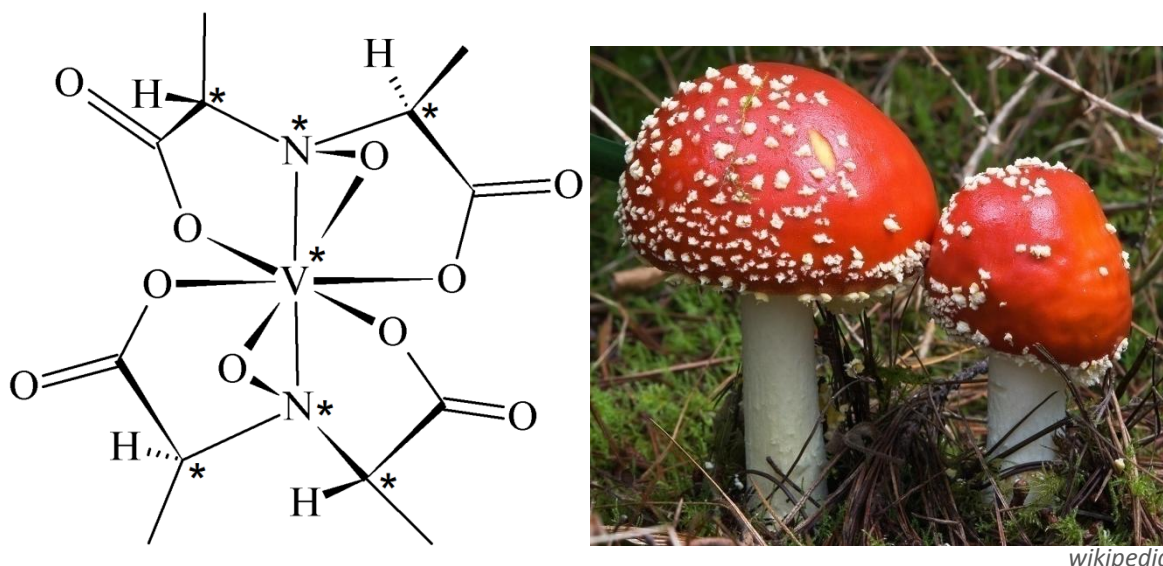


Figure 1.3: (Left) Structure of amavadinium, showing the chiral centres (*) on the ligands, as well as the chiral arrangement of the ligands around the metal. (Right) Mushrooms of the genus *Amanita*.

1.3.2 Proteins involved in vanadium transport and binding

Vanadium from the environment can enter cells either as an oxygen bound anion, or as a cation; mechanisms of uptake range from facilitated diffusion through cell membranes to energy-dependent binding by specialised proteins.

Vanadium is mainly gathered in high concentrations by lower plant species, such as the fungi, lichens and mosses. In the mushroom species mentioned above, for example, the concentration of vanadium can be as high as 2 mmol/kg of dry weight. Interestingly, the highest concentrations of the element are found in the Ascidiacea (350 mmol/L), more commonly known as ascidians, or “sea squirts” (Figure 1.4).³⁰ Of interest is how the various oxidation states of vanadium are exploited for its uptake, transport and storage. Initially, a divalent metal transport system is responsible for the transport of vanadium(V) across the plasma membrane. V(V) is reduced to V(IV) inside the cytoplasm, where it is then bound by vanabin, which transports the V(IV) to the vacuole. Inside the vacuole, V(IV) is reduced to V(III), and is stored there in this oxidation state.

Vanabins form a unique class of metallochaperone proteins; they are the only proteins known to specifically bind vanadium, with a binding affinity of 2×10^{-5} M.²⁹ To date, these proteins have only been found in ascidians. The proteins are composed of four α -helices, which are linked by nine disulfide bonds. They contain amine-bearing amino acids, such as arginine, lysine and histidine, which are responsible for binding the VO^{2+} cations. Each protein binds approximately 10 to 20 vanadyl cations.

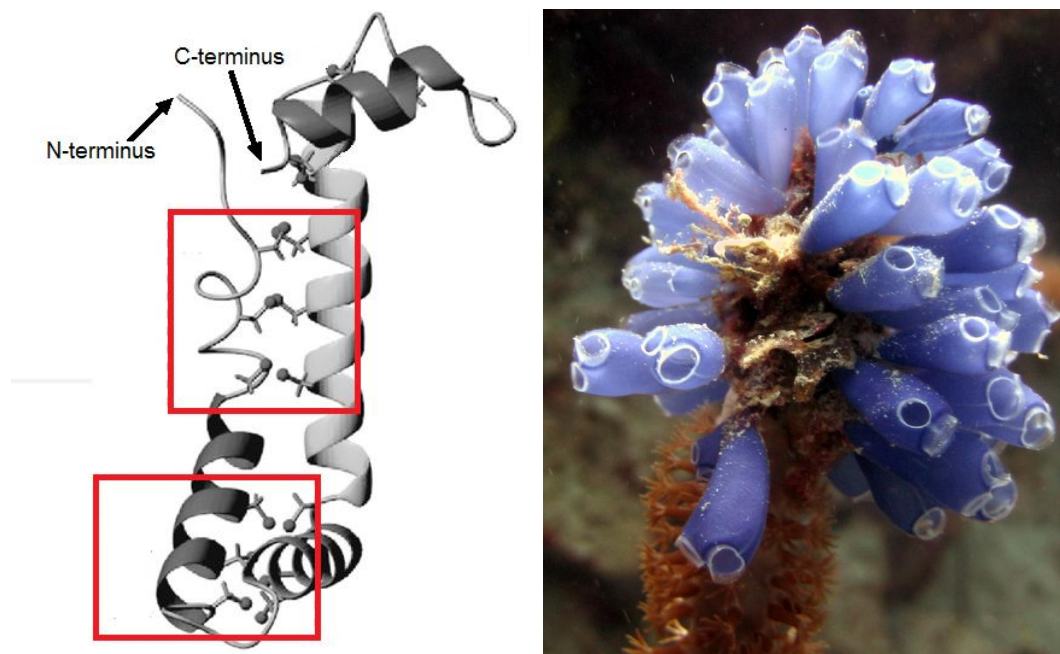


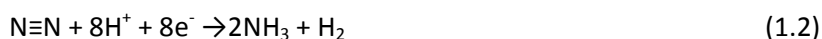
Figure 1.4: (Left) 3-D model of the transport protein, Vanabin2. Vanadium binding sites are highlighted by the red boxes (picture modified from Ref. 32). (Right) the Blue-Bell tunicate, an ascidian; no other group of organisms on the planet sequester more vanadium from the environment, relative to their body weight, than these ones.³¹

In animals, there are dedicated transport proteins to transport vanadium across cell membranes and between the various cellular compartments, but they lack any transporters in their bodily fluids. Rather, fluid transport of vanadium occurs *via* its binding to proteins that are non-specific for the metal.

1.3.3 Vanadium-requiring enzymes

There are two classes of proteins that make use of vanadium for their functioning, the nitrogenases³³ (found in bacteria) and the haloperoxidases³⁴ (found in algae, fungi and lichens).

1.3.3.1 Nitrogenases: vanadium-dependent nitrogenases are nitrogen fixing enzymes that make use of an iron-sulfur-vanadium cluster.³² This is analogous in both structure and function to the molybdenum-iron cofactor of other nitrogenases. Not much information is known about this enzyme, although it is believed that the vanadium is in the +3 oxidation state. The overall reaction is:

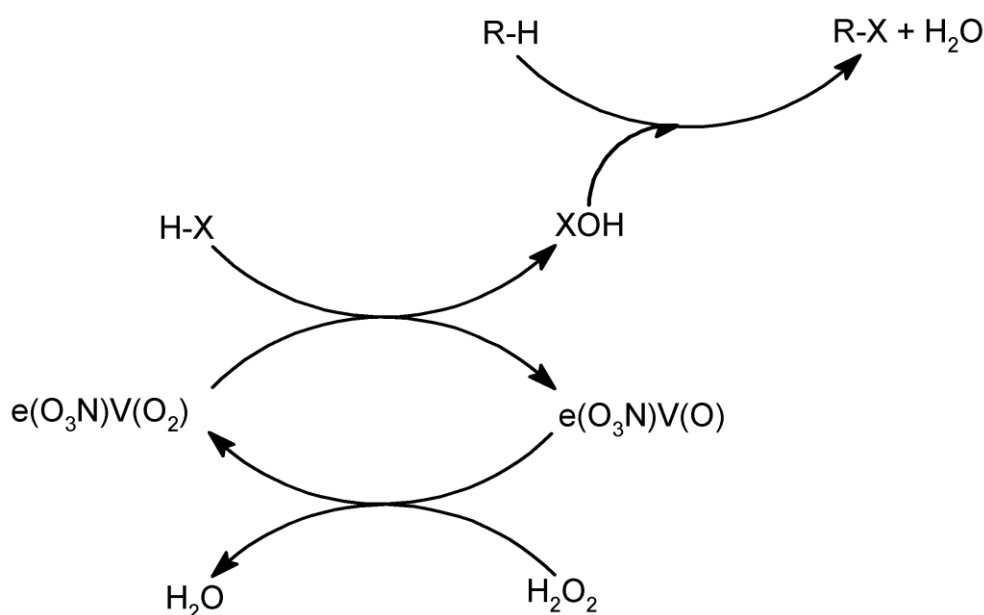


Here, vanadium does not serve as the main element of choice for the cell, but is rather used as a substitute when molybdenum is not available. It was the discovery of vanadium-dependent nitrogenases, though, that was partially responsible for the increased interest in vanadium chemistry in general. The ability to reduce atmospheric dinitrogen *via* a catalytic pathway that is both efficient and facile is highly desirable. The actual mechanism of nitrogen cleavage and reduction of this vital enzyme is entirely unknown.²⁹

1.3.3.2 Haloperoxidases: much like the nitrogenases, haloperoxidases can be divided into two classes: iron-haeme based and vanadium dependent.³³ Iron-haeme haloperoxidases are found in

mammals, while the vanadium derivatives are found in most other organisms. The function of haloperoxidases is to catalyse the oxidation of halogens – in higher organisms, this serves as a vital protective function against halogenated pathogenic substances. They are named according to their electronegativity, *i.e.* to the most electronegative halide they can oxidise. For example, a bromoperoxidase can oxidise both bromides and iodides, but is unable to oxidise chlorides.

These vanadium-dependent enzymes are mainly employed by the lower organisms to generate organic halides.³³ Hydrogen peroxide (H_2O_2) provides the oxidative power in this reaction. H_2O_2 is first bound by the vanadium cofactor, where, once bound, a water molecule is cleaved off and two electrons are donated to the complex. The complex then donates the oxygen to a halogen to form a reactive halogen species. It is this species that then becomes incorporated into an organic compound (Scheme 1.1).



Scheme 1.1: Catalytic cycle of the vanadium-dependent haloperoxidases; “e” represents the enzyme to which the cofactor is attached.

1.4 Medicinal features and applications of vanadium complexes

1.4.1 Insulin mimic

Insulin is the chemical signalling molecule (cytokine) that promotes uptake of glucose when its levels in the blood increase, thus promoting carbohydrate metabolism. Insulin functions by initiating the insulin signalling cascade, a series of phosphorylation and dephosphorylation steps. In diabetic individuals, insulin is either not secreted, or the receptors for the protein become unresponsive. However, certain phosphorylation/dephosphorylation steps can be initiated by vanadium compounds.³⁵ The advantage of vanadium compounds over the traditional strategy of administering insulin injections is that vanadium compounds are orally available. This could potentially reduce the treatment for diabetes to taking an oral supplement.

Inorganic salts of V(IV) and V(V) have been extensively tested, both *in vivo* and *in vitro*, and some of the findings have been very encouraging. V(V) compounds that were orally administered to diabetic animals were able to restore, either partially or completely, the activity of several organs involved in glucose regulation. The main goal of their development has since focused on reducing the harmful side-effects of prolonged vanadium administration.

Evaluation of compounds for activity *in vitro* usually involves testing the compounds for inhibition or stimulation of phosphotyrosines phosphatases (PTPases) or tyrosine kinases, respectively. The vanadium complex with maltol, bis(maltolato)oxovanadium(IV) (BMOV), has become the standard reference compound for these and other tests.³⁶ The ethyl version of this compound is currently undergoing clinical trials. [VO(salen)] has also been tested, and was found to effectively lower glucose levels when administered orally (Figure 1.5).

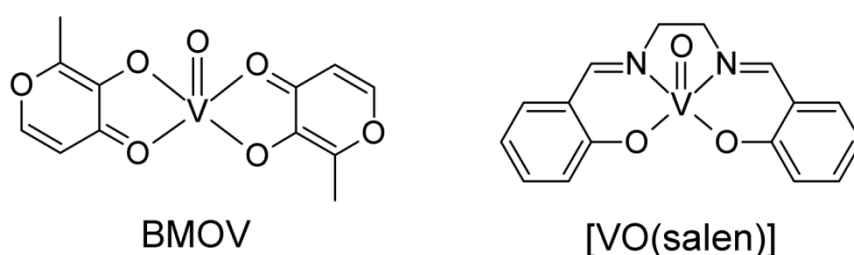


Figure 1.5: Two vanadium complexes tested for insulin mimetic properties: (left) bis(maltolato)oxovanadium(IV) (BMOV), one of the most well characterised compounds, is used as a reference for the evaluation of new insulin mimetic candidates; (right) (*N,N'*-disalicylidineethylenediamine)oxovanadium(IV) ([VO(salen)]), a Schiff base compound that has shown encouraging results.

1.4.2 Parasites

In addition to insulin mimicking, vanadium complexes have also been explored as anti-parasitic agents, particularly against Trypanosomes, Leshmania, and Amoebas.³⁷ The reasoning behind this is that many compounds that are effective against human cancers are also effective against these human parasites. This research is still in its infancy, although early results have been promising. For a more detailed discussion on the potential of vanadium complexes for this application, the reader is directed to the review by Gambino.³⁷

1.4.3 Cancer

The first sign that vanadium compounds could be effective chemotherapeutic agents was in 1965 when Kieler, Gromek and Nissen showed that certain salts displayed antineoplastic effects.³⁸ When *cis*-platin was discovered, also in the 1960's, this triggered an interest in metal-based treatments for cancer. Vanadium interest was further sparked by English *et al*¹¹ and Thompson *et al*,¹¹ who found that vanadium salts inhibited terminal differentiation of cancer cells, and also inhibited induced mammary carcinogenesis respectively. Furthermore, it seemed that [VO(SO₄)] was possibly also a preventative agent in the diet.¹¹

Since then, many examples of vanadium compounds with different oxidation states and ligands have been examined for chemotherapeutic properties. Rather than attempting to discuss every

compound that has been examined, it would be more pertinent to examine the general effects vanadium compounds can have on cancerous cells, and the mechanisms by which they function.

There are four criteria that must be met by any compound if it is to be used as an anti-cancer drug. Firstly, the compound must have an anti-proliferative effect on the cancer cells; being able to arrest the cell-cycle at some point. Secondly, a cytotoxic, or at least cytostatic, effect must be present as well. This effect can be in the form of induced apoptosis (programmed cell death) or just as necrosis. Thirdly, the ability of the cancerous cells to spread and invade healthy tissue must be completely or partially inhibited. Lastly, the compounds must not cause the cancerous cells to develop drug resistance, either against itself or other anti-cancer compounds that may be administered. Ideally, the compound will decrease the extent of drug-resistance of the aberrant cells. In vanadium compounds, all four of these criteria can be met.^{11,38} How it achieves this for each of the above will be considered in further detail.

1.4.3.1 Vanadium's effect on cell proliferation: In general, it is not so much a matter of the vanadium compound, but rather, the amount of the compound administered that affects cell proliferation.¹¹ At low concentrations ($< 10^{-10}$ M), vanadium species will encourage cell proliferation, and it is only as the concentration increases ($> 10^{-10}$ M) that the proliferation of tumour cell colonies is suppressed.³⁹ The mode of the suppression appears to be related to the compounds ability to arrest the cell cycle at the G₂-M phase, i.e. cell growth is stopped at the point before mitosis.⁴⁰ Interestingly, if the concentration given is low enough, then the inhibitory effects can be reversed on withdrawal of the vanadium species, but at higher concentrations, the inhibition of cell propagation is irreversible.¹¹ These are encouraging results, as the side-effects of vanadium compounds on healthy cells could potentially be mitigated if the compound was directed primarily to cancerous cells only.

There are several mechanisms by which vanadium species may exert their inhibitory effects, however, the primary means seems to be by inhibiting PTPases.^{11,39} This, as we shall see, is major cause of most of vanadium's activity *in vivo*. Although there are many processes where PTPase is needed, one of them is in phosphorylating the p34^{cdc2} subunit of the p34^{cdc2}-cyclin complex. This complex is needed to induce mitosis, and without the phosphorylation of p34^{cdc2}, it cannot occur.⁴¹

Other mechanisms include the V(IV) mediated activation of p38 mitogen activated protein kinase (MAPK), which signals for the eventual production of nuclear transcription factor- κ B (NF- κ B).⁴² NF- κ B affects the cell cycle and may also lead to apoptosis. Anti-proliferative effects may also be the result of direct damage to the DNA, rather than through a signalling cascade.⁴³ Vanadocene dichloride (Figure 1.6) is a well-known complex that interacts with the DNA in a non-covalent fashion, altering its transcription, *etc.*⁴⁴ Other V(IV) and V(V) species have been shown to cause breaks in the DNA strand (both single and double) either through direct interaction or indirectly through reactive oxygen species generation.

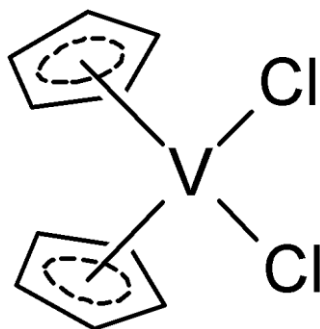


Figure 1.6: Structure of vanadocene dichloride, an organometallic vanadium compound, and one of the most promising of the cyclopentadienyl complexes tested against cancer. It forms labile complexes with DNA, rather than covalent ones, as does cisplatin.

1.4.3.2 Vanadium's cytotoxic effects – apoptosis: Drugs can exert their cytotoxic effect on cancer cells either through necrosis, or apoptosis. Necrosis is the destruction of a cell from non-nuclear changes, i.e. by direct damage of the membrane and organelles. Apoptosis involves cell death mediated by nuclear changes, and is commonly known as programmed cell death. It is a normal part of cell life-cycle, but, if the process malfunctions, the result can lead to cancer. Vanadium compounds, by and large, exert their cytotoxic properties *via* apoptosis.¹¹

As mentioned, vanadium species can inhibit PTPases and activate tyrosine kinases. Phosphorylation is used in the signalling process, either activating or deactivating many of the cytokines (chemical signalling molecules) present in the cells. When these two proteins are inhibited and activated, respectively, an accumulation of phosphorylated proteins will occur.¹¹ These cytokines are necessary for growth, differentiation, transformation and apoptosis. In addition to the p34^{cdc2}-cyclin complex, vanadium species can regulate the extent and duration of phosphorylation for the signalling proteins: AP-1, ERK-1, NF- κ B, PI-3K, JNK-1 and MEK-1.¹¹ These proteins signal for pathways linked to DNA damage prevention and reactive oxygen species (ROS) protection. Of the cytokines mentioned, NF- κ B has the most dramatic effect on gene regulation.

NF- κ B, although linked to activities such as inflammation and cell-cycle suppression, does not necessarily cause apoptosis. When it is being activated, it can stimulate the expression of genes related to both cell protection and death. The exact nature of the response will depend on what type of cell is being treated, the exact identity of the vanadium compound used, and the concentration which is being delivered to the cell.^{45,46,47} Hence, the vanadium species used and its concentration will determine whether or not apoptosis will be stimulated or inhibited.

Vanadium induced production of ROS may also lead to apoptosis. Cell damage caused by ROS can induce an upsurge of cytochrome-C production, which in turns leads to activation of caspases. Certain caspases can cause even more cell damage and activation of additional substrates that ultimately results in apoptosis.⁴⁸

1.4.3.3 Anti-proliferative effects: Cancer cells proliferate when they detach from a malignant tumour and re-attach elsewhere in the body. Vanadium compounds can prevent them from re-attaching, and thus confer anti-proliferative effects.¹¹ Again, this occurs *via* stimulating phosphorylation of regulatory proteins. Tyrosine phosphorylation regulates activity of cell-to-cell and cell-to-matrix

adhesion proteins, as well as actin proteins.^{49,50} Actin is a cytoskeletal protein needed to transport adhesion molecules, amongst others, through the cell cytoplasm to where they are needed.

Even simple vanadium compounds can also inhibit the generation of adhesion proteins. Vanadate has been shown to deactivate PTPases,⁵⁰ leading to a decrease in the concentration of tumour necrosis factor (TNF), which is a major inducer of adhesion proteins. Furthermore, an increase in tyrosine phosphorylation prevents aggregation of cells by inhibiting cadherin, a major protein required for this process.⁵¹ Orthovanadate, vanadate and vanadyl can all inhibit platelet aggregation by blocking PTPase activity as well; endothelial cell adhesion can be prevented in this way.¹¹

1.4.3.4 Effect of vanadium compounds on drug-resistance: Multi-drug resistance can either be enhanced or decreased by vanadium compounds.¹¹ In general, at low concentrations, vanadium species tend to activate drug resistance in a reversible fashion, while at higher concentrations, resistance is inhibited and is non-reversible. The mode of action is likely to be related to vanadium-related inhibition of ATPases and actin fibres.⁵² ATPase is necessary to produce the energy needed for the P-glyco-protein (P-gp) pump, which acts as a drug efflux pump when needed.⁵²

1.4.3.5 In vivo mechanisms: The above four points illustrated the nature of vanadium's activity. It is of course necessary to understand the chemistry behind this activity.

The pH of the *in vivo* environment is such that, vanadium in any other oxidation state besides +4 is rapidly oxidised or reduced to vanadyl (VO^{2+}), depending on whether the species introduced is +3 or lower or +5 respectively.²⁹ Also, physiological conditions vary between healthy and cancerous cells. In a typical cancer cell, the pH is lower, there is more H_2O_2 , levels of anti-oxidant enzymes are reduced and the volume of H_2O is higher.⁵³ In these conditions, it is possible for vanadium to generate free radical/ROS through several different pathways. These are typically chain reactions, and so a little vanadium is needed for each one. The major product of these reactions that affects cell cycle is the hydroxyl radical, OH^\bullet .⁵⁴

In general, the two most likely reactions to occur are:⁵³



and



In Equation 1.3, a vanadyl ion is oxidised when it forms a complex with H_2O_2 , and cleaves it to produce a hydroxyl radical. Reducing conditions will rapidly revert the V(V) to a V(IV) species. In Equation 1.4, V(IV) forms a complex with superoxide ($\text{O}_2^{\bullet-}$), and reduces it to form a hydroxide ion and a hydroxyl radical. Hydroxyl radicals formed can form $\text{O}_2^{\bullet-}$ from dissolved O_2 . This diradical is rapidly converted by superoxide dismutase (SOD) to hydrogen peroxide, which is then free to bind the vanadium species present.⁵³ In this way, the cycle repeats.

As mentioned, once V(V) species have been formed, they will rapidly undergo reduction, usually by the action of glutathione-reductase or NAD(P)H. Reduction of V(V) to V(IV) can generate additional hydroxyl radicals. This would be an example of a Fenton-like reaction.⁵⁵

In addition to these processes, V(IV) species can form peroxovanadyl (V(IV)–OO[•]) and vanadyl hydroperoxide (V(IV)–OOH[•]) complexes when V(V) reacts with superoxide.⁵⁶ These processes are shown in Equations 1.5, 1.6 and 1.7.



Firstly, V(IV) is oxidised directly by O₂ to form V(V); the dioxygen is reduced to form superoxide (Eqn. 1.5). V(V) then binds superoxide to form a complex (Eqn. 1.6). When this complex is reduced by NAD(P)H, a hydroperoxide vanadyl complex forms (Eqn. 1.7). Either of the complexes formed in Eqn. 1.5 or 1.6 will then undergo decomposition by superoxide dismutase; forming H₂O₂ (Eqn. 1.8). H₂O₂ is the necessary substrate for the main hydroxyl radical producing pathways of vanadium (Eqn. 1.2). Therefore, the radical production cycle can be maintained, even in conditions where H₂O₂ has been depleted, provided there is sufficient O₂.¹¹



Peroxides promote the inhibition of tyrosine phosphatases, leading to the accumulation of tyrosine phosphorylated proteins (TPPs). At a critical concentration of these TPPs, a respiratory burst occurs, which increases the concentration of superoxide radicals, maintaining the catalytic cycle.⁵⁷

Much has been said about vanadium's ability to inhibit the phosphorylating enzymes. This is caused in part by radicals formed; however, the hydroxyl radicals have a very short half-life (< 1 ns). As such, they react very close to their point of origin. Their predominant reaction with enzymes, such as tyrosine phosphorylase, is because of vanadium's stereo- and coordination chemistry. Vanadium compounds are able to mimic an analogue of the transition state for these enzymes, and bind to their cysteine residues.⁵⁸ Thus, when a radical is formed, they will react with the enzyme, inhibiting it.

Vanadium complexes are also able to mobilise iron stored in iron-sequestering proteins, *e.g.* ferritin. Iron is released in the +2 oxidation state, and is as a result able to participate in Fenton reactions with H₂O₂.¹¹ This generates even more hydroxyl radicals, adding to the effects caused by the vanadium compounds. For a more detailed look at the role of radicals, see Box 1.1.

Box 1.1: The regulation of radicals.

It is considered that the “primary” radical formed *in vivo* is the superoxide (SO) radical, O₂^{•-}.⁵⁹ Decomposition of this radical to form other “secondary” radicals is not particularly fast. However, there is an enzyme that catalyses this reaction; this enzyme is known as superoxide dismutase (SOD).⁶⁰ SOD catalyses the conversion of superoxide to H₂O₂ by a rate of four orders of magnitude faster than normal. Under normal cellular conditions, proteins are present that remove H₂O₂ from the cytosol, such as catalase. In cancerous cells, concentrations of these proteins are lower than required, and H₂O₂ levels subsequently increase.⁵³

The redox activity that would generate these radicals is determined predominantly by the concentration of free iron. Usually, there is very little free iron; however, under stressful oxidative

conditions (as when vanadium is generating superoxide) – particularly the generation of excess amounts of superoxide – iron can be released from storage molecules. Typically it is the 4Fe-4S clusters that are oxidised to release Fe(II).⁶¹ Fe(II) released participates in Fenton reactions ($\text{Fe(II)} + \text{H}_2\text{O}_2 \rightarrow \text{Fe(III)} + \text{OH}^\bullet + \text{OH}^-$). The Fe(III) so formed can be reduced by numerous reagents, which include $\text{O}_2^{\bullet-}$ ($\text{Fe(III)} + \text{O}_2^{\bullet-} \rightarrow \text{Fe(II)} + \text{O}_2$).⁶² Hence, once there is an excess amount of superoxide, iron gets released, increasing the oxidative stress yet further, and perpetuating the radical generating cycle.

1.5 Oxovanadium(IV) complexes of the salen, and salen like, ligands

N,N'-disalicylalethylenediamineoxovanadium(IV), [VO(salen)], and its derivatives are one of the more commonly encountered groups of compounds. As such, many of their properties have been extensively studied, and their chemistry is well understood. In addition to their chemistry, their biochemistry has also been investigated for various properties, the most common of which is for cancer chemotherapy. These two aspects, their chemistry and medicinal applications, will be considered in the following two sections.

1.5.1 Chemistry of oxovanadium(IV) Schiff base complexes

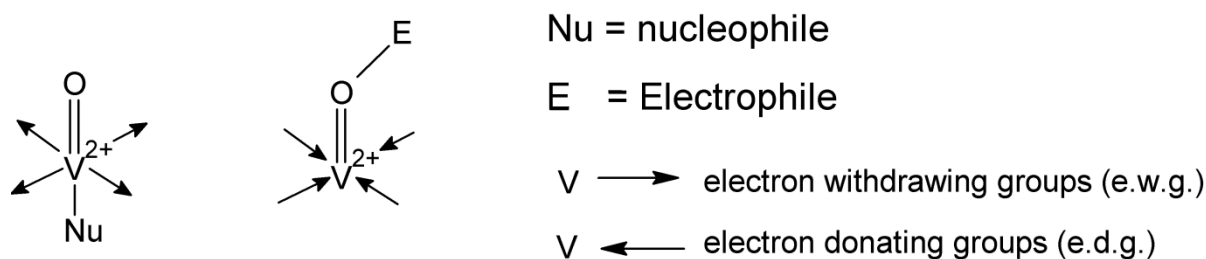
One of the most widely used Schiff base ligands is the salen ligand. It is a Schiff base compound, with a tetradentate, N,N,O,O donor set. The salen ligand was first used to coordinate to cobalt(II); the procedure is very robust, and was published very early on in *Inorganic Syntheses*.⁶³ The ligand and its derivatives are ideally suited for chelating the vanadyl species, as they are able to stabilise vanadium in a wide range of oxidation states, while still leaving a coordination position vacant. Because of this vacant position on the vanadium centre, it is free to participate in other reactions.^{64,65}

Vanadium typically adopts a pseudo-square-pyramidal coordination geometry when a tetradentate ligand is bonded to the vanadyl unit. Reactions of these five-coordinate complexes can occur at either the vacant, axial position, or at the vanadyl's O atom.⁶⁶ If the vanadium becomes oxidized during the course of a reaction, the metal's coordination geometry changes to octahedral. It will also move into the plane of the tetradentate ligand's donor atoms.⁶⁷

Literature regarding the reactivity of the vanadyl O atom is very scarce. However, the little research that has been done has yielded insightful results. Vanadyl can act as a donor group to group 14 and 15 Lewis acids. Bonds form through the O atom, and have the structure of V–O–M. An example of such a structure is the adduct with [VO(salen)]–Ph₃SnCl.⁶⁸ Here, the bond forms spontaneously when the two complexes are mixed together in acetonitrile. Although the number of vanadium complexes investigated is limited, it appears that the most reactive complexes are those with the most electron rich co-ligands.⁶⁹ The salen ligand, with its aromatic system, was found to confer the most reactivity on the vanadyl (VO²⁺) cation. This has important implications, as coordination by the vanadyl unit seems to be implicated in a number of reducing reactions for the complexes.

In stark contrast to the above class of vanadyl O-atom reactions, reactions involving the vacant axial site on vanadium have been well studied. These usually, but not always, involve the concomitant oxidation of V(IV) to V(V).⁷⁰ Adducts of the vanadyl complexes and a coordinating anion can be easily synthesised from an oxovanadium(IV) precursor.^{71,72} An oxidizing agent must be added (for example,

perchloric acid) to form the vanadate. Usually, any anions present that can coordinate will do so. If the anion is unable to do so, a cationic complex will form with a neutral donor so that the vanadate has an octahedral geometry; the anion will then occupy the outer coordination sphere (Scheme 1.2).



Scheme 1.2: The two possible modes of adduct formation for [VO(salen)] and derivative complexes.

Adducts can also be synthesised, such that there is a bridge between two vanadium centres, or even a bridge between vanadium and a different metal, $\text{M}-\text{O}-\text{V}=\text{O}$.^{73,74,75,76} Depending on the reactions conditions, either a di- μ -hydroxo-bridge forms (Figure 1.7 a), or a single hydroxo anion bridges the two V(V) centres (Figure 1.7 b), in the latter case, the charge is balanced by an anion in the outer coordination sphere. The oxidation can be accomplished by a salt, such as NH_4PF_6 , which does not coordinate, or by a coordinating oxidizing agent. This can be displaced to form the divanadium complex.

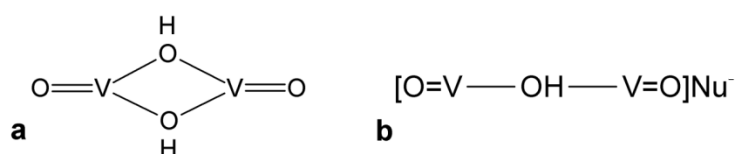


Figure 1.7: Examples of hydroxo-bridged vanadium dimers, a) with two hydroxo anions, and b) with one hydroxo anion and a non-coordinating nucleophile.

The ability of these VO(salen)-type complexes to form adducts with anions, and their general robustness has seen them find application as oxidation catalysts.⁷⁰ Although the exact oxidising agent may vary, in general it is a peroxide; the most notable ones being hydrogen peroxide, H_2O_2 , and tertiary-butyl hydrogen peroxide, *t*-BuOOH.^{77,78} Dioxygen has also been used to provide the oxidising force for these reactions, but this is a less common approach.⁷⁰ Oxidations catalysed by these vanadium compounds include epoxidations, oxidations of alkenes to alcohols, alcohols to aldehydes or ketones, aldehydes to carboxylic acids and sulfoxidations.⁷⁹ The activity of the catalyst is highly dependent on the nature of electron withdrawing/donating groups attached to the ligand, however. The less electron density the ligand donates, the higher the reactivity of the vanadyl for these oxidation reactions. This is the opposite of that needed for vanadyl O-atom donation.

1.5.2 Biological activity of oxovanadium(IV) Schiff base complexes

For use against cancerous cells, only a limited number of investigations of [VO(salen)] complexes and their derivatives have been performed. [VO(salen)] has been tested for its hydrogen peroxide and superoxide scavenging abilities,⁸⁰ as well as its ability to interfere in the iron-driven Fenton reaction leading to the peroxidation of liver homogenate, in relation to its potential use as a chemopreventative agent. In leukemic K562 cells, it was able to arrest cell cycle development at the

G2/M phase, i.e. it was chemostatic and was also a sensitizer of the cells towards taxol.⁸¹ Chemopreventative action was also conferred on Weister rats, which had been injected with CCl_4 .⁸⁰

Hydroxyl-derivatives of [VO(salen)] were tested for their DNA cleaving ability (Figure 1.8).⁴³ Activity was only achieved in the presence of an activator, which could be either a reducing or oxidising agent. The compound with hydroxyl groups at the *para*-position to the imine groups on the aromatic ring was found to be the most effective in inducing strand breaking (Figure 1.8c). Hydroxyl groups are implicated in the compound's ability to associate with guanidine bases of the DNA.

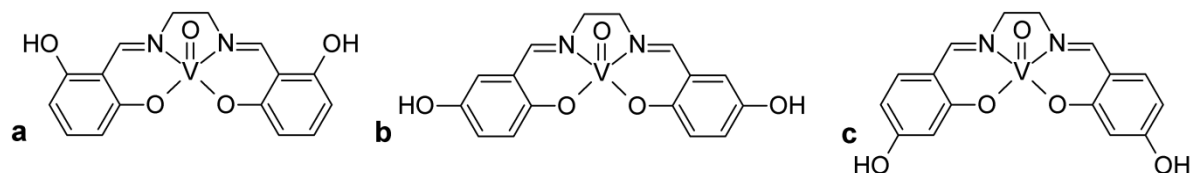


Figure 1.8: Hydroxy-salen oxovanadium(IV) complexes able to induce DNA strand breakage. Compound **c**, with the hydroxyl groups in the *para*-position, was the most effective in causing DNA strand breakage.

1.6 Aims of project

- To synthesise five novel, salen-derived ligands, with aromatic substituents on the imine carbon (Fig. 1.9).
- To chelate oxovanadium(IV) with these ligands, to form a series of novel and stable oxovanadium(IV) Schiff base complexes (Fig. 1.10).
- To characterise the synthesised ligands and V(IV) complexes by mass spectrometry, infrared, UV-vis, EPR and NMR spectroscopy, determine their melting/decomposition-point temperatures, and where possible, to perform single-crystal X-ray diffraction determinations.
- To determine the V(IV) complexes' ability to bind hydrogen peroxide, and to follow these reactions by ^{51}V NMR.
- To perform computational studies on the Schiff base ligands and oxovanadium(IV) complexes with a view to determining their bonding geometries and potential reaction sites.
- To perform preliminary investigations into the vanadium compounds' anticancer properties.

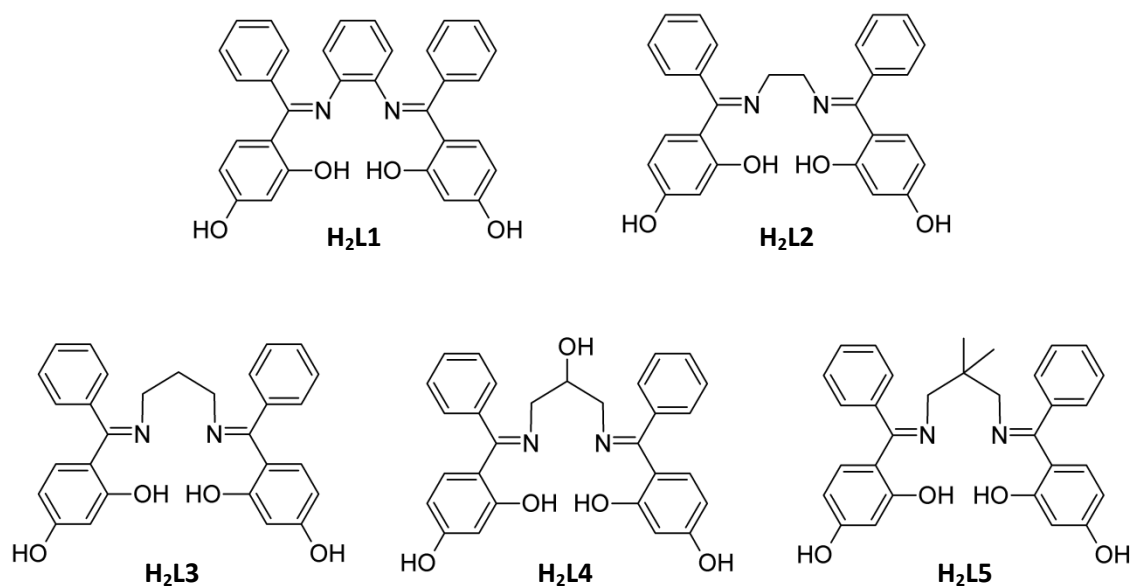


Figure 1.9: Proposed structures of Schiff base ligands to be synthesised.

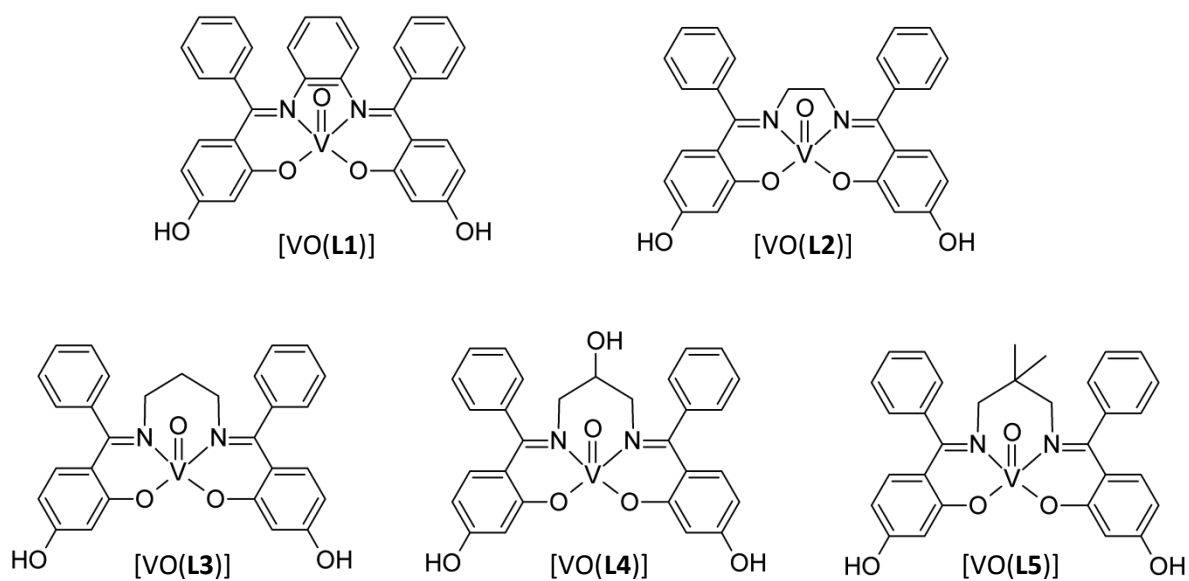


Figure 1.10: Proposed structures for the target oxovanadium(IV) complexes.

Chapter 2 | *Experimental*

2.1 General Procedures

2.1.1 Materials

Vanadylsulfate pentahydrate, 2,4-diaminobenzophenone, salicylaldehyde and all alkyl diamines were purchased from Sigma-Aldrich and used as received without further purification. 1,2-diaminobenzene, hydrochloric acid (32 %), sodium hydroxide pellets, methanol, dimethyl sulfoxide (DMSO) and deuterated-dimethyl sulfoxide (DMSO- d_6) were obtained from Merck. All amines were stored at 4 °C.

2.1.2 Characterisation procedures

IR spectra were recorded on a Perkin-Elmer Spectrum 100 FTIR, with a diamond ATR sample probe. ^1H , ^{13}C and ^{51}V NMR spectra were recorded in DMSO- d_6 on a 400 MHz Bruker Avance III spectrometer, equipped with a 9.4 T magnet and 5 mm BBOF probe. The solvent signal was used as the reference for both ^1H and ^{13}C spectra. For ^{51}V , a sample of NH_4VO_3 was used as an external reference prior to experimentation. All spectra were recorded at 298 K. Mass spectral data were recorded using a Waters LCT Premier mass spectrometer, DMSO was used to obtain the mass lock. UV-vis spectra were recorded in DMSO on a PG Instruments T80 UV/VIS PC spectrophotometer using 1 cm pathlength quartz cuvettes.

2.2 Synthesis of Schiff base Ligands

2.2.1 Synthesis of 4,4'-{benzene-1,2-diylbis[nitrilo(1E)phen-1-yl-1ylidene]}dibenzene-1,3-diol ($\text{H}_2\text{L1}$)

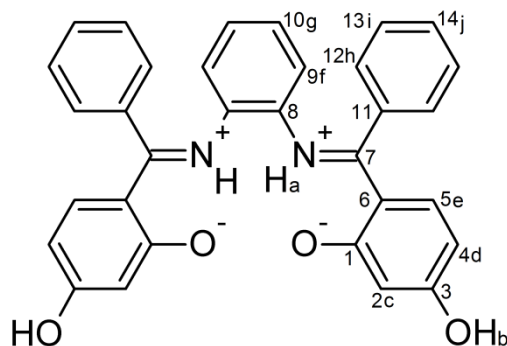


Figure 2.1: Diagram of 4,4'-{benzene-1,2-diylbis[nitrilo(1E)phen-1-yl-1ylidene]}dibenzene-1,3-diol ($\text{H}_2\text{L1}$) showing the relevant atom numbering.

The reactants 2,4-dihydroxybenzophenone (1.4 g, 6.5 mmol) and 1,2-diaminobenzene (0.29 g, 2.6 mmol) were dissolved in methanol (15 ml), and the solution was refluxed for 24 hours. The solvent was then evaporated, and the residue was heated at 70-80 °C for a further 24 hours. During this time an orange solid formed, which was suspended in methanol and filtered to leave a yellow solid.

Yield = 0.597 g, 46 %. Important peaks TOF MS ESI⁺: m/z 501.18 (100 %) M⁺. UV-Vis (DMSO) [λ_{\max} , nm (ϵ , M⁻¹ cm⁻¹): 322 (1.895 x 10⁴). IR (powder, cm⁻¹): 3229 [br, v(O-H)] 3084 [br, v(O-H)] 2608 [br, v(N-H)] 1520 [s, v(C=N)]. ¹H NMR (400 MHz; DMSO-d₆, 298 K) δ (ppm) = 6.22-6.25 (dd, 2H, *c*, $J_1 = 2.28$ Hz $J_2 = 6.56$ Hz); 6.3 (d, 2H, *d*, $J = 2.45$ Hz), 6.52-6.54 (q, 2H, *e*, $J = 2.33$ Hz, $J = 2.43$ Hz $J_3 = 3.54$ Hz), 6.66-6.68 (q, 2H, *f*, $J = 2.33$ Hz, 2.43 Hz 3.54 Hz), 6.74-6.76 (d, 2H, *g*, $J = 8.81$ Hz), 7.13-7.16 (m, 4H, *h*, $J = 3.46$ Hz), 7.36-7.38 (m, 6H, *i* and *j*, $J = 2.83$ Hz), 10.21 (s, 2H, *b*), 14.70 (s, 2H, *a*). ¹³C NMR (400 MHz, DMSO-d₆, 298 K) δ (ppm) = 103.5, 107.6, 112.6, 123.2, 124.7, 128.5, 128.7, 129.5, 134.1, 134.7, 139.8 (ar), 162.9, 164.8, 173.2 (1, 3 and 7).

2.2.2 Synthesis of 4,4'-{ethane-1,2-diylbis[nitrilo(1*E*)phenyl-1-yl-1-ylidene]}dibenzene-1,3-diol (**H₂L2**)

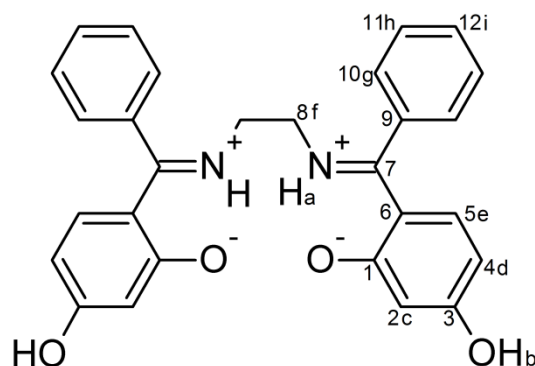


Figure 2.2: Diagram of 4,4'-{ethane-1,2-diylbis[nitrilo(1*E*)phenyl-1-yl-1-ylidene]}dibenzene-1,3-diol (**H₂L2**) showing the relevant atom numbering.

To a round-bottomed flask were added 2,4-dihydroxybenzophenone (0.5 g, 2.30 mmol) and ethylenediamine (0.07 g, 1.15 mmol), which were subsequently dissolved in methanol (10 ml) and refluxed for 24 hours. During this time a yellow precipitate formed, which was filtered off under vacuum and washed with methanol.

Yield = 0.472 g, 91 %. TOF MS ESI⁺: m/z 475.16 (100 %) NaM⁺. UV-Vis (DMSO) [λ_{\max} , nm (ϵ , M⁻¹ cm⁻¹): 312.5 (1.873 x 10⁴). IR (powder, cm⁻¹): 3027 [br, v(O-H)] 2623 [br, v(N-H)] 1532 [s, v(C=N)]. ¹H NMR(400 MHz, DMSO-d₆, 298 K) δ (ppm) = 3.17 (s, 2H, *f*); 3.42 (s, 2H, *f*); 6.07-6.10 (dd, 2H, *c*, $J_1 = 6.30$ Hz, $J_2 = 2.41$ Hz); 6.19 (d, 2H, *d*, $J = 2.28$ Hz); 6.45-6.47 (d, 2H, *e*, $J = 8.85$ Hz); 7.15-7.17 (q, 4H, *g*, $J = 3.58$ Hz); 7.50-7.51 (m, 6H, *h* and *i*, $J = 2.52$ Hz); 9.79 (s, 2H, *b*); 15.64 (s, 2H, *a*). ¹³C NMR (400 MHz, DMSO-d₆, 298 K) δ (ppm) = 51.3 (8), 103.1, 111.9, 127.1, 127.6, 128.7, 129.0, 133.3 (ar), 161.7, 166.0, 168.0, 174.0 (1, 3 and 7).

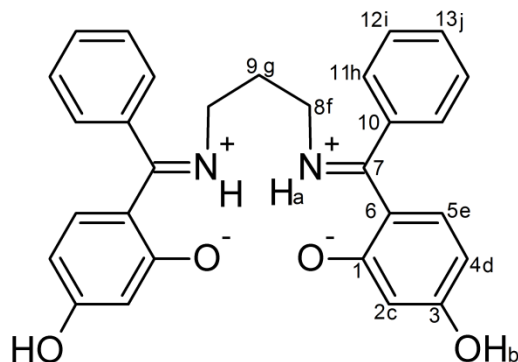
2.2.3 Synthesis of 4,4'-{propane-1,2-diylbis[nitrilo(1*E*)phen-1-yl-1-ylidene]}dibenzene-1,3-diol (**H₂L3**)

Figure 2.3: Diagram of 4,4'-{propane-1,2-diylbis[nitrilo(1*E*)phen-1-yl-1-ylidene]}dibenzene-1,3-diol (**H₂L3**), with numbers shown for all non-hydrogen atoms.

The reactants, 2,4-dihydroxybenzophenone (0.95 g, 4.4 mmol) and 1,3-propanediamine (0.16 g, 2.2 mmol), were dissolved in methanol (15 ml) and refluxed for 36 hours. A bright, yellow precipitate formed, which was collected by vacuum filtration.

Yield = 0.668 g, 66%. TOF MS ESI: m/z 467.20 (100 %) M^+ . UV-Vis (DMSO) [λ_{max} , nm (ϵ , $M^{-1} cm^{-1}$): 311.5 (2.066×10^4). IR (powder, cm^{-1}): 3055 [br, v(O–H)] 2499 [br, s, v(O–H)] 2285 [br, s, v(N–H)] 1564 [s, v(C=N)]. 1H NMR (400 MHz, DMSO- d_6 , 298 K) δ (ppm) = 1.84 (p, 2H, *g*, $J = 6.90$ Hz), 3.21 (t, 4H, *f*, $J = 6.79$ Hz), 6.06 (dd, 2H, *c*, $J_1 = 8.45$ Hz, $J_2 = 2.52$ Hz), 6.17 (d, 2H, *d*, $J = 2.50$ Hz), 6.45 (d, 2H, *e*, $J = 8.74$ Hz), 7.18 (dd, 4H, *h*, $J_1 = 6.43$ Hz, $J_2 = 2.29$ Hz), 7.48 (m, 6H, *i* and *j*, $J = 2.28$ Hz), 9.86 (s, 2H, *b*), 15.85 (s, 2H, *a*). ^{13}C NMR (400 MHz, DMSO- d_6 , 298 K) δ (ppm) = 47.8 (*9*), 49.1 (*8*), 103.7, 106.6, 112.3, 127.5, 129.1, 129.5, 133.1, 133.6 (ar), 162.2, 167.1, 173.9 (*1*, *3* and *7*).

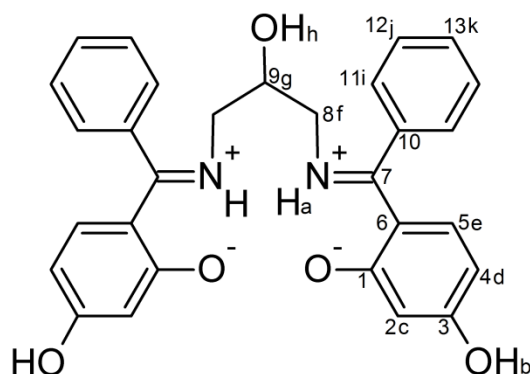
2.2.4 Synthesis of 4,4'-{(2-hydroxypropane-1,3-diyl)bis[nitrilo(1*E*)phen-1-yl-1-ylidene]}dibenzene-1,3-diol (**H₂L4**)

Figure 2.4: Diagram of the ligand 4,4'-{(2-hydroxypropane-1,3-diyl)bis[nitrilo(1*E*)phen-1-yl-1-ylidene]}dibenzene-1,3-diol (**H₂L4**) showing the relevant atom numbering.

H₂L4 was synthesised by refluxing 1,3-diamino-2-propanol (0.27 g, 3.0 mmol) and 2,4-dihydroxybenzophenone (1.32 g, 6.1 mmol) in methanol (15 ml) for 18 hours. During this time, a yellow precipitate formed. The precipitate was isolated by vacuum filtration and washed with methanol.

Yield = 0.672 g, 46 %. TOF MS ESI: m/z 483.20 (100 %) M^+ . UV-Vis (DMSO) [λ_{max} , nm (ϵ , $M^{-1} cm^{-1}$): 311 (1.811×10^4). IR (powder, cm^{-1}): 3244 [br, $\nu(O-H)$] 2445 [br, $\nu(N-H)$] 1539 [br, s, $\nu(C=N)$]. 1H NMR (400 MHz, DMSO- d_6 , 298 K) δ (ppm) = 3.17 (s, 4H, *f*), 3.87 (p, 1H, *g*), 6.06 (dd, 2H, *c*), 6.17 (d, 2H, *d*, $J_1 = 8.81$ Hz, $J_2 = 2.55$ Hz), 6.45 (d, 2H, *e*, $J = 2.25$ Hz), 7.18 (m, 4H, *i*, $J = 8.78$ Hz), 7.48 (m, 6H, *j* and *k*, 3.57 Hz), 9.71 (s, 2H, *b*), 15.83 (s, 2H, *a*). ^{13}C NMR (400 MHz, DMSO- d_6 , 298 K) δ (ppm) = 49.1 (*g*), 54.5 (*h*), 103.7, 106.5, 112.4, 127.7, 129.1, 129.4, 133.1, 133.7 (*ar*), 162.2, 167.3, 174.2 (*1*, *3* and *7*).

2.1.5 Synthesis of 4,4'-[2,2-dimethylpropane-1,3-diyl]bis[nitrilo(1E)phen-1-yl-1-ylidene]}dibenzene-1,3-diol (**H₂L5**)

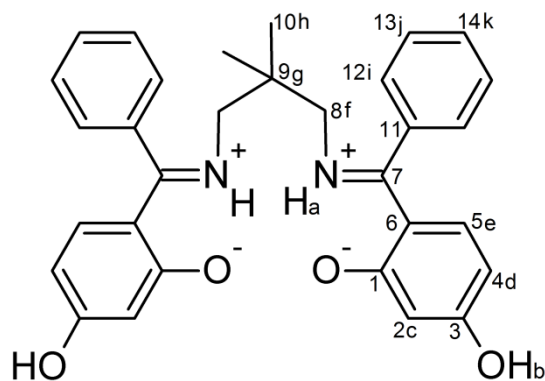


Figure 2.5: Diagram of 4,4'-[2,2-dimethylpropane-1,3-diyl]bis[nitrilo(1E)phen-1-yl-1-ylidene]}dibenzene-1,3-diol (**H₂L5**).

The ligand was synthesised by dissolving 2,2-dimethyl-1,3-diaminopropane (0.33 g, 3.2 mmol) and 2,4-dihydroxybenzophenone (1.37 g, 6.4 mmol) in methanol (15 ml), and refluxing the resulting bright yellow solution for 18 hours. During the course of the condensation, a bright yellow precipitate formed, which was filtered off and washed with methanol.

Yield = 0.734 g, 46 %. TOF MS ESI: m/z 495.23 (100 %) M^+ . UV-Vis (DMSO) [λ_{max} , nm (ϵ , $M^{-1} cm^{-1}$): 312 (1.828×10^4). IR (powder, cm^{-1}): 2961 [br, $\nu(O-H)$] 2876 [br, $\nu(O-H)$] 2459 [br, s, $\nu(N-H)$] 1475 [s, $\nu(C=N)$]. 1H NMR (400 MHz, DMSO- d_6 , 298 K) δ (ppm) = 0.92 (s, 6H, *h*); 3.03 (s, 4H, *f*); 6.08 (dd, 2H, *c*, $J_1 = 8.75$ Hz, $J_2 = 2.28$ Hz); 6.20 (d, 2H, *d*, $J = 2.55$ Hz); 6.45 (d, 2H, *e*, $J = 8.80$ Hz); 7.11 (dd, 4H, *i*, $J_1 = 7.23$ Hz, $J_2 = 1.79$ Hz); 7.47 (m, 6H, *j* and *k*); 9.91 (s, 2H, *b*); 15.95 (s, 2H, *a*). ^{13}C NMR (400 MHz, DMSO- d_6 , 298 K) δ (ppm) = 24.35 (*h*); 36.18 (*g*); 59.00 (*g*); 103.61, 106.61, 112.39, 127.54, 129.16, 129.43, 133.05, 133.75 (*ar*); 162.20, 166.82, 174.15 (*1*, *3*, and *7*).

2.2.6 Synthesis of *N,N'*-disalicylaethylenediamine (*salen*)

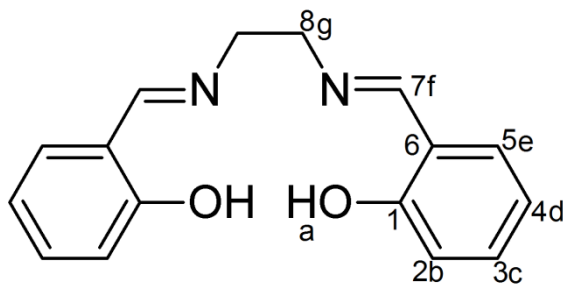


Figure 2.6: Structure of the salen ligand.

To a flask containing salicylaldehyde (1.04 g, 8.5 mmol), ethylenediamine (0.28 ml, 4.2 mmol) was added. A bright yellow solid was formed instantly. This was washed with distilled water and dried.

Yield = 1.06 g, 95 %. TOF MS ESI⁺: m/z 269.13 (100 %) M⁺. ¹H NMR (400 MHz, DMSO-d₆, 298 K) δ (ppm) = 3.29 (s, 1H, *a*); 3.92 (s, 4H, *g*); 6.84-6.89 (m, 4H, *c* and *d*); 7.31 (t, 2H, *e*, $J_1 = 8.08$ Hz, $J_2 = 1.74$ Hz); 7.41 (dd, 2H, *b*, $J_1 = 6.02$ Hz, $J_2 = 1.58$ Hz); 8.58 (s, 2H, *f*). ¹³C NMR (400 MHz, DMSO-d₆, 298 K) δ (ppm) = 59.25 (s, *8*); 79.41 116.90, 119.00, 132.08, 132.75 (2, 3, 4, 5 and 6); 161.03 (s, 1); 167.34 (s, 7).

2.3 Synthesis of Oxovanadium(IV) Schiff base complexes

2.3.1 Synthesis of 2,2'-[benzene-1,2-diylbis[nitrilo(1*E*)phen-1-yl-1-ylidene]]bis(5-hydroxyphenolate)-vanadyl ([VO(L1)])

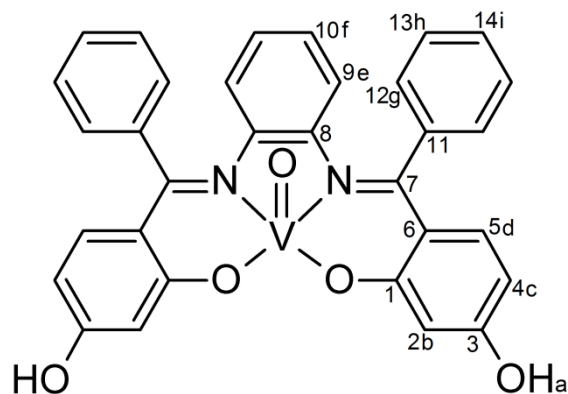


Figure 2.7: Numbered diagram of the complex 2,2'-[benzene-1,2-diylbis[nitrilo(1*E*)phen-1-yl-1-ylidene]]bis(5-hydroxyphenolate)-vanadyl ([VO(L1)]).

Method A: VOSO₄·5H₂O (0.034 g, 0.21 mmol) and H₂L1 (0.101 g, 0.18 mmol) were mixed together thoroughly in a pestle and mortar. Triethylamine (3 ml) and methanol (5 ml) were added to this mixture and ground together to form a brown coloured paste. As the solvents evaporate, a green solid is left. The precipitate was washed with distilled water to remove any excess VOSO₄.

Yield = 0.113 g, 95 %. TOF MS ESI⁺: m/z 565.10 (100%) M⁺. IR (powder, cm⁻¹): 3417 [br, ν (O–H)] 2930 [br, ν (C–H)] 1600 [s, ν (C=C)] 1515 [s, ν (C=N)] 962 [s, ν (V=O)]. UV-Vis (DMSO) [λ_{\max} , nm (ϵ , M⁻¹ cm⁻¹): 320 (1.514 x 10³). Anal. Data: Calculated: C, 67.97; H, 3.92; N, 4.95 %; Found: C, 64.02; H, 4.56; N, 5.29 %. ⁵¹V NMR (400 MHz, DMSO-d₆, 298 K) δ (ppm) = -538.5 (s).

Method B: The ligand, **H₂L1**, was suspended in distilled water (20 ml) and the pH of the solution was adjusted to *ca* 13; this causes the ligand to dissolve and form a yellow solution. An excess of VOSO₄·5H₂O (1:1.3), dissolved in a minimal amount of water, was then added. The solution turns a red-brown colour instantly. The pH is then adjusted carefully back-down to between 7 and 8. At this point, a green precipitate forms, which was filtered off, and washed with distilled water and methanol.

2.3.2 Synthesis of 2,2'-{ethane-1,2-diylbis[nitrilo(1*E*)phen-1-yl-1-ylidene]}bis(5-hydroxyphenolate)-vanadyl [VO(L2)]

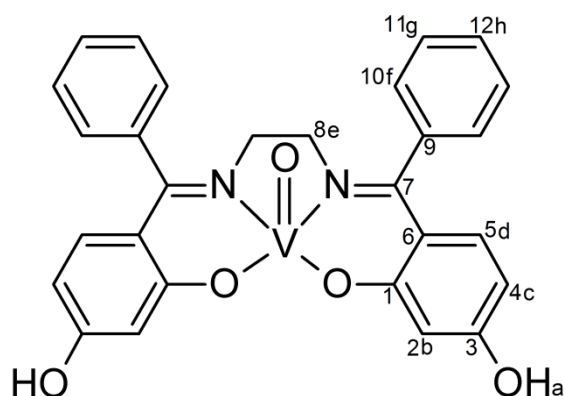


Figure 2.8: Numbered diagram of 2,2'-{ethane-1,2-diylbis[nitrilo(1*E*)phen-1-yl-1-ylidene]}bis(5-hydroxyphenolate)-vanadyl, [VO(L2)].

Method A: The ligand (0.20 g, 0.45 mmol) and VOSO₄·5H₂O (0.13 g, 0.45 mmol) were dissolved in 1 ml of DMSO. Triethylamine (0.30 g, 3.0 mmol) was added, and the solution was placed in an ultrasound bath for several minutes to facilitate complete dissolution of the reactants. After 5 minutes, a dark green solution forms. Distilled water (10 ml) was added to this solution, which caused the product to precipitate out as a green powder. This was washed further with distilled water.

Yield = 0.20 g, 85 %. TOF MS ESI⁺: m/z 517.10 (100%) M⁺. IR (powder, cm⁻¹): 3377 [br, ν (O–H)] 3062 [br, ν (ar-C–H)] 2606 [br, s, ν (alkyl-C–H)] 1574 [s, ν (C=C)] 1526 [s, ν (C=N)] 981 [s, ν (V=O)]. UV-Vis (DMSO) [λ_{\max} , nm (ϵ , M⁻¹ cm⁻¹): 301(1.572 x 10⁴). Anal. Data: Calculated: C, 64.99; H, 4.29; N, 5.41 %. Found: C, 63.13; H, 4.37; N, 5.73 %. ⁵¹V NMR (400 MHz, DMSO-d₆, 298 K) δ (ppm) = -552.9 (s).

Method B: The ligand was dissolved in an aqueous solution of NaOH (pH \approx 13, 15 ml). VOSO₄·5H₂O was added in a slight excess to this solution, which then rapidly turned a brown-yellow colour. The solution was neutralised using a concentrated HCl (aq) solution, at which point a dull green precipitate forms. This was filtered off, and washed with distilled water until the filtrate was no longer coloured.

2.3.3 Synthesis of 2,2'-{propane-1,3-diylbis[nitrilo(1E)phen-1-yl-1-ylidene]}bis(5-hydroxyphenolate)-vanadyl [VO(L3)]

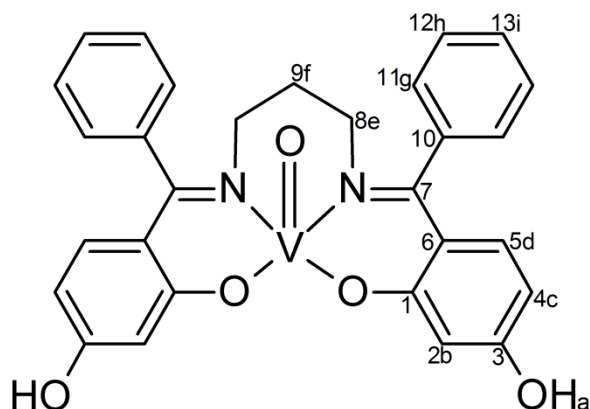


Figure 2.9: Numbered diagram showing the structure of 2,2'-{propane-1,3-diylbis[nitrilo(1E)phen-1-yl-1-ylidene]}bis(5-hydroxyphenolate)-vanadyl ([VO(L3)]).

The ligand **H₂L3** (0.08 g, 0.17 mmol) and VOSO₄·5H₂O (0.05 g, 0.32 mmol) mixed together, and suspended in distilled water (20 ml) by agitation. The solution was made alkaline by the addition of concentrated NaOH (aq); pH was approximately equal to 13. A yellow-brown colour develops rapidly as the pH goes above 12.5. The pH of the solution was then adjusted down to approximately 7.5-8 by addition of a concentrated HCl (aq) solution. A green precipitate forms. The precipitate was filtered, washed with distilled water until the filtrate no longer is coloured, and dried.

Yield = 0.084 g, 93 %. TOF MS ESI⁺: *m/z* 531.11 (100 %) M⁺. IR (powder, cm⁻¹): 3416 [br, ν(O-H)] 3060 [br, s, ν(ar-C-H)] 2874 [br, ν(alkyl-C-H)] 1586 [s, ν(C=C)] 1568 [s, ν(C=C)] 1479 [s, ν(C=N)] 979 [s, ν(V=O)]. UV-Vis (DMSO) [λ_{max}, nm (ε, M⁻¹ cm⁻¹): 307.5 (1.709 × 10⁴). Anal. Data: Calculated C, 50.61; H, 3.48; N, 4.03 %. Found: C, 50.50; H, 3.38; N, 6.02 %. ⁵¹V NMR (400 MHz, DMSO-d₆, 298 K) δ (ppm) = -529.6 (s).

2.3.4 Synthesis of 2,2'-((2-hydroxypropane-1,3-diyl)bis[nitrilo(1*E*)phen-1-yl-1-ylidene]}-bis(5-hydroxyphenolate)vanadyl ([VO(L4)])

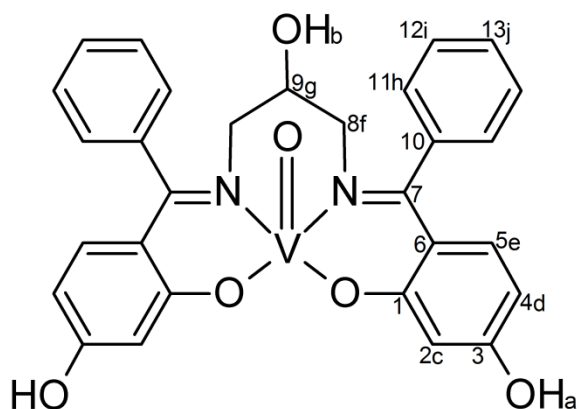


Figure 2.10: Numbered diagram for the vanadyl complex, 2,2'-((2-hydroxypropane-1,3-diyl)bis[nitrilo(1*E*)phen-1-yl-1-ylidene]}-bis(5-hydroxyphenolate)vanadyl [VO(L4)].

To an open beaker is added **H₂L4** (0.16 g, 0.33 mmol), which is then dissolved in distilled water (20 ml) by adjusting the pH to 13 using concentrated NaOH (aq). An excess amount of VOSO₄·5H₂O (0.13 g, 0.51 mmol) was then added, which changed the solution colour from yellow to brown. The pH was adjusted to 7-8 using HCl (aq), which caused a brown precipitate to form. The precipitate was filtered, washed with distilled water, and air dried.

Yield = 0.15 g, 83 %. TOF MS ESI⁺: *m/z* 547.11 (100 %) M⁺. IR (powder, cm⁻¹): 3394 [br, ν(O-H)] 3061 [br, s, ν(ar-C-H)] 2602 [br, ν(alkyl-C-H)] 1584 [s, ν(C=C)] 1537 [s,ν(C=N)] 982 [s, ν(V=O)]. UV-Vis (DMSO) [λ_{max}, nm (ε, M⁻¹ cm⁻¹): 320 (1.514 × 10³). Anal. Data: Calculated: C, 59.65; H, 4.32; N, 4.80 % (for [VO(L4)]·2H₂O); Found: C, 60.19; H, 4.37; N, 5.59 %. ⁵¹V NMR (400 MHz, DMSO-d₆, 298 K) δ (ppm) = -473.3 (s).

2.3.5 Synthesis of 2,2'-((2,2-dimethylpropane-1,3-diyl)bis[nitrilo(1*E*)phen-1-yl-1-ylidene])bis(5-hydroxyphenolate)-vanadyl [VO(L5)]

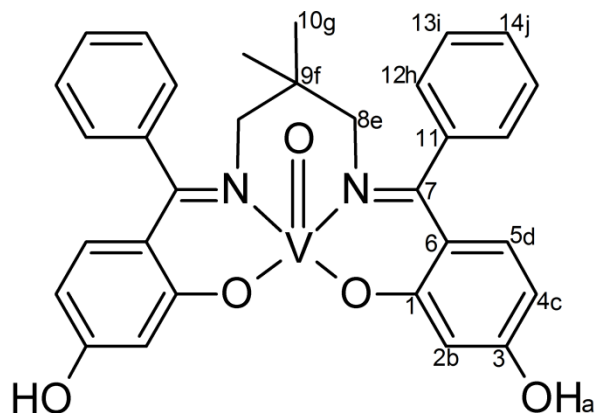


Figure 2.11: Numbered diagram of 2,2'-((2,2-dimethylpropane-1,3-diyl)bis[nitrilo(1*E*)phen-1-yl-1-ylidene])bis(5-hydroxy-phenolate)-vanadyl, [VO(L5)].

The ligand, **H₂L5**, (0.08 g, 0.16 mmol) was dissolved in 20 ml distilled water, whose pH had been adjusted to 12.5 using concentrated NaOH (aq). The metal salt, VOSO₄·5H₂O (0.61 g, 0.24 mmol) was added to this solution in excess; turning the solution brown upon addition. The solution was stirred until all particulate matter had dissolved. The pH was then adjusted to 7-8 using concentrated HCl (aq), which caused a green precipitate to form. This was filtered, washed several times with distilled water, and air dried.

Yield = 0.079 g, 88 %. TOF MS ESI⁺: *m/z* 560 (100 %) M⁺. IR (powder, cm⁻¹): 3419 [br, v(O-H)] 2965 [br, s, v(ar-C-H)] 2618 [br, s, v(alkyl-C-H)] 1584 [s, v(C=C)] 1534 [s, v(C=N)] 976 [s, v(V=O)]. UV-Vis (DMSO) [λ_{max}, nm (ε, M⁻¹ cm⁻¹): 270 (3.114 × 10³). Anal. Data: Calculated: C, 66.55; H, 5.04; N, 5.01 %; Found: C, 64.44; H, 5.05; N, 4.76 %. ⁵¹V NMR (400 MHz, DMSO-d₆, 298 K) δ (ppm) = indiscernible.

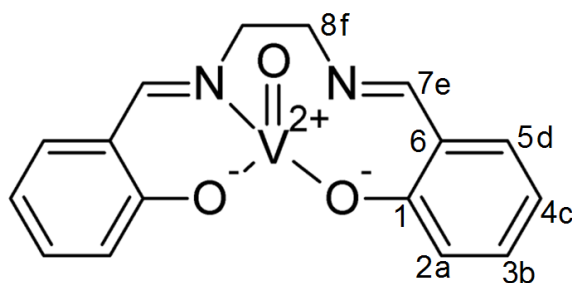
2.3.6 Synthesis of *N,N'*-bis(*o*-hydroxybenzylidene)ethylenediamine vanadyl ([VO(salen)])

Figure 2.12: Diagram of the structure of the complex [VO(salen)], synthesised as part of this study.

[VO(salen)] was made according to the modified procedure of Diehl and Hach. Salen (0.195 g, 0.73 mmol) and $\text{VO}(\text{SO}_4)_2 \cdot 5\text{H}_2\text{O}$ (0.23 g, 1.1 mmol) were dissolved in ethanol (20 ml), and refluxed for 1.5 hours. The solution was left to stand overnight. Blue-green crystals form in a light brown solution during this time. The solution was discarded, and the crystals were dissolved in tetrahydrofuran, to give a blue-green solution and a blue precipitate. The precipitate was filtered off, and the filtrate collected. Solvent was removed *via* rotary evaporation to yield the bright green solid.

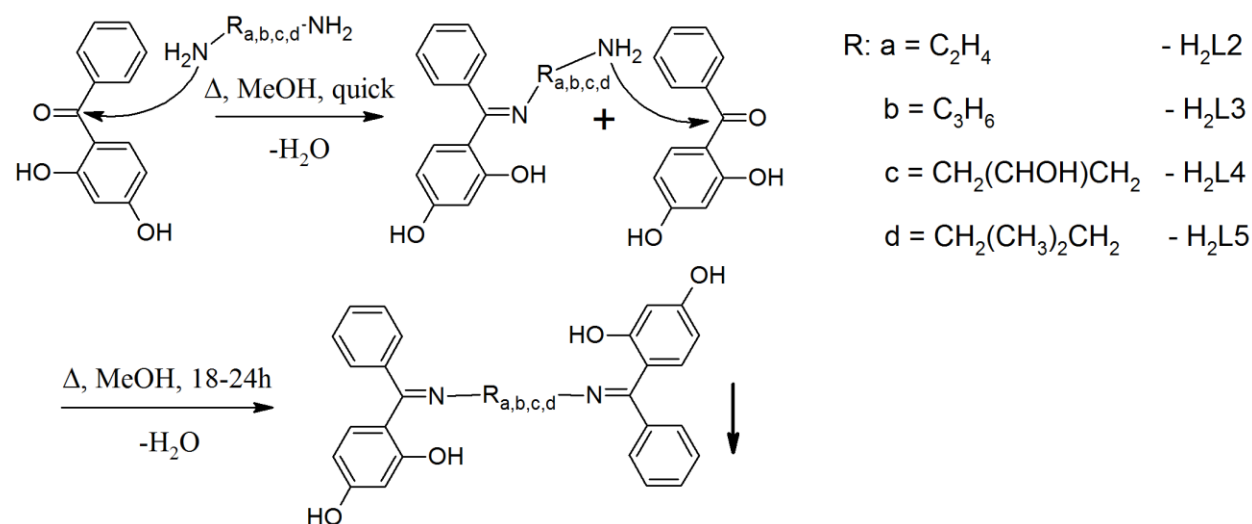
Yield = 0.21 g, 80 %. TOF MS ESI⁺: m/z 356.04 (100 %) NaM^+ . Anal. Data: Calculated: C, 57.67; H, 4.23; N, 8.41 %; Found: C, 60.88; H, 5.07; N, 6.37 %.

Chapter 3 | *Synthesis, Spectroscopic Characterisation and X-ray Diffraction*

3.1 Synthesis

3.1.1 Ligands

In this study, the ligands made can be considered to be derivatives of salen-type ligands. The salen ligand derives its name from the two starting materials that are used to synthesize it, *viz.* salicylaldehyde and ethylenediamine. Synthesis of the salen-derivatives is accomplished by the condensation between a primary amine, which is either aliphatic or aromatic, and a ketone to form an imine (Scheme 3.1).⁶³ Because there are always aryl groups attached to the carbon atom of the imine group, the ligands can be termed *Schiff bases*.⁸² The aromatic group has the effect of stabilizing the product with regards to hydrolysis. Most of the reactions were straightforward, and acceptable yields were typically obtained.



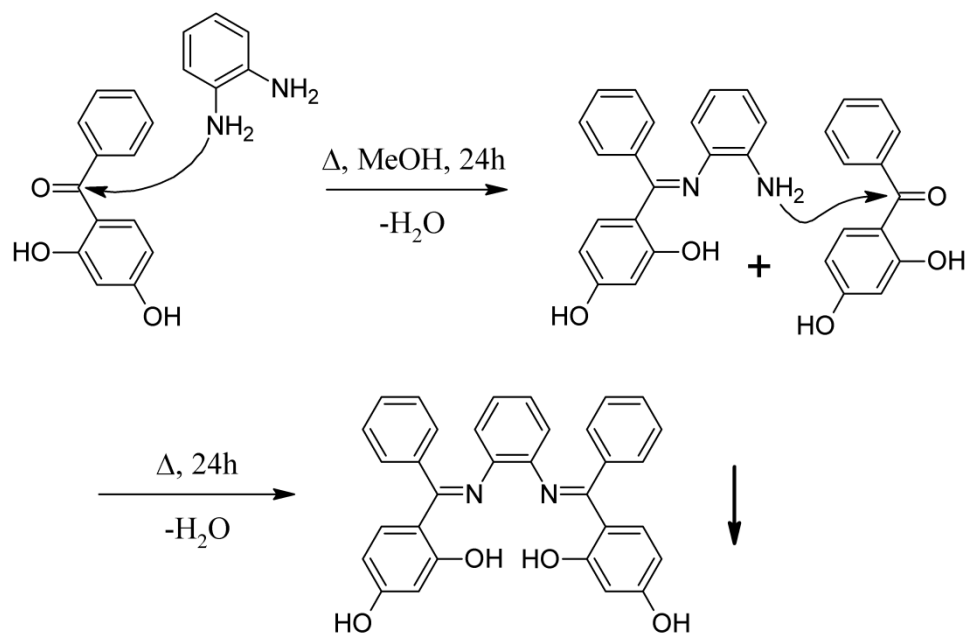
Scheme 3.1: Typical reaction pathway for synthesis of Schiff-base ligands. The amine attacks the electron deficient carbonyl carbon, resulting in hemiaminal formation and then dehydration to form the imine.

For all but **H₂L1**, ligand synthesis is very easily achieved. Methanol was chosen as a solvent, as both starting materials are soluble in it, whereas the product is not. The precipitated product can therefore be filtered and washed with methanol; no further work-up is required (Scheme 3.2). Precipitation of the product from solution also provides an additional driving force for the reaction. This additional shift of the equilibrium is most likely very necessary, as the ketone is positioned between two bulky aromatic rings. This bulk no doubt hinders the approach of the attacking nucleophile, and is the reason for the lengthy reaction times*.

For **H₂L1**, refluxing in methanol did not result in precipitation, even after prolonged reaction times (of the order of several days). Analysis of these solutions by ¹H and ¹³C NMR showed that the reaction was only proceeding to the half-addition product. Refluxing the reactants in solvents with higher boiling

*For comparison, the reaction of ethylenediamine with salicylaldehyde, which does not have a hindered ketone group, is extremely rapid; occurring within seconds of the two reactants being added together.

points also resulted in only one of the amino groups on 1,2-diaminobenzene condensing to form a Schiff base. Microwave synthesis using a basic alumina support was also fruitless; the ketone decomposed after several minutes before any condensation with the amine could occur. It was therefore suspected that condensation of the first amine to a ketone results in deactivation of the other amine through the aromatic ring. This deactivation has been observed in other systems employing the ortho-substituted diaminobenzene.⁸³ Addition of a large excess of ketone is still insufficient to cause formation of the second imine group. However, by allowing the solvent to evaporate, while still maintaining a high temperature, complete conversion to the disubstituted version can be achieved. As with the other ligands in the series, the product is insoluble in methanol, and can be washed with this solvent to remove all starting materials and side products. Further purification is not required.



Scheme 3.2: Synthetic procedure for H₂L1; the second step is performed by removing solvent from the reaction mixture and continuing to add heat.

3.1.2 Complexes

As can be seen in Chapter 2, there are several procedures that can be used to synthesize the oxovanadium(IV) complexes. Initially, due to the inherent insolubility of the ligands, very few solvents were available in which to perform the complexation. DMSO was the first solvent that proved suitable for dissolving the ligand. Chelation of the VOSO₄ starting material proceeded rapidly in this solvent with the addition of excess triethylamine. Triethylamine was added to deprotonate the ligand, which would facilitate binding to the vanadyl unit.

Colour is a very good indicator for the oxidation state and coordination environment of vanadium species in general, and was equally applicable to these systems. A DMSO solution of the ligand is yellow, and one of VOSO₄ is blue; mixing these two solutions together gives a light green solution. However, adding triethylamine turns the colour brown. This is most likely the result of the ligand binding to the

metal, as expected, but also of hydroxide ions being formed, which then oxidise the vanadium(IV) species to vanadium(V)*. Hydroxide is formed due to the deprotonation of water, present in low concentrations, that is deprotonated by triethylamine. It was found that if minimal amounts of DMSO were used (e.g. <1 ml), water could be used to precipitate the product complex as a green powder. Precipitation only occurs once all the triethylamine evaporates from the solution.

Complexing the ligands and vanadium in DMSO was not ideal though, as only small amounts of complex could be prepared at a time. Larger amounts of reactants required more DMSO to solubilise them; as the volume of DMSO was increased, water induced precipitation of the complex became less effective. As a result, the yields obtained by this method dramatically decreased. Owing to these reasons, a solid state approach to the chelation was attempted. The advantages of using no solvent for environmental reasons are obvious,⁸⁴ and it was hoped that this would be a practical method for synthesizing the complexes. Triethylamine was used to deprotonate the ligand again, as without it no complexation occurred, as observed by mass spectral analysis. However, a less volatile solvent had to be used to prevent the triethylamine from evaporating during the mixing process; the solvent used was methanol. It appeared though that the complex formed was dissolving in the methanol – this led to the final procedure for chelation.

The ligand, although insoluble in water, as well as most organic solvents, will readily dissolve if treated with a mild base, like triethylamine, that can deprotonate the hydroxyl and iminium groups. The pKa of the aromatic hydroxyl groups has not yet been determined for the Schiff bases used, but appears to be approximately the same for that of other aromatic hydroxyl groups, such as on phenol.⁸⁵ Hence, if the pH of a solution is above 10, as it would be in one containing sufficient triethylamine, removal of all ionisable protons most likely occurs. Ligand, suspended in an aqueous solution, rapidly dissolves as the solution pH is adjusted to 10 or above. When excess $\text{VO}_2\text{SO}_4 \cdot 5\text{H}_2\text{O}$ is added to an alkaline ligand solution, a brown colour, evident of the vanadium oxidation from +4 to +5 and chelation by the ligand, rapidly occurs. In addition to this, the pH of the solution drops slightly as free SO_4^{2-} is released. When a solution's pH was lowered using HCl (aq), the colour changes first from dark brown to green** as the pH approaches 10, due to the reduction of V(V) to V(IV). At a pH between 7 and 8.5, the complex precipitates out of the aqueous solution. Care must be taken not to adjust the pH below a minimum of 5; this is to prevent the complex from becoming demetallated. The precipitate can be collected by filtration, and all excess vanadium salt washed off using distilled water. The complexes thus formed are stable in air for several months.

*Vanadium(V) ions in an aqueous or DMSO solution are yellow, and thus the brown colour is indicative of chelation.

**For the complex $[\text{VO}(\text{L4})]$, the colour does not change, but remains dark brown. The precipitate too is this colour. An oxovanadium(IV) complex is formed though, as evidenced by the paramagnetic measurements of it (See section 4.3 and 5.3).

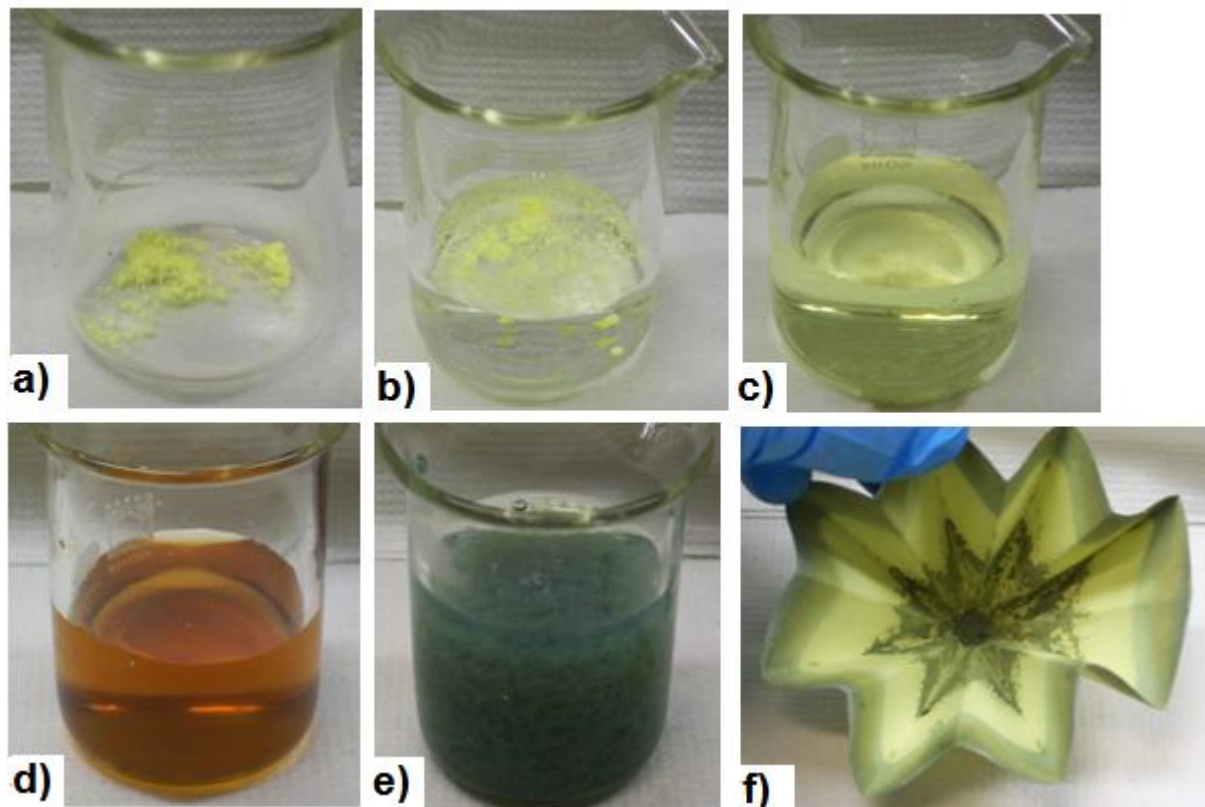


Figure 3.1: The steps involved in chelating vanadium to one of the tetradentate Schiff base ligands – shown is the procedure for $[\text{VO}(\text{L3})]$ synthesis. The steps are as follows: **a)** an amount of ligand is weighed-out; this is the limiting reactant; **b)** adding water to the ligand does not dissolve it, the pH must be adjusted to above 10 for dissolution of the ligand **c)** **d)** an excess amount of VOSO_4 (typically 1.3:1) is added to the alkaline solution, turning it brown; **e)** lowering the pH to just above neutrality causes the complex to precipitate; **f)** the green precipitate can be isolated by filtration.

3.2 Characterisation

3.2.1 Melting points

Melting points for the ligands were measured to determine their thermal stability. All compounds decomposed before melting. The decomposition occurred at relatively high temperatures for ligands, and it can thus be concluded that they are all very stable compounds. Temperatures of decomposition ranged between *ca* 230 to 320 °C. The bridging group appears to play a major role in the ligand's thermal stability, as can be seen by the large difference between the decomposition temperatures. A trend observed is that the decomposition temperature decreases as the chain length increases. Therefore, compounds $\text{H}_2\text{L1}$ and $\text{H}_2\text{L2}$ that have only two carbon atoms between the iminium nitrogens, are the most stable, decomposing above 300 °C. The other compounds with three carbons between the iminium nitrogens are less thermally stable; however, it must be noted that the presence of an alcohol group on the propyl chain destabilises the compounds, while methyl groups appear to increase the stability. Table 3.1 shows the ranges over which the ligands decomposed.

Table 3.1: Ranges of decomposition for the ligands **H₂L1**, **H₂L2**, **H₂L3**, **H₂L4** and **H₂L5**, as well as selected differences between the compounds. The number of carbon atoms between connecting the imine nitrogens appears to play a significant role in the thermal stability of the compounds.

Compound	Decomposition Temperature / °C	Chain length /C atoms	Substituents
H₂L1	308-314	2	Ar
H₂L2	320	2	none
H₂L3	251-253	3	none
H₂L4	235-237	3	alcohol
H₂L5	275-280	3	di-methyl

3.2.2 Infrared spectroscopy

Analysis of the ligands and complexes by infrared spectroscopy shows the expected absorptions for functional groups. There is a broad peak located typically in the region from 3370 to 3415 cm^{-1} for the benzylic O–H groups, as well as the anticipated stretching frequency for the imine group located from 1515 to 1570 cm^{-1} . Coordination of a ligand to the vanadyl cation results in the disappearance of certain O–H stretching frequencies, and the appearance of V=O stretching frequencies; differences in these spectra are shown for the free ligand **H₂L2** and its coordination complex, [VO(**L2**)], in Figure 3.2.

More importantly than this, however, are the stretching frequencies observed for the vanadyl unit. Typically, for a mononuclear species, a stretching frequency of $985 \pm 50 \text{ cm}^{-1}$ is expected for the vanadyl unit.^{86,87} In the spectra of the complexes, stretching frequencies of 965 to 980 cm^{-1} can be observed. These were not previously visible in the spectra of the free ligands, and are thus due to the presence of mononuclear vanadyl species. Mononuclear, because the stretching frequency of a vanadium–oxygen double bond is reduced by coordination at the other axial position, as would occur for an octahedral vanadium(V) compound or a vanadium(IV) polymeric species.⁸⁸

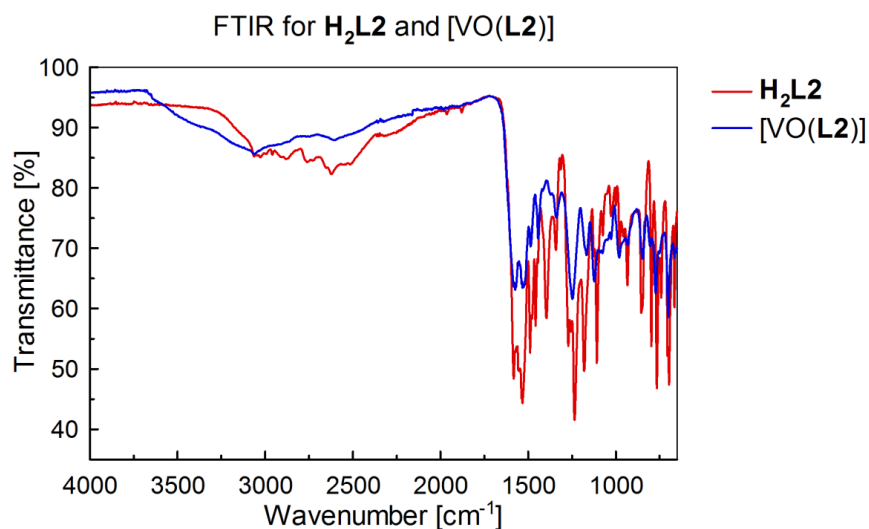


Figure 3.2: The IR spectra of **H₂L2** and [VO(**L2**)] superimposed to show the change in frequencies caused by chelation of the vanadyl cation.

3.2.3 NMR Spectroscopy

NMR spectroscopy was used to probe the structure of the free ligands, as well as the purity and tentative assignment of the complexes. For the ligands, ^1H and ^{13}C NMR spectra were obtained; $\text{H}_2\text{L3}$ ^1H and ^{13}C NMR spectra are shown as typical examples of those displayed by the ligands (Figures 3.3 and 3.4). As expected, there are peaks upfield that correspond to the alkyl bridging group, several peaks within the 6.5-8 ppm range expected for aromatic protons and a broad singlet at approximately 9.5 ppm for the exchangeable aromatic alcohol protons. Additionally, there is also a very sharp signal that is shifted very far down-field for all of the compounds, at approximately 16 ppm. This corresponds to the iminium proton, which can be thought of as a proton that is involved in very strong hydrogen bonding. Observation of this signal in the solution NMR spectra suggests that the zwitterionic structure seen in the solid state by XRD (see Section 3.3), persists in solution as well. The ^{13}C NMR spectra show the predicted number of peaks at the appropriate shifts for these symmetrical, aromatic compounds as well. All chemical shifts have been referenced internally to the solvent.

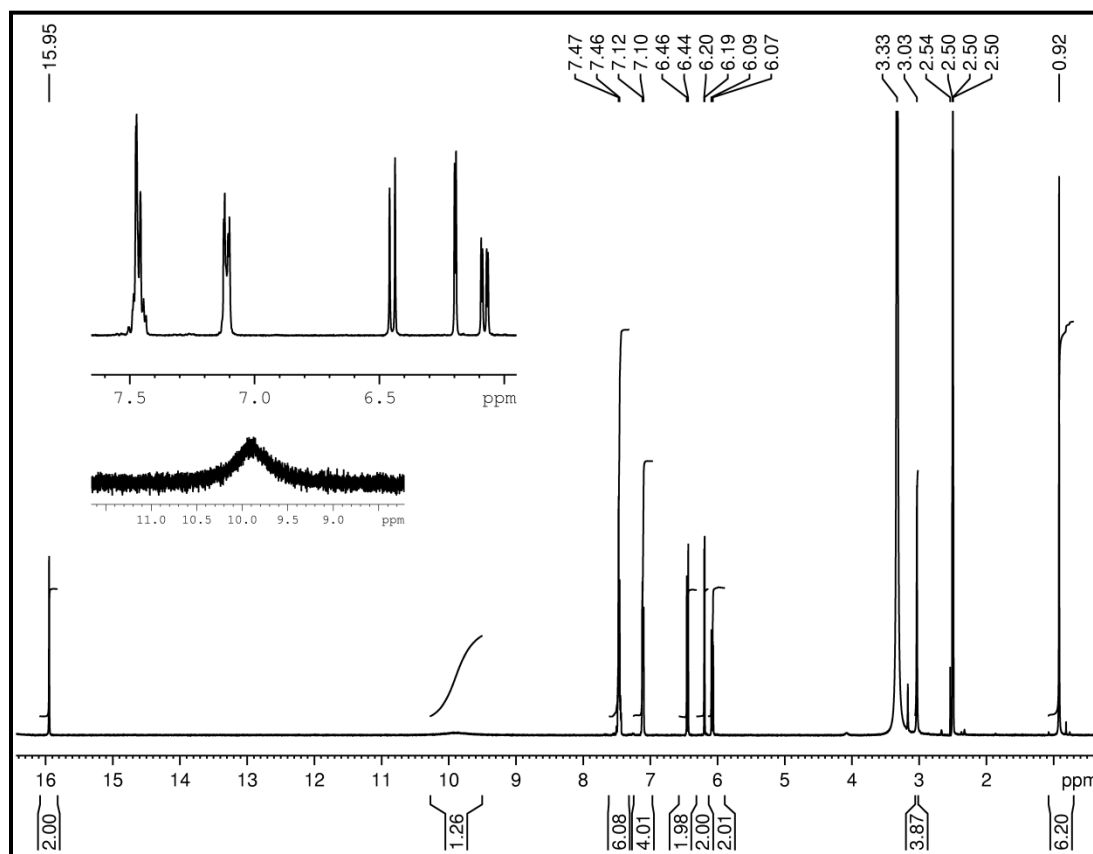


Figure 3.3: ^1H NMR spectrum of $\text{H}_2\text{L3}$, showing integration and assignment of peaks. The spectrum was recorded in DMSO-d_6 at 298 K; the chemical shifts are referenced to the solvent.

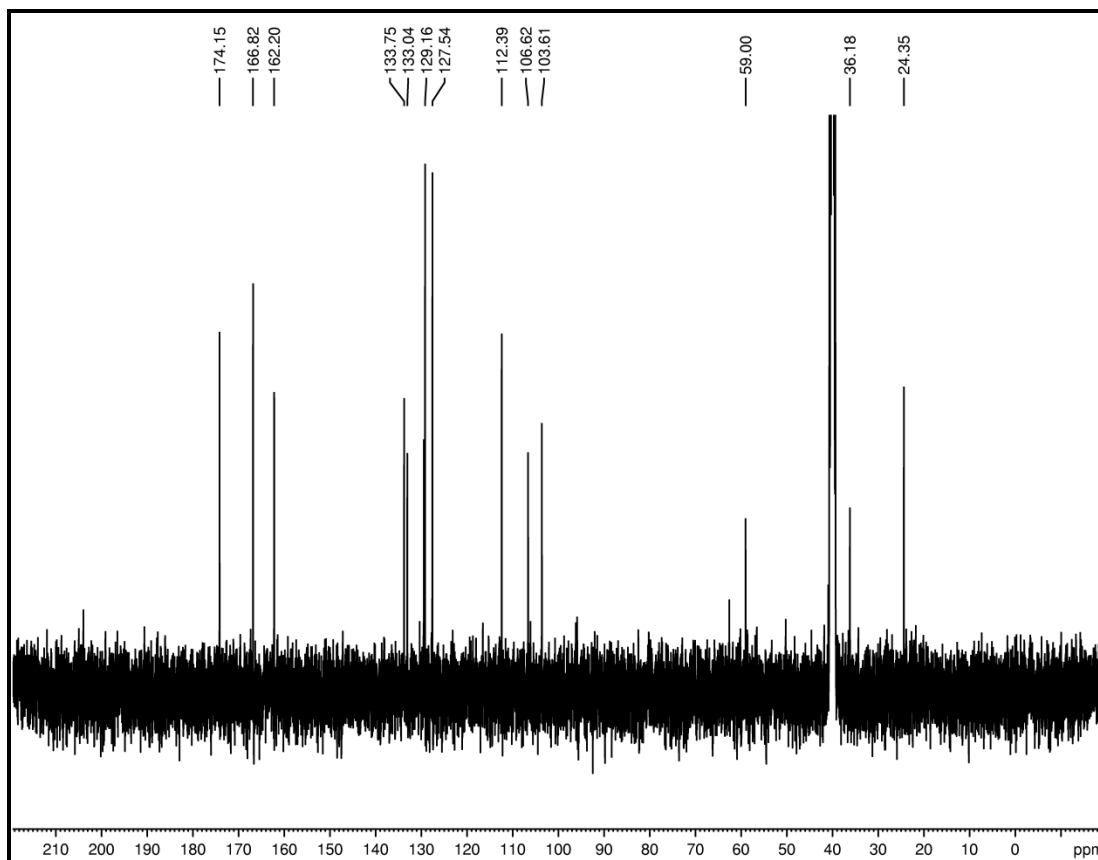


Figure 3.4: ^{13}C NMR spectrum for $\text{H}_2\text{L3}$. Assignment of peaks is shown. The spectrum was recorded at 298 K in DMSO- d_6 . The solvent was used as the reference for the chemical shifts.

Owing to the paramagnetic nature of the oxovanadium(IV) complexes, their ^1H NMR spectra displayed very broad peaks that were unidentifiable. The same trend was observed for the ^{13}C NMR of these complexes. However, the natural abundance of ^{51}V – the NMR spectroscopically active isotope – is 97 percent.⁶ Therefore, even though the relaxation time for the paramagnetic species is very fast, there is a high enough abundance that a small peak is usually visible. This was the case for all but one of the complexes synthesised, *viz.* $[\text{VO}(\text{L5})]$, whose ^{51}V peak could not be observed. The ^{51}V NMR spectra for the complexes are presented below (Figures 3.5 – 3.8). The chemical shifts are referenced externally to NH_4VO_3 .

As expected for oxovanadium(IV) Schiff-base complexes, the ^{51}V peaks are located downfield between -450 to -550 ppm. There is one major peak for $[\text{VO}(\text{L2})]$, $[\text{VO}(\text{L3})]$ and $[\text{VO}(\text{L4})]$. $[\text{VO}(\text{L1})]$ shows two major peaks between -520 and -550 ppm that are of approximately equal magnitude. Their chemical shifts are too close together to suggest that they are completely different species, and are most likely the result of different geometrical coordination isomers, *i.e.* if the shielding at the vanadium centre was different between the two isomers, then the chemical shifts would be expected to be different as well (See Figure 3.9 for an illustration).

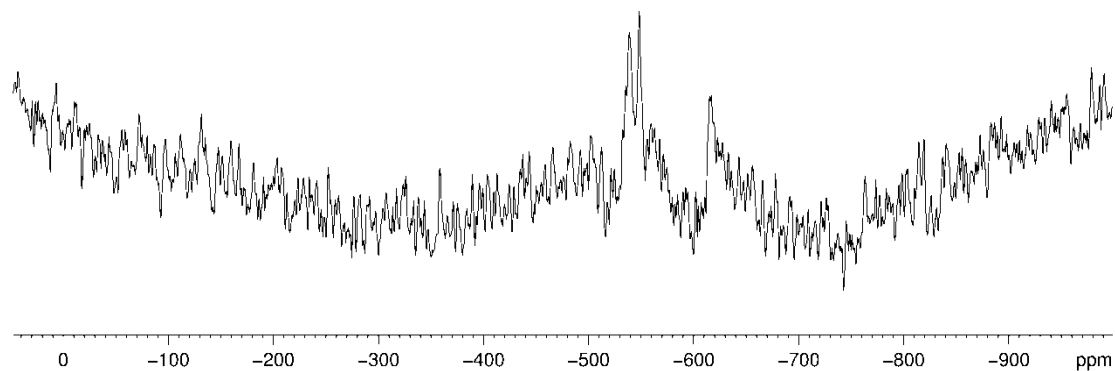


Figure 3.5: ^{51}V NMR spectrum for [VO(L1)], recorded in DMSO-d₆ at 298 K. NH_3VO_3 is the reference peak that has been set in the acquisition parameters.

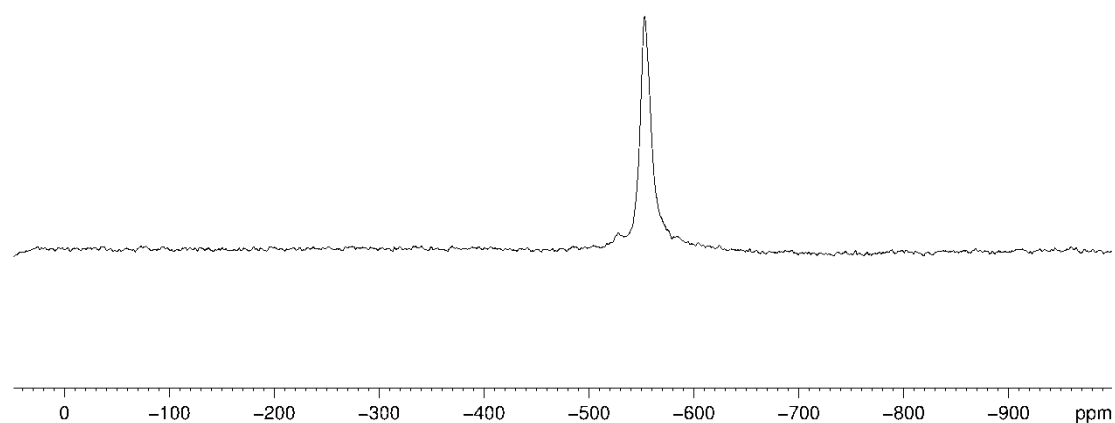


Figure 3.6: ^{51}V NMR spectrum for [VO(L2)] recorded in DMSO-d₆ at 298 K. NH_4VO_3 is the reference for the chemical shift.

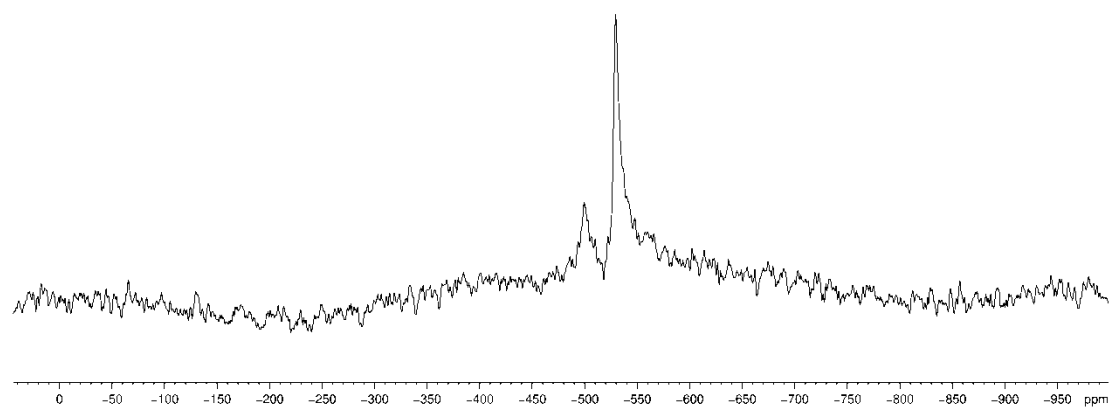


Figure 3.7: ^{51}V NMR spectrum for [VO(L3)]. The spectrum was recorded in DMSO-d₆ at 298 K. The reference for the chemical shifts is NH_4VO_3 .

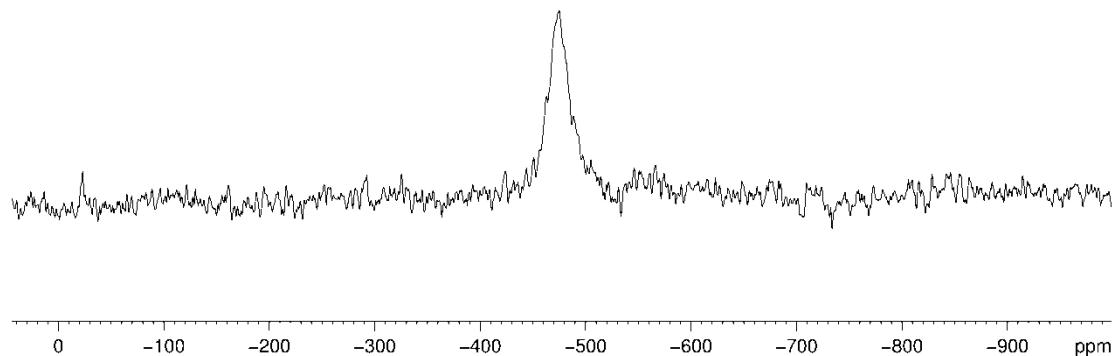


Figure 3.8: The ^{51}V NMR spectrum for $[\text{VO}(\text{L4})]$ measured in DMSO-d_6 at 298 K. NH_4VO_3 was used to reference the chemical shift of $[\text{VO}(\text{L4})]$.

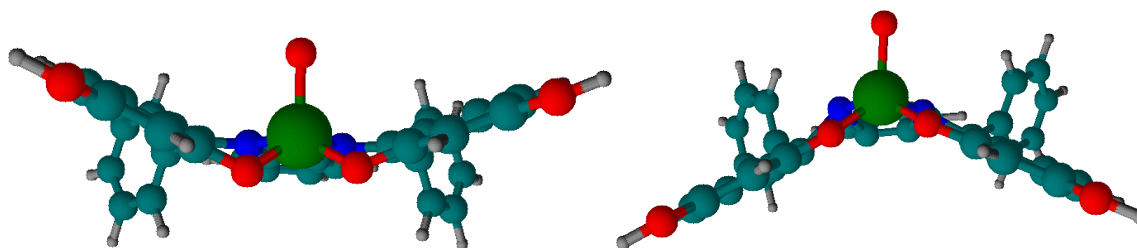
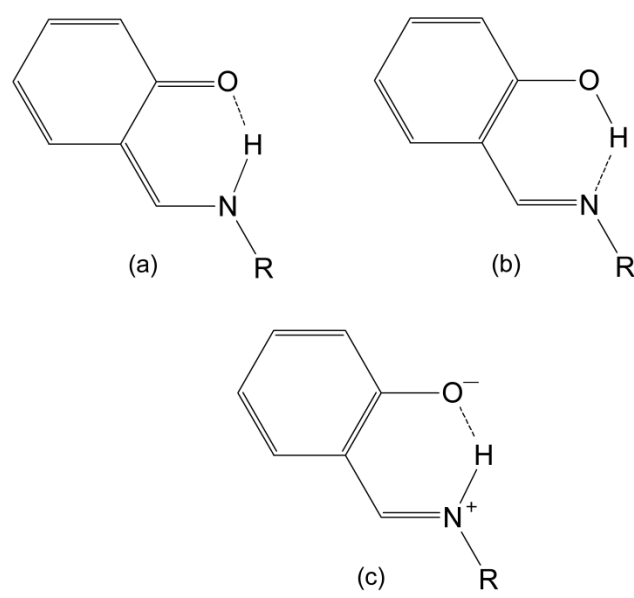


Figure 3.9: Two possible geometrical coordination isomers for the complex $[\text{VO}(\text{L1})]$ that could give rise to the two ^{51}V peaks observed in the NMR spectrum for this compound. (Left) an isomer where the ligand shields the equatorial region of vanadium, and (right) where the ligand distorts to expose the vanadium.

3.3 X-ray Diffraction

3.3.1 Description of zwitterion X-ray structures

There are three possible forms that an *o*-hydroxy Schiff base can adopt, *viz*, a keto-amine (a), phenol-imine (b) or zwitterionic (c) form (Scheme 3.3).⁸⁹ The first two can be regarded as keto (O—H)-enol (N—H) tautomeric forms of each other,⁹⁰ whereas the zwitterion can be thought of as intermediary between the two neutral forms. However, it does resemble the keto, N—H form more closely. Of these three forms, the zwitterions are the least commonly encountered. They can be distinguished from the formal keto form by their $\text{N}^+\text{—H}$ bond length, which is longer than for the standard, neutral N—H bond length of 0.87 Å. Otherwise, the bond lengths of the other heteroatoms can also be used, *i.e.* the C—O and the C—N bond lengths, although they are less sensitive to change than the N—H bond. For a truly zwitterionic form, the anionic C—O[−] bond length will be approximately the same as that of neutral C—O bond length. Likewise, the C—N bond length should be relatively the same as for a formal C—N double bond, although some lengthening can be expected. Also, the changes in, or extent of, aromaticity in the aromatic rings can give an indication as to whether or not a keto or phenolate group is present. In a keto-amine system, the C—C bonds adjacent to the keto group are expected to be lengthened relative to a standard C—C bond length for a benzyl ring, while the C—N bond is the same length as that of a neutral C—N bond.



Scheme 3.3: Tautomeric forms that are possible with *o*-hydroxy Schiff base species: (a) keto-amine, (b) phenol-imine and (c) zwitterionic.

3.3.2 X-ray structure determination of H_2L5

$C_{31}H_{30}N_2O_4$, fw = 494.57 amu, $a = 9.0766$ (7) Å, $b = 21.5777$ (19) Å, $c = 14.1584$ (12) Å, $\alpha = 90^\circ$, $\beta = 104.782$ (5) $^\circ$, $\gamma = 90^\circ$, $V = 2681.2$ (4) Å³, monoclinic, $P2_1/c$, $Z = 4$, $D_c = 1.225$ mg m⁻³, $\mu = 0.08$ mm⁻¹, $T = 100$ K, $R_1(wR_2) =$ for 4261 unique data ($R_{int} = 0.052$).

X-ray diffraction data were recorded on a Brüker APEX-II CCD diffractometer equipped with an Oxford Instruments Cryojet. The data were collected at 100 K with graphite monochromatized Mo $K\alpha$ ($\lambda = 0.71073$ Å) radiation by φ - ω scans. Data collection and reduction were performed by the program SAINT.⁹¹ Empirical absorption corrections were applied using SADABS.⁹¹ The structure was solved by direct methods using SHELXS97, and further refined by full-matrix least-squares on F^2 using SHELXL97. Publication material was prepared by publCIF. The H atoms were located in a difference map; however, those attached to carbon atoms were repositioned geometrically. Disordered solvent was removed by applying the SQUEEZE algorithm by PLATON. Separate tables of the crystal structure and refinement details are given in Appendix B.

3.3.3 Discussion of X-ray structure of H_2L5

The ligand, H_2L5 , crystallises in the monoclinic space group $P2_1/c$ with $Z = 4$. There is one molecule in the asymmetric unit (Figure 3.10). The ligand displays both intra- and intermolecular hydrogen bonding, involving $N^+ - H \cdots O^-$, $O - H \cdots O$ and $C - H \cdots \pi$ interactions. This hydrogen bonding extends to form a three dimensional network. Analysis of the $C=N$, $N-H^+$ and $Ar-C-O^-$ bond lengths reveals that the ligand is a *bis*-zwitterionic compound, and not a keto- or an enol- tautomer. A summary of selected bond lengths and angles is presented in Table 3.2.

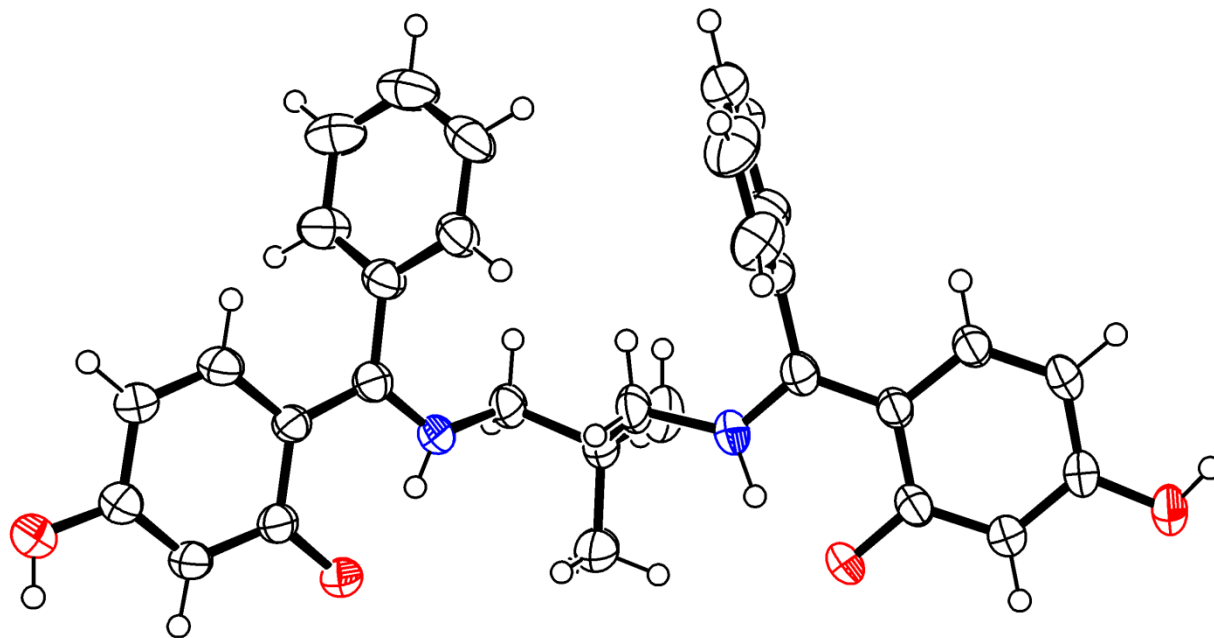


Figure 3.10: ORTEP thermal ellipsoid plot of the Schiff base **H₂L5** showing a 50% probability surface for carbon (black), nitrogen (blue) and oxygen (red). Hydrogen atoms are shown as spheres with an arbitrary covalent bond radius 0.37 Å.

The Schiff base is non-symmetric, and as such displays different bond lengths and angles for each half of the molecule. This non-symmetry between the two halves has important implications for the tautomerism they can exhibit. Keto-enol tautomerism depends not on the parent aromatic aldehyde, but on the stereochemistry of the Schiff base itself.⁹² For the intramolecular bond $N2^+—H102\cdots O3$, the N—H bond distance is longer than expected for a neutral N—H bond, that is, it is 0.98 Å; significantly longer than 0.87 Å. The C19—O3 bond length is intermediate between that for a single and double bond length (1.362 and 1.222 Å respectively) at 1.31 Å, which is closer to the value for a single bond.⁹² The hybridization at N2 is sp^2 , as determined by the bond angle $\angle C16—N2—C17$, which measures 126° , and the N2—C17 bond length of 1.32 Å, which is between the values for a single and double bond length (1.339 and 1.279 Å respectively).⁹² The N2—C17 bond length is also much shorter than the N2—C16 bond length of 1.47 Å; confirming its double bond character. Thus, on this half of the molecule, it is clear that a zwitterion has formed between the iminium N atom and phenolate O atom as $N2^+—H102\cdots O3^-$. A summary of selected parameters for the intramolecular hydrogen bonds is given in Table 3.2.

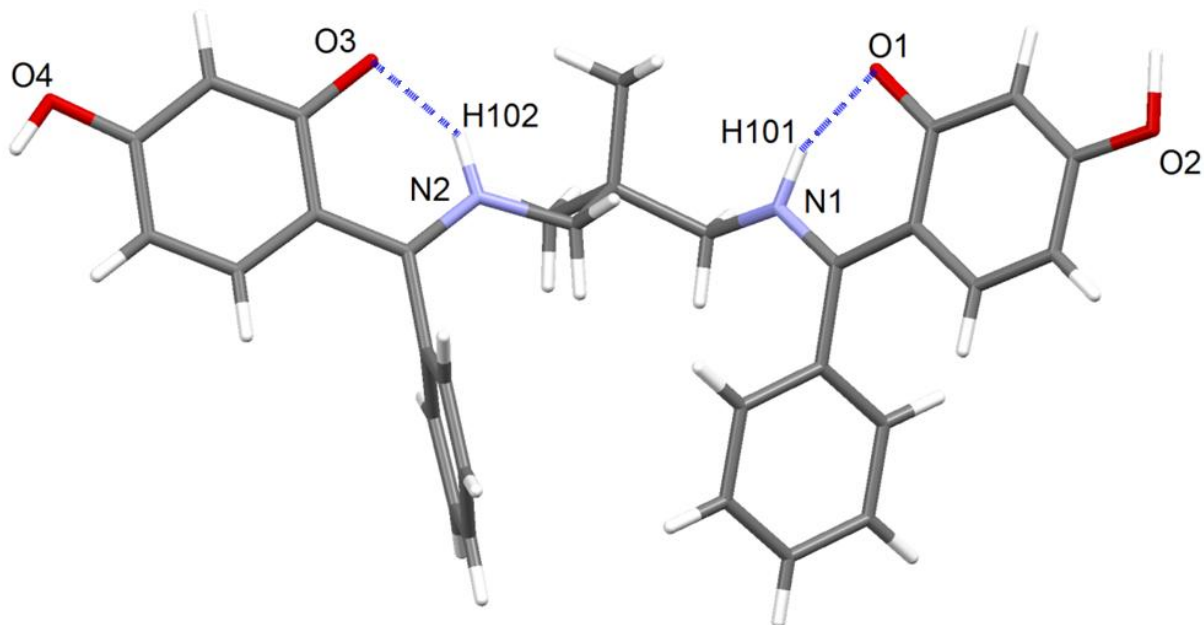


Figure 3.11: Diagram of the crystal structure of **H₂L5** showing the intramolecular hydrogen bonding, and the labelling scheme for the atoms involved.

For the intramolecular hydrogen bond between O1 and N1, the N1—H101 bond length is shorter than expected for a zwitterion. At 0.83 Å, it is even shorter than that presupposed for a neutral N—H bond length. Even when compared to the other half of **H₂L5**, this N—H bond is still much shorter than anticipated. However, on closer inspection it can be seen that this is a zwitterion, despite this greatly shortened bond. Firstly, the hybridisation of N1 is sp^2 , as it has very similar bond lengths and angles to that of N2 (see Table 3.2). Secondly, the C1—O1 bond length (1.30 Å) is very similar to that for C19—O3. It is slightly shorter though, reflecting a stronger double bond character. The increase in double bond character does influence the observed aromaticity on the aromatic ring it is connected to. Hence, it is an iminium N atom that has been protonated, and is hydrogen bonding to a phenolate O atom. Why the N1—H101 bond length is so much shorter than expected can be explained by the stereochemistry of the ligand.

Table 3.2: Hydrogen bond geometry.

<i>D</i> —H--- <i>A</i>	<i>D</i> —H	H--- <i>A</i>	<i>D</i> --- <i>A</i>	<i>D</i> —H--- <i>A</i>
N1—H101---O1 ⁱ	0.83 (1)	1.76 (3)	2.541 (2)	156 (3)
O4—H41---O1 ^{ii†}	0.84 (1)	1.78 (1)	2.586 (2)	160 (1)
N2—H102---O3	0.98 (2)	1.62 (2)	2.493 (2)	160.3 (1)
O2—H21---O3 ^{iii†}	0.84 (1)	1.67 (1)	2.509 (3)	175 (1)

Symmetry codes: (i) $-x, y+1/2, -z-1/2$; (ii) $x, -y-1/2, z+1/2$;

(iii) $-x, -y, -z$.

†Intramolecular hydrogen bonding – not shown in Figure 3.11.

As mentioned above, stereochemistry of a Schiff base influences the tautomerism, rather than the identity of the parent compounds. In compound **H₂L5**, the stereochemistry about N1 is significantly different from that of N2 on two accounts. The iminium(dimethyl)propylene propylene chain is in a gauche conformation for the torsion angle of \angle N1—C14—C15—C16, which is 64.7° (Figure 3.13). For the torsion angle of \angle N2—C16—C15—C14, the expected, anti-bonding conformation is observed, with an

angle of 170.1° . The gauche effect could possibly allow for hyperconjugation between the electron deficient $C14-N1^+$ σ bonding orbital and the $C15-C16$ σ^* anti-bonding orbital. The extent to which the dimethyl-propylene chain is able to donate electron density is also increased by the two methyl groups, as other o-hydroxy Schiff bases with gauche conformation do not display this shortened N—H bond length.⁹³ These compounds did not have electron-rich alkyl chains though.

In addition to the gauche conformation for the shortened half of the ligand, the dihedral angles formed between the planes of the substituted and no-substituted aromatic rings are also different. For the side with the standard N—H bond length, the two rings are twisted out of plane from each other by 89.3° (Figure 3.12). It is therefore expected that the extent of conjugation between the two aromatic systems would be negligible. However, the angle that the aromatic rings are twisted out of plane from each other, on the side exhibiting the shortened N—H bond, is only 62.6° . Hence, there is far more possibility for π electron delocalisation between these two systems and donation to the electron deficient $N1^+$ atom. Given this fact, and the fact that there may also be hyperconjugation from the dimethyl-propylene chain, it is possible that a shortened N—H bond has formed, rather than a neutral N—H bond. This structure then, highlights the effects that increased conjugation and stereochemistry can have on the tautomerism of Schiff bases.

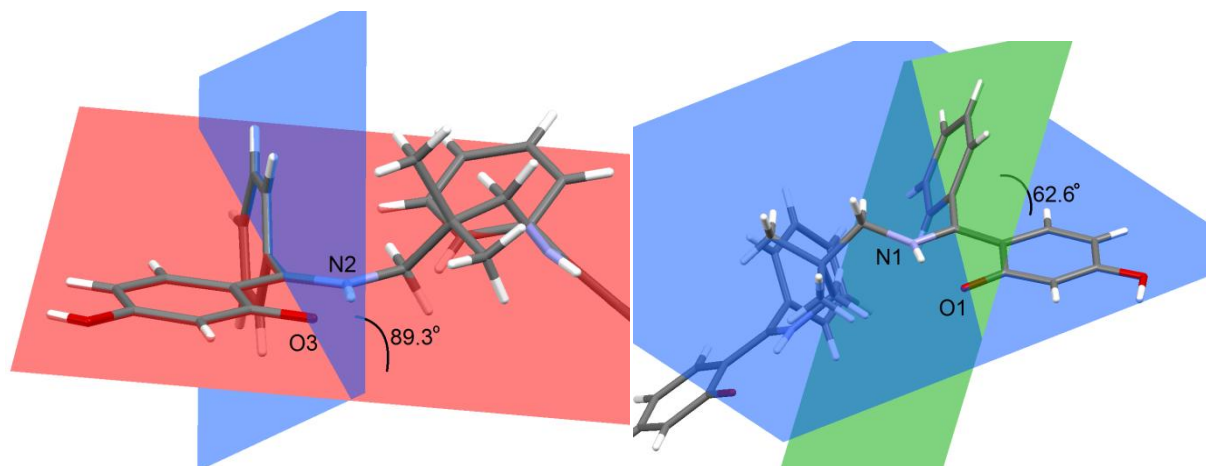


Figure 3.12: Angle formed between the planes bisecting the aromatic rings on each iminium group. For the iminium with the longer N—H⁺ bond length on the left, the angle formed by the planes is 89.3° , while for that with the shorter N—H⁺ bond length, the smallest angle between the bisecting planes is 62.6° .

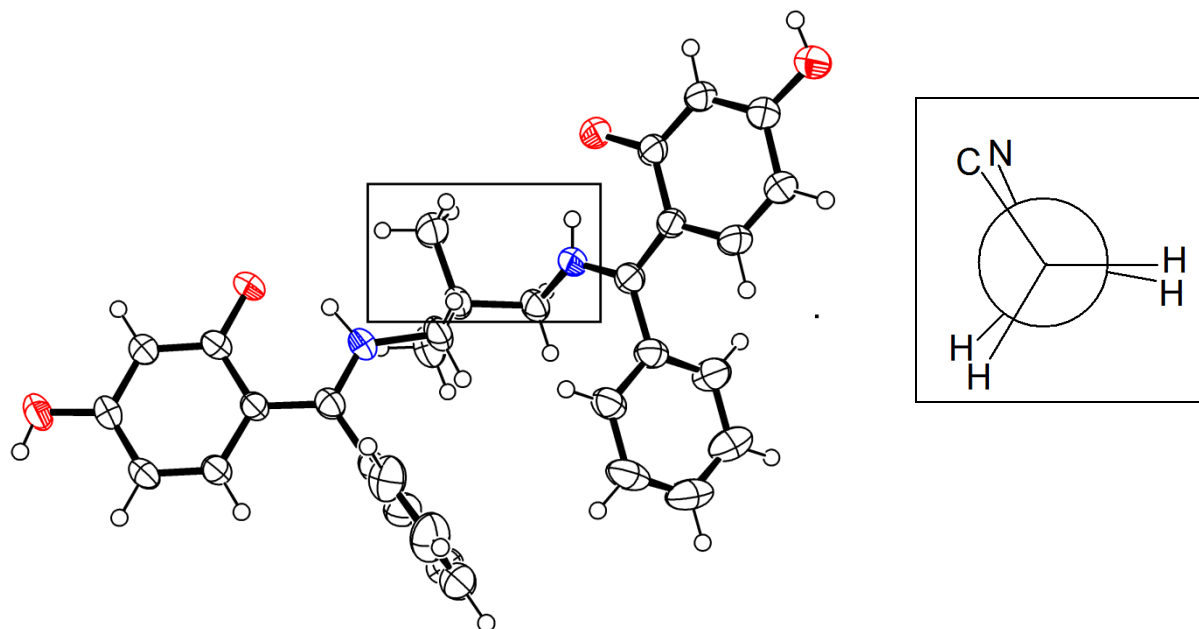


Figure 3.13: (Left) View of H_2L5 showing the gauche conformation about the iminium group with the shortened $N-H^+$ bond (highlighted within the black box). (Right) Inset showing the eclipsed formation of methyl and iminium N atom.

In addition to these intramolecular hydrogen bonds, each phenoxide O atom is also engaged in hydrogen bonding with the H atom of a phenol group on a neighbouring molecule. The donor H atoms to the phenoxide each come from a different, neighbouring molecule, and the result of this is the extension of the structure in two dimensions. These $O\cdots H-O$ bond lengths also differ marginally. For the $O-H\cdots O3$ hydrogen bond, the $O3\cdots H$ distance is 1.67 Å, while for the $O-H\cdots O1$ hydrogen bond, the $O1\cdots H$ distance is 1.78 Å. This represents the slight difference between single and double bond character of O1 and O3. O1, with slightly more double bond character, forms a slightly weaker hydrogen bond with the neighbouring molecule than does O3.

The third dimension of the structure is built up by soft $C-H\cdots\pi$ interactions involving two benzyl and one substituted aromatic ring that bind cooperatively to make each three-ringed motif. The substituted ring of the first compound donates a proton to two carbons on the benzyl ring of a neighbouring molecule, which in turn donates a proton back to the benzyl ring of the first compound (Figure 3.14). In total, there are four $C-H\cdots\pi$ bonds per three-ringed motif. This is not surprising, as $C-H\cdots\pi$ bonds are known to work cooperatively.⁹⁴

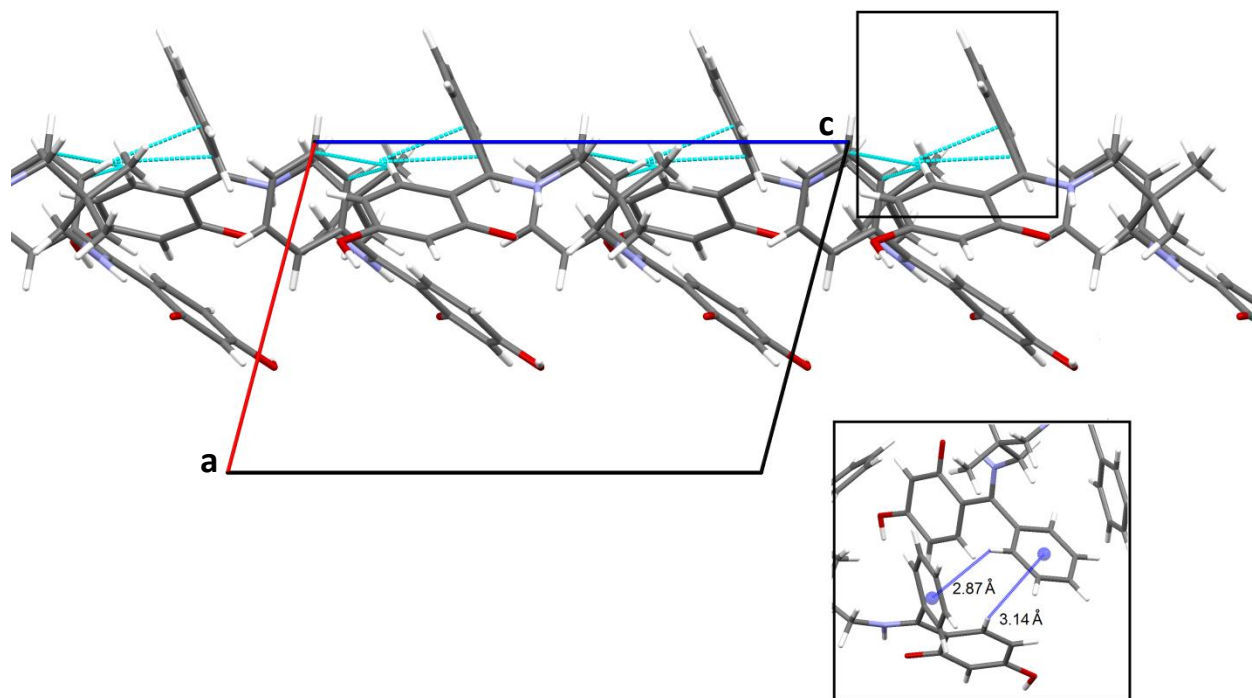


Figure 3.14: View along the b-axis showing the CH- π bonding, responsible for propagating the crystal structure along the c-axis. Insert shows the groups responsible for this CH- π bonding.

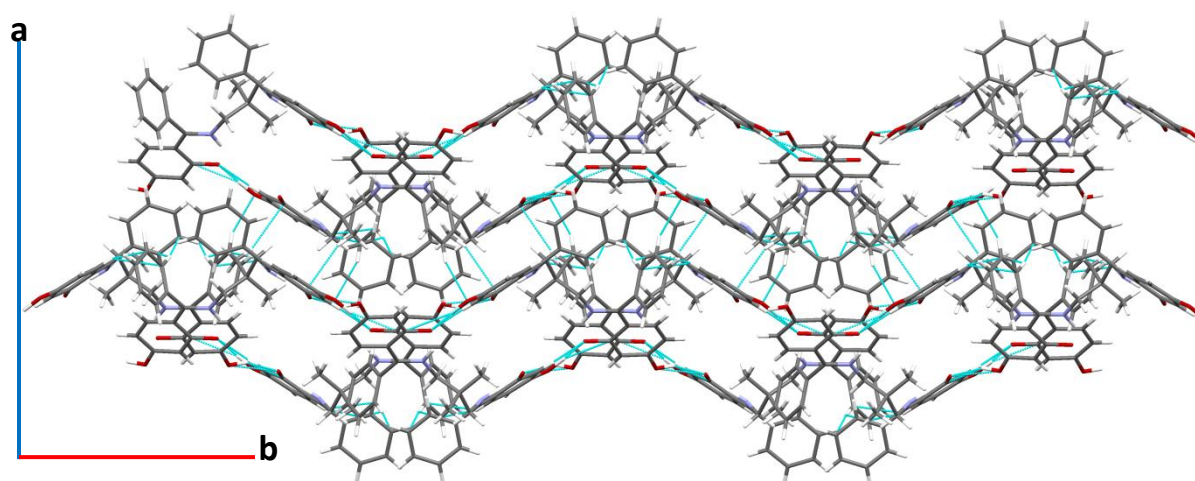


Figure 3.15: View along the c-axis of the crystal structure, showing the extended crystal structure formed by intermolecular H-bonding.

The crystal structure is extended along the b-axis by H-bonding between the phenol groups on one molecule and the phenoxide groups on another (Figure 3.15). Between the two phenol groups on a single molecule, one H-bond is significantly stronger than the other. The length of the bond formed by O3-H103---O1 is 1.82 Å, while that formed between O4-H104---O2 is 1.44 Å. This possibly reflects the greater electron excess on the O2 anion, whose H-bonding iminium proton is further away from it than it is for O1. Furthermore, this is added evidence of the zwitterionic nature of the compound. Were there

a formal double bond between O2 and C1, there would be less electron density on O2 resulting in a weaker H-bond between O2 and H104; instead, a strong H-bond is seen between these two atoms. The phenol groups are also involved in CH–O hydrogen bonding with an aromatic proton from a neighbouring molecule. The bond forms between C12–H12---O4, and has a length of 2.41 Å. This weak H-bond facilitates the stacking of the molecules along the a-axis.

Chapter 4 | Electronic Spectroscopy

4.1 Introduction

Vanadium(IV), with a single, unpaired electron with a simple spin of 1/2, a nuclear spin of 7/2 and a high natural abundance (> 99 %) of the ^{51}V nucleus, has made it possible to determine the bonding of ligands to the divalent, VO^{2+} ion, vanadyl.²⁰ Additionally, being able to determine which ligands are bound to vanadyl centres ($\text{V}=\text{O}$) has been exploited for investigating the role of metal ions in biological systems.

Early models used to explain the electronic transitions culminated in the Ballhausen-Gray theory, which is still widely used for simple vanadyl systems, such as $[\text{VO}(\text{H}_2\text{O})_5]^{2+}$.⁹⁵ In these systems, three bands are observed in room temperature solutions, and have been ascribed to $d-d$ transitions of the unpaired electron from the b_2 orbital to the $e\pi^*$ (I), b_1^* (II) and $1a_1^*$ (III), which occur between 625 – 910 nm, 525 – 690 nm and 330 – 476 nm, respectively (Figure 4.1).

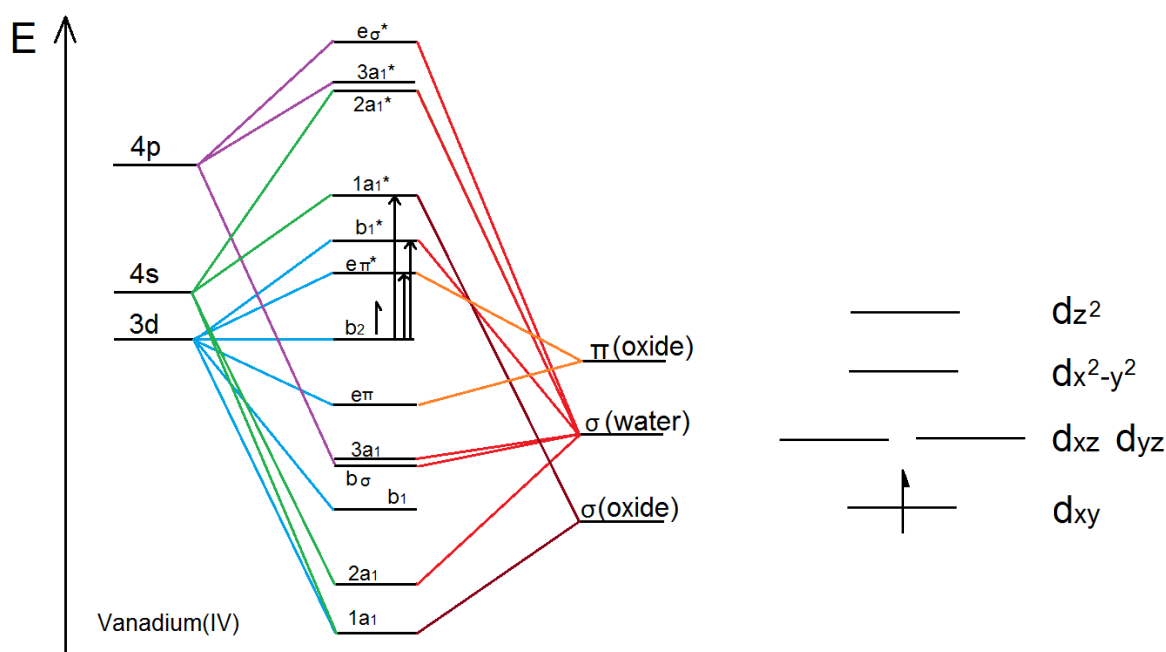


Figure 4.1: (Left) Electronic structure and transitions as set forth for an aqueous vanadyl ion, $[\text{VO}(\text{H}_2\text{O})_5]^{2+}$, in the Ballhausen-Gray theory. The unpaired electron occupies the b_2 molecular orbital formed by a $3d$ atomic orbital on vanadium; the $d-d$ transitions on this electron are shown by black arrows. (Right) The location of the unpaired electron in the d orbitals; in its lowest energy state, it is in the non-bonding, d_{xy} orbital.

In addition to these $d-d$ transitions, charge transfer from the vanadium to the ligand can also take place. As the size of the ligand(s) increases, other ligand-based electronic transitions can take place as well.⁹⁶ Interpretation of larger molecules can become complicated when molecular orbitals are spread out over many atoms, such that no one orbital can be said to be responsible for the transition. Thus, interpretation of larger complexes often requires that calculations of the orbitals involved in the transitions be done.⁹⁶

To study the electronic state of the vanadyl complexes $[\text{VO}(\text{L1})]$, $[\text{VO}(\text{L2})]$, $[\text{VO}(\text{L3})]$, $[\text{VO}(\text{L4})]$ and $[\text{VO}(\text{L5})]$, electronic absorption and electron paramagnetic resonance (EPR) spectroscopy were

employed. Electronic absorption spectroscopy was used to determine the effects of chelation on the energy of the ligand orbitals, as well as which molecular orbitals were involved in the transitions. DFT calculations were performed to aid in this investigation, the results of which are presented in Chapter 6. EPR spectroscopy was used to determine the identity and orientation of the ligands bonded to the vanadyl ion. Because electronic absorption spectroscopy is already well understood, only an introduction to EPR spectroscopy, and how it relates to vanadyl ions, is given below.

4.1.1 EPR spectroscopy – the technique

EPR spectroscopy is used to study the transitions of unpaired electrons between their different spin states. These spin states arise due to coupling of the electron to the magnetic moment of a nucleus; the exact number of spin states depend on the spin of the electron and the nucleus to which it is coupled.²⁰ The simple case where an electron with spin $1/2$ is coupled to a nucleus with spin $1/2$ is shown in Figure 4.2. Here, there are different orientations for the electron's spin, *viz.* $m_s = +1/2$ and $m_s = -1/2$, with one spin state being at a higher level of energy than the other. However, because of the magnetic spin of the nucleus, the energy of both of these spin states is further raised or lowered, to produce four non-degenerate energy levels. Therefore, there are two observable transitions for the unpaired electron. This coupling of the electron to the nucleus is termed hyperfine coupling. The number of lines observed can be predicted by multiplying the spin state of the nucleus by 2, and adding "1" ($2I + 1 = n$). Therefore, for ^{51}V , the spin state is $7/2$, and the total number of lines observed for an ideal sample is 8.

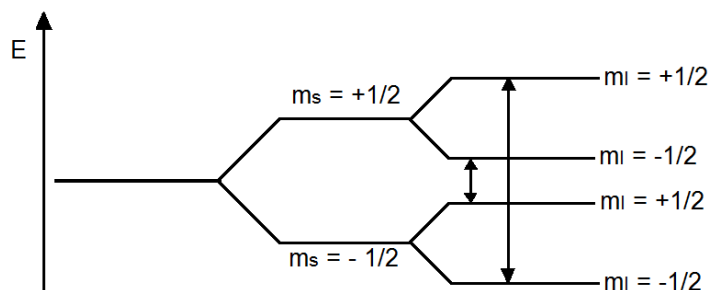


Figure 4.2: The spin state transitions for an electron with spin $S = 1/2$ coupled to a nucleus with $I = 1/2$. The nuclear spin results in two transitions being observed as the electron spin-state changes in the magnetic field.

In addition to the hyperfine coupling observed between an electron and its nucleus of origin, superhyperfine coupling can also be observed between the electron and a neighbouring nucleus, such as ^{14}N , if that nucleus is in a suitable orientation.²⁰ However, because the unpaired electron in VO^{2+} is localised in the d_{xy} orbital, away from the equatorial plane of the donor atoms, this superhyperfine coupling is not usually resolved.²⁰

When an electron is placed in an external magnetic field, the degeneracy of the energy levels is split even further. Resonance of the electron between these energy levels is caused when electromagnetic radiation of suitable energy is supplied to the electron.⁹⁷ The energy of this transition can be described Equation 4.1:

$$h\nu = g\beta H \quad (4.1)$$

Where h is Planck's constant, ν is the frequency of the radiation, g , is the "g-value", β , is the Bohr magneton and H is the magnitude of the externally applied magnetic field. The value of g can be viewed as the proportionality constant between the magnetic moment of the free electron and the product of the Bohr magneton and the spin angular moment of the electron. This g value is dependent on the environment of the electron; for a free electron, $g_e = 2.002319304386$ (one of the most precisely known physical constants).⁹⁷ For vanadyl complexes, the value of g is typically less than that for the free electron.

In a continuous-wave (cw) -EPR experiment, the frequency of the radiation is held constant, and the strength of the magnetic field is varied progressively across a range. For magnetic fields generated by an iron-core magnet, the range of microwave frequencies used can vary from 3 – 45 GHz. Table 4.1 gives the band names and frequency ranges typically associated with commercial EPR spectrometers. In the experiments that follow, an EPR spectrometry using X-band frequencies in the 9 – 10 GHz range has been used.

Table 4.1: Frequencies, band-names and magnetic field strengths (in Tesla) of commercially available EPR spectrometers.

Band Name	Frequency / GHz	B / Tesla
S	3.0	0.107
X	9.5	0.339
K	23	0.820
Q	35	1.25
W	95	3.30

The situation described above is for a simple, isotropic system. In most systems, however, the electronic configuration around the vanadium(IV) ion is not symmetric, and the EPR spectrum is said to be for an anisotropic species.⁹⁷ If there is a unique axis of symmetry, the complex's symmetry is described as axial. The anisotropic EPR spectra for complexes having axial symmetry appear as two, eight-line spectra superimposed on each other. Because of the strong vanadium–oxygen interaction in the vanadyl unit, most EPR spectra for oxovanadium(IV) complexes display axial symmetry.²⁰ In some instances, all three axes may be electronically distinct, in which case three different sets of spectra will be observed. This last type of symmetry is termed rhombic symmetry. The isotropic EPR spectrum for a complex with axial, or rhombic, symmetry can be observed if the complex is dissolved in a solvent. When in solution, the thermal motion of the complexes will result in a situation where the individual axes are not resolved from one another, and an eight-line spectrum will be obtained. If this solution is frozen, so that thermal motion is greatly reduced, then the anisotropy will no longer be averaged away, and the more complicated anisotropic spectrum will once again be observed.⁹⁸

In an anisotropic spectrum, each unique electronic configuration exhibits different hyperfine coupling constants, A . There are different g -values associated with each of these axes as well. The principal values for g can be extracted from powder, or frozen solution, EPR spectra.²⁰ If all three principle axes are identical, the g values would be identical such that $g_x = g_y = g_z$. For vanadyl complexes with the typical axial symmetry, $g_x = g_y \neq g_z$; the tensors g_x and g_y are then represented by the combined term g_{\perp} , while the g_z term is referred to as g_{\parallel} . The same relationship applies for the

hyperfine coupling constants, which are resolved according to the principle axes to give the terms A_{\perp} and A_{\parallel} . For isotropic spectra, because they are an average of all other spectra, their g tensor and hyperfine coupling constant are also averages of all their constituent, anisotropic terms. In referring to these isotropic values, the symbols g_o and A_o are used.

Hyperfine coupling constants, as well as g values, have several components, *viz.* parallel and perpendicular. The average values for both (g_o and A_o) can be read directly off the EPR spectrum, although the units should be converted from Gauss or Tesla to MHz. Calculation of the individual components is preferable, as it allows for direct comparison to other compounds. To calculate the parallel hyperfine coupling constant, A_{\parallel} , (the most useful value to obtain) the parallel g value, g_{\parallel} , must first be determined. This is done by using Equation 4.1, where the magnetic field value used is the average between the two outermost lines of the spectrum, and solving for g . The difference between the two outermost lines is then determined and divided by seven (for ^{51}V), to obtain an A_{\parallel} value in terms of g . A_{\parallel} is then multiplied by g_{\parallel} and the Bohr magneton, β , to arrive at a value of A_{\parallel} in wavenumbers.²⁰

4.1.2 EPR spectroscopy – application to vanadyl systems

For solutions of vanadyl complexes, where only a single species is present, an eight-line spectrum is therefore typically observed. However, the EPR spectrum of the same sample as a powder or from a frozen solution can give rise to multiple signals. This is because there may be anisotropy, which is not averaged away by the motion of molecules in solution.²⁰ That is, the electronic configuration may have a unique axis of symmetry. This axis of symmetry is typically the result of the very strong bonding between the V and O atoms of the vanadyl unit, such that molecules whose V=O bond is parallel to the magnetic field exhibit larger hyperfine coupling constants than those whose V=O bond is aligned perpendicularly to the field. In a solution, the random motion of the molecules is such that only a single eight-line spectrum is observed, with the hyperfine coupling constant being the average of the parallel and perpendicular terms. In powder or frozen solution, two superimposed spectra are often observed, and even a third spectrum may be seen if there is an additional axis of symmetry.⁹⁷

Although EPR spectroscopy is a powerful tool by itself, the vanadium(IV) nucleus of the vanadyl ion offers certain advantages over others that greatly enhance its usefulness.²⁰ In addition to the readily observed and easily identifiable eight-line spectrum mentioned above, the hyperfine coupling constant is very sensitive to the character and orientation of the donor atoms. The sensitivity is such that the inner coordination environment of the vanadyl unit can be determined from an EPR spectrum alone with relative accuracy. Owing to this dependence, vanadyl has often been substituted for other metals in enzymes, or other complex molecules, to determine the possible coordination environment of the original/naturally occurring metal ion.

Determining the number and types of ligands through the A_{\parallel} values is possible because of the additivity relationship.²⁰ Because each ligand makes an individual contribution to A_{\parallel} , the sum of all their contributions will give the A_{\parallel} value observed. In general, the ligands that are stronger electron donors contribute less to A_{\parallel} than those that are weaker donors. Caution must be taken though, as there are several combinations of ligands that can give the same A_{\parallel} ; it is thus important to have an idea of what the possible ligands are before trying to interpret an EPR spectrum. The situation is less complicated when all possible ligands are known, such as exists in this study where only a single, tetradentate ligand and solvent are present in the system.

Table 4.2: Donor groups and the contribution they make to the parallel hyperfine coupling constant, A_{\parallel} . (values stated are in units of $\times 10^{-4} \text{ cm}^{-1}$). Table adapted from reference 20.

Binding group	A_{\parallel} contribution	Reference
H ₂ O	45.7	99
Perp. imidazole		
=N-	45.5	100
Aliphatic imine		
=N-	44.4	99
Cl ⁻	44.1	101
Amide (DMF)		
HC(O)NRR'	43.7	102
RCO ₂ ⁻ , ArCO ₂ ⁻	42.7	99
PO ₄ ³⁻	42.5	103
Pyridine =N-	40.3	99
RNH ₂	40.1	99
Par. imidazole		
=N-	40	100
OH ⁻	38.7	99
ArO ⁻	38.6	104
acac, 1 O eq.		
=C-O ⁻	37.6	104
RO ⁻	35.3	99
ArS ⁻	35.3	99
	30-32 (ligand charge -2); 37-	
Deprot. amide	43 (ligand charge -4)	104,99
RC(O)NR'		
RS ⁻	31.9	99

In addition to the effect that the nature of the donor atom has on the parallel hyperfine coupling constant, the symmetry of the ligands can also influence the hyperfine coupling constant significantly. The A_{\parallel} value for vanadyl with aromatic nitrogen donor ligands (specifically for imidazole) decreases as the distortion from an ideal square-pyramidal geometry increases.¹⁰⁵ This can be explained through the interaction of the π electrons on the ligand with the vanadium's σ orbitals. When the ligand is orientated perpendicular to the V-O unit, the p-orbital on the nitrogen is positioned to overlap with the non-bonding d_{xy} orbital on vanadium, thus increasing the ligand to metal electron donation and decreasing A_{\parallel} . When the ligand is orientated parallel to the V-O unit, however, the p-orbital is in position to overlap with the d_{xz} , d_{yz} orbitals, which are already involved in strong bonding interactions with the vanadyl O atom. This unfavourable orientation leads to an increase in A_{\parallel} .²⁰ An illustration of this effect is provided in Figure 4.3. Thus, the additivity relationship can allow for an understanding of the coordination geometry about the vanadyl unit, in addition to predicting the types of ligands coordinated.

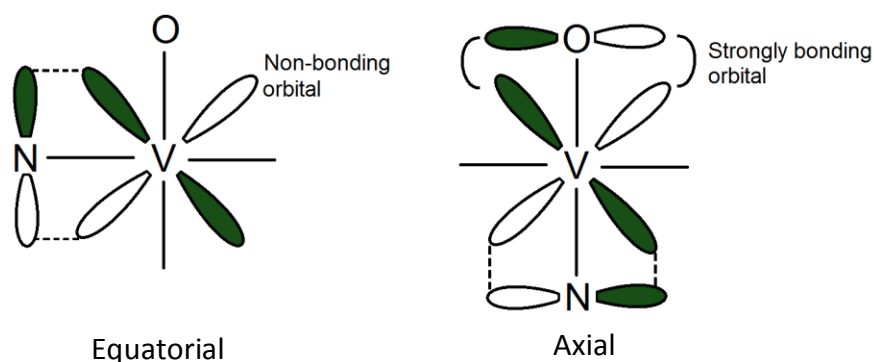


Figure 4.3: The different orientations of ligand and the V–O unit, and how this influences which molecular orbitals interact with the donor atom’s p-orbital.

The vanadyl complexes [VO(salen)] and [VO(salpn)] (Figure 4.4), were some of the early vanadyl complexes to be investigated by EPR spectroscopy.¹⁰⁶ Seeing as the compounds under investigation here are [VO(salen)] or [VO(salpn)] derivatives, there should be similarities between the A_o and $A_{||}$ values of the two sets of compounds. The A_o values for [VO(salen)] and [VO(salpn)] were, respectively, 100.0 G and 100.8 G in pyridine; these values showed little dependence on the solvent used, with any variation being attributed to the solvents’ different dielectric constants. Additionally, [VO(aceten)] and [VO(acetpn)] (Figure 4.4), where the imine H atom had been replaced by a CH_3 , showed lower A_o values than the salen/salpn complexes by *ca* 1.0 – 1.8 G. This suggests that the electron is somewhat more delocalised onto the ligands in these systems, and is thus farther from the vanadium nucleus. According to this trend then, the compounds studied here, with benzene rings attached to the imine C atom, were expected to exhibit enhanced pi-backbonding and greater delocalisation of the unpaired spin over the ligand framework, leading to smaller A -values.

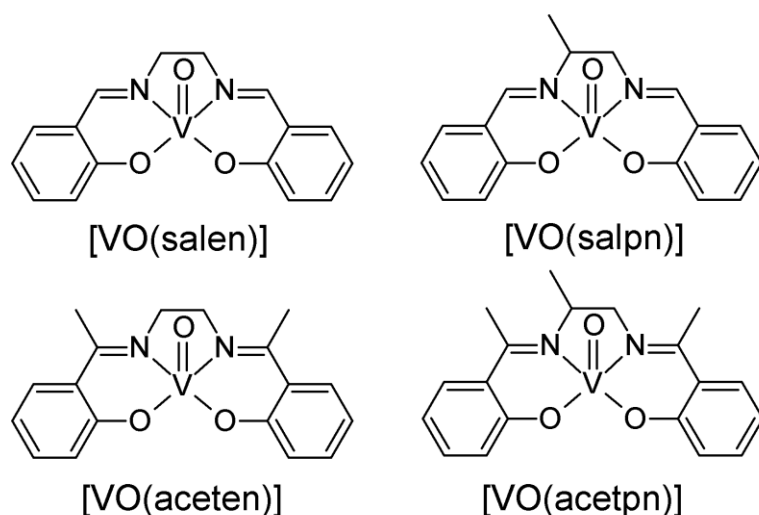


Figure 4.4: Vanadyl complexes bearing resemblance to those under investigation, whose EPR and electronic absorption spectra been reported.¹⁰⁵

4.1.3 Theoretical assumptions

The electronic absorption and EPR spectra recorded for the vanadyl complexes of this study must be interpreted within a framework. Unfortunately, no crystal structures were obtained for any of the complexes, which would have provided a basis for the interpretation of their spectra. Therefore, DFT

calculations were performed to determine the possible structures of the complexes; the full results of the calculations are given in Chapter 6. In summary though, the calculated geometry is very similar to that expected for an oxovanadium(IV) Schiff base complex, namely a square-pyramidal coordination, with the four donor atoms of the tetradentate ligand positioned equatorially. The vanadium is displaced from this equatorial plane, and the typical C_s space group was therefore used to interpret the spectra (Figure 4.5).

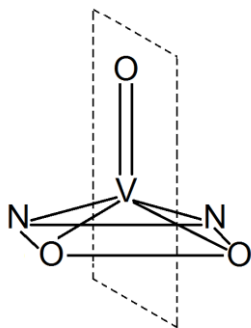


Figure 4.5: Point group about the vanadyl ion that will be used in the interpretation of the electronic spectra observed for the complexes [VO(L1)], [VO(L2)], [VO(L3)], [VO(L4)] and [VO(L5)].

4.2 Experimental

Electronic spectra were recorded in dimethyl sulfoxide on a PG Instruments T80 UV/VIS PC spectrophotometer using 1 cm pathlength quartz cuvettes. EPR spectra were recorded on a Bruker X-band spectrometer. Isotopic spectra were recorded at 298 K in DMSO.

4.3 EPR spectroscopy

Both solution and powder EPR spectra were recorded for the vanadyl complexes. In addition, both CHCl_3 and DMSO were used for the solution study to determine whether or not there was an appreciable solvent interaction at the vacant, axial position.

4.3.1 Powder EPR spectroscopic study

Powder EPR spectra for the oxovanadium(IV) Schiff base complexes were observed to determine their hyperfine coupling constants, and to determine whether or not the complexes possessed any symmetrically unique axes. It can be seen from their spectra (Figure 4.6a-e) that all the complexes possess axial symmetry. As mentioned in the introduction to this section, this axial symmetry is typical for vanadyl complexes. The g tensor and hyperfine coupling constant (in units of gauss and cm^{-1}) responsible for the parallel component of the spectrum for each complex is given in Table 4.3. These are the most relevant values needed for discussing the additivity relationship.

Table 4.3: Average, parallel and perpendicular g and A tensors for the oxovanadium(IV) Schiff base complexes.

Complex	g_{\parallel}	A_{\parallel} / G	$A_{\parallel} / \times 10^{-4} \text{ cm}^{-1}$
[VO(L1)]	1.955	175.0	159.6
[VO(L2)]	1.957	172.6	157.6
[VO(L3)]	1.983	188.0	169.9
[VO(L4)]	1.946	177.3	161.0
[VO(L5)]	2.062	180.9	174.1

The donor atom set for each complex consists of two phenoxide atoms (ArO^-) and two neutral imine nitrogens. Because the imine is part of a highly conjugated system, it can be considered equivalent to the N donor atom of pyridine, which has an A_{\parallel} contribution of $40.3 \times 10^{-4} \text{ cm}^{-1}$ according to Table 4.3. Using this value and that of $38.6 \times 10^{-4} \text{ cm}^{-1}$ for ArO^- , the expected A_{\parallel} value for the complexes is $157.8 \times 10^{-4} \text{ cm}^{-1}$. This is very close to the value obtained for [VO(L1)] and [VO(L2)]. For these two complexes then, a binding mode can be proposed that places the donor atoms in the equatorial plane, with little distortion from the ideal square-pyramidal geometry.

The complexes [VO(L3)], [VO(L4)] and [VO(L5)] all show larger than expected A_{\parallel} values. There are two possible reasons for the higher than predicted A_{\parallel} values. Either, the identity of the donor atoms is different, i.e. certain donors have been displaced by others, or the geometry is distorted from an idealised square-pyramid. The former reason is more likely to occur in solution, where other donor atoms are available, however these are solid state samples. Also, the nature of the tetradentate structure of the ligands makes them far less likely to only partially bind to vanadium. Rather, distortion from the square-pyramidal geometry is a more likely cause for the increased A_{\parallel} constants observed. This distortion arises because the three carbon-long alkyl chain results in the formation of a six-membered chelate ring. This is a more strained conformation than exists for the five-membered ring; hence some of the donors are displaced from the equatorial plane (See Section 6.4.1 for further details on the alkyl chain induced distortion).

This reasoning leads to the conclusion that more distortion to the coordination geometry is caused by the addition of two methyl groups onto the alkyl chain, than the absence of them. The hydroxyl group however, had the opposite effect to the two methyl groups, by lowering the A_{\parallel} value. Sterically, the hydroxyl group represents more bulk than the hydrogens on the un-substituted chain. Most likely then, the hydroxyl group interacts with the vanadyl unit in some way, altering the coordination geometry to something more favourable; that is, one where the donor atoms are in the equatorial plane. From the list of values given in Table 4.3, the extent to which the donor groups are brought into the equatorial plane appears to be intermediate between that of the five- and six-membered chelate ring formed by the simple ethyl- or propyl-chain, respectively.

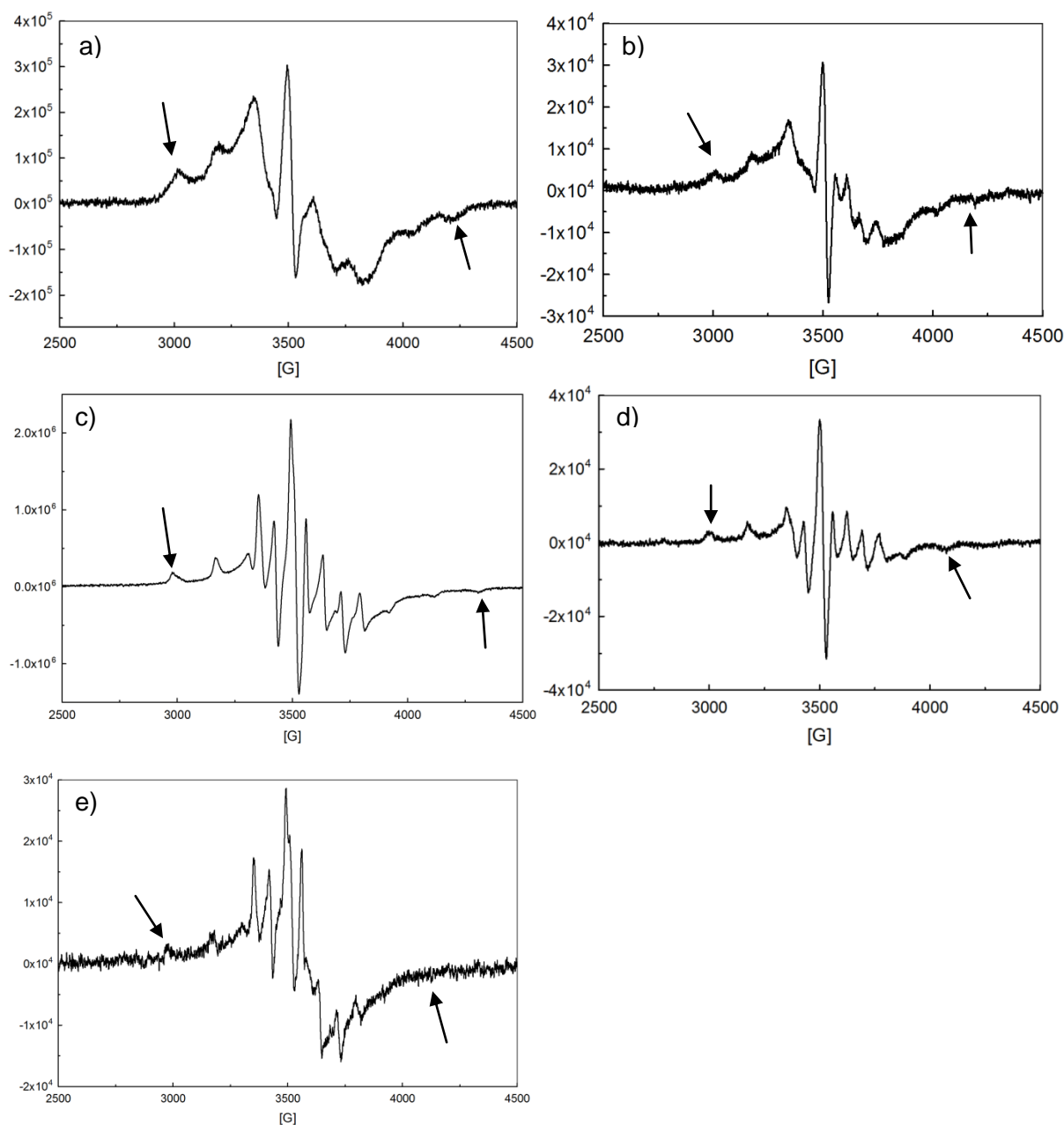


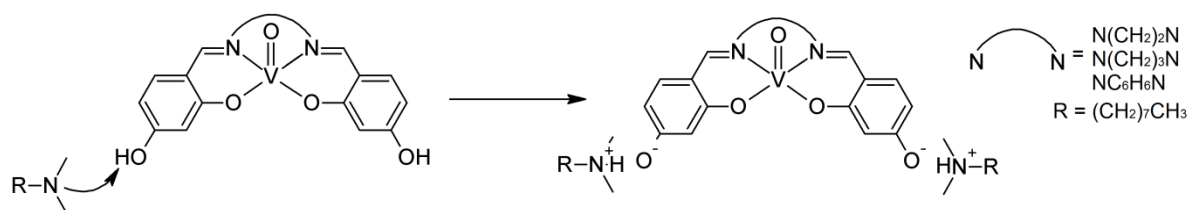
Figure 4.6: Powder EPR spectra for the oxovanadium (IV) Schiff base complexes: a) [VO(L1)], b) [VO(L2)], c) [VO(L3)], d) [VO(L4)] and e) [VO(L5)] recorded at 298 K. The outermost absorption peaks (straight arrows) were used for the calculation of the parallel contribution to the hyperfine coupling constants.

4.3.2 Solution EPR spectroscopic study

In addition to determining which ligands are coordinated to the VO^{2+} centre, or what their orientation is, the ability of VO^{2+} to coordinate another donor at the vacant, axial position opposite the vanadyl oxygen can be assessed using EPR spectroscopy. This is done by recording the spectrum for a given complex in different solvents, and observing how significant the change in the isotropic hyperfine coupling constant is.* A small change of the hyperfine coupling constant between solvents, *ca* 0.2 – 3 G, does not necessarily indicate that coordination has taken place. This difference can be a result of the solvent's hydrogen-bonding, or dielectric constant, effects.^{106,107}

*To precisely determine whether or not coordination of a solvent, or other, molecule is taking place, a variable temperature study needs to be performed. This was omitted, due to a lack of suitable equipment.

Initially, the isotropic EPR spectra of all complexes were recorded in DMSO at room temperature. The limited solubility of the compounds greatly reduced the number of solvents available, and as would be expected, the remaining solvents were very similar to DMSO, e.g. dimethyl formamide (DMF). Ideally, the solvents used should have differing coordinating abilities; hence, a method was devised to dissolve the complexes in chloroform. Each complex possesses two mildly acidic, aromatic hydroxyl groups, which can be deprotonated with a mild base, such as a tertiary amine. To dissolve the complexes in chloroform then, a few drops of *N,N*-dimethyloctylamine was added to a powder of each complex, effectively forming an ionic liquid, which was then dissolved in chloroform (Scheme 4.1). Unfortunately, this approach is not suitable for protic solvents, as they appear to oxidise the vanadium, as evident by a colour change from green to yellow, and an absence of any EPR signal. Additionally, [VO(L4)] gave no signal when dissolved in chloroform with the tertiary amine, presumably due to the presence of the hydroxyl on the propyl chain. [VO(L5)] was only sparingly soluble in the chloroform/amine solution, and was not concentrated enough to obtain an EPR spectrum. It is important to note though that by deprotonating the phenol groups, the electronic structure of the complex changes. How this affects their EPR spectra will be seen shortly.



Scheme 4.1: Deprotonation of aromatic hydroxyl groups with the tertiary amine *N,N*-dimethyloctylamine to facilitate dissolution in chloroform.

For those instances where vanadium was oxidised from +4 to +5, only H₂O and (CH₃)₂N(CH₂)₇CH₃ are present. It is unlikely that the tertiary amine could be responsible for the oxidation of vanadium, as aliphatic amines are known reducing agents of V(V) species. For example, [VOCl₃] and NMe₃, when combined, result in the formation of [VOCl₂(NMe₃)₂] and HNMe₃Cl. The more acidic α -protons on the tertiary amine, the more effective a reducing agent it will be.^{108,109} Note that the tertiary amine used here has eight α -protons; one less than the maximum amount. Contrary to this, hydroxide is a known oxidising agent of vanadium (see equation 5.7 in Chapter 5). Therefore, any water present would most likely be deprotonated by the amine to hydroxide, which would then oxidise the vanadium from +4 to +5.

For vanadyl complexes, it is often the case that the g_0 -value for the unpaired electron is slightly less than, or close to, that of the free electron value. This is true for the vanadyl complexes studied here. For complexes dissolved in chloroform, the g_0 -values ranged from 1.97-1.98, a very small variation. The DMSO solutions, however, gave g_0 -values slightly higher than that of the free electron value of 2.0023. This shows that the electron is coupling to the angular momentum of additional electrons from another source. When the g_0 -value of a complex is greater than 2.0023, it is because it is coupling to the angular momentum from other electrons, and this effect is generally seen for systems like copper(II) (d^9) where there are additional electrons in the d -orbitals.⁹⁷ Vanadium(IV)'s d^1 electronic configuration usually results in lowered g_0 -value, because the electron's angular momentum is retarded by its coupling to the nucleus only. Hence, for the vanadyl complexes here to have higher than expected g_0 -values in DMSO, means that additional electron density is available

nearby the unpaired electron, with which it is coupling. That there is little variation between the different complexes shows that the g_0 -value is not affected by the slight structural changes in the ligands. Consistency of the g_0 -value for a family of related complexes is expected for vanadyl species.¹⁰⁶

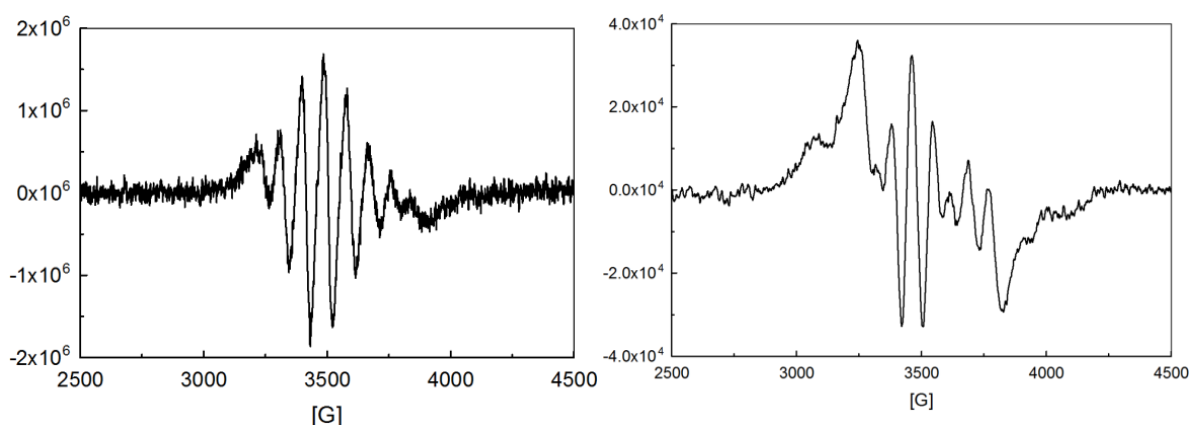
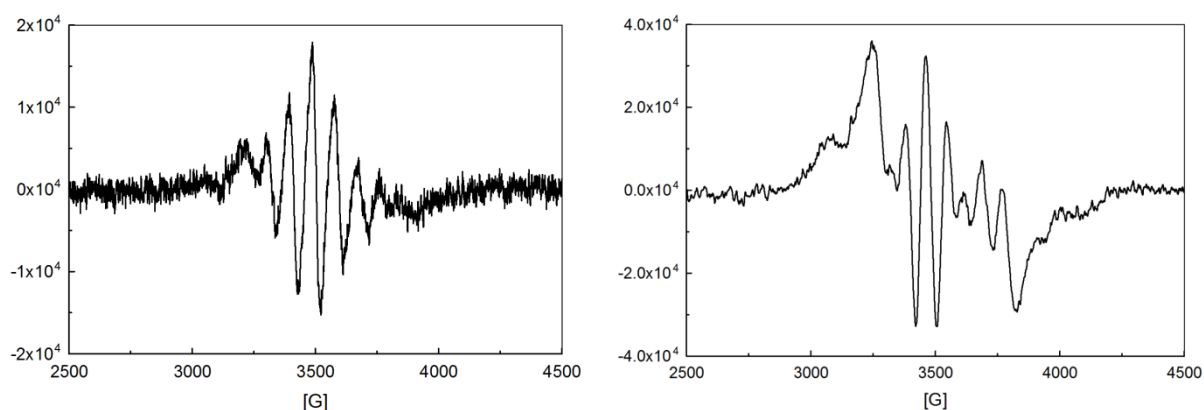
The isotropic hyperfine coupling constant is expected to decrease with increasing ligand field strength. For the related oxovanadium(IV) Schiff base complexes (shown in Figure 4.4), those with a substituent on the imine carbon were predicted to have a greater ligand field strength than for the unsubstituted imines, and therefore, it was no surprise when their hyperfine splitting was less than that observed for the unsubstituted imines (Section 4.1.2).¹⁰⁶ Therefore, with the addition of benzene rings to the imine groups in the complexes, the A_0 values were predicted to be even lower than for the previously observed [VO(Salen)] and [VO(Aceten)] complexes. However, the values observed for the DMSO solution spectra were much higher than anticipated (Table 4.2). The increase was from ca. 10 to almost 20 G; a much greater magnitude and in a different direction to that theorized. The origin of this effect is most likely not electronic, but structural in nature.

When the substituent is small, there is little steric bulk to prevent the ligand from adopting its optimum geometry. However, as the steric bulk of these groups is increased, they hinder the ligand from chelating in the ideal square-pyramidal shape. It was already seen in the powder EPR section that, by comparing the parallel hyperfine coupling constant, there is some geometrical distortion between the different complexes. If the contribution for the conjugated imine donors is lower than $40.3 \times 10^{-4} \text{ cm}^{-1}$ (contribution for pyridine), then it is possible that the actual amount of distortion for all complexes is greater than anticipated. This is suggested here by the isotropic hyperfine coupling constants.

Furthermore, the A_0 values were markedly lower for those complexes whose EPR spectra were obtained in chloroform. The difference between the A_0 values from samples dissolved in chloroform to those dissolved in DMSO ranged from 13 to $19 \times 10^{-4} \text{ cm}^{-1}$ (12 – 18 G). As noted for other vanadyl complexes, a decrease in the isotropic hyperfine coupling constant occurs when the sigma donor strength of the ligand increases, such that more ionic ligands, such as acetylacetonate (acac), yield vanadyl complexes with large A_0 values, and more covalent ligands, such as porphyrins, give rise to vanadyl complexes with very small A_0 values.^{105,106} This, therefore, represents a large increase in the ligand field strength for these complexes. That chloroform is somehow coordinating to lower the hyperfine splitting is extremely unlikely.¹⁰⁵ Rather, it is probably due to the deprotonation of the phenol groups to form phenoxides. It is well-known that an alcohol group on an aromatic ring has the effect of donating electron density to the ring, thus activating it for certain reactions.¹¹⁰ Furthermore, if this group is deprotonated, it will donate even more electron density to the ring. For the ligand, this means there is more electron density available to donate to the metal centre; that is, the ligand field strength is increased. It is this increase in ligand field strength that then results in a lower A_0 value being observed in the EPR spectra. That the coordination strength can be so greatly increased by deprotonation of a simple hydroxyl substituent has an implication for ligand design where an alkaline environment is present.

Table 4.4: Isotropic g -values and isotropic hyperfine coupling constants for the vanadyl complexes in chloroform or DMSO determined from spectra recorded at 298 K.

Complex	Solvent	g_0	A_0 / G	$A_0 / \times 10^{-4} \text{ cm}^{-1}$
[VO(L1)]	CHCl ₃	1.974	91.0	83.8
	DMSO	2.029	109.0	103.2
[VO(L2)]	CHCl ₃	1.978	98.6	91.0
	DMSO	2.039	117.0	113.0
[VO(L3)]	CHCl ₃	1.980	96.1	88.8
	DMSO	2.031	108.0	102.3
[VO(L4)]	CHCl ₃	na	na	na
	DMSO	2.053	118.4	113.4
[VO(L5)]	CHCl ₃	na	na	na
	DMSO	2.033	113.4	107.6

**Figure 4.7:** Solution EPR spectrum of [VO(L1)] in chloroform (left) and DMSO (right) at room temperature.**Figure 4.8:** EPR spectrum of [VO(L2)] in chloroform (left) and DMSO (right).

For [VO(L3)], the expected eight-line spectrum was obtained in a chloroform solution. However, the complex was not sufficiently stable in DMSO solutions over the time-frame of the experiment. To increase the signal-to-noise ratio, the sample was scanned for several hours. During this time, multiple peaks developed that were not present initially. Either the ligand decomposes in the DMSO solution over time, or an adduct with DMSO forms gradually.

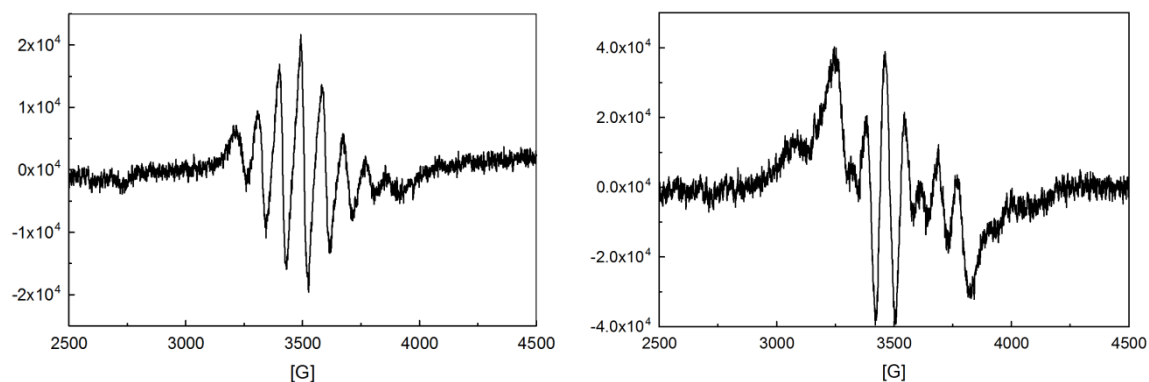


Figure 4.9: Chloroform (left) and DMSO (right) solution EPR spectra of [VO(L3)], recorded at room temperature.

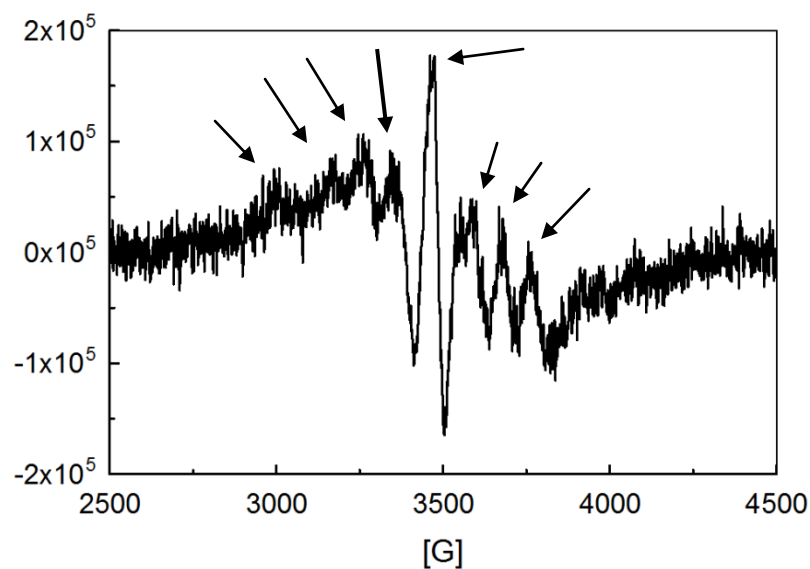


Figure 4.10: EPR spectrum of [VO(L4)] in a DMSO solution at 298 K. Although the solvent generates a high level of noise, the typical eight-line spectrum for an oxovanadium(IV) species can be seen.

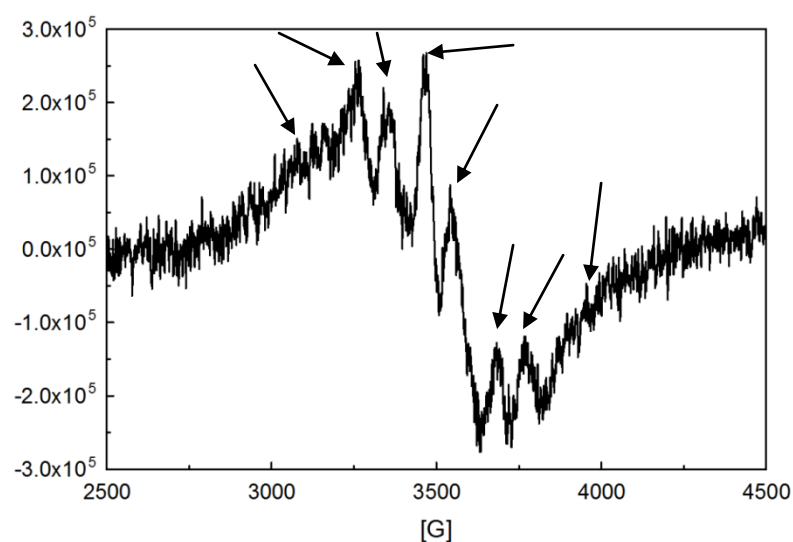


Figure 4.11: EPR spectrum of [VO(L5)] in a room temperature, DMSO solution.

4.4 Electronic absorption spectroscopy

4.4.1 $\pi \rightarrow \pi^*$ transitions

All ligands investigated herein possess either four or five aromatic rings, and consequently show very strong $\pi \rightarrow \pi^*$ transitions at ultraviolet wavelengths. On coordination to a vanadyl ion, the electronic structure over the aromatic rings changes as new molecular orbitals are formed. The formation of these new orbitals causes a change in the energy of the $\pi \rightarrow \pi^*$ transitions, which can be observed in the electronic absorption spectra for the complexes. The spectra for three representative free ligands and their respective complexes are shown below in Figures 4.12-4.14; these ligands are **H₂L1**, **H₂L2** and **H₂L4**. For **H₂L1**, the system is expected to be completely conjugated, and should be the least sensitive to changes at the donor atoms. **H₂L2** represents the ligands/complexes that have only an alkyl chain bridging the two iminium groups. Lastly, **H₂L4** is the only compound with a heteroatom on the alkyl chain; the heteroatom being one that is capable of interacting with the vanadyl unit.

All $\pi \rightarrow \pi^*$ transitions occur in the ultraviolet region between 350 and 270 nm. This is not surprising, as one of the starting materials for the ligands, 2,4-dihydroxybenzophenone, is used as a UV protecting agent in polymers.¹¹¹ For all vanadyl complexes, the intensity of the transitions is diminished compared to the free ligand, the effect being most pronounced for **H₂L4**, and least noticeable for **H₂L1**. Furthermore, the absorption maxima are red-shifted with respect to those of the free ligands. This red-shift is more pronounced when moving from an aromatic to an aliphatic bridging group. As expected then, the energy of these orbitals is lowered when binding vanadium, as electron density is donated from the ligand to the metal centre. The difference between [VO(**L1**)] and [VO(**L2**)] shows that the bridging group is involved in electron donation to the aromatic rings, and hence the vanadium, and that the alkyl chain is a weaker donor of electron density to the conjugated donor groups than the aromatic ring is. This is in agreement with the EPR spectroscopic results for the two complexes in DMSO, where the smaller A_0 value for [VO(**L1**)] compared to [VO(**L2**)] suggests that there is better π -backbonding to, and σ -donation from, the fully conjugated ligand to the vanadium ion.

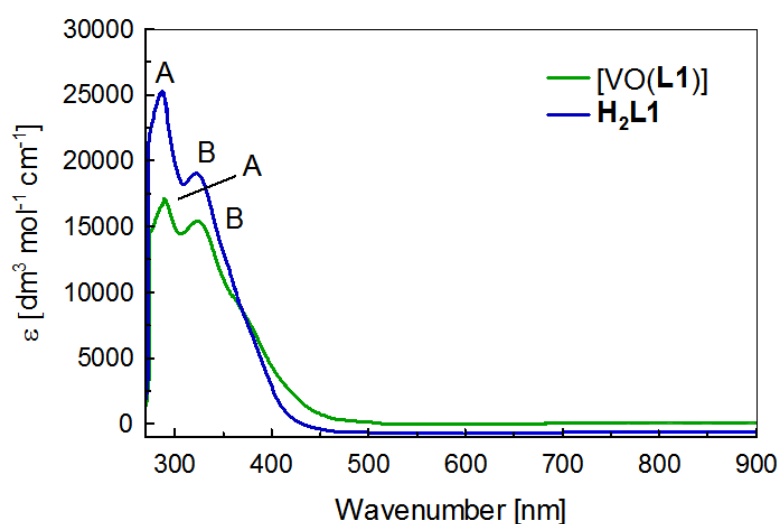


Figure 4.12: Overlay of the electronic absorption spectra for [VO(**L1**)] (green) and **H₂L1** (blue). Labelled peaks correspond to the $\pi \rightarrow \pi^*$ transitions for the ligand and complex. Note how the intensity of the $\pi \rightarrow \pi^*$ peaks has diminished, and how they have undergone a slight red-shift due to chelation of vanadium.

For the dark brown complex $[\text{VO}(\text{L4})]$, both the intensity of the $\pi \rightarrow \pi^*$ transitions and the energy associated with them, were greatly reduced compared to the previous complexes. Most likely, the hydroxyl substituent on the propyl chain is preventing the aromatic donor system from withdrawing large amounts of electron density from the bridging group, so that electron donation to vanadium results in a greatly lowered energy for the conjugated molecular orbital.

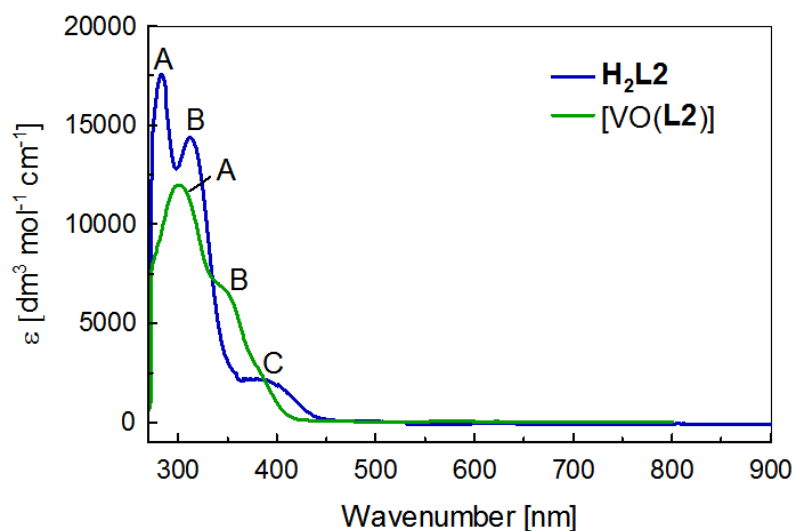


Figure 4.13: An overlay of $[\text{VO}(\text{L2})]$'s (green) and $\text{H}_2\text{L2}$'s (blue) electronic absorption spectra. The $\pi \rightarrow \pi^*$ transitions (peaks labelled A and B) for the aromatic rings can be clearly seen for both the free ligand and the complex; however both the intensity and energy of the peaks have diminished as a result of complexation.

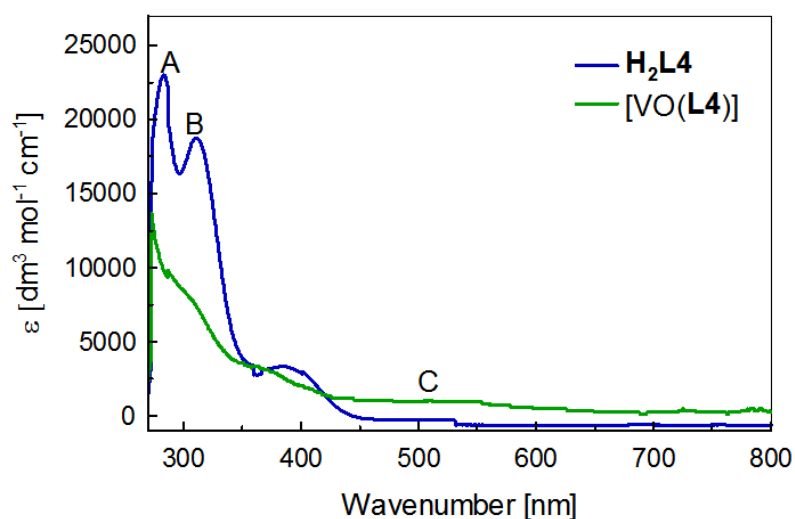


Figure 4.14: The electronic absorption spectra for $\text{H}_2\text{L4}$ (blue) and $[\text{VO}(\text{L4})]$ (green) overlaid on to each other. Peaks A and B correspond to the $\pi \rightarrow \pi^*$ transitions of the aromatic rings. The colour of $[\text{VO}(\text{L4})]$ is notably different from the other complexes, and arises due to LMCT, labelled C, which is much stronger in this complex as compared to the others (see above figures and text).

4.4.2 Transitions of the unpaired electron – MLCT

The unpaired electron localised in a non-bonding d-orbital of vanadium, which was observed in the previous section by EPR spectroscopy, is also responsible for electronic transitions in the visible region.⁹⁵ These are typically metal-to-ligand charge transfer (MLCT) processes, best described by the Ballhausen-Gray theory, and are responsible for the green colour of the vanadyl complexes.^{96,112} Figure 4.15(a-e) shows the spectra for the complexes over the region of absorption for the unpaired electron.

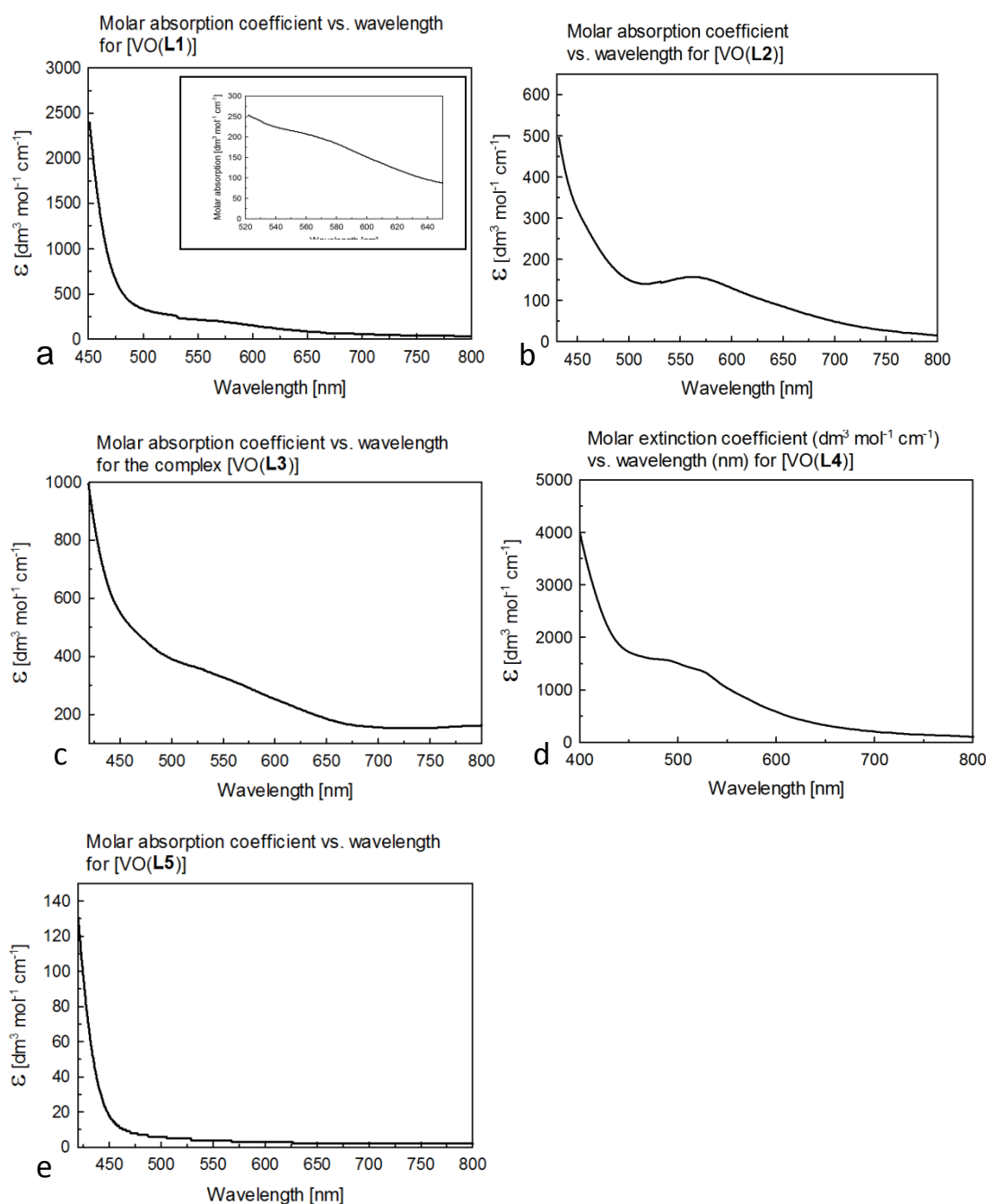


Figure 4.15: Electronic absorption spectra over the spectral window where MLCT is observed for the complexes: **a)** [VO(L1)], **b)** [VO(L2)], **c)** [VO(L3)], **d)** [VO(L4)] and **e)** [VO(L5)]. This transition occurs in the visible region of the spectrum, and is responsible for the green or brown colour of the complexes.

It can be from the above spectra that the absorption maximum for the complexes occurs between ca. 480 and 570 nm. In most instances, the peaks were difficult to resolve from one another, being obscured by the long-wavelength extrema of the $\pi \rightarrow \pi^*$ transition bands, so that the peak fitting software, *fityk*,¹¹³ had to be used to resolve them. As expected for room temperature spectra of vanadyl complexes, the individual d-d transitions could not be resolved, only the single point of maximum absorption for all complexes, except for [VO(L4)], which will be discussed separately.

The energy of the MLCT transitions is dependent on two factors, *viz.* the strength of the non-axial ligand field and the extent to which coordination of solvent at the vacant axial position of vanadium

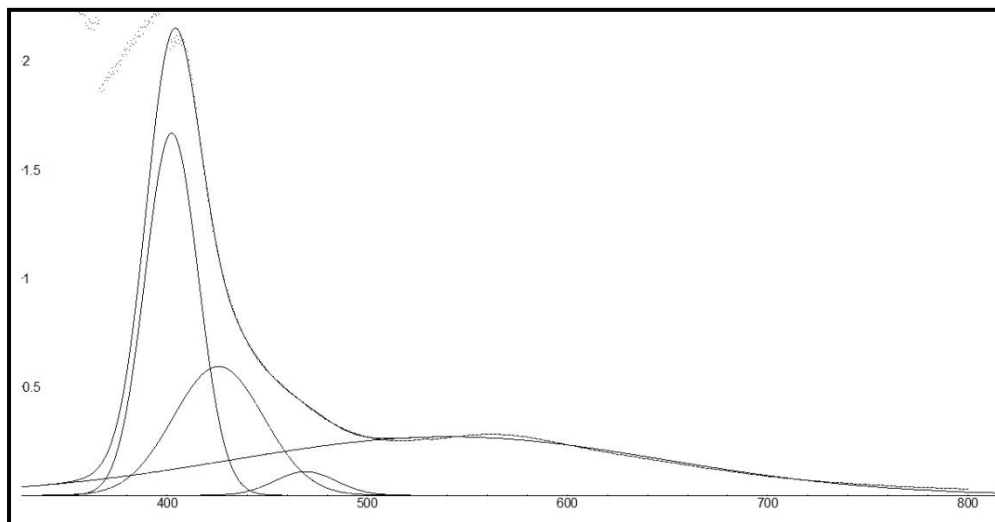


Figure 4.16: A typical fit of gaussian functions to the experimental data using the *fityk* software, to determine the position of underlying absorption bands. The example shown is for the region of d-d transitions for the complex, [VO(L2)].

is occurring. Coordination of solvent affects the energy of the V–O double bond, and hence the energy “gap” between the electron in the d-orbital and the oxide’s anti-bonding orbitals. The lowest energy MLCT transition observed is for the fully conjugated complex [VO(L1)]. All other complexes are blue-shifted relative to this complex. For the complexes with alkyl groups, the energy of the absorption maximum is red-shifted as the bulk of the alkyl chain is increased. There is additional splitting of the MLCT bands for the complex [VO(L4)], as well as a greatly increased intensity for the transitions. The energy of these bands is also higher than those seen for [VO(L1)]. The approximate location and intensity of the absorption maxima are given in Table 4.5.

Table 4.5: The approximate wavelength of maximum absorbance for the d-d bands of vanadyl complexes and the absorption intensity associated with each one.

Complex	Abs. Max. (nm)	ϵ (dm ³ mol ⁻¹ cm ⁻¹)
[VO(L1)]	572	250
[VO(L2)]	478	250
[VO(L3)]	525	350
[VO(L4)]	493 & 538	1888 & 1195
[VO(L5)]	567	2

The wavelength of the MLCT transitions becomes progressively longer for the alkyl chain bearing complexes as the length and bulk of the chain increases. As previously mentioned, it is expected that the strength of the ligand field decreases as the size of the alkyl chain is increasing. This causes the difference between the energy levels of the non-bonding d-orbital and the ligands' anti-bonding orbitals to decrease, and therefore, longer wavelengths are required to cause the transitions. However, the fully aromatic complex [VO(L1)] has been shown to have the highest electron donating ability, and hence the highest ligand field strength, of all the complexes; its conjugated nature should also make it a good π -acceptor ligand. It should therefore have the highest energy MLCT transitions according to this reasoning. The discrepancy is solved by considering the effect ligand field strength has on solvent coordination, and the subsequent effects that solvent coordination has on the molecular orbitals of the vanadyl unit.

For a weak field ligand, an octahedral coordination geometry is most likely, as the vanadyl unit will be electron deficient without coordination at the axial positions.²² Conversely, strong-field ligands result in the typical square-pyramidal geometry seen for most vanadyl complexes. For the complexes presented here then, it is more likely that coordination of solvent is occurring for the less strongly donating, alkyl-chain bearing ones. The solvent that coordinates then increases the splitting of the vanadyl's molecular orbitals so that a transition from the non-bonding orbital to a σ^* or π^* orbital requires higher frequency (shorter wavelength) radiation.

This also explains the anomalous behaviour of [VO(L4)], with its well-separated transitions. The hydroxyl group on a propyl-chain of salen derivative vanadyl complexes has been known to assist in the capture and coordination of solvent molecules, like water (Figure 4.16),⁸⁸ and is most likely performing the same function here. Firstly, the energy of the non-axial ligand field would be lowered by this electron-withdrawing hydroxyl group. This then, favours the coordination of solvent at the vacant axial position, which is assisted by the close proximity and hydrogen bonding properties of the hydroxyl group. The hydroxyl group that helps to capture a solvent molecule would reduce the amount of random motion, and therefore significantly increase the number of allowed transitions, which would account for the greatly increased intensities of the transitions for this complex compared to the others. The two peaks are most likely due to the transitions between the vanadium's d_{xy} orbital and the vanadyl oxide's π^* orbital, and from the d_{xy} orbital to ligand donor's σ^* orbital.

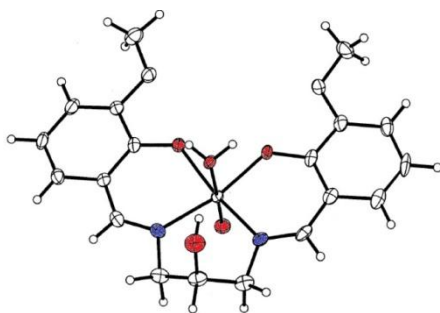


Figure 4.17: The X-ray determined crystal structure of the similar Schiff base complex, $\text{VO}(\text{H}_2\text{O})(\text{C}_{19}\text{H}_{20}\text{N}_2\text{O}_5) \cdot 2\text{C}_2\text{H}_4\text{Cl}_2$; figure modified from Ref. 88. In this complex, the hydroxyl group facilitated the binding of a solvent molecule *via* a hydrogen bond.

4.5 Conclusion

EPR spectroscopic results for the powdered vanadyl complexes showed that they possess axial symmetry, typical of oxovanadium(IV) complexes. Application of the additivity rule to their powder spectra, when using the typical contributions to A_{\parallel} for phenoxide and pyridine donors for the ligands' donor phenoxide and imine nitrogens, respectively, gave a predicted value almost identical to that obtained for [VO(L1)] and [VO(L2)]. This suggested that the donor atoms for these two complexes are located in the equatorial plane, and that there is some distortion from the ideal square-pyramidal geometry for the other oxovanadium(IV) complexes. Further studies are required to determine the exact contribution to A_{\parallel} that the highly substituted imine nitrogen is making to vanadium. These results do show, however, that the amount of distortion increases as the length and bulk of the alkyl chain increases.

Room temperature studies using DMSO gave a higher than usual isotropic g -value, which was interpreted as the result of electron coupling to a nearby, weakly coordinated solvent molecule. The A_0 values obtained in DMSO were higher than expected when considering the trend in isotropic hyperfine coupling constants for vanadyl Schiff base complexes. Presumably, this is because of distortion of the ligand caused by the sterically bulky benzyl rings on the imine carbons. If this is the case, then the contribution from the imine nitrogens must be much stronger than that of a pyridine nitrogen donor to lower the parallel hyperfine coupling constant as much as was observed for the powder spectra.

Deprotonation of the non-bonding aromatic hydroxyl substituents in a room temperature chloroform solution resulted in a far lower isotropic hyperfine coupling constant than that observed for the DMSO solution EPR spectra, by as much as 18 G. This is believed to be due to the additional electron density that becomes delocalised in the aromatic system of the donor groups. Time constraints prevented further research into this effect, but would have involved deprotonating the phenol groups in DMSO so that a direct comparison could be made with the protonated forms of the complexes.

Electronic absorption spectra provided information about the change of the energy level of the aromatic system upon coordination of vanadyl. For all ligands and complexes, it was found that chelation of vanadium resulted in a red-shift of the $\pi \rightarrow \pi^*$ transitions that was dependent on the nature of the bridging group. These transitions showed the least amount of change for an aromatic linker, while alkyl groups were less able to supply the needed electron density, and so the $\pi \rightarrow \pi^*$ transitions for these complexes showed a greater decrease in energy upon vanadium chelation.

The MLCT bands observed through electronic spectroscopy were too close together, and their intensities too low in most instances, for them to be resolved from one another. Therefore the point of maximum absorption was used for comparisons. The energy of the MLCT transitions was higher for those complexes with alkyl linkers than for [VO(L1)], which can be explained when considering solvent effects. The less strongly coordinating ligands are believed to facilitate the coordination of solvent to the vacant axial position on vanadium, which affects the molecular orbitals of the vanadyl unit, raising its energy. This increase in energy causes the MLCT bands to be blue-shifted relative to that of a non-solvent coordinating vanadyl complex. The presence of a hydroxyl group further facilitates the capture and coordination of a solvent molecule; stabilising the octahedral complex, and resulting in an increased intensity of the MLCT transitions.

Chapter 5 | *Hydrogen peroxide binding studies*

5.1 Background

As highlighted in the introduction, much of the biological activity of vanadium compounds seems to be related to their ability to bind peroxidic species and generate ROS through the cleavage of these species. Consequently, this ability of vanadium to readily bind peroxides has been exploited for numerous catalytic processes, and has been the focus of many publications, including several reviews.^{70,78,79,114} It is thus crucial that the vanadium complexes of this study be able to form complexes with peroxide. Fortunately, the ⁵¹V isotope is amenable to study by NMR spectroscopy, having a natural abundance of 99.75 % and receptivity relative to ¹H at natural abundance of 0.383.⁶ This means that the technique can provide fairly detailed information on the speciation of these complexes in solution. These aspects – the binding of peroxide by vanadium, reactions of the oxoperoxovanadium(V) Schiff base complexes, and the study of vanadium species by NMR spectroscopy – will be considered in this introductory section.

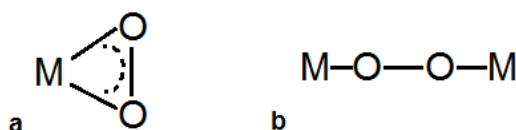
5.1.1 Hydrogen peroxide – structure and properties

Hydrogen peroxide (H₂O₂) is a colourless liquid, and resembles water in many respects.¹³ It is strongly hydrogen-bonded, to the extent that it is denser than water by 40 %. It is a powerful oxidizing agent, and is readily decomposed by metal to form OH[•] and HO₂[•] radicals. This redox chemistry is demonstrated and summarized by its redox potentials:



The structure of hydrogen peroxide can be described as a skew chain, where the hydrogens are positioned *anti* to each other. The O–O bond is long (1.49 Å) compared to that in neutral diatomic oxygen (1.21 Å).¹³

As a ligand, peroxide (O–O²⁻) can bind to vanadium either as a bidentate ligand, so as to form a three-membered chelate rings, or end-on.^{79,115,116} Usually, when peroxide binds end-on, it serves to bridge two vanadium atoms together, such as seen in vanadium-amino acid complexes when hydrogen peroxide is added at suitable pH values. These coordination modes are illustrated in Scheme 5.1.



Scheme 5.1: The two possible binding modes of peroxide are, **a)** side-on and **b)** end-on.

5.1.2 Peroxide-vanadium interactions

5.1.2.1 Structure of Peroxo-complexes: When considering whether or not a vanadium species will bind peroxide, it is important to understand the structural requirements that must be met, and the environmental conditions that would facilitate the chelation.⁷⁹ The vanadium ion's ability to coordinate peroxide is well known, and the oxoperoxovanadium complexes formed are very stable compared to other metal-peroxides. Elucidation of their structures has been mainly limited to the solid state, where infra-red and Raman spectroscopy have been predominantly employed.⁷⁹ In some cases, the crystal structures of these compounds have been determined as well, such as that of Mimoun *et al.*¹¹⁷

As mentioned, the peroxide ligand itself is usually bidentate and triangular, coordinating in an η^2 fashion.^{78,79} In almost every instance, the peroxide coordinates at the equatorial positions of vanadium, and the metal can coordinate more than one peroxide ligand at a time, to form a mono- or a di-peroxo complex. The geometry of these complexes can, in general, be described as pentagonal bipyramidal, as there are seven V–L bonds (Figure 5.1 (left)). Sometimes, the axial position is not formally coordinated, and the structure can be thought of as pentagonal pyramidal; although, the vanadyl O atom of another complex can be coordinated to this position, so as to form a dimer, or even a polymer. This oxo- ligand can then be thought of as the seventh ligand (Figure 5.1 (right)). When only a single peroxide ligand is bound, the length of the two V–O (peroxides) bonds is identical. When two peroxides coordinate, however, the V–O_{trans} bond is slightly longer than the V–O_{cis} bond, where the 'cis-' bonds are those adjacent to each other, and the 'trans-' bonds are those separated by an additional ligand (Figure 5.2).⁷⁹

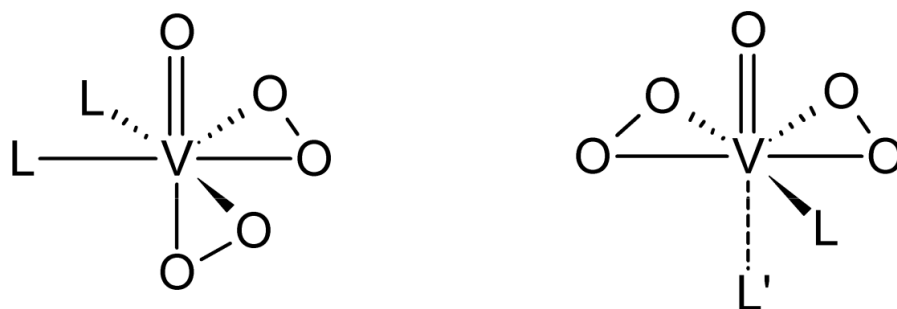


Figure 5.1: The coordination geometry of oxoperoxovanadium complexes can be described as (left) pentagonal-bipyramidal, or (right) pentagonal pyramidal. In the latter case, a seventh ligand is usually weakly associated with the axial position.⁷⁸



Figure 5.2: V–O bond lengths can vary depending on the position of the bound peroxide relative to other ligands.⁷⁸

Peroxides can also bridge vanadium centres in two different molecules by forming end-on, or side-on bonds to the metals.^{78,79}

5.1.2.2 Formation of peroxovanadium complexes: Complexes of oxoperoxovanadium(V) can be formed from either V(IV) or V(V) precursors. Formation kinetics and mechanisms can become complicated in the latter, however with the former, a very simple relationship exists.¹¹⁸

In the presence of excess peroxide, V(IV) is oxidised to V(V), and cleaves the bound peroxide to form hydroxyl radicals (OH[•]). The mechanism proposed by Tanaka and co-workers is an associative interchange process, where the rate-limiting step is the addition of the peroxide to V(IV). After it has bound, a rapid electron transfer process occurs, which oxidises V(IV) to V(V). The rate law derived is:

$$\text{rate} = k[\text{V(IV)complex}][\text{H}_2\text{O}_2] \quad (5.4)$$

And thus, there is no dependence on the solvent polarity, or on the solution pH, but only on the concentrations of the two species.^{79,118}

The formation of OH[•] has been observed by EPR and 5,5-dimethyl-1-pyrroline-N-oxide (DMPO), where a signal corresponding to a DMPO–OH radical is formed with the addition of H₂O₂ to a solutions with various vanadate species.¹¹⁹ It was found, through competition experiments with other OH[•] scavengers, that there are at least two ways that the radical could form. Either, the peroxide can be cleaved and an OH[•] can be released into the solution, or the oxoperoxovanadium complex can interact directly with the DMPO to add a hydroxyl radical.

Solution studies of V(V) species have largely focused on simple compounds, typically VO₂⁺. As the vanadium cannot be further oxidized, the binding of peroxide becomes a pH dependent equilibrium. Only at very low pH values is the mono-peroxide complex formed; from pH ≥ 2, two peroxides will coordinate. However, up to four peroxides are able to bind as the pH is increased.¹²⁰

Extensive kinetic studies have been done to determine the mechanism of formation and disassociation of V(V) peroxide complexes.¹²⁰ In general though, peroxide binding is highly pH dependent, but also depends on the solvent used to a small extent. This appears to be due to the different protonation states of the complexes. The di-peroxo complex, for example, is acidic, and so its formation is suppressed in non-polar solvents.

A proposed mechanism for the dissociation of diperoxovanadium complexes in an aqueous solution involves a two step protonation of one of the peroxides.¹²⁰ The first H⁺ adds rapidly to form the monodentate HO₂⁻ ligand. The second step is the rate-determining step, where HO₂⁻ is protonated for a second time and dissociates. There is now a vacant position available for coordination on the vanadium ion, which becomes occupied by a water molecule.

5.1.3 Oxovanadium Schiff-base complexes and their interactions with peroxide

Schiff-base complexes of vanadium have been very popular choices for the oxidation of sulfides to sulfoxides (sulfoxidation), where the primary oxidizing agent is hydrogen peroxide.¹²¹ In particular, they have shown to be extremely useful as chirality inducing agents. Early work in this field was performed by Bolm and co-workers (Figure 5.3 a).¹²² Using a simple biphasic water/dichloromethane system, hydrogen peroxide, VO(acac)₂ and the chiral ligand of choice were introduced. Tailoring the system eventually produced enantiomeric excesses in excess of 99 %. Obviously, the ability to select certain enantiomers is very useful in a biological environment, where enzyme-substrate interactions are highly specific – to the point of selecting only a single enantiomer. Potentially, a complex could be tailored that would only have a single target *in vivo*, thus eliminating harmful side-effects common with most chemotherapeutics.

In addition to these, tetradentate and pentadentate Schiff-base chelates of vanadium have also been examined for the abilities to catalyze sulfoxidation reactions (Figure 5.3 b).¹²¹ Kinetically, the rates of oxidation of the pentavalent complexes were, in general, slower than for the tetradentate ones. More importantly than the denticity, though, was the steric bulk of the substituents on the aromatic rings. Where there were large groups, the rate was significantly slower, but where there were no substituents, the rate of oxidation for the pentavalent complexes was much faster; almost identical to that of [VO(salen)]. However, as long as the complexes could bind peroxide, they were able to catalyze an oxidation.

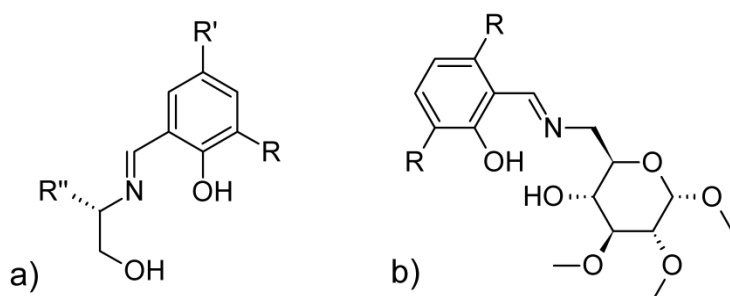


Figure 5.3: Schiff-base ligands used as chirality inducing oxidation catalysts, in conjunction with hydrogen peroxide and vanadium(IV)/(V). Compound **a**) is one of the early ligands investigated by the Bolm group, while **b**) is a ligand developed by the Maeda group for sulfoxidations.

5.1.4 Speciation of oxoperoxovanadium(V) complexes

In the introduction, the speciation of vanadium in solutions containing peroxide over a wide concentration range was briefly considered. However, the ligand(s) present affect the binding of peroxide to vanadyl or vanadate ions. This situation is even more complex in biological systems where pH values fluctuate significantly depending on the environment, and the number of biological small molecules that are potential ligands for vanadium is extensive. In determining the speciation, both ⁵¹V NMR and potentiometry have been used to elucidate the various species.¹²⁰ In addition to this, certain guidelines concerning which ligand types are more effective for promoting peroxide binding over a large pH range, and the general ⁵¹V chemical shifts observed for unbound, mono- and diperoxo-bound vanadate species, were determined. These guidelines will be reviewed.

Over the pH range of 0.5 – 10.5, many ligands do not bind vanadate effectively at high or low values.¹²⁰ What's more, binding is often enhanced by the addition of peroxide to a vanadate-ligand

solution. The general trend is for molecules with aromatic nitrogen donors to bind peroxovanadate the strongest, followed by ligands with an aromatic nitrogen and aliphatic oxygen. Aliphatic nitrogen donors are less efficient than the previous two, while aliphatic oxygen donors are the weakest.¹²⁰ The association constant for the peroxovanadium complex is, in general, lowered (*viz.* weakened) as the pH is increased. The most likely reason for this is the protonation of donor groups, or competition for them by “free” protons in solution.

The ⁵¹V NMR shift is very useful in determining the nature of the peroxo-species present. For a simple vanadate-ligand system, the lowest observed shift is -570 ppm.⁶ This shift is, of course, highly dependent on the nature of the ligand. When conditions favour the formation of only the monoperoxovanadate-ligand system, shifts in the region of -540 to -670 ppm are observed. If the equilibrium is shifted so that diperoxovanadium-ligand systems form, then shifts as low as -670 to -770 ppm are seen. It must be noted that the range boundaries that distinguish the different forms are not well separated from each other, and may overlap to a certain extent. They are therefore not definitive, and the speciation for peroxovanadate systems must be determined for each ligand system used.

5.1.5 ⁵¹V NMR spectroscopy

Having seen that peroxo-vanadium complexes can form a multitude a different structures depending on H₂O₂ concentration and pH, it becomes necessary to distinguish between the various forms that may be forming in solution. As mentioned above, NMR spectroscopy is a useful tool for probing the environment around the vanadium atom.

Vanadium-51 (⁵¹V) is a suitable nucleus for NMR spectroscopy.⁶ Its natural abundance is 99.76 %, has a nuclear spin of 7/2, and has a nuclear moment of 5.139 (in nuclear magneton units), and has receptivity versus ¹³C of 2150, and a quadrupole moment of 1/2.¹²³ Line widths can vary greatly, from <2 Hz up to approximately 3000 Hz. These represent extreme examples, however; the typical line width being between 20 and 200 Hz.⁶ The broadness of these peaks arises from the quadrupole moment, but is seldom an issue of concern, as the chemical shifts between different vanadium species are so widely separated that there is sufficient resolution of the individual peaks. This is illustrated in Chart 5.1; distribution for related species does not often overlap as changes in the coordination environment of vanadium lead to large changes in its chemical shift.

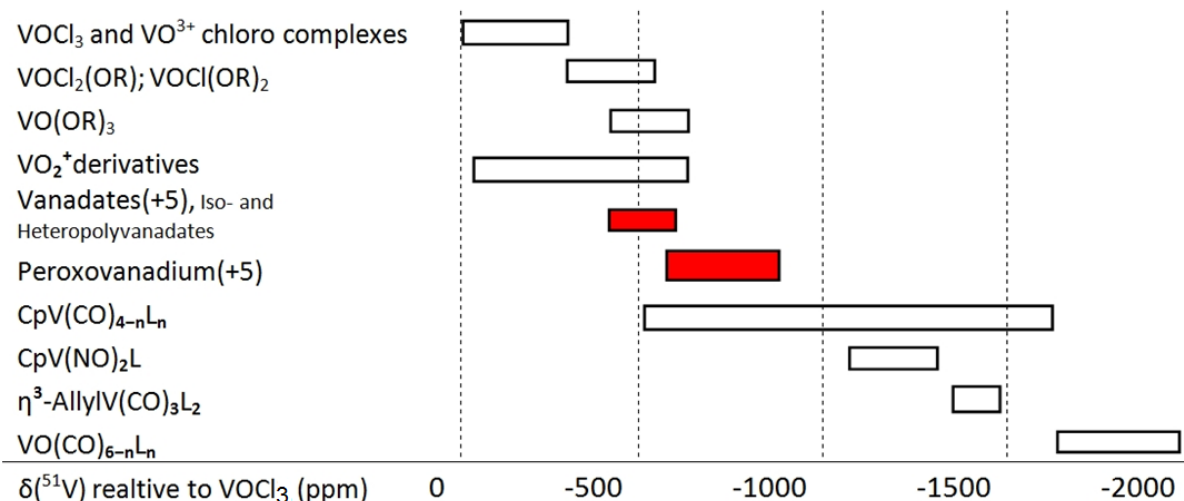


Chart 5.1: Distribution of ^{51}V resonance in ppm. Values are relative to VOCl_3 . Highlighted bars show the typical distribution for the species of interest in this study, namely vanadates – formed by oxidation of vanadyl, and peroxovanadium(V). Distribution for other species shown is for comparison.

The location of $\delta(^{51}\text{V})$ depends largely on the ligand's ability to alter the HOMO–LUMO energy gap (ΔE). An increased ΔE leads to increased ligand-to-metal charge transfer, and subsequently, a larger up-field shift of $\delta(^{51}\text{V})$. The greater the extent of the covalent binding of a ligand to vanadium, the greater ΔE becomes, and the further up-field the shift will be. For peroxo-vanadium species, protonation of the peroxide ligand can result in an up-field shift of $\delta(^{51}\text{V})$ by as much as 50 ppm. If, as in the case of metavanadate, an O^{2-} ligand is replaced by a peroxide (O_2^{2-}) ligand, an increase of up to 100 ppm can be seen.

The complexes $[\text{VO}(\text{L1})]$, $[\text{VO}(\text{L2})]$, $[\text{VO}(\text{L3})]$, $[\text{VO}(\text{L4})]$ and $[\text{VO}(\text{L5})]$ all contain V(IV) nuclei, which, as shown by their EPR spectra in Chapter 4, have an unpaired electron, and are thus paramagnetic. A paramagnetic sample is active for NMR, but the signal relaxes very quickly, sometimes too quickly for observation, and thus the intensity of the signal observed by NMR is very weak, i.e. extensive line-broadening occurs. However, because H_2O_2 is an oxidizing agent, when added it should oxidize the V(IV) species to a V(V) one. The electronic configuration of the vanadium changes from d^1 to d^0 , and is now no longer paramagnetic but diamagnetic.¹²⁴

5.2 H_2O_2 titrations – monitored by ^{51}V NMR spectroscopy

5.2.1 General procedure

Exact amounts varied between compounds, but in general 3.5 mg was dissolved in 500 μl of DMSO- d_6 . Aliquots of typically 20 μl of a hydrogen peroxide (6 % v/v in H_2O) solution were added until the total volume reached 600 μl . If the peak correlating to that for the V(IV) species was still present, additional 40 μl aliquots of the H_2O_2 solution were added until the all traces of the V(IV) species had disappeared, or the intensity of the V(V) peak(s) no longer increased.

Several standard samples were run before the V(IV) samples were titrated; these were NH_4VO_3 , $\text{VOSO}_4 \cdot 5\text{H}_2\text{O}$ and $\text{VO}(\text{salen})$ (Figure 5.4). NH_4VO_3 was chosen because it already contains a vanadium in the +5 oxidation state, and so the intensity of $\delta(^{51}\text{V})$ should not change, only the chemical shift should be altered by peroxide addition. $\text{VOSO}_4 \cdot 5\text{H}_2\text{O}$ is a starting material for the complex synthesis.

If demetallation of the oxovanadium(IV) Schiff base complexes was to occur, the VO^{2+} unit would probably be released, and their spectra would most likely resemble that of the $\text{VOSO}_4 \cdot 5\text{H}_2\text{O}$ species. $[\text{VO}(\text{salen})]$ is already known to bind peroxide, and has been used for several different catalytic reactions where this ability is essential. It also bears a strong resemblance to the Schiff base complexes of this study, and therefore its ^{51}V spectra are likely to resemble those of the V(IV) species under investigation, provided they remain intact.

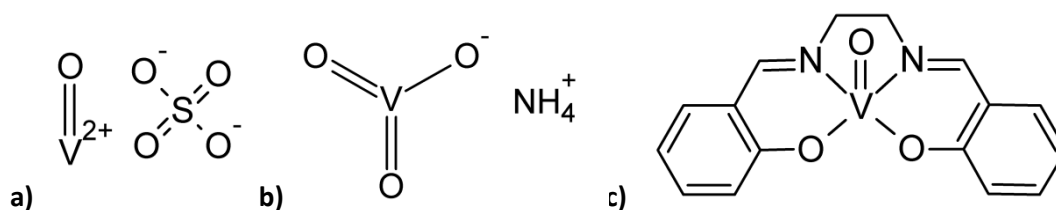


Figure 5.4: Structures of the three samples used as standards when evaluating the ^{51}V NMR spectra of the oxovanadium(IV) Schiff base complexes: **a)** vanadyl sulfate (VOSO_4), **b)** ammonium metavanadate (NH_4VO_3) and **c)** $[\text{VO}(\text{salen})]$ – a comparable oxovanadium(IV) Schiff base complex.

5.2.2 Results and Discussion

5.2.2.1 Standard samples: spectral overlays for the standard samples are presented in figure 5.5 (for NH_4VO_3), figure 5.6 (for VOSO_4) and figure 5.7 (for $[\text{VO}(\text{salen})]$). A summary of the spectral data for these standards and the oxovanadium(IV) Schiff bases is given in Table 5.1.

For NH_4VO_3 , there is initially one large peak at -578 ppm, and one very small peak, both of which are sharp; this is expected for a V(V) species. Addition of H_2O_2 results in a second large, sharp peak forming up-field at -689 ppm. At the same time, the intensity of the peak at -578 ppm diminishes. After a sufficient amount of H_2O_2 has been added, the peak at -578 ppm disappears completely, and is only the peak at -689 ppm remains. This very large difference can be attributed to the replacement of an O^{2-} ligand for an O_2H^- one. Had an O_2^{2-} ligand been bound, the difference in chemical shifts between the two ^{51}V peaks would have been expected to be less than 100 ppm (Figure 5.5).⁶

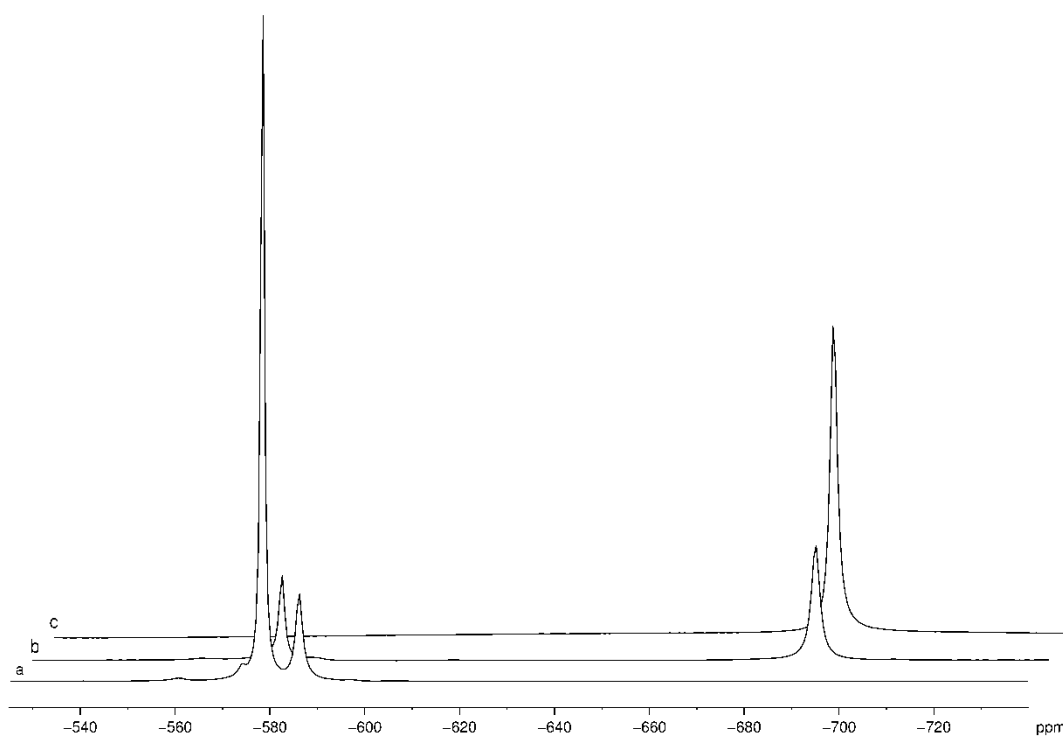


Figure 5.5: Spectral overlay of ^{51}V NMR spectra for NH_4VO_3 , showing the effects of addition of H_2O_2 . The bottom spectrum, a) is for NH_4VO_3 with no added H_2O_2 , b) when a drop of H_2O_2 has been added, and c) when an excess of H_2O_2 is added so as to completely convert all VO_3^- to the peroxo-species.

The VO_3^- sample showed unexpected spectra on addition of H_2O_2 . There was a single small, sharp peak at -528 ppm, which is typical for a V(IV) species. However, addition of peroxide caused a down-field shift to -481 ppm; the newly formed peak being very broad in comparison to the starting peak. A smaller peak did form down-field at -536 ppm though. The colour of the solution did change during this time as well, from blue to yellow, giving visual confirmation of oxidation. The location is probably due to a new peroxo-vanadium-sulfate species forming, where the sulphate ligand is less tightly bound by the vanadium. The difference between the peaks suggests that the smaller peak is due to a protonated peroxide ligand (Figure 5.6).

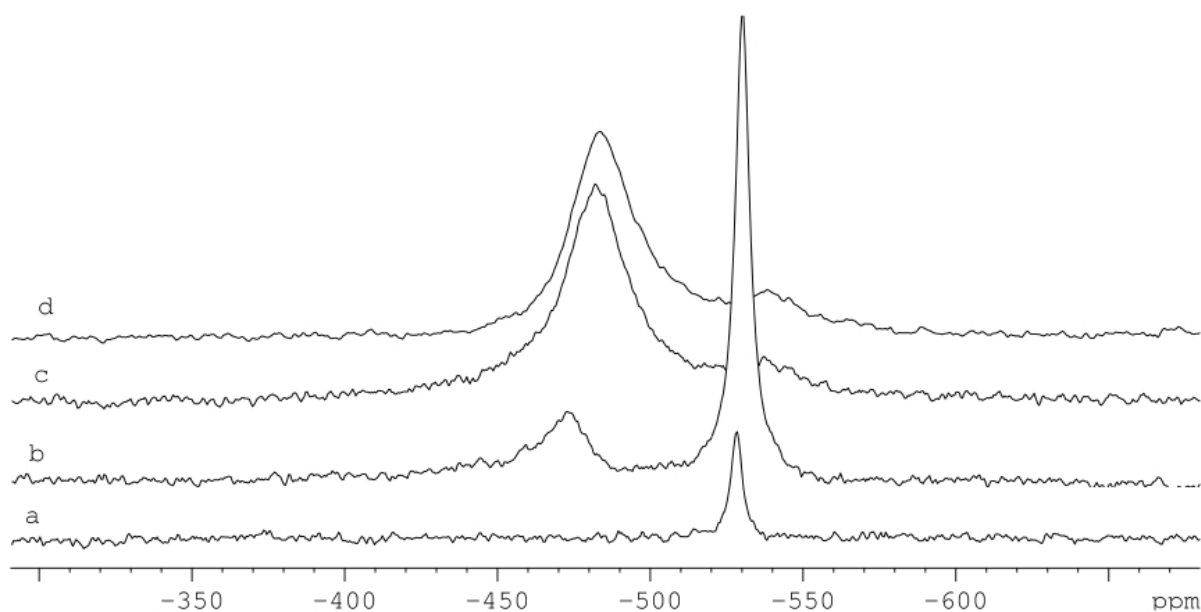


Figure 5.6: ^{51}V NMR spectra of VOSO_4 in DMSO-d_6 , a) before addition of peroxide, b) after the addition of one drop of H_2O_2 , c) after sufficient peroxide is added to cause the solution colour to change from blue to yellow, and d), the same yellow solution after 15 hours.

The initial V(IV) peak for the $[\text{VO}(\text{salen})]$ complex was located at -554 ppm. On addition of H_2O_2 , this peak slowly decreased in intensity, and two new peaks formed up-field at -636 ppm and -650 ppm. The intensity of these two peaks was also different, the larger one being at -636 ppm. The ratio between the two was 1.1:1. The difference between the two peroxide induced peaks is 14 ppm, and is most likely the result of the second peak being due to a protonated peroxide ligand.

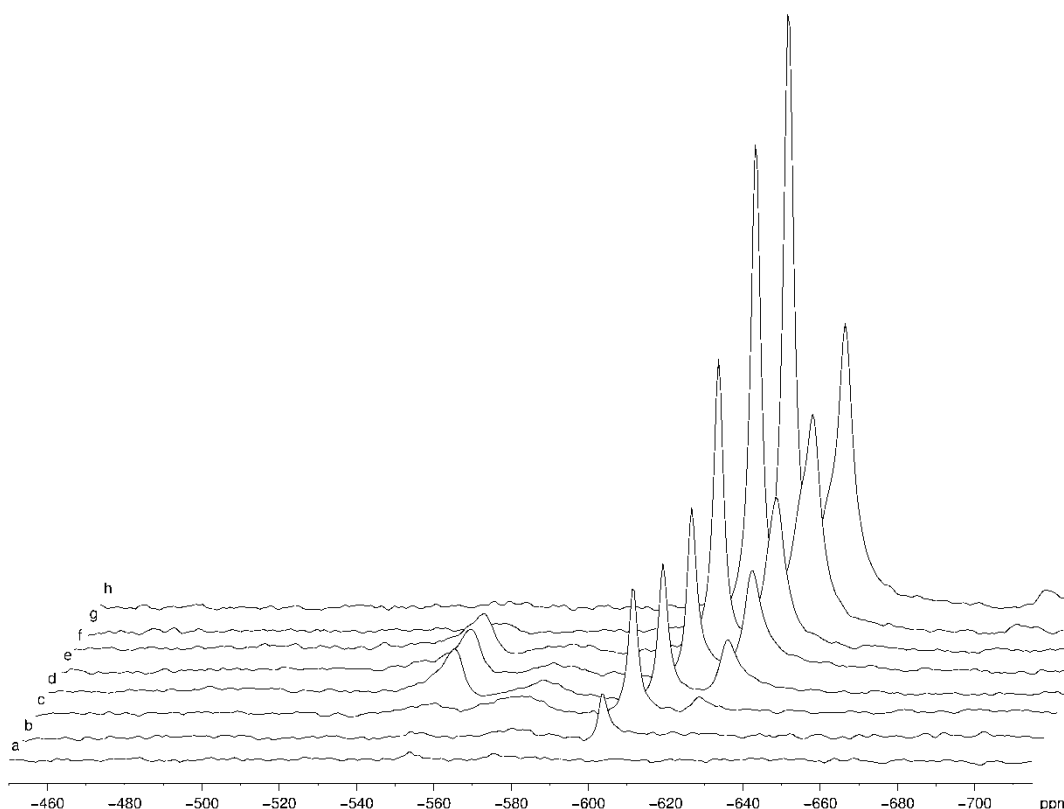


Figure 5.7: ^{51}V NMR spectral overlay for the titration of $[\text{VO}(\text{salen})]$ with H_2O_2 (6 % v/v) in DMSO-d_6 , having added: a) no H_2O_2 , b) $20\ \mu\text{l}$, c) $40\ \mu\text{l}$, d) $60\ \mu\text{l}$, e) $80\ \mu\text{l}$, f) $100\ \mu\text{l}$, g) $140\ \mu\text{l}$ and h) $180\ \mu\text{l}$ of H_2O_2 . All $\text{V}(\text{IV})$ species are completely consumed, and two large, sharp peaks form correlating to the peroxo- species.

5.2.2.2 Oxovanadium(IV) Schiff base complexes: Sequential addition of hydrogen peroxide to DMSO-d_6 solutions of the oxovanadium(IV) Schiff base complexes gave spectra very similar to that observed for the titration of $[\text{VO}(\text{salen})]$. In general, a small peak was observed, which disappeared with addition of peroxide. At the same time, two other, much larger and sharper peaks formed up-field from this first one. These two, newly formed peaks had different intensities from each other, with the one located slightly further down-field typically being the larger; the ratio between the two was approximately 80:20. The exact chemical shifts for all the samples are given in Table 5.1. Irregularities were for $[\text{VO}(\text{L5})]$, where the initial $^{51}\text{V}(\text{IV})$ peak was too small to be identified, and $[\text{VO}(\text{L3})]$, where the intensities between the two peaks varied, and eventually the largest peak was the one located furthest up-field. Spectral overlays for all these H_2O_2 additions are shown in the following figures.

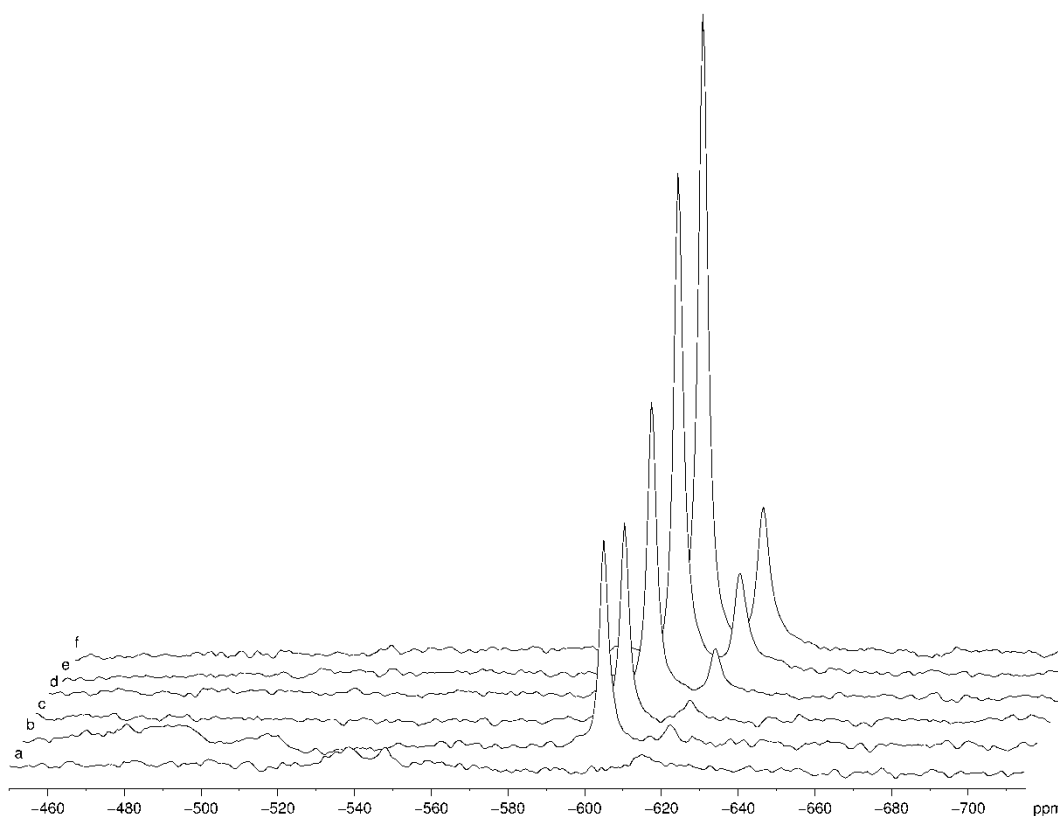
Table 5.1: A summary of the ^{51}V chemical shifts for the standard and test samples, and selected distances between them.

Compound	δ (51V) / ppm			Difference / ppm	
	Initial	Final(Major)	Final (Minor)	Initial - Final**	Final(Mjr) - Final(Mnr)
VOSO_4	-528	-481	-536	47	55
NH_4VO_3	-578	-689	na	-111	na
[VO(salen)]	-554	-636	-650	-82	14
[VO(L1)]	-548	-625	-640	-77	15
[VO(L2)]	-552	-615	-631	-61	16
[VO(L3)]	-529	-667	-653	-138	-14
[VO(L4)]	-475	-632	-646	-157	14
[VO(L5)]	na*	-612	-629	na	17

*initial peak too small to be seen.

**Calculated using the chemical shift from the larger of the two final peaks.

Figure 5.8 shows the spectral overlay for the fully conjugated complex, [VO(L1)]. The V(IV) peak can be distinguished from the background noise, but is very small and broad. The normalised intensity ratio between the two V(V) peaks that form is approximately 78:22.

**Figure 5.8:** Stacked ^{51}V NMR spectra for the titration of [VO(L1)] with a solution of H_2O_2 (6 % v/v): a) 0 μl , b) 40 μl , c) 60 μl , d) 80 μl and e) 100 μl of H_2O_2 . The single, broad peak due to the V(IV) ion is gradually replaced by two sharper peaks of unequal intensity as the vanadium is oxidised and binds a peroxy-moiety.

The spectral overlay for [VO(L2)] is shown in Figure 5.9. Unlike [VO(L1)], the peak due to the V(IV) species is much more easily discerned, standing out clearly from the background noise. The normalised ratio between the two V(V) peaks is 72:28.

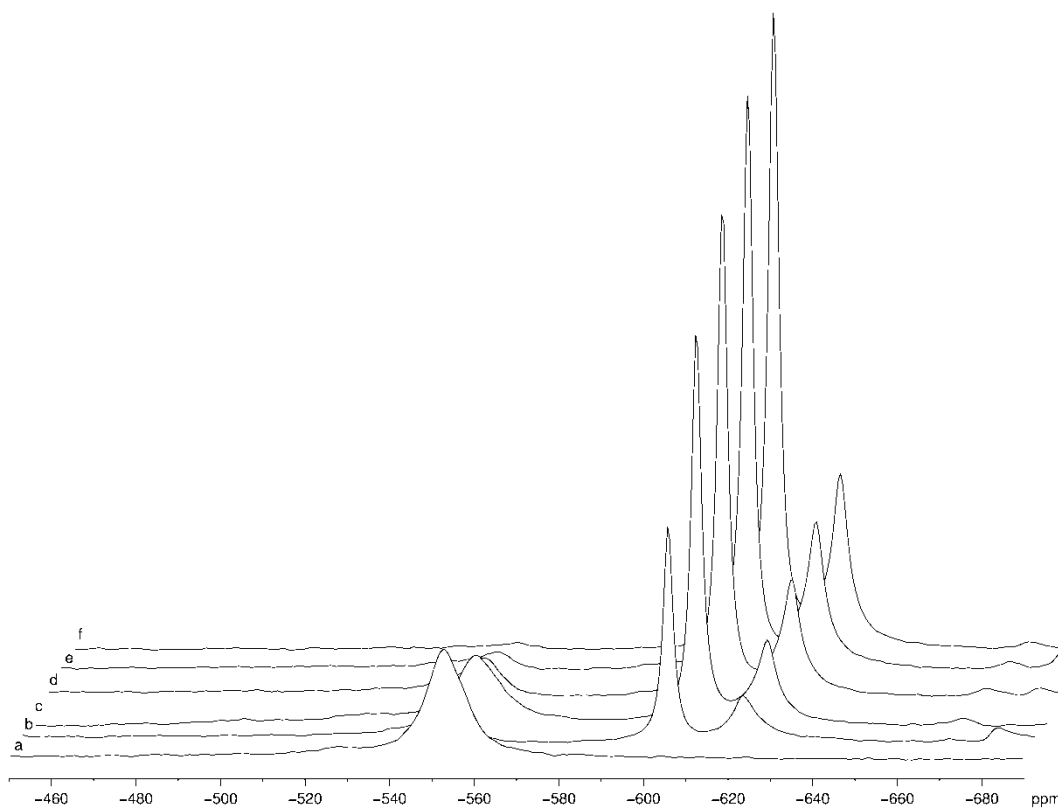


Figure 5.9: ^{51}V NMR spectra for the titration of [VO(L2)] with an H_2O_2 solution in DMSO: a) spectrum before addition of any H_2O_2 , b-f) 20 μl aliquots of H_2O_2 (6 % v/v) added for each one. Note that the developing peaks are much sharper, and also their intensity is much higher, relative to the one they are replacing.

The spectrum for [VO(L3)] without any added peroxide, displayed a very broad signal for the V(IV) species, much like that observed for [VO(L1)]. [VO(L3)] did, however, not oxidise as readily as any of the other V(IV) species. After the addition of 100 μl of H_2O_2 , only very small peaks had formed up-field, as can be seen in figure 5.10. It was only after the addition of several hundred microlitres of H_2O_2 (aq) that large peaks corresponding to the V(V) peroxo species formed. Additionally, the ratio of these peaks was constantly changing; the peak located further up-field gradually increasing as the amount of H_2O_2 added was increased. Figure 5.11 shows the spectra for all the additions of H_2O_2 ; notice that it was only when almost 200 μl H_2O_2 (aq) had been added that the V(V) related peaks became visible. When these V(V) peaks appeared though, they appeared very rapidly. Most likely, the V(IV) species, in this instance, was shielding the diamagnetic V(V) nuclei, and it was only when most of the V(IV) species was oxidised that signal for the V(V) complexes could be detected. Lastly it can also be seen from the spectra that the peaks due to the V(IV) species still did not disappear completely, even after such large amounts of H_2O_2 had been added.

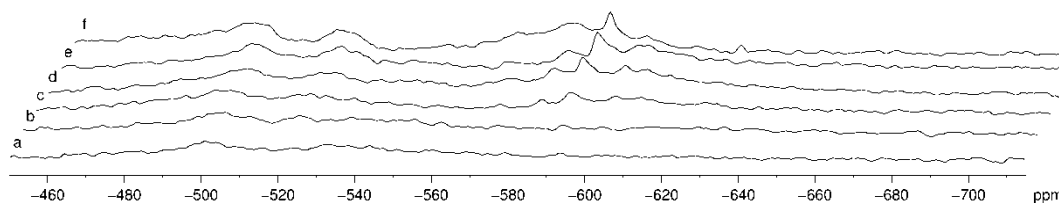


Figure 5.10: Spectral overlay to show what the spectra of [VO(L3)] looked like after the addition of the same amount of peroxide as had been added for the previous complexes: a) 20 μl , b) 40 μl , c) 60 μl , d) 80 μl , e) 100 μl and f) 140 μl H_2O_2 (6 %, v/v).

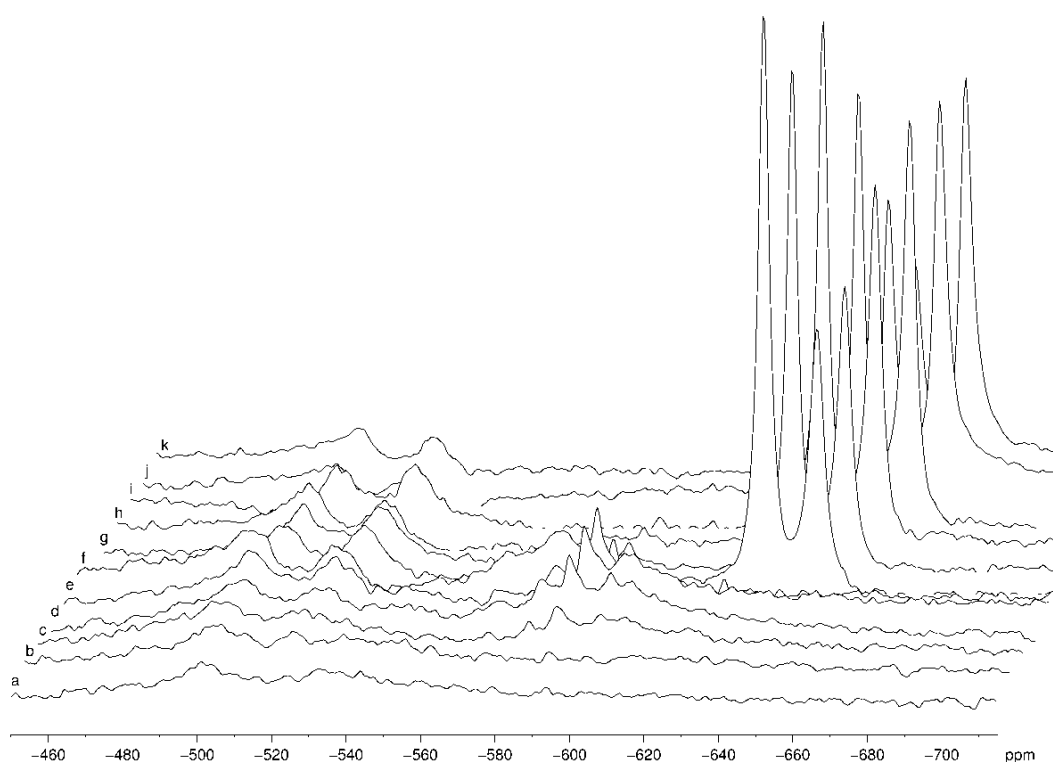


Figure 5.11: Overlay of all the spectra for the titration of [VO(L3)] with H_2O_2 (6 %, aq, v/v), after the addition of a) 20 μl , b) 40 μl , c) 60 μl , d) 80 μl , e) 100 μl , f) 140 μl , g) 180 μl , h) 200 μl , i) 240 μl , j) 300 μl and k) 400 μl of the H_2O_2 solution. Interestingly, for this compound, the equilibrium between the two peroxy-species was shifted from one to the other as the concentration was increased. Also, the broad peaks corresponding to the initial vanadyl compound did not disappear, even after excessive amounts of peroxide had been added.

As mentioned, the intensities of the two peaks formed by the addition of peroxide to the DMSO- d_6 solution of [VO(L3)] changed as the amount of peroxide added was increased. This too can be explained by the most up-field peak being that for the protonated peroxide species. As more H_2O_2 is added, the acidity of the solution should increase slightly, as peroxide decomposes in solution to form O_2 and H^+ . Initially, OH^- is probably being formed by the cleavage of peroxide by vanadium, which would deprotonate the peroxides. As more of the mildly acidic H_2O_2 (aq) solution is added, the pH is adjusted so that the protonated species forms instead (Figure. 5.12).

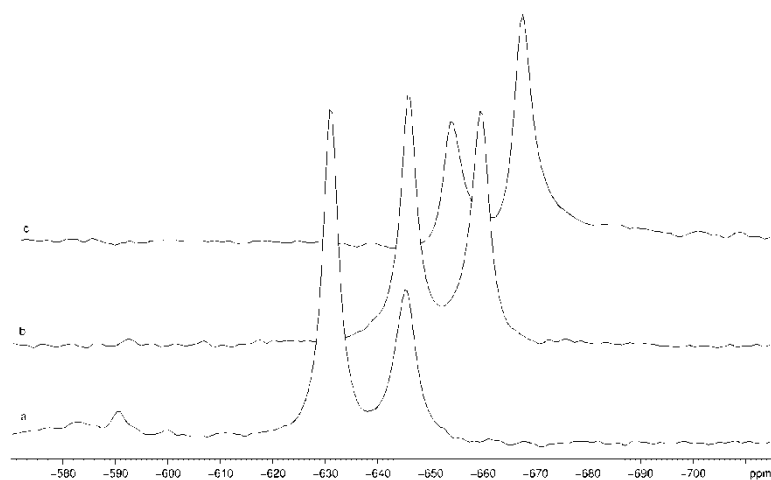


Figure 5.12: Overlays of the ^{51}V NMR for $[\text{VO}(\text{L3})]$ after the addition of a) 200 μl , b) 400 μl and c) 600 μl of H_2O_2 (6 %, aq, v/v) to show the change in intensity of the two $^{51}\text{V}(\text{V})$ peaks.

The $[\text{VO}(\text{L4})]$ spectral overlay is shown in figure 5.13. Of interest in this spectrum is the very prominent V(IV) peak, which only disappears after fairly large amounts of H_2O_2 (aq) are added. Much like the spectra for $[\text{VO}(\text{L3})]$, the peroxy-V(V) peaks are not very evident initially, but only appear after a reasonably large amount of H_2O_2 has been added – in this case, only after 230 μl H_2O_2 (aq).

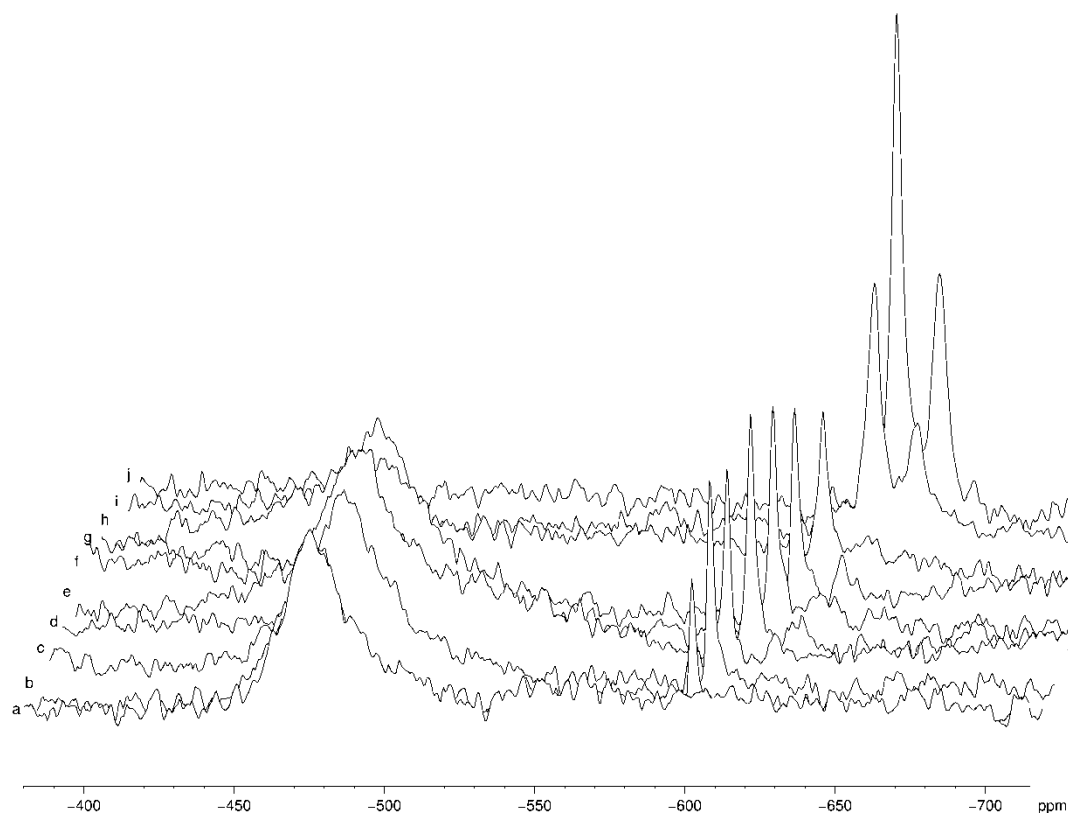


Figure 5.13: Overlay of ^{51}V NMR spectra $[\text{VO}(\text{L4})]$ with serial additions of an H_2O_2 (6 %, aq, v/v) solution. The aliquots were as follows: a) no H_2O_2 added, b) 10 μl , c) 20 μl , d) 30 μl , e) 50 μl , f) 70 μl , g) 90 μl , h) 130 μl , i) 230 μl and j) 330 μl H_2O_2 solution added.

The serial addition of a hydrogen peroxide solution to a sample of [VO(L5)] in DMSO-d6 resulted in the formation of two sharp peaks, which were located up-field, at about -630 ppm (Figure. 5.14). This is the same region as for the other peroxide induced V(V) peaks. The paramagnetic V(IV) species could not be seen in the initial spectrum before any peroxide had been added. The $^{51}\text{V(V)}$ peaks appeared readily on addition of peroxide; that is, there was no apparent shielding effects from the V(IV) nucleus. The normalised ratio of the two peaks was 78:22, with the larger peak being located slightly down-field to the smaller one. Again, the reason for the appearance of the two peaks is believed to be due to protonation of the peroxide ligand, yielding the smaller peak.

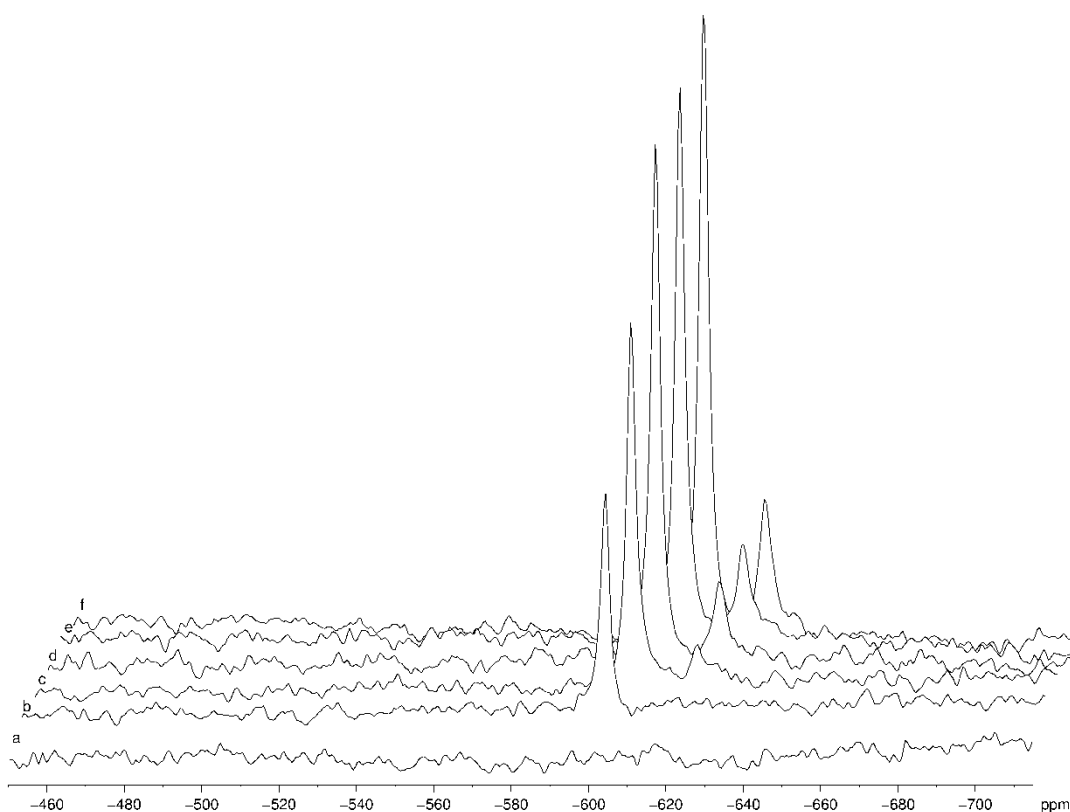


Figure 5.14: ^{51}V NMR spectra for the titration of [VO(L5)] with H_2O_2 (6 %, aq, v/v). Spectra are for: a) no H_2O_2 , b)-f) successive 20 μl aliquots of the H_2O_2 solution.

In all of the above spectra, it can be seen how the addition of hydrogen peroxide leads to the formation of a new vanadium species, as each peak in a spectrum represents a different vanadium species. As mentioned in the background to this section, the chemical shift of each peak gives information on the type of vanadium species present. All the peaks formed by the addition of peroxide correlate well to the generally accepted chemical shift of a peroxy-vanadium species. It can thus be conferred that oxoperoxyvanadium(V) species are forming in solution.

Additionally, the exact location of the chemical shift can give information on the strength of the complex formed. The further up-field a chemical shift occurs, the stronger the covalent bonding between the vanadium nucleus and the ligand. Hence, for the V(IV) complexes, the strongest chelate formed appears to be [VO(L2)], followed by [VO(L1)]. [VO(L3)] has a slightly more positive value, and is therefore weaker than either of the ethyl-bridged complexes. Interestingly, [VO(L4)] is apparently a much weaker chelate than any of the above. It appears then, that the longer the bridging chain length, the weaker the complexation; the addition of substituents to the bridging group increase the

distortion, and hence the instability, even further. It is noteworthy that [VO(salen)] has a greater up-field shift than any of the other V(IV) complexes synthesised, and the addition of phenyl rings to the imine carbon significantly increases the distortion of the complex, weakening the ligand field strength.

These results are very similar to those obtained by EPR spectroscopy (Section 4.2); only the order of [VO(L1)] and [VO(L2)] was reversed. Disparity between these results is probably due to the inaccuracies of applying ^{51}V NMR spectroscopy to paramagnetic species. Despite this shortcoming, ^{51}V NMR spectroscopy still represents a useful tool for probing the ligand field strength of vanadium complexes, one that remains useful even when the metal oxidation state changes. Further support for these conclusions about ligand/complex distortion is given by DFT calculations of the vanadyl complexes. The bond lengths and angles around the coordination environment of the vanadium show the same sequence in distortion from an ideal square-pyramidal geometry as determined by EPR spectroscopy (see Section 6.4).

In addition to giving an estimate of the coordination strength for the oxovanadium(IV) complexes, the extent of metal-ligand bonding for the oxoperoxovanadium(V) complexes can also be estimated and compared with one another. For all complexes concerned, the ^{51}V chemical shift is more negative for the peroxo-complex, signifying a greater vanadium-ligand bond strength overall. This is not to say that all ligand-vanadium bonds are stronger, but that there is more electron density over the vanadium nucleus. Thus, there is a greater covalent character for the vanadium-ligand bonds overall. No direct comparison can be made between the oxo- and oxoperoxo-complexes either, as the oxidation state of the vanadium changes over the course of the reaction. The electron density of the nucleus is thus different, and will give a different chemical shift even with the same ligands.

However, the relative differences between the two chemical shifts for the oxo- and oxoperoxo-vanadium complexes can give an indication of how favourable the formation of one oxoperoxo-complex is relative to another, for the different complexes. A definite trend can be observed for the complexes, *viz.* the stronger the initial complex, that is, the more negative the chemical shift, the weaker the oxoperoxo-complex is relative to this oxo-complex, *i.e.* the smaller the difference between the chemical shifts for the two complexes. For [VO(L2)], which was determined to have the strongest coordinating bonds to vanadium, coordination of peroxide caused the smallest up-field shift, and hence, the smallest increase in coordinating strength. [VO(L1)] had a slightly greater increase in vanadium-ligand bond strength. The complexes [VO(L3)] and [VO(L4)], which shows the weakest chelating strength – presumably due to ligand distortion – showed a far greater increase in the vanadium-ligand bond strength upon coordination of vanadium. The standard [VO(salen)] sample, which is known to coordinate peroxides, showed an increase in the vanadium-ligand bond strength as well, but only slightly more so than for [VO(L1)] and [VO(L2)]; the difference is still much less than for [VO(L3)] and [VO(L4)]. Unfortunately, due to the poor sensitivity of the V(IV) nucleus in [VO(L5)], comparisons of this complex with its oxoperoxovanadium(V) counterpart cannot be performed. Based on the above trend, it is predicted to be a strong binder of peroxide though.

The differences between the two oxoperoxo-complex peaks formed for each complex are all approximately the same, being within 14 to 17 ppm of each other. They can therefore be attributed, not to a property of the individual complexes, which should result in more significant differences between the two values, but rather to a property of the peroxide ligand itself, *i.e.* protonation and

deprotonation. This would affect the coordinating strength of the ligand slightly, enough to cause these minor changes in the ^{51}V chemical shift.⁶

5.3 Magnetic susceptibility

Any compound will be affected by an external magnetic field; the degree to which it is influenced is termed its magnetic susceptibility, χ_m . There are no units for magnetic susceptibility, as it is a dimensionless constant that is proportional to the strength of the external magnetic field. In order to determine unequivocally whether or not the vanadium compounds had been oxidised to the 5+ oxidation state by peroxide, a series of magnetic susceptibility measurements were performed, *via* a modification of the Evans NMR method, with various reagents.

Traditionally, a Gouy balance is used to measure χ_m . In this method, a sample of known weight is suspended in a magnetic field. The apparent change in weight that the sample experiences while in the field can be used to determine its χ_m . In these experiments, however, the Evans method was employed as it has several advantages over the former. Firstly, Guoy balances are specialized instruments that are not as readily available as NMRs, which can be found in almost any chemistry department, thus making the Evans technique more readily available. Secondly, the amount of sample needed for an experiment is much less than that needed when for the operation of a Guoy balance. Lastly, the measurements are taken in solution when using the NMR. Seeing as we are interested in the solution complexes being formed, rather than the solid state ones, the need for a determination of χ_m in solution is obvious.^{125,126,127}

A modified procedure of the Evans NMR method was used to determine the relative oxidation state of the complexes. For a description of the theory of this method, see Box 5.1. In practice, a sealed capillary – filled with the standard, solvent and species under investigation, or test sample – is placed inside an NMR tube, which is then filled with the standard and solvent to the same concentration as in the capillary. However, in these experiments, deuterated dimethylsulphoxide was used as the solvent, and the small amount of residual protonated solvent present in the deuterated solvent was used as the standard. By using the solvent for both applications, the preparation of samples is simplified, as the concentration of the standard is guaranteed to be the same for both capillary and sample solutions. Further modifications were made to the method, which, while preventing the accurate determination of the magnetic susceptibility for the compounds, does provide strong evidence that the magnetic susceptibility of the complex, and hence its oxidation state, has changed. So, instead of placing the test sample in the capillary, it is dissolved in the outer-solvent; this allowed for multiple additions of reagents to the same sample. However, because the test sample is now completely enveloping the internal standard, it affects the strength of the magnetic field exerted by the magnet on the inner sample/standard, and thus alters the chemical shift of this standard as well. This perturbation of the magnetic field is not evident when a diamagnetic species forms, as would be the case for a vanadium(V) complex, and thus changes in the oxidation state of the vanadium species can be observed.

Box 5.1: Derivation of bulk magnetic susceptibility from a NMR chemical shifts.

The Evans method relies on the principle that the position of a proton's resonance is directly related to the magnetic susceptibility of the bulk solution, when the proton resonance observed is from a diamagnetic species (the test compound). The difference in chemical shifts of the test compound from before and after addition of a paramagnetic species can be used to calculate the magnetic susceptibility.^{125,126,128,129}

The position of a line for a proton resonance is related to the bulk magnetic susceptibility of the medium in which the molecule is situated. For an inert substance the shift is given by the following theoretical equation (5.5):

$$\frac{\Delta H}{H} = \frac{-4\pi}{3} \Delta\kappa \quad (5.5)$$

Where $\Delta\kappa$ is the change in volume susceptibilities. $-4\pi/3$ is the correction factor that must be applied for the superconducting magnet*. When the paramagnetic species is introduced, a new expression can be derived from equation (5.5). Usually, the volume susceptibility, X , is replaced by the mass susceptibility, χ_i , which is related to the volume susceptibility as $\chi_i = X/\rho$. Rearranging for the mass susceptibility of the paramagnetic species gives equation (5.6):

$$\chi_i = \frac{3}{-4\pi} \cdot \frac{\delta\nu}{\nu_o} \cdot \frac{1}{\rho} + X_o + X_o \frac{(d_o - d_s)}{\rho} \quad (5.6)$$

Where $\delta\nu$ is the shift in frequency of the proton resonance from that of the pure solvent, ν_o , ρ is the density of the solute in g ml^{-1} , X_o is the volume magnetic susceptibility of the solvent, and d_o and d_s are the densities of the pure solvent and solution respectively. The third term can often be ignored, as the difference between densities will vary so little that the numerator will tend to zero. For practical purposes, this term has been omitted in determining the magnetic susceptibilities of the oxovanadium complexes. The volume susceptibility of the solvent can then be replaced by its initial volume susceptibility, χ_o . Hence, equation (5.6) can be simplified to equation (5.7):

$$\chi_i = \frac{3}{-4\pi\rho} \cdot \frac{(\nu_o - \nu_i)}{\nu_o} + \chi_o \quad (5.7)$$

The molar susceptibility, χ_m , is the obtained by finding the product of χ_i and the molar mass of the paramagnetic compound. The answer is expressed in c.g.s units ($\text{cm}^3 \text{mol}^{-1}$), however. Conversion to SI ($\text{m}^3 \text{mol}^{-1}$) is done by multiplying with the correction factor, $4\pi \times 10^{-6}$.

*In earlier works, the correction factor $2\pi/3$ was used. This was for non-superconducting magnets, where the orientation and strength was different and weaker, respectively. Hence the effect has a smaller and oppositely signed, correction factor.

The spectrum for [VO(L1)] is shown in Figure 5.15. It is clear from this that the chemical shift of the DMSO is affected by the paramagnetic species present in solution. Note that there is a significant amount of line broadening of the DMSO quintet as well – further evidence of the paramagnetic species' presence in solution. The DMSO in the capillary ("internal reference" in Figure 5.15) does not experience this line broadening; making the individual peaks far more discernable than for the "exposed sample."

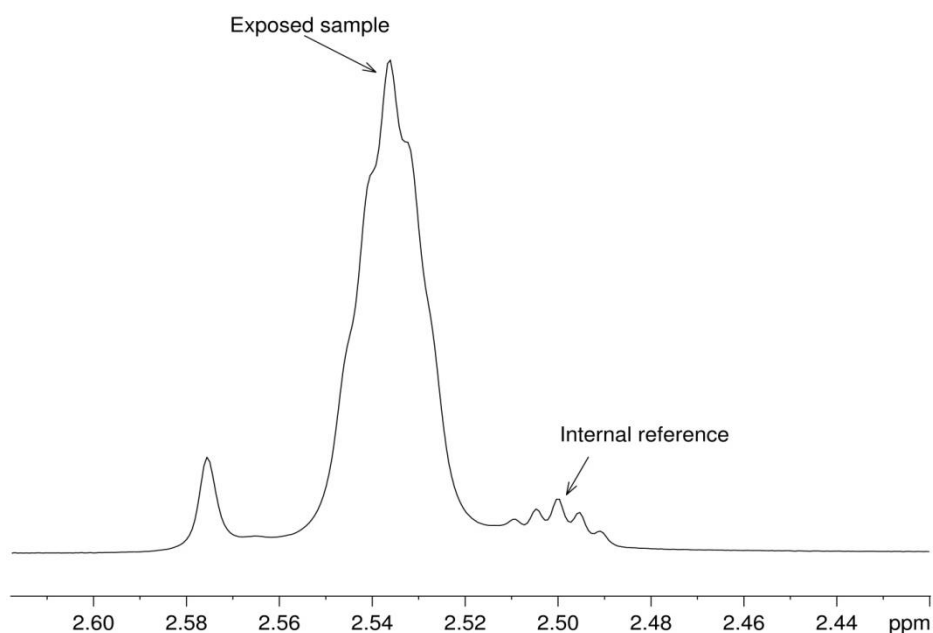


Figure 5.15: The difference in chemical shifts between a DMSO solution, and internal DMSO reference solution caused by the addition of the paramagnetic compound [VO(L1)].

Comparison of the DMSO peaks for this, and the other complexes, show that the exposed DMSO sample is shifted down-field relative to the capillary-sealed DMSO. The amount by which the exposed sample is shifted is very small, ranging between 5 and 15 Hz. The difference in chemical shifts for these exposed and sealed DMSO standard peaks, for the oxovanadium(IV) complexes, is given in Table 5.2.

Table 5.2: Differences in location of chemical shift for DMSO samples that were isolated or exposed to vanadium species in different oxidation states.

Added	Difference in δ / Hz				
	[VO(L1)]	[VO(L2)]	[VO(L3)]	[VO(L4)]	[VO(L5)]
None	14.45	15.67	7.02	5.06	15.42
H ₂ O ₂	-58.46	-80.38	-54.63	-59.02	-56.27
NaOH	-47.61	-52.04	-41.32	-93.92	-34.35

Once the spectrum with the added capillary was recorded for the oxovanadium(IV) complexes, the capillary was removed, and H₂O₂ was added to the test solution. Once sufficient H₂O₂ had been added, the DMSO-containing capillary was included once again into the sample tube, and the ¹H spectrum was recorded. There was a noticeable difference between the chemical shifts for the sealed and exposed DMSO, which was larger than observed for the V(IV) sample, and in the opposite direction. That is, the exposed DMSO's chemical shift is up-field of that of the internal standard's, and the displacement is of a much larger magnitude. The spectrum for [VO(L1)] is shown in Figure 5.16; the chemical shift difference for this species, and the other complexes, are given in Table 5.2.

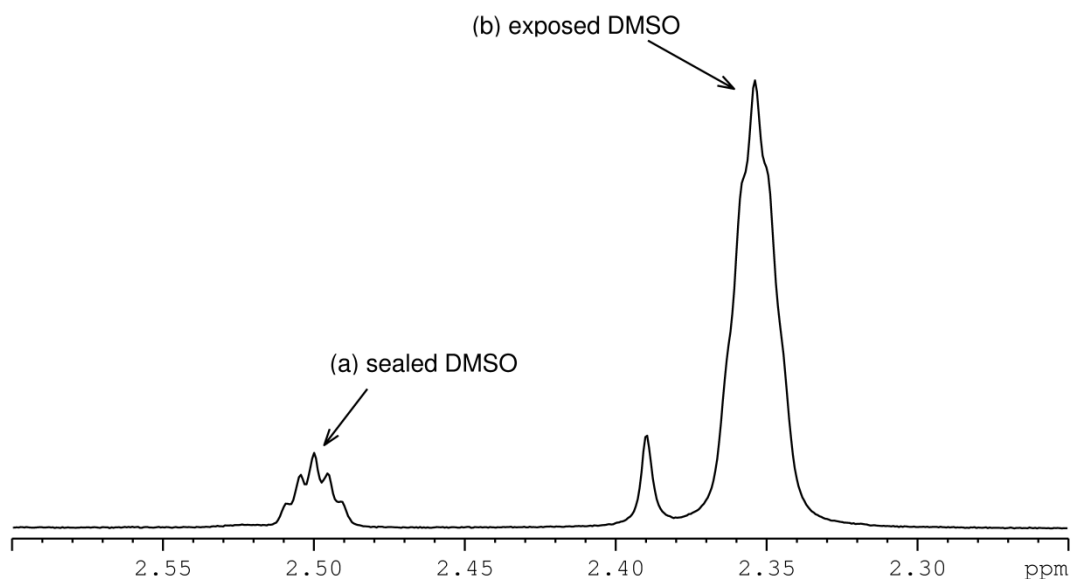


Figure 5.16: Proton resonance positions for (a), sealed internal reference DMSO and (b), DMSO exposed to the oxovanadium complex, [VO(L1)] after hydrogen peroxide had been added to the solution. The exposed DMSO's resonance has shifted upfield relative the sealed DMSO – contrary to the complex without hydrogen peroxide where a downfield shift was observed.

It can be seen from the spectra in Figures 5.14 and 5.15, and from the summary of the data in Table 5.2, that there are significant differences in the chemical shifts of the exposed DMSO sample when the oxidizing species are added to the solution. Such large variation in the chemical shifts would not occur unless the magnetic environment of the solution was changing considerably. Mere oxidation of the organic components in solution by peroxide would not cause such a large difference as that observed, as the hydroxyl radical is too short lived to contribute such a large paramagnetic moment. This effect is better accounted for by the oxidation of paramagnetic V(IV) to diamagnetic V(V). The paramagnetic V(IV) increased the magnetic susceptibility of its solution, and thus shifted the ^1H resonances down-field of the internal standard's ^1H resonance.

To ensure that the differences in chemical shifts of the DMSO samples are indeed caused by the oxidation of V(IV) to V(V), additional titrations were performed using NaOH (titration results are given in Section 5.4). At sufficiently high pH values, the VO^{2+} cation is oxidised to a VO_2^+ species (Equation 5.7);¹³ additionally, no hydroxyl radicals are introduced into solution, and can thus be ruled out as a cause of any magnetic effects.



The spectra and values obtained for the magnetic susceptibility experiments using NaOH as titrant matched those of the H_2O_2 titrations very well. Figure 5.17 shows the spectrum for [VO(L1)] after the addition of NaOH; the position of the exposed DMSO's proton resonance peaks relative to that of the internal standards, matches that of the samples where peroxide had been added. The magnitude of the chemical shift difference for the diamagnetic solutions varied, but this is most likely due to precipitate forming in several of the experiments. This occurs as the various phenol groups on the complexes ionise at higher pH values, making the complexes less soluble in the organic solvents. It

can therefore be concluded that the vanadium(IV) complexes are oxidised by hydrogen peroxide to vanadium(V), which can only be occurring if the peroxide is being bound by the vanadium.

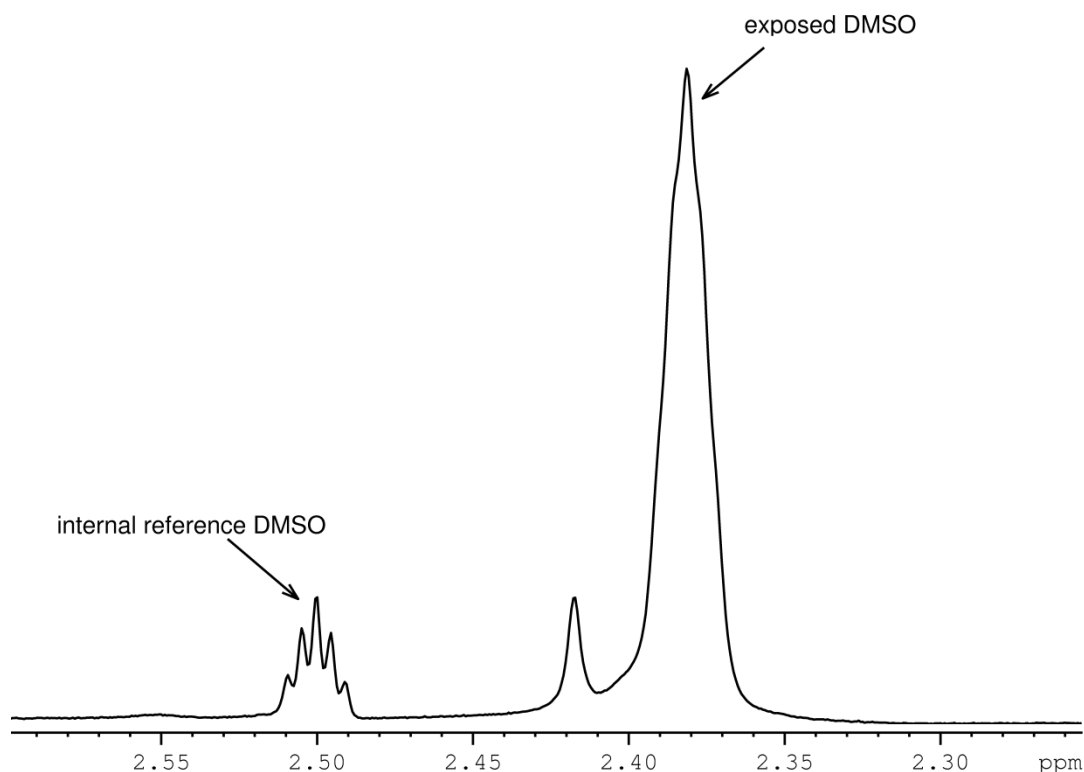


Figure 5.17: The difference in chemical shifts between the internal reference DMSO solution and the exposed DMSO for the solution containing $[\text{VO}(\text{L1})]$ and NaOH, which would oxidise the V(IV) to V(V). Note that the direction and magnitude of the chemical shift for the exposed sample is almost identical to that for the solution containing hydrogen peroxide.

5.4 Titration with NaOH

It was also a possibility that the hydrogen peroxide had dissociated in solution and generated hydroxide ions, which had simply oxidised the vanadium complexes in much the same way that the sodium hydroxide had. To determine whether or not a peroxide or hydroxide complex was forming, titrations of the V(IV) complexes with NaOH were performed, and monitored *via* ^{51}V NMR spectroscopy. The complexes were titrated with 0.02 M sodium hydroxide solution; an example titration is shown for $[\text{VO}(\text{L1})]$ in figure 5.18 (other spectra are given in Appendix A).

Typically, during the course of the titration, three peaks will form for any one of the complexes. The most likely cause for this is that the previously vacant axial coordination position on the vanadyl ion becomes susceptible to nucleophilic attack once oxidised to vanadate. This position is substitutionally labile, and will readily substitute one nucleophile for another, depending on their concentration in solution. This exchange effect has been demonstrated by several authors for vanadium Schiff base complexes similar to the ones under discussion here.^{72,124,130} There are at least three nucleophiles in each solution, *viz.* the hydroxide anion, DMSO and the hydroxide groups on the complexes themselves, formed when sodium hydroxide is added. Additionally, the complexes may have formed dimeric units in solution, bridged by several hydroxides. It is evident that these groups are deprotonated, as the initial additions of sodium hydroxide added cause very little change in the

oxidation state of the vanadyl. Presumably then, the hydroxyl groups are deprotonated first as the pH is increased. Hence, larger volumes of the NaOH solution were also needed to completely oxidise the complexes. For example, in the addition of NaOH to [VO(L1)] 200 μ l of a 0.02 M solution were required before the V(IV) could no longer be seen, whereas on 100 μ l of the 6 % H₂O₂ solution were required to reach the same point previously. A summary of the data for the initial final ⁵¹V chemical shifts is given in Table 5.3.

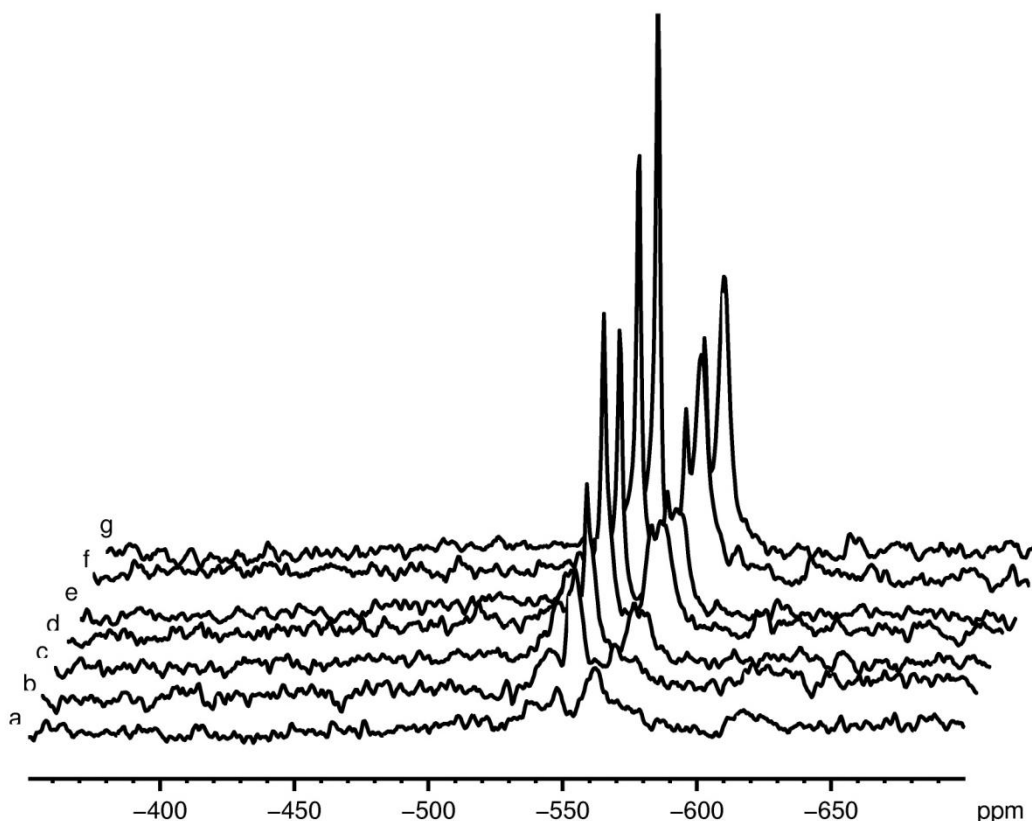


Figure 5.18: Stacked spectra for the titration of [VO(L1)] with 0.02 M NaOH in 0.5 ml DMSO-d₆: a, 0 ml NaOH, b, 20 μ l NaOH, c, 40 μ l NaOH, d, 60 μ l NaOH, e, 80 μ l NaOH, f, 120 μ l NaOH, and g, 200 μ l NaOH. The chemical shift of this species changes very little in comparison to that for the same compound with hydrogen peroxide. Their line shapes are also very different, which shows that they are not the same species.

Examination of the spectra, and chemical shift values obtained, for the vanadium complexes, shows that the up-field shift caused by the addition of sodium hydroxide is very small when compared to that caused by the hydrogen peroxide. For the ethyl-bridged complexes, [VO(L1)] and [VO(L2)], the difference in position of the shifts is very small; it is only on a closer inspection that a change in chemical shifts is noticeable. This shows that there is very little advantage in oxidation of the vanadyl, as the extent of covalent bonding is almost identical between the +4 and +5 complexes. For the propyl-bridged complexes however, a more discernable difference in $\delta(^{51}\text{V})$ is observed. Particularly for [VO(L4)], the up-field shift in ⁵¹V resonance is very marked, and shows that there is a large increase in covalency over the vanadium nucleus. Interestingly, [VO(L4)] required far more NaOH to complete the oxidation – approximately 600 μ l – several hundred more than was required for any of the other complexes. What is more, unlike the other complexes, which showed multiple species formed in roughly equal amounts, only one prominent peak was observed for [VO(L4)]⁺. Thus, despite the choice of nucleophiles, and coordination modes potentially available, only one species' formation is favoured in solution.

In general, the trend, but not the magnitude, seen for the stability increase (or increased covalency) of vanadium coordination when adding sodium hydroxide, is the same as that seen for the addition of peroxide. That is, the ethyl-bridge complexes show the smallest up-field shift, while the increased distortion of the propyl-bridged groups results in a larger up-field shift for $\delta(^{51}\text{V})$. However, the unusually large values obtained for [VO(L4)] for both peroxide and hydroxide additions, and the preference for the formation of only a single species in solution suggest involvement of the propyl-hydroxyl group, perhaps in a hydrogen bonding mode.

Table 5.3: Summary of the initial, major and minor peaks formed due to the addition of sodium hydroxide to the oxovanadium(IV) Schiff base complexes in a DMSO-d6 solution.

Compound	Initial	Final			Ratio	Difference / ppm*
		Major	Minor	Minor		
[VO(L1)]	-548	-557	-574	-581	43:17:39	9
[VO(L2)]	-552	-557	-574	-581	66:16:18	5
[VO(L3)]	-529	-554	-550	-575	33:30:37	25
[VO(L4)]	-475	-548	-560	na	92:8	73
[VO(L5)]	na	-575	-551	-570	80:13:7	na

*Difference is between initial and major, final peak.

When comparing the above spectrum, as well as the results for the other spectra for the NaOH titrations, to those obtained from the H₂O₂ titrations, it is clear that the vanadium species formed in solution are not the same. Not only are the line shapes of the spectra for each respective compound different, but also the location of the NaOH induced ⁵¹V chemical shifts are located significantly downfield to those of the H₂O₂ induced peaks. Therefore, the idea that peroxide is dissociating in solution, and oxidising V(IV) to V(V) *via* a mechanism other than directly binding to the vanadium centre, can be disregarded.

5.5 Conclusion

NMR spectroscopy of ⁵¹V nuclei, due to their high sensitivity and natural abundance, is a convenient method of determining what vanadium species are present in solution. For the oxovanadium(IV) Schiff base complexes studied, a relative assessment of their stability, based on the extent of conjugation present on the vanadium nuclei, was possible, and showed that the ethyl-bridged complexes were more stable than the propyl-bridged complexes. Reasons for this are speculated to be due to the distortion of the coordination geometry about the vanadium from its ideal pseudo-square pyramidal shape.

Addition of hydrogen peroxide resulted in the formation of oxoperoxovanadium(V) complexes. The peroxide ligand can undergo protonation, with a resulting increase in the covalent character over the vanadium centre. The weaker the electron donating ability of the tetradentate ligand was for the starting vanadium(IV) complex, the greater the increase in electron donation to the vanadium in the resulting vanadium(V)-peroxo complex. This effect was most marked for [VO(L4)], with the hydroxyl group on the propyl chain. Hence, [VO(L4)] represents the most likely candidate for successfully binding peroxide ligands in a polar medium.

The effect of the complexes on the bulk magnetic susceptibility was investigated using ¹H NMR, and a modification of the Evans method. It was observed that addition of hydrogen peroxide to a DMSO-

d6 solution of the complexes causes a change in the bulk magnetic susceptibility. Substitution of hydrogen peroxide for sodium hydroxide, which is known to oxidise vanadium(IV) to vanadium(V) species, resulted in similar changes in the bulk magnetic susceptibility for each of the complexes; thus, the effects are due to a change in the oxidation state of vanadium, and not a build-up of radical species.

That the oxovanadium(IV) complexes were binding peroxide, and not a by-product of peroxide decomposition, *viz.* hydroxide, the complexes were titrated with sodium hydroxide, while being monitored by ^{51}V NMR spectroscopy. The spectra were significantly different from those of the hydrogen peroxide titrations for each complex, indicating that different species are formed. Notably, there is a preference for only a single species to form for $[\text{VO}(\mathbf{L4})]$, which is also much more stable than for the other complexes. $[\text{VO}(\mathbf{L4})]$ therefore, appears to facilitate the binding of an additional ligand to the vanadium nucleus.

In summary, the oxovanadium(IV) Schiff base complexes interact with hydrogen peroxide to form a species significantly different from that formed by simple, oxidising conditions, that are located within the “typical” region for vanadium-peroxo complexes, and undergo concomitant oxidation from V(IV) to V(V), implicating the involvement of the vanadium nucleus itself in the binding process. Of all the complexes examined, $[\text{VO}(\mathbf{L4})]$, with its hydroxyl group in close proximity to the vanadium nucleus, appears to facilitate this process of coordinating an additional ligand more so than the other vanadium complexes examined.

Chapter 6 | Computational Chemistry

6.1 Introduction

6.1.1 Theoretical aspects of DFT

Computational chemistry (or theoretical chemistry, or molecular modelling) derives from the development of quantum mechanics, developed in the early 1900s.¹³¹ Max Planck, building on the experimental observations of earlier physicists on black-body radiation, in 1900 proposed that microscopic particles were emitted in discrete units of energy. When it was discovered that particles of matter had bounded energies, and that matter could also be shown to have a wavelike properties, a new form of physics had to be developed to account for this. Quantum mechanics was the result of the attempt to resolve this discrepancy. Quantum mechanics, or QM, states as its fundamental postulate that there is a wave function for any system. When an appropriate operator acts on the wave function, ψ , the corresponding property of the system is given. For the energy of the system, the Schrödinger equation is used:¹³²

$$H\psi = E\psi \quad (7.1)$$

Where H is the Hamiltonian operator and E is the energy of the system. Therefore, to find the energy for a particular system, or in our case, molecule, the Hamiltonian and wave function have to be calculated. In general, every physical observable – not just energy – can have an operator, O , that when acting on a wave function appropriate to the state and condition of the system returns a value for the observable, or eigenvalue, ω .¹³¹ The eigenvalue equation can be given as:

$$O\psi = \omega\psi \quad (7.2)$$

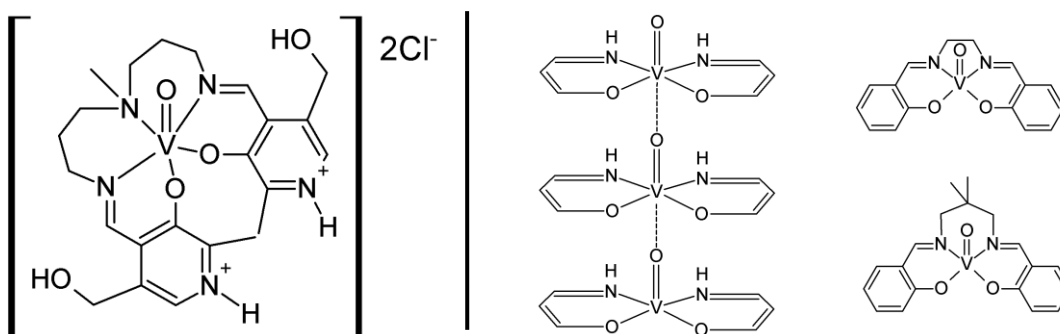
This approach can be followed for any system; however, the time required for these calculations would soon become prohibitive. To simplify the approach, both intuitively and in terms of computational resources, density functional theory (DFT) was developed.¹³³ DFT was developed in the mid-1920s, but is applied in practical work according to its formulation by Kohn and Sham. In DFT, the Hamiltonian operator is dependent on the positions and atomic number of the nuclei, and the total number of electrons. The density of the electron cloud, when integrated, can give the total number of electrons, and the position and nuclear atomic numbers correspond to the positions and densities respectively of local maxima of the overall electron density. The fundamental difference between DFT and the molecular orbital (MO) theory derived from quantum mechanics is that DFT optimises an electron density, while MO theory optimises a wave function. The disadvantage of DFT is that it must be known how the property of the molecule is affected by the electron density, i.e. the property functional of the density must be known. For MO theory based calculations, a quantum mechanical operator for the wave function needs to be known; however, these are already well characterised, and can be applied more broadly than a density property functional.¹³³ DFT does still, however, provide the best route to attaining a certain level of accuracy with the lowest associated cost in time/resources.

When performing a DFT calculation, there are various methods, corresponding to different levels of theory, which can be used. In addition to this, different basis sets are available within the various methods.¹³³ Calculations for the molecules discussed in this chapter used the B3LYP level of theory,

and the 6-311G(d,p) basis set for the protonated ligands, and the LAN2DZ basis set for the oxovanadium(IV) Schiff-base complexes. B3LYP is a hybrid functional, because it combines the LYP method, which is a generalised gradient approximation (GGA) correlation function designed to compute the full correlation energy, B, which is also a GGA exchange functional, and incorporates a three-parameter functional expression that has been empirically derived, hence the implied "3" in the name. B3LYP was compiled by Stephens *et al.*,¹³⁴ and is one of the most popular functionals currently in use.¹³⁵ 6-311G(d,p) is a split valence basis set – valence-triple- ζ – and includes the hyperpolarizabilities for d and p orbitals, where the "d" term means that the d-functions may be added to polarize the p-orbitals, and the "p" term means that the p-orbitals may be added to polarize the s-orbitals. Incorporation of polarization functions permits the modelling of electronic density distributions around atomic centres in molecules. The LAN2DZ basis set, developed by Hay and Wadt,¹³⁷ uses an effective core potential, and only includes the valence electrons in calculations; this has the effect of reducing the accuracy, but greatly decreasing the time needed to perform a calculation. Hence, for the vanadium complexes, only those electrons involved in the chemistry were taken into consideration when determining the geometry, energy and infra-red and UV-visible spectra; the uninvolved, inner sphere of electrons were only approximated.

6.1.2 Previous use of DFT for vanadyl complexes

DFT is the preferred computational method for transition metal chemistry; as such, it has been used in a number of studies.¹³³ Much emphasis has been placed on determining the magnetic dipole moment of vanadyl units, as a means to predicting their EPR spectra (Scheme 6.1).¹³⁸ For example, a number of oxovanadium(IV) Schiff base complexes were studied using the B3PW91 hybrid functional with the 6-31G and 6-311G basis sets for the ligand and vanadium, respectively. A close convergence with experimental ESEEM data was achieved.¹³⁹ DFT calculations of oxovanadium(IV) Schiff base complexes using the B3LYP functional with a 6-31G(d) basis set have also been used by the group of Pessoa to determine the structure, vibrational frequencies and mulliken charges, while TD(time-dependent)-DFT calculations at the same level of theory were performed to determine the complex's UV-Vis spectrum (Scheme 6.1).⁹⁶ Studies have not been limited to isolated small molecules; the group of Abe has performed DFT calculations to obtain the stabilisation energy of dimerisation for two vanadyl Schiff base complexes in methanol.¹⁴⁰ The B3LYP functional was used here as well, to achieve good correlation with the experimental conductivity measurements.



Scheme 6.1: (left) an oxovanadium(IV) complex whose structure was optimised using DFT at the B3LYP/6-31G(d) level of theory, which achieved a close correlation to the experimentally determined crystal structure. (right) a representation of the polymerisation that can occur with vanadyl Schiff base complexes, and two of the complexes examined. DFT was used to determine the magnetic exchange between the vanadyl units for a number of Schiff base complexes, when in this arrangement, as a means to better predicting their EPR spectra.

6.2 Computational method

All density function calculations were performed using the GAUSSIAN09 software package implemented using an Intel Corei7tm (2.67 GHz) processor. The B3LYP method and 6-311G(d,p) basis set were used to calculate the optimised geometries for the gas phase structures of the protonated ligands. NMR spectra were calculated for the protonated ligands *via* the GIAO method using the same level of theory mentioned above. Chemical shifts predicted for ¹H and ¹³C NMR were determined with reference to those predicted for TMS. Natural population analysis (NPA) for the protonated ligands was used to determine atomic orbital electron populations and partial charge distributions. The HOMO and LUMO for each compound was subsequently determined.

For the complexes, DFT calculations were performed using the same software and processor as for the ligands. Optimised gas phase structures were calculated at the B3LYP/LANL2DZ level of theory for all complexes, except for [VO(L1)], which was calculated using the B3LYP/6-311G (d,p) level of theory as B3LYP/LANL2DZ failed to converge on the final, optimised structure for [VO(L1)], necessitating the higher level of theory for this complex. Natural population analysis was performed for all complexes using a full natural bond orbital analysis at the B3LYP/LANL2DZ level of theory. Vibrational frequency calculations were performed routinely for all optimized geometries to vindicate location of true minima on the potential energy surface. Transition energy calculations were performed using the time-dependent-self-consistent field (TD-SCF) method. Selected data from the simulations were plotted using KyPlot version 3.0; molecular drawings and measurements on final structures were made using Mercury 3.0. All molecular orbital diagrams were based on MO analyses performed with GuassView 5.0.

6.3 Computational results for the Schiff base ligands

6.3.1 Geometry optimisation results for the Schiff bases

Geometry optimisations were performed on the Schiff base ligands and, where possible, the X-ray determined structure was used to provide the starting coordinates for the calculation. Of interest for the optimisation results is the fact that **H₂L5** is a zwitterion in the solid state and displayed intramolecular hydrogen bonding (for a discussion of this, see section 3.4). This was confirmed in the geometry optimisation for the compound. ¹H NMR suggests this is the case in solution as well, not only for **H₂L5**, but for the other ligands in this work. The structure optimisations were therefore performed with the aim of seeing whether or not this intramolecular hydrogen bonding was predicted to be occurring in the related Schiff bases. Additionally, if the H-bonding was occurring intramolecularly, then the extent to which this occurred for both H-bonding regions on the same ligand would be determined.

In general, the structures were optimised into an “open-chain” conformation. Bonding about the imine groups was in the *E*-configuration, so that the benzene rings were positioned on the same side of the compound, and the phenoxide and imine H were positioned on the other side. Diagrams of the optimised structures for each ligand are shown in Figures 6.2 to 6.4. The phenoxide and imine groups are the most likely donor groups for metal chelation; their orientation on the same side of the molecules suggests that they are pre-organised for chelation.

Selected bond lengths and angles are given in Table 6.1 for the optimised ligand structures, as well as the crystallographically determined values for the ligand **H₂L5**, which are provided for comparison. Values are for the hydrogen bond associated groups, *viz.* the donor (N), hydrogen and acceptor (O). The C–O bond length should also be susceptible to changes in H-bonding, and reflects the nature of the tautomerism. Therefore, for these compounds to be considered zwitterions, the C–O bond length must be about the same length as a formal C–O single bond. The numerical assignment of atom labels was done in a left-to-right fashion; the left- and right-hand side being determined by positioning the molecule so that the benzene rings are viewed as facing into the page (Figure 6.1).

Table 6.1: Selected DFT-calculated bond lengths and angles for the intramolecular hydrogen-bonding groups of the Schiff bases, and the experimentally determined values for **H₂L5**.

Structural feature	H ₂ L1	H ₂ L2	H ₂ L3	H ₂ L4	H ₂ L5	H ₂ L5 (Exp.)
<u>Bond lengths / Å</u>						
N1–H1	1.09	1.06	1.01	1.05	1.05	0.83
N2–H2	1.08	1.06	1.05	1.04	1.06	0.98
C–O1	1.27	1.26	1.23	1.26	1.27	1.30
C–O2	1.27	1.27	1.27	1.27	1.27	1.31
O1- -H1	1.49	1.58	NA*	1.65	1.60	2.54
O2- -H2	1.49	1.60	1.60	1.66	1.59	2.51
<u>Bond angles / °</u>						
<N1–H1- -O1	149	146	NA*	141	145	156
<N2–H2- -O2	150	145	145	142	146	160

*Groups were positioned away from each other, so that no hydrogen bonding could take place.

Comparison of the experimental and simulated data for **H₂L5** shows that the N–H bond lengths have been overestimated by 0.08 to 0.22 Å, while the C–O bond lengths are shortened by *ca* 3 Å each. Additionally, the H-bond lengths have been shortened significantly compared to the experimentally observed distances. It can be inferred from these results that the same deviation has been predicted for the other compounds, where no crystal structure has been obtained. From the data in Table 6.1, it can be seen that for all compounds, except **H₂L3**, the extent of the H-bonding is predicted to be approximately equal on both halves of the molecules. That is, the length of the N–H, C–O and N–H---O bonds are all approximately the same for each half. Furthermore, these bond lengths are almost the same for all of the compounds. Assuming that the extent of the errors present at the B3LYP/6-311G(d,p) level of theory are the same for all of the compounds, then the N–H and C–O bond lengths are most likely close to the values seen in the crystal structure of **H₂L5**. This suggests that all the Schiff bases are in fact zwitterions. The N–H bonds would therefore be in the N–H⁺ state; the C=N group can thus be thought of as an iminium group. A neutral N–H bond is typically less than 0.87 Å, and any bonds longer than this are considered to be charged.⁹² The C–O bonds are shorter than those of protonated phenol groups, but longer than that of the characteristic C=O bond (1.22 Å).⁹² This suggests that the C–O bonds listed in Table 6.1 can be regarded as C–O[−], or phenoxide, groups. Computationally, then, the compounds are predicted to display intramolecular hydrogen bonding, and that they are zwitterions possessing both positive and negative charges on the same molecule. For all but one group, the charged regions are those involved in the intramolecular H-bonding.

For **H₂L3**, despite the fact that the left-hand side is clearly not able to form an H-bond, the bond lengths suggest that it still possess zwitterionic character on this half of the molecule. Interestingly, the C–O[−] bond length is calculated to be shorter than any other C–O[−] bond on the other compounds, the distance closely approaching that of a formal C=O bond. The N–H⁺ bond is also shorter than the other N–H⁺ bond lengths predicted. This demonstrates how intramolecular H-bonding has not occurred in this region.

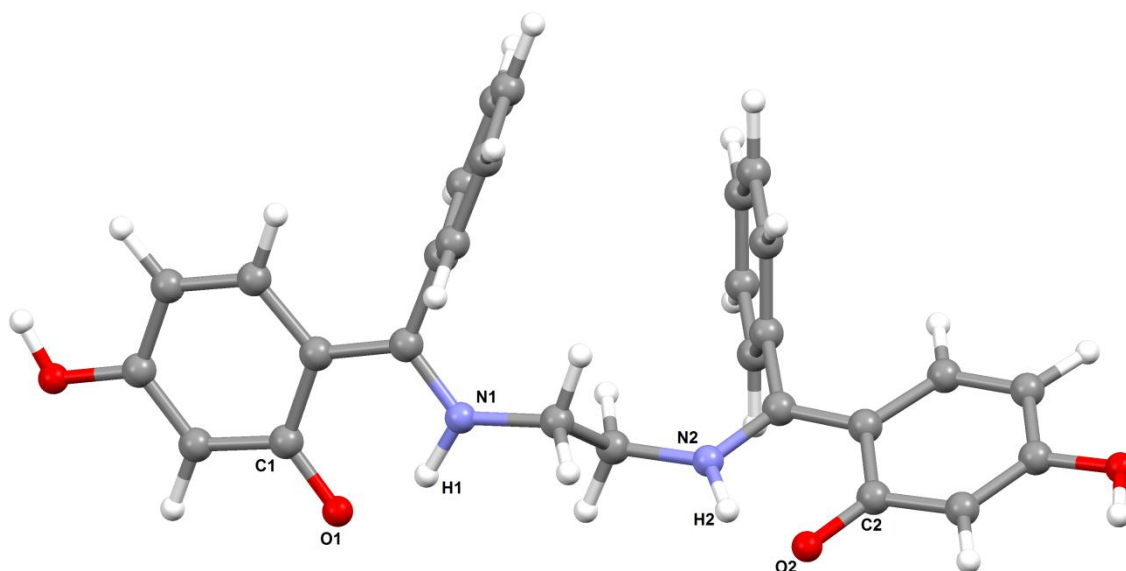


Figure 6.1: The generalised notation used in describing the bond lengths and angles for the various Schiff bases. The choice of left and right when discussing symmetry is made by positioning the molecule so that the benzene rings are directed away from the viewer.

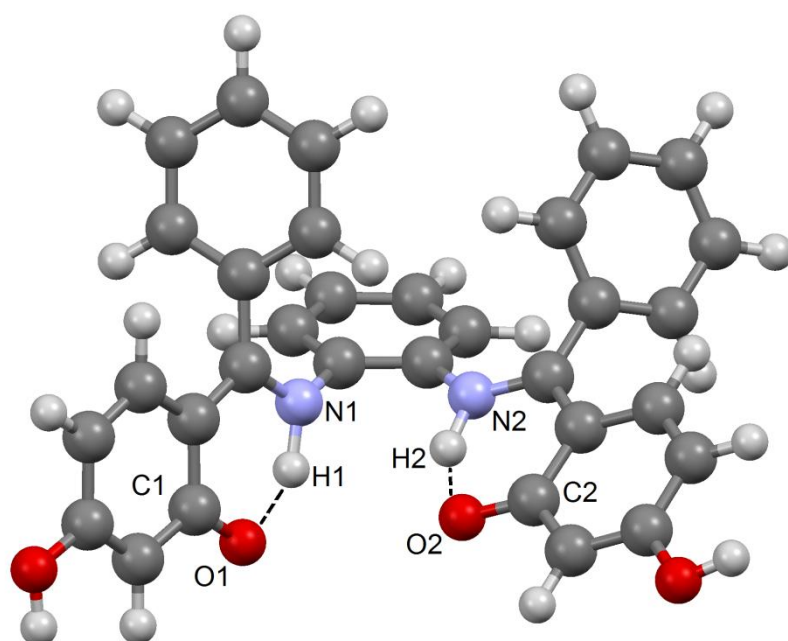


Figure 6.2: Optimised geometrical structure for the Schiff base ligand **H₂L1**.

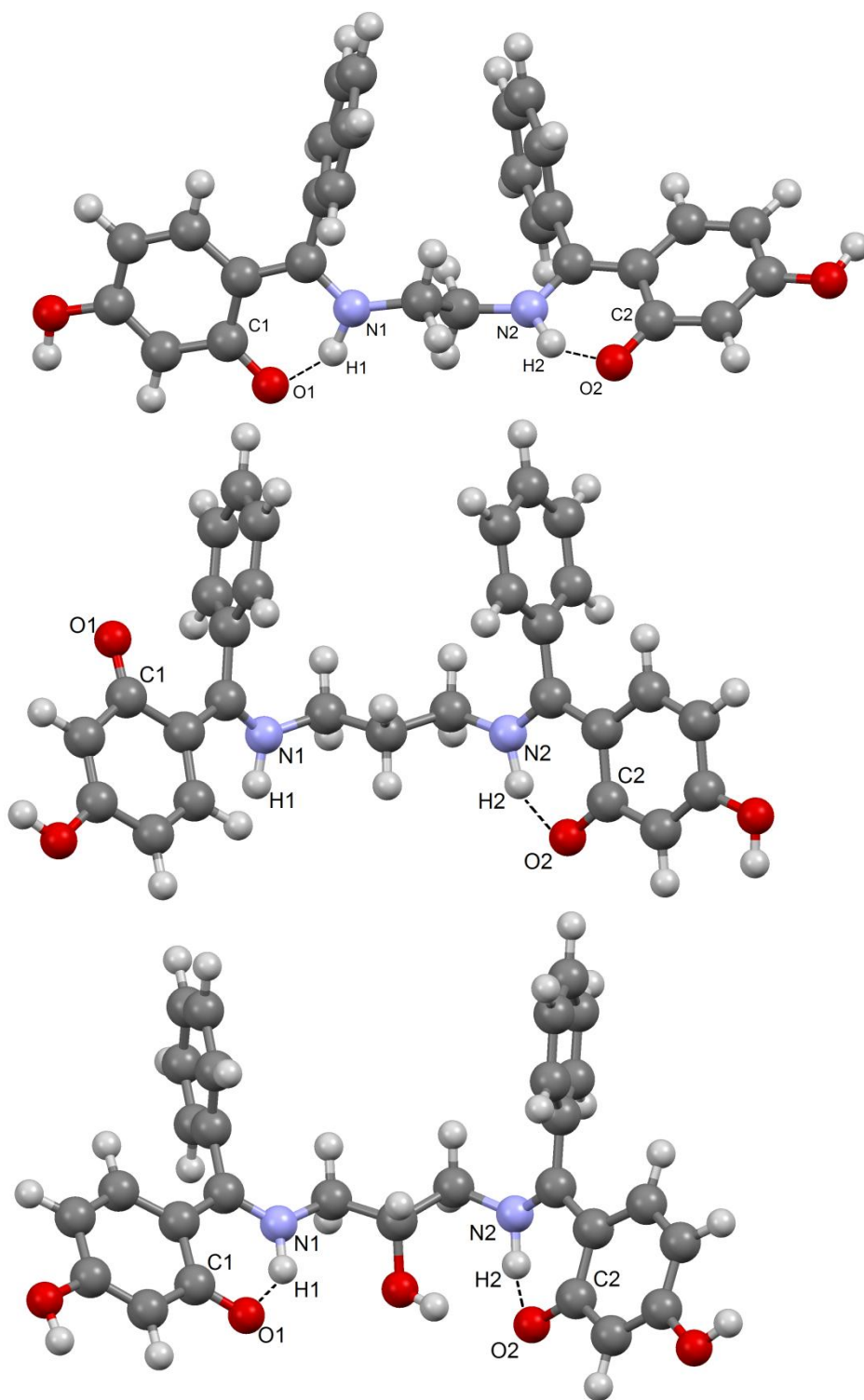


Figure 6.3: Optimised geometrical structure for the Schiff base ligands H_2L_2 (top), H_2L_3 (middle) and H_2L_4 (bottom).

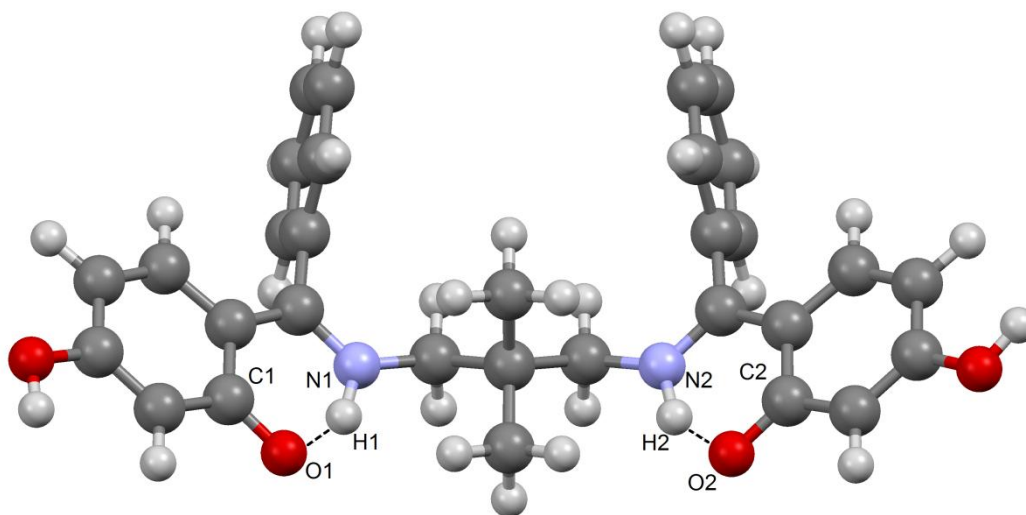


Figure 6.4: Optimised geometrical structure for the Schiff base ligand **H₂L5**.

6.3.2 Natural bond orbital analysis for Schiff bases

The total energy of Schiff bases **H₂L1** – **H₂L5** was determined using the geometrically optimised structures for the ligands. The natural population analysis was performed *via* a full natural bond orbital (NBO) analysis. The electronic charge distribution across the molecules is represented fractionally. The charge distribution is also shown graphically by the atom colouring scheme in the figures below. In this scheme, negative charge is represented by red colouring and positive charge by green colouring. The intensity of the colour is scaled to the extent of the charge character on the molecule.

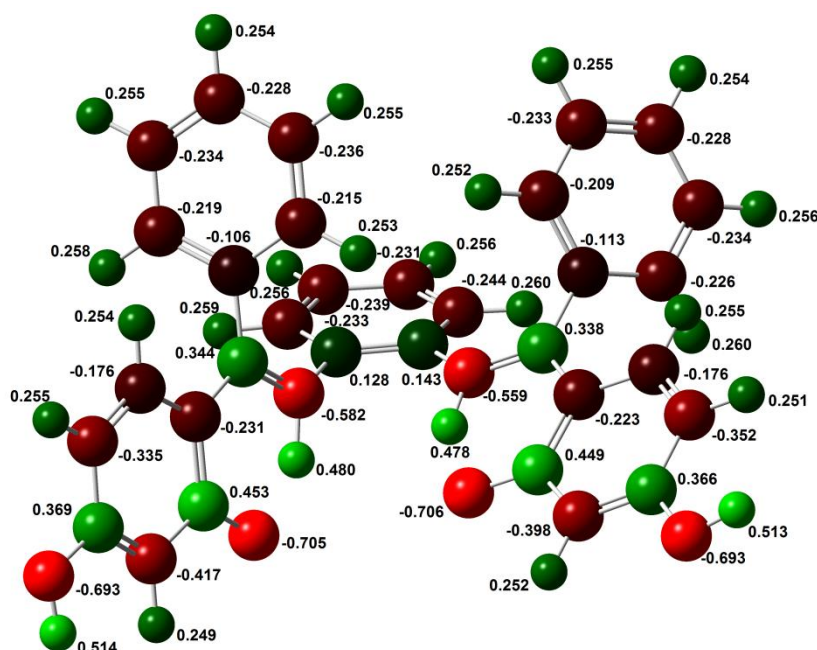
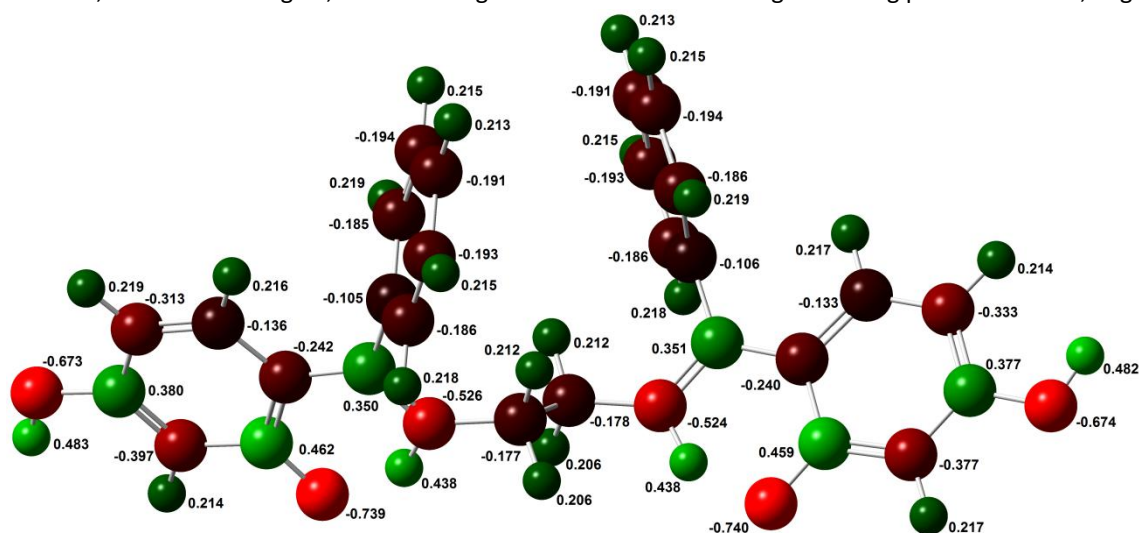
The purpose of performing the natural bond orbital analysis on the compounds was to determine their predisposition to binding a charge-deficient cation like V(IV) or V(V). That is, the extent of negative charge localised on the potential phenoxide and imine donor atoms would give an indication of their ability to balance and/or stabilise the positively charged vanadyl group. As can be seen in the labelled diagrams (Figure 6.5 – 6.9), the iminium N atom and the phenoxide O atom all have very high negative charges relative to the majority of the atoms constituting the rest of the molecule. This provides a very good indication that the ligands' donor groups are suitably charged to chelate the vanadyl cation.

In addition to the negative charges on the donor atoms, the positive charges on the iminium protons also give an indication of the charge stabilising ability of the donor groups. The protons can be thought of as “place-holders” for the vanadyl cation. These iminium protons, although not the most highly charged protons on the Schiff bases, have a higher calculated charge than that calculated for the other protons, even the aromatic protons, which are in themselves generally considered to be electron deficient. This suggests even further that the ligands are well disposed to effectively binding a highly positive metal cation, e.g. VO^{2+} .

Table 6.2: The selected highest positive and negative charge locations for a single atom for the Schiff base ligands, and the charge on the iminium proton.

Compound	Highest Positive Charge		Highest Negative Charge		Charge on Iminium H	
	Value	Assignment	Value	Assignment	Left*	Right*
H ₂ L1	0.514	Phenol-OH	-0.706	Phenoxide	0.480	0.478
H ₂ L2	0.483	Phenol-OH	-0.740	Phenoxide	0.438	0.438
H ₂ L3	0.483	Phenol-OH	-0.742	Phenoxide	0.400	0.438
H ₂ L4	0.483	Phenol-OH	-0.780	Propyl-O	0.444	0.429
H ₂ L5	0.482	Phenol-OH	-0.745	Phenoxide	0.440	0.441

*The designation of "Left" and "Right" is arbitrary, and merely serves to distinguish one iminium proton from another.

**Figure 6.5:** Electronic charge distribution over the Schiff base H₂L1. Values shown for the charge are fractions, rather than integers, and the charge is correlated to colour – green being positive and red, negative.**Figure 6.6:** Electronic charge distribution over the Schiff base H₂L2. Values shown for the charge are fractions, rather than integers, and the charge is correlated to colour – green being positive and red, negative.

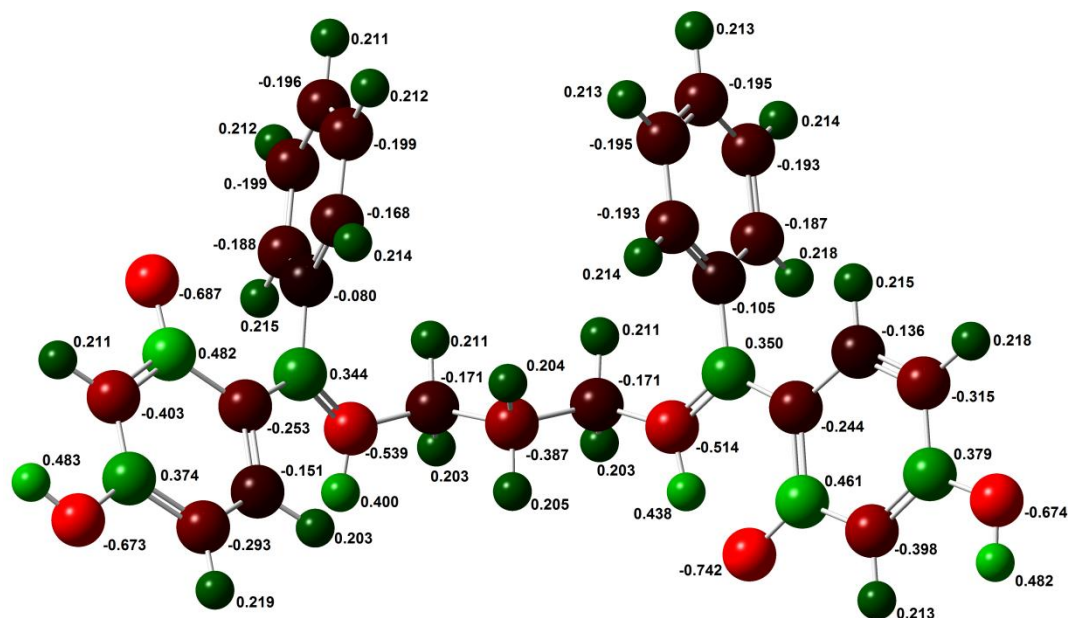


Figure 6.7: Electronic charge distribution over the Schiff base H₂L3. Values shown for the charge are fractions, rather than integers, and the charge is correlated to colour – green being positive and red, negative.

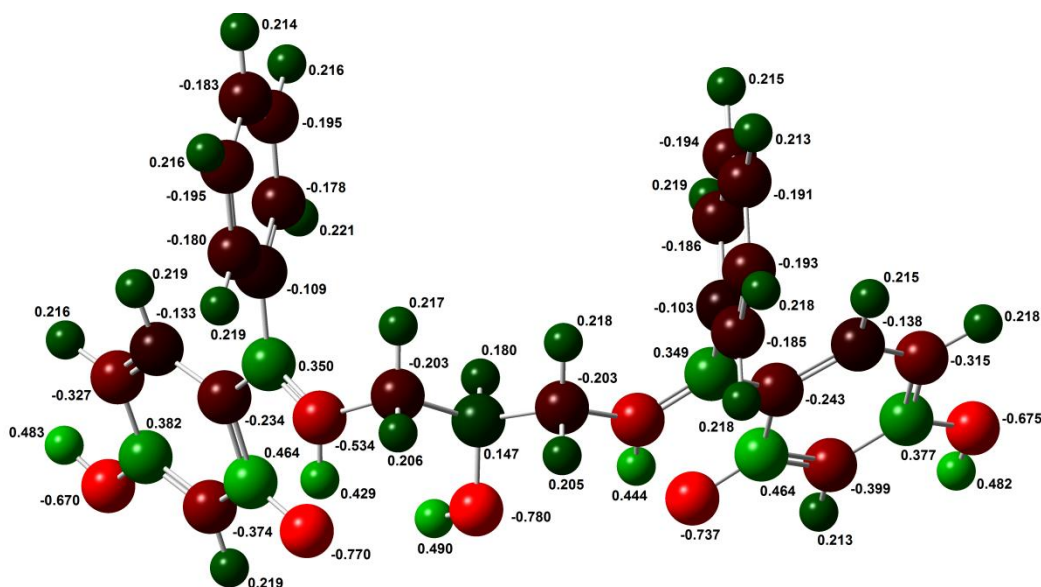


Figure 6.8: Electronic charge distribution over the Schiff base H₂L4. Values shown for the charge are fractions, rather than integers, and the charge is correlated to colour – green being positive and red, negative.

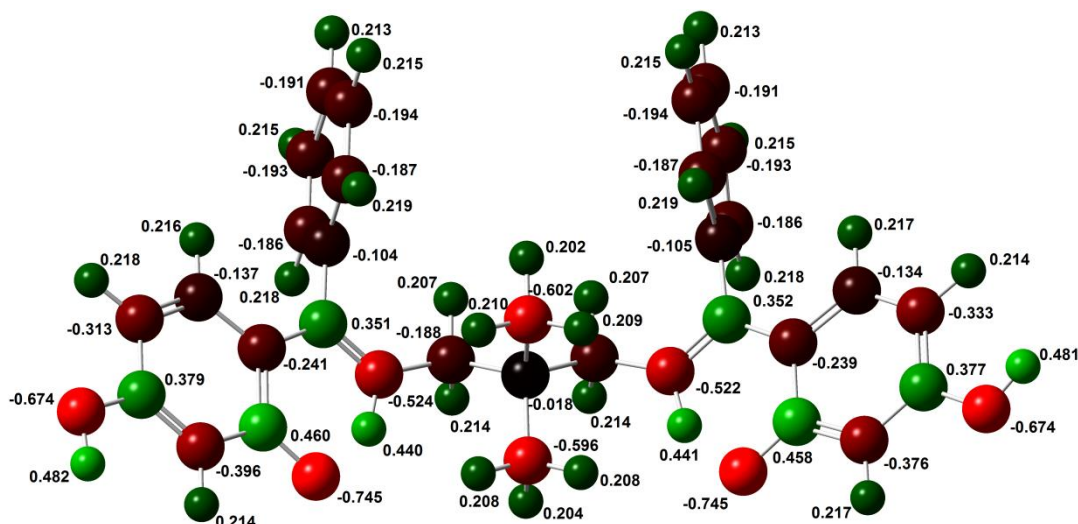


Figure 6.9: Electronic charge distribution over the Schiff base H_2L5 . Values shown for the charge are fractions, rather than integers, and the charge is correlated to colour – green being positive and red, negative.

6.3.3 Vibrational frequency analysis for Schiff base ligands

Vibrational frequencies were calculated to determine whether or not the Schiff bases had been optimised to a minimum, and to compare them to the appropriate spectra for each ligand. The former of these two is done by examining the spectra for any negative eigenvalues (frequencies). A negative frequency would be imaginary, and thus the geometry would not have been optimized to a minimum on the potential energy surface, but to a saddle point. No negative eigenvalues were obtained for any compound, showing that the structures were genuine minima on the potential energy surface.

Comparison of the calculated vibrational spectra with the experimentally determined ones was done to determine the accuracy of the calculations, specifically, the energy prescribed to the various bonds. A general shift in the calculated spectra towards a higher or lower energy (blue or red shift, respectively) would mean that the energy of the calculated ligand structures is higher or lower than that of the actual compounds. Several peaks were chosen in both the calculated and experimental spectra that correlated to the same functional group vibrational mode for the comparison. An overlay of an example spectrum is shown in Figure 6.10; the peaks selected for the comparison are those labelled in the spectra.

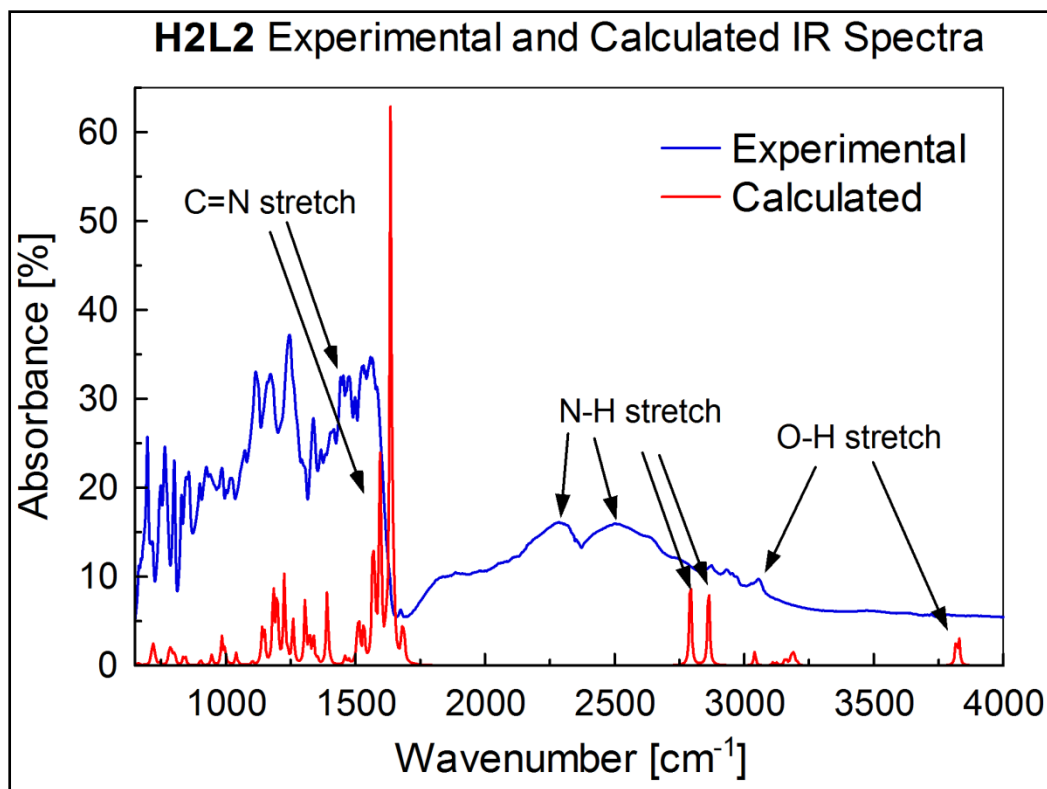


Figure 6.10: Overlay of the calculated (red) IR spectrum over the experiment (blue) IR spectrum for the ligand H_2L_2 .

The percentage difference values calculated for the various functional groups and ligands are given, along with the experimental and calculated values used to derive them, in Table 6.3. The sign obtained for each percentage difference value provides information on whether or not the calculated energy for a specific functional group is higher or lower than that determined by direct observation. For almost every functional group, the sign obtained is negative, meaning that the energy *required* for the vibrational modes is higher than in reality. Or in other words, the optimised structures have a lower energy than the actual sample, as the bonds are stronger and so require more energy, at a higher wavenumber, to induce vibration.

This effect is however, more marked for the O–H and N–H groups than for the C=N group in most instances. Although it cannot be said with certainty, this is probably the result of hydrogen bonding between Schiff bases in the solid state. If a hydrogen bond formed, it would weaken the donor–H covalent bond, and subsequently reduce the vibrational frequency of this bond. At the same time, broadening of this line would occur, which is seen in the experimental spectra. It is only for the ligand H_2L_1 that a positive sign for the percentage difference is seen, and this for the N–H bond. The conformation of this compound is very different to the others due to the rigid aromatic ring, which forces the N–H groups “inwards” where hydrogen bonding to other molecules is limited. This perhaps strengthens the N–H bonds more so than is predicted by theory.

Table 6.3: Selected calculated and experimentally determined values for vibrational frequencies of the Schiff base ligands, and the percentage difference between the two values.

Vibrational Group	H ₂ L1			H ₂ L2		
	Exp.	Calc.	% Diff.**	Exp.	Calc.	% Diff.**
O-H	3229	3809	-18.0	3027	3817	-26.1
N-H*	2608	2828	-8.4	2623	2793	-6.5
C=N	1520	1603	-5.5	1532	1594	-4.0
Vibrational Group	H ₂ L3			H ₂ L4		
	Exp.	Calc.	% Diff.**	Exp.	Calc.	% Diff.**
O-H	3055	3815	-24.9	3244	3817	-17.7
N-H*	2285	2875	-25.8	2445	2976	-21.7
C=N	1564	1637	-4.7	1539	1627	-5.7
Vibrational Group	H ₂ L5					
	Exp.	Calc.	% Diff.**			
O-H	2961	3817	-28.9			
N-H*	2459	2829	-15.0			
C=N	1475	1593	-8.0			

*There are generally two values for the N-H stretching frequency; where necessary, the lower of the two values was used.

** Percentage differences (% Diff.) were calculated as: $\% \text{ Diff.} = \left(\frac{\text{Exp.} - \text{Calc.}}{\text{Exp.}} \right) \times 100\%$.

6.3.4 Electronic transition calculations for ligands

Electronic absorption spectra were calculated for the Schiff-bases to gain an understanding of which molecular orbitals were involved in the absorption. Calculations were performed using the TD-SCF method solving for twelve excited states. DFT computations were performed at the B3LYP/6-311G (d,p) level of theory. This same level of theory has been used for other Schiff base compounds, to calculate their electronic spectra. In general, it was observed that the simulated peaks are blue-shifted compared to the experimentally determined ones.^{141,142}

The calculated electronic absorption spectra for the Schiff bases generally matched the profile of their experimentally determined spectra with a reasonable amount of accuracy (see Figure 6.11 for an example spectral overlay for H₂L5). Both types display two prominent peaks towards the ultra-violet region. The UV absorbing property is not surprising, as the starting material 2,4-dihydroxybenzophenone is well known for its ability to absorb UV radiation, and derivatives of it have been the subject of patents for UV resistant polymers.¹¹¹

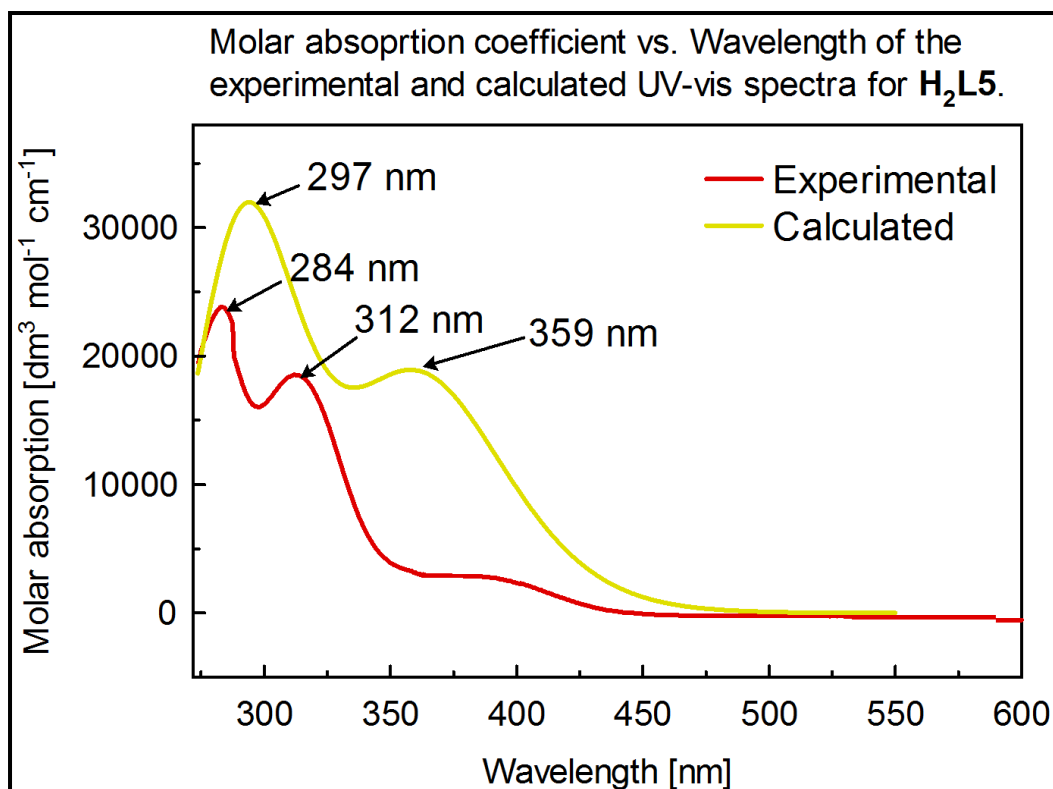


Figure 6.11: Overlay of the calculated (red – in simulated DMSO medium) and experimental (yellow – 298 K in DMSO) electronic absorption spectra for the Schiff base ligand, H_2L5 . The profile of the calculated spectrum matches that of the experimental one reasonable well; however the intensity and wavelength are significantly different.

A summary of the major transitions for each ligand is listed in Table 6.4; spectral overlays for all ligands of the DFT-calculated and experimentally determined UV-vis spectra are given in Appendix C. Although the profile of the spectra have been determined reasonably well, the extent of the absorption has been, in general, overestimated, as can be seen from the spectral overlay (Figure 6.11). The oscillator strengths listed show how the trend is similar for all the ligands concerned. The only example where the strength of absorption in the UV region was underestimated is for the Schiff base H_2L3 . Additionally, the wavelength for each absorption peak has also been overestimated, or red shifted, in all cases. A longer wavelength corresponds to a lower energy, and thus the energy gap predicted between the donor and acceptor molecular orbitals has been underestimated. This is in contrast to other reported studies, where the energy band-gap was overestimated.^{141,142} These differences may be due to the zwitterionic nature of the compounds being underestimated, where charge stabilisation of the H-bonding groups would lower the HOMO energy, thus increasing the HOMO–LUMO transition energy.

The plot of the molecular orbitals involved in the excitations suggests that they are of π symmetry. Hence, the nature of the transitions has been attributed to $\pi \rightarrow \pi^*$ excitations. No σ or σ^* orbitals were involved in any of the major transitions; this reflects the highly conjugated nature of the ligands. For the ligand H_2L2 however, LUMO orbitals on the ethyl group do show σ symmetry, and their phase suggests that they participate in the conjugation of the π system. Plots of the HOMO and LUMO for each Schiff base are shown in Figures 6.12 and 6.13; the delocalised π electron clouds are clearly evident for both of these MOs.

Table 6.4: Selected calculated and experimentally determined electronic absorption peaks for the Schiff-base ligands. The orbitals most responsible for this transition, their hybridisation character and oscillator strength are also given.

Ligand	Absorption wavelength/nm		Molecular Orbitals of Strongest Transition	Character	Oscillator Strength
	Exp.	Calc.			
H₂L1	287	296	HOMO-6 → LUMO	$\pi \rightarrow \pi^*$	0.3251
		330	HOMO-5 → LUMO+1	$\pi \rightarrow \pi^*$	0.2245
	322	412	HOMO → LUMO	$\pi \rightarrow \pi^*$	0.1926
H₂L2	284	230	HOMO-2 → LUMO	$\pi \rightarrow \pi^*$	0.6442
	312	372	HOMO → LUMO	$\pi \rightarrow \pi^*$	0.3864
H₂L3	283	311	HOMO-3 → LUMO	$\pi \rightarrow \pi^*$	0.3149
		311	354	HOMO → LUMO+1	$\pi \rightarrow \pi^*$
		414	HOMO → LUMO	$\pi \rightarrow \pi^*$	0.1792
H₂L4	283	285	HOMO-2 → LUMO+1	$\pi \rightarrow \pi^*$	0.2375
		301	HOMO-3 → LUMO	$\pi \rightarrow \pi^*$	0.2455
		309	HOMO-2 → LUMO	$\pi \rightarrow \pi^*$	0.1915
	311	360	HOMO → LUMO+1	$\pi \rightarrow \pi^*$	0.1976
H₂L5	284	297	HOMO-2 → LUMO	$\pi \rightarrow \pi^*$	0.5275
		312	359	HOMO-1 → LUMO	$\pi \rightarrow \pi^*$
		367	HOMO → LUMO	$\pi \rightarrow \pi^*$	0.2232

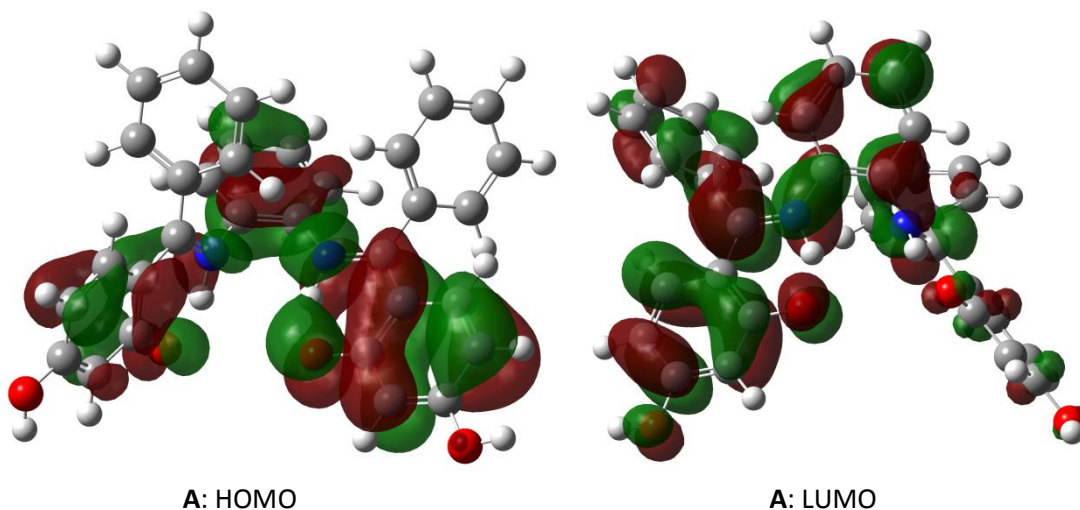


Figure 6.12: DFT-calculated HOMO and LUMO for the ligand H₂L1 (A).

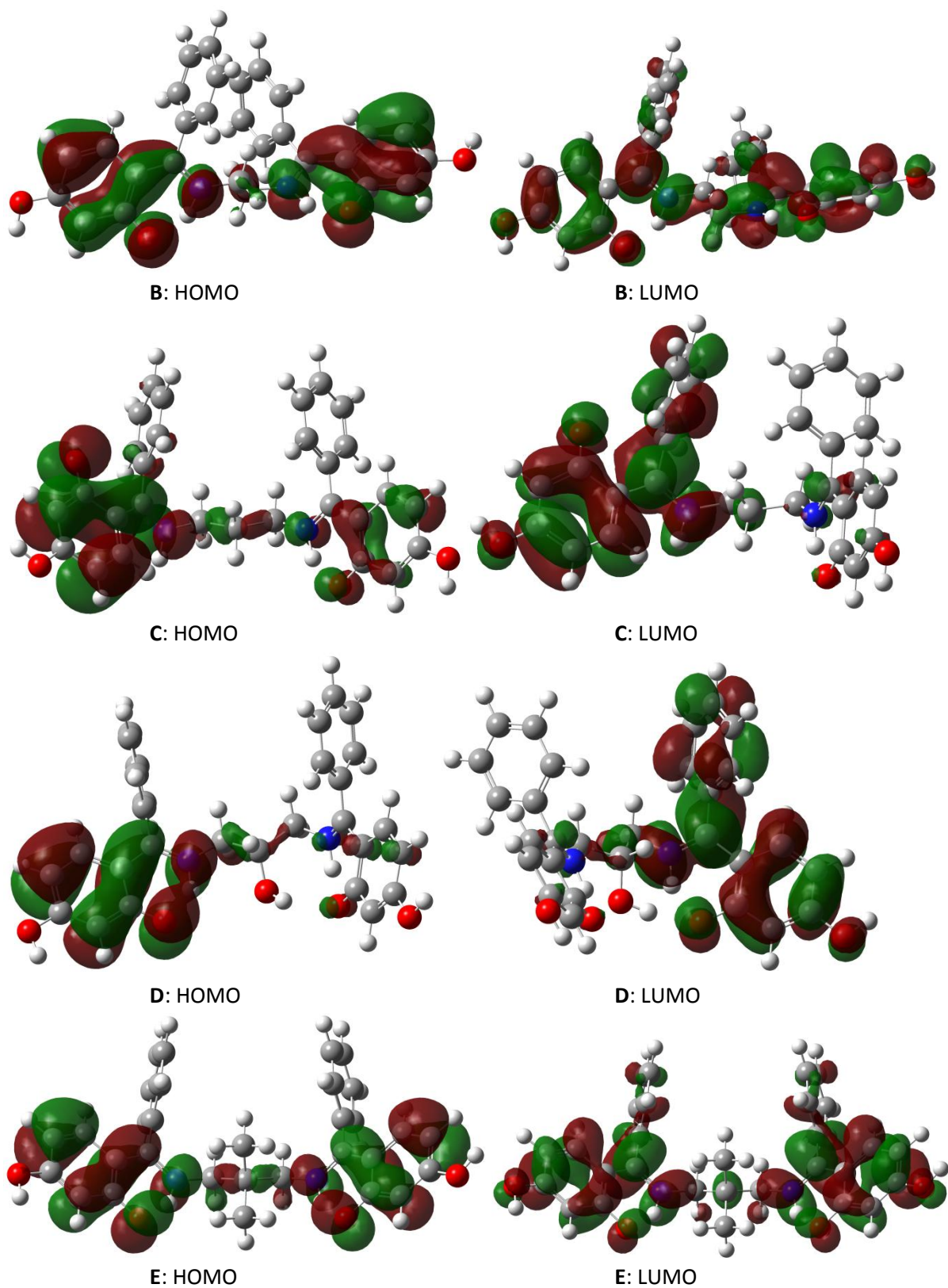


Figure 6.13: DFT-calculated HOMO and LUMO for the Schiff base ligands H_2L_2 (B), H_2L_3 (C), H_2L_4 (D) and H_2L_5 (E).

6.3.5 NMR simulations for the Schiff base ligands

The ^1H and ^{13}C NMR chemical shifts for the five Schiff base compounds were calculated using the GIAO method at the B3LYP/6-311G (d,p) level of theory. The IEFPCM solvent method was used to include a dielectric field equivalent to solvation with dimethyl sulfoxide for the calculations. The chemical shift for the reference tetramethyl-silane (TMS) was also calculated under the same conditions and using the same level of theory.

Chemical shifts for the protons were in most instances severely underestimated. The exceptions to this were for the iminium H shift, which was overestimated for **H₂L1** and **H₂L2**, and only moderately overestimated for the remaining ligands. The phenol proton chemical shifts are very significantly underestimated, with the lowest percentage difference obtained between an experimental and calculated value was 49%. Chemical shifts correlating to specific methylene protons were able to be identified in the experimental spectra, and so were also used for the accuracy assessment in addition to the phenol and iminium protons. The predicted shifts compare moderately well to the experimental frequencies being, in general, underestimated. They are, however, still in closer agreement than the phenol proton chemical shifts.

The majority of the remaining proton chemical shifts cannot be used to assess the accuracy of the calculations, as they belong to aromatic protons. The aromatic protons are too closely positioned together in the experimental spectra to accurately determine which peak correlates to which proton. Because of this uncertainty in assignment of peaks, only the limited selection of values given in Table 6.5 can be used. The labelling scheme used for assigning chemical shifts to specific protons is shown in Figure 6.14.

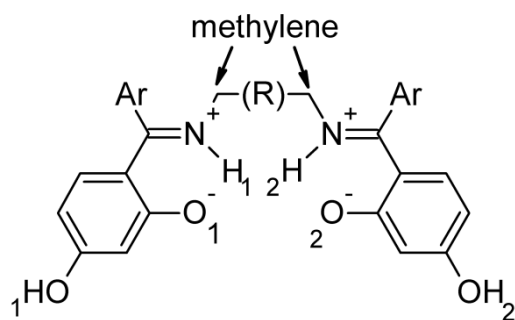


Figure 6.14: Numbering/labelling scheme for the Schiff base ligands used for the assignment of the proton NMR spectra.

Table 6.5: Selected experimental and calculated proton chemical shifts for the Schiff bases, and the percentage differences between the corresponding values.

H₂L1 δ / ppm				H₂L2 δ / ppm			
Proton	Exp.	Calc.	% Diff. ‡	Proton	Exp.	Calc.	% Diff. ‡
NH1	14.7	18.5	-25.9	NH1	15.6	15.9	-1.9
NH2	14.7	19.3	-31.3	NH2	15.6	16.4	-5.1
OH1	10.2	4.8	52.9	OH1	9.8	5.0	49.0
OH2	10.2	4.5	55.9	OH2	9.8	4.8	51.0
CH ₂ [†]	NA	NA	NA	CH ₂ [*]	3.3	3.8	-15.2

H₂L3 δ / ppm				H₂L4 δ / ppm			
Proton	Exp.	Calc.	% Diff. ‡	Proton	Exp.	Calc.	% Diff. ‡
NH1	15.9	15.3	3.8	NH1	15.8	14.5	8.2
NH2	15.9	5.5	65.4	NH2	15.8	13.4	15.2
OH1	9.9	4.3	56.6	OH1	9.7	4.2	56.7
OH2	9.9	4.1	58.6	OH2	9.7	4.3	55.7
CH ₂ [*]	3.21	2.7	15.9	CH ₂ [*]	3.5	2.7	22.9

H₂L5 δ / ppm			
Proton	Exp.	Calc.	% Diff. ‡
NH1	16.0	15.5	3.1
NH2	16.0	15.1	5.6
OH1	9.9	4.1	58.6
OH2	9.9	4.3	56.7
CH ₂ [*]	3.0	2.5	17.5

†There are no methylene protons on **H₂L1**.

‡Percentage difference was calculated as: % Diff. = $\left(\frac{Exp.-Calc.}{Exp.}\right) \times 100\%$.

*In some instances, there was more than one chemical shift associated with a pair of methylene protons in the experimental spectra; computational spectra always showed more than shift per methylene group. Therefore, the average of these values has been tabulated and used in the % Diff. calculations.

In contrast to the proton chemical shifts, the *in silico* ¹³C chemical shifts compared far better to their corresponding experimental spectra (Table 6.6). As with the proton spectra, only the peaks that could be unambiguously matched to the carbon from which they originated were used to compare the experimental and computational spectra. Figure 6.15 shows which carbon atoms were used for the comparison of the spectra, as well as the labelling scheme employed.

In general, the chemical shifts were overestimated slightly. The only exceptions to this were for the methylene carbons. These carbon chemical shifts were predicted very well, with the greatest amount of deviation (expressed as percentage deviation) evident for **H₂L4** (-14.3%), the smallest deviation was for **H₂L5**, where there was no difference observed at the level of theory used for the simulations. For the O bonded carbons, C-O β , with the protonated O atom, always showed less of a difference between the predicted and experimental values than for the C-O α carbons. Both the α and β C-O ¹³C chemical shifts are, however, reasonably well matched to the experimental values. The calculated C=N ¹³C chemical shifts also match the experimental values; percentage differences are between -3.4 and -6.4 %. Interestingly, the calculations at this level of theory predict that the location of the C=N ¹³C shift is between those of the two C-O ¹³C shifts, whereas experimentally, it is located further downfield than either of them.

For both the ^{13}C and ^1H spectra, only a small selection of the total values calculated could be used to determine the accuracy of the computational data. Additionally, these values were mostly for highly variable groups, e.g. protons on hetero-atoms and aromatic carbons bonded to hetero-atoms. It is clear that the ^{13}C values predicted were more accurate than the ^1H values. However, the general location of the iminium proton peak was correctly determined to be furthest down-field and the chemical shift value was reasonably well predicted. It can be said then, that the B3LYP/6-311G (d,p) level of theory using the GIAO method yields reasonable results for the carbon spectra, but generally poor results for proton spectra. This has been noted for DFT-calculated ^1H NMR spectra of other Schiff bases,¹⁴¹ and therefore, extreme care should be exercised when assigning proton peaks, especially when they are bonded to hetero-atoms.

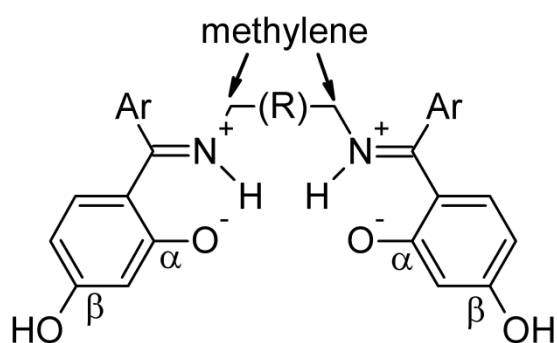


Figure 6.15: Labelling scheme for the ^{13}C chemical shift assignments for the Schiff bases.

Table 6.6: Selected experimental and calculation carbon chemical shifts for the ligands, and the percentage differences between corresponding values.

$\text{H}_2\text{L1 } \delta / \text{ppm}$				$\text{H}_2\text{L2 } \delta / \text{ppm}$			
Carbon	Exp.	Calc.	% Diff.**	Carbon	Exp.	Calc.	% Diff.**
C=N	173	184	-6.4	C=N	174	184	-5.7
C-O α	165	178	-7.9	C-O α^*	167	190	-13.8
C-O β	163	169	-3.7	C-O β	162	173	-6.8
CH ₂	NA	NA	NA	CH ₂	51	50	2.0
$\text{H}_2\text{L3 } \delta / \text{ppm}$				$\text{H}_2\text{L4 } \delta / \text{ppm}$			
Carbon	Exp.	Calc.	% Diff.**	Carbon	Exp.	Calc.	% Diff.**
C=N	174	180	-3.4	C=N	174	181	-4.0
C-O α	167	186	-11.4	C-O α	167	187	-12.0
C-O β	162	173	-6.8	C-O β	162	173	-6.8
CH ₂	49	44	10.2	CH ₂	49	56	-14.3
$\text{H}_2\text{L5 } \delta / \text{ppm}$							
Carbon	Exp.	Calc.	% Diff.**				
C=N	175	182	-4.0				
C-O α	167	187	-12.0				
C-O β	162	173	-6.8				
CH ₂	59	59	0.0				

*The experimental spectrum displayed two peaks corresponding to these carbons; the average between the two values is shown in the table, and was used for the calculation of percentage difference.

**Percentage difference was calculated as follows: $\% \text{ Diff.} = \left(\frac{\text{Exp.} - \text{Calc.}}{\text{Exp.}} \right) \times 100\%$.

6.4 Computational results for the oxovanadium(IV) complexes

6.4.1 Geometry optimisation results for the oxovanadium(IV) complexes

An understanding of the stereochemistry of the complexes is crucial in the elucidation of their *in vitro* and *in vivo* activity; namely, determining their biological targets is greatly aided by knowing their geometries. In addition to this, the coordination geometry around the vanadium ion plays a crucial role in determining the donor–vanadium bond strengths, how readily peroxide, or other nucleophiles, can be bound to the vanadium, and if the approach of these nucleophiles will be hindered in any way. The strength of the coordinating bonds will determine the stability of the complexes. With no crystal structures obtained as yet for the complexes, the importance of DFT calculations to determine their geometry takes on an even greater significance.

The geometries for the oxovanadium(IV) Schiff-base complexes were optimised as gas-phase models. To determine if the potential energy minima had been reached for each complex, additional frequency calculations were also performed (results of these frequency calculations are given in Section 6.4.3). No negative eigenvalues were determined, showing that the complexes had indeed been optimised to a minimum. Calculations were performed at the B3LYP level of theory, with the LAN2DZ basis set being used for the complexes [VO(L2)], [VO(L3)], [VO(L4)] and [VO(L5)]. [VO(L1)] failed to converge using the LAN2DZ basis set, and so the 6-31G basis set, which does not use an effective core potential, but takes into account the orbitals for all the electrons, had to be used.

6.4.1.1 General notation: In all complexes, the vanadium is located above the plane formed by the equatorial bonding atoms, so as to adopt a distorted, square-pyramidal geometry. Distortion from an idealised geometry is significantly affected by the steric constraints of the bridging group. For simplicity, the notation shown in Figure 6.16 will be adopted for referring to the bonds and bond angles about the vanadyl unit.

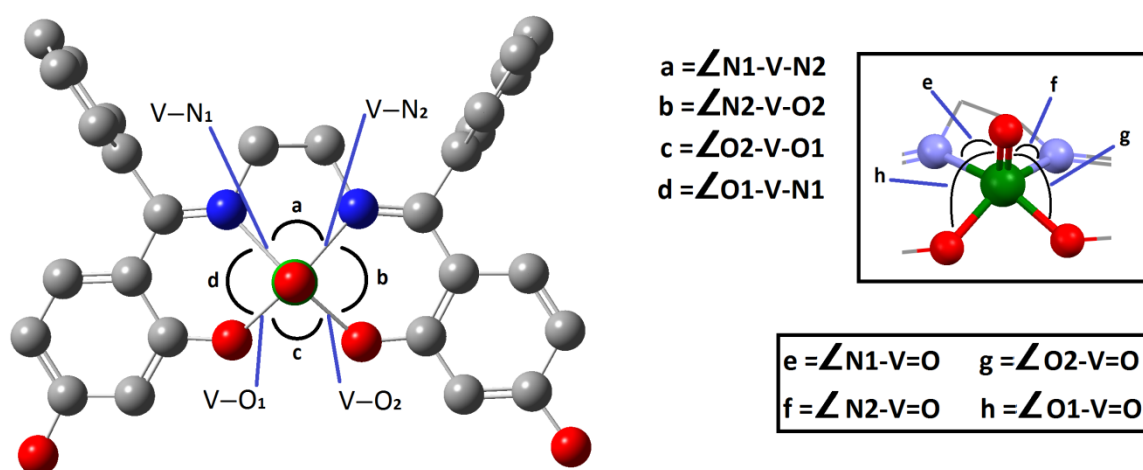


Figure 6.16: Assignment of terminology for significant bonds and angles in the calculated oxovanadium(IV) Schiff-base complexes. [VO(L2)] is shown as an example complex. Symbols **a–d** represent the four angles formed between a two donor atoms and vanadium, while symbols **e–h** represent the angles formed between a donor, vanadium and the vanadyl O atom.

6.4.1.2 Coordination geometry–bond distances: As mentioned above (Section 6.4.1), the geometry about the vanadyl ion can give an indication of the complex's stability. In general, the shorter the vanadium–donor bond length is, the stronger that bond will be. The shortest V–N bond lengths are for [VO(L1)]. The complex is almost perfectly symmetric; hence the bond lengths are the same. Bonds to the phenoxide O atom are, interestingly, longer for this complex than for the V–O bonds on the alkyl-bridged complexes.

The other complexes follow a definite trend – as the molecular weight (i.e. chain length) of the alkyl bridge increases, so the length of the V–N bond also increases. There is very little difference between the V–O bond lengths, and they are most likely not perturbed by the nature of the alkyl bridge. The only change in bond strength would therefore be predicted to arise due to changes around the imine groups. A weaker coordinating bond not only implies that the complex will be less stable, but also, that the vanadium will more readily coordinate another nucleophile.

6.4.1.3 Coordination geometry–bond angles: Geometry optimisations also predict a distorted, square-pyramidal coordination geometry for vanadium, where the metal is above the basal plane of the donor atoms. It would be expected though, that the degree to which the vanadium is raised above this plane would be the same for all equatorial points. In other words, the angles formed between the vanadyl O atom, vanadium and donor atoms should all be approximately the same, and greater than 90°. Additionally, the donor(D)–vanadium–D angle should be approximately equal to 90°. This matches the predictions of other vanadium Schiff base complexes, where a distorted square-pyramidal geometry was predicted at the BLYP/DNP¹⁴³ or B3LYP/6-311+G(d,p)¹⁴⁴ levels of theory.

Calculated structures for the complexes [VO(L1)] and [VO(L2)] position the vanadium as expected, with little perturbation of the pseudo-square-pyramidal structure. However, for the complexes [VO(L3)], [VO(L4)] and [VO(L5)], there is an increasing amount of distortion from this idealised vanadium coordination geometry as the amount of bulk on the propyl chain increases. Clearly, from the structure determined for [VO(L3)], the six-membered chelate ring is strained to bind to the vanadium. The inclusion of different substituents on the propyl-chain only decreases the conformational flexibility of the chelate ring, which further twists the vanadium out of its preferred coordination geometry. Values for all angles around the vanadium centres are given in Table 6.7. The greatest differences are 25.5° between angles **e** and **h** for [VO(L3)], 26.1° between **f** and **g** for [VO(L4)] and 28.0° between **e** and **h** for [VO(L5)]. It can be inferred, therefore, that the coordination to vanadium is not as stable for the three-carbon bridged complexes as it is for the two-carbon bridged ones. The displacement of the vanadium atom above the basal plane can be seen in Figures 6.17 and 6.18.

Table 6.7 Summary of significant calculated bond lengths and angles of the coordination sphere about the vanadyl centre for the oxovanadium(IV) Schiff-base complexes. [VO(L1)], [VO(L2)], [VO(L3)], [VO(L4)] and [VO(L5)].

Structural feature	[VO(L1)]	[VO(L2)]	[VO(L3)]	[VO(L4)]	[VO(L5)]
<i>Bond lengths / Å</i>					
V-N ₁	2.070	2.073	2.117	2.070	2.124
V-N ₂	2.070	2.075	2.072	2.125	2.081
V-O ₁	1.947	1.914	1.899	1.892	1.900
V-O ₂	1.947	1.925	1.943	1.943	1.936
V=O	1.605	1.605	1.605	1.605	1.606
<i>Bond Angles / °</i>					
a	80.10	81.51	88.34	88.68	90.11
b	84.49	85.77	84.77	85.14	85.66
c	90.77	87.73	87.53	87.57	86.34
d	84.50	85.34	84.94	84.61	84.53
e	105.98	100.38	94.99	108.81	93.76
f	105.96	106.26	109.51	94.54	110.32
g	108.31	107.73	102.04	120.59	101.67
h	108.33	114.24	120.45	102.18	121.80

Accompanying this distortion of the coordination sphere, it can also be seen how the benzene rings are being twisted relative to the plane of the donor atoms, and to each other. For [VO(L1)], the difference between the two is not noticeable; the complex is calculated to have good symmetry. In [VO(L2)], there is a more noticeable difference in the orientation of each benzene ring, which is caused by the conformation of the strained ethyl bridge. As the chain length is increased to a propyl bridge, the extent of the twist in the molecule also increases; this can be clearly seen by how the benzene rings are positioned on opposite sides of the donor atom plane. Increasing the bulk of the bridging chain causes the trend to continue; the twist in the molecule increases, and the benzene rings become even more displaced from each other in opposite directions. Calculated structures of the complexes are shown in Figures 6.17 and 6.18; the amount of distortion caused by the bridging groups can be seen clearly from the illustrations.

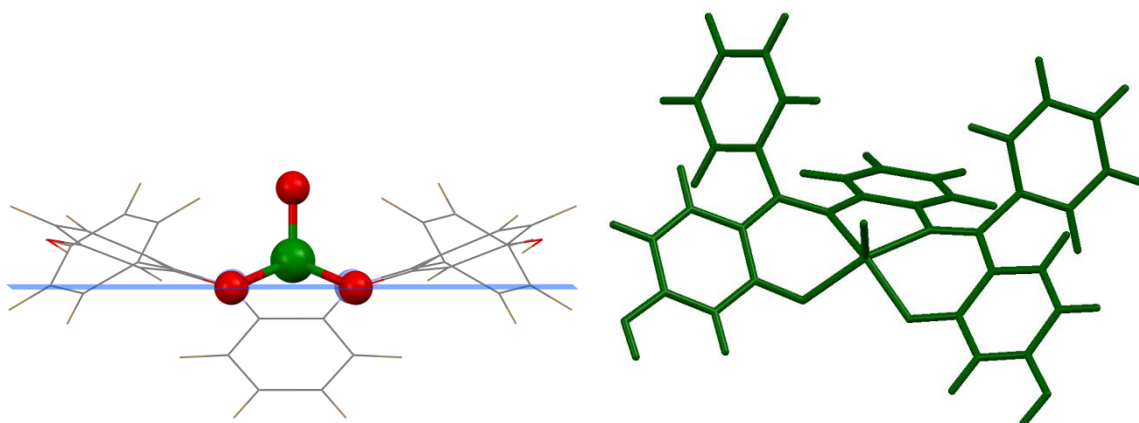


Figure 6.17: DFT-calculated geometry optimised structure for [VO(L1)] (right); the pseudo-squarepyramidal geometry of vanadium and its displacement from the basal plane are highlighted (left).

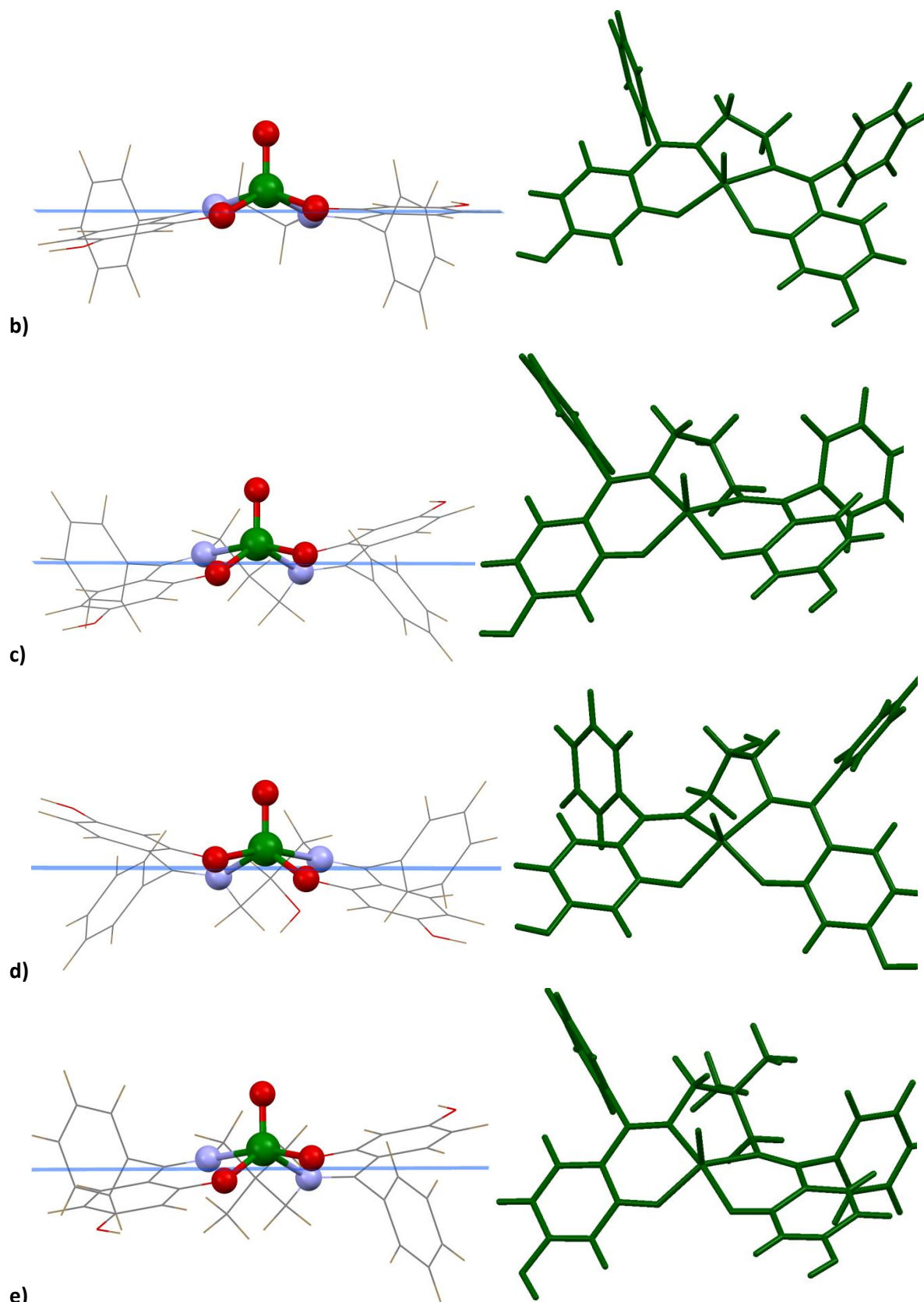


Figure 6.18: Calculated structures showing the optimised geometry for the oxovanadium(IV) Schiff base complexes: **b)** (l, r) [VO(L2)], **c)** (l, r) [VO(L3)], **d)** (l, r) [VO(L4)] and **e)** (l,r) [VO(L5)], where “l” is “left” and “r” is “right.” The blue plane in the left-hand side figures is the calculated plane connecting the donor atoms; vanadium’s displacement from this plane and its pseudo-squarepyramidal geometry can be seen here.

How these optimisations compared to experimental data could not be done for the complexes, as no crystal data was available for comparison. However, similar complexes whose crystal structure data was available in the Cambridge Structural Database (CSD) could be used for a less precise, but still meaningful comparison.

The crystal structures, identified by their CSD codes: MAHVIB, ABUZAY, NECCUT, BEGHEB and HOWVUK, were used to determine an RMS fit for the optimised geometries of [VO(L1)], [VO(L2)], [VO(L3)], [VO(L4)] and [VO(L5)], respectively. The RMS fit for these complexes is shown graphically in figure 6.19. A reasonably good fit to the calculated structures was obtained, with RMSD values of

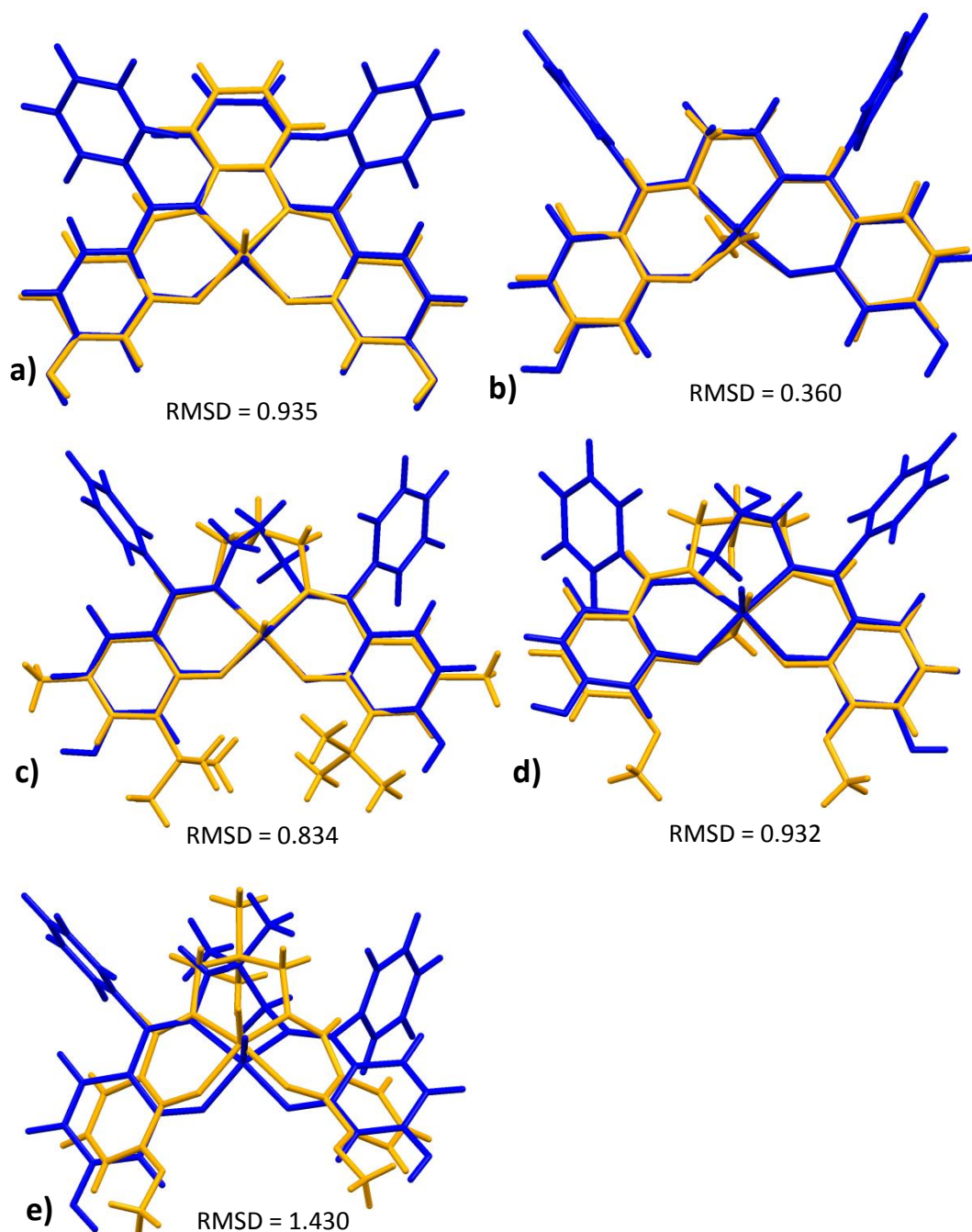


Figure 6.19: RMS fit between the DFT-calculated complexes (blue): a) [VO(L1)], b) [VO(L2)], c) [VO(L3)], d) [VO(L4)] and e) [VO(L5)] and the crystal structures of related compounds (yellow): MAHVIB, ABUZAY, NECCUT, BEGHEB and HOWVUK, respectively. Crystal structures were obtained from the CSD.

0.935, 0.360, 0.834, 0.932 and 1.430 for the couples **a**), **b**), **c**), **d**) and **e**), respectively (Figure 6.19). This shows that the structures predicted by the B3LYP/LANL2DZ level theory can be regarded as generally accurate, and any trends observed in theory can be expected to exist in reality as well.

6.4.2 Natural bond orbital analysis for the oxovanadium(IV) Schiff-base complexes

For each complex, the optimised structure was used when determining the total energy of the molecule. Calculated illustrations, showing the charge distribution on each atom, are given below for each of the complexes. Numbers displayed are fractional and symmetric; the colouring of the atoms too is symmetric, that is, green is used to represent positive charge, while red is used to represent negative charge. A greater colour intensity on an atom, represents a greater amount of charge localisation present there. Illustrations of the complexes showing their charge distribution according to this scheme are given in Figures 6.20 ([VO(L1)] and [VO(L2)]), 6.21 ([VO(L3)] and [VO(L4)]) and 6.22 ([VO(L5)]). For all the complexes calculated, the most positive atom was always vanadium. This is significant, because the ability of the complexes to perform various catalytic roles, e.g. binding peroxide, relies on the vanadium centre being positively charged. The stronger this charge is, the more effectively it would be predicted to form adducts with nucleophiles. For [VO(L1)], [VO(L2)], [VO(L3)], [VO(L4)] and [VO(L5)], the charge, in electron units, on the vanadium was 0.867, 0.844, 0.843, 0.845 and 0.848, respectively. Thus, there is little difference between the complexes bearing an alkyl bridge, despite the length of this group. Also, the presence or absence of substituents on the bridge does not cause a significant difference in the charge distribution over the donor atoms, or vanadium.

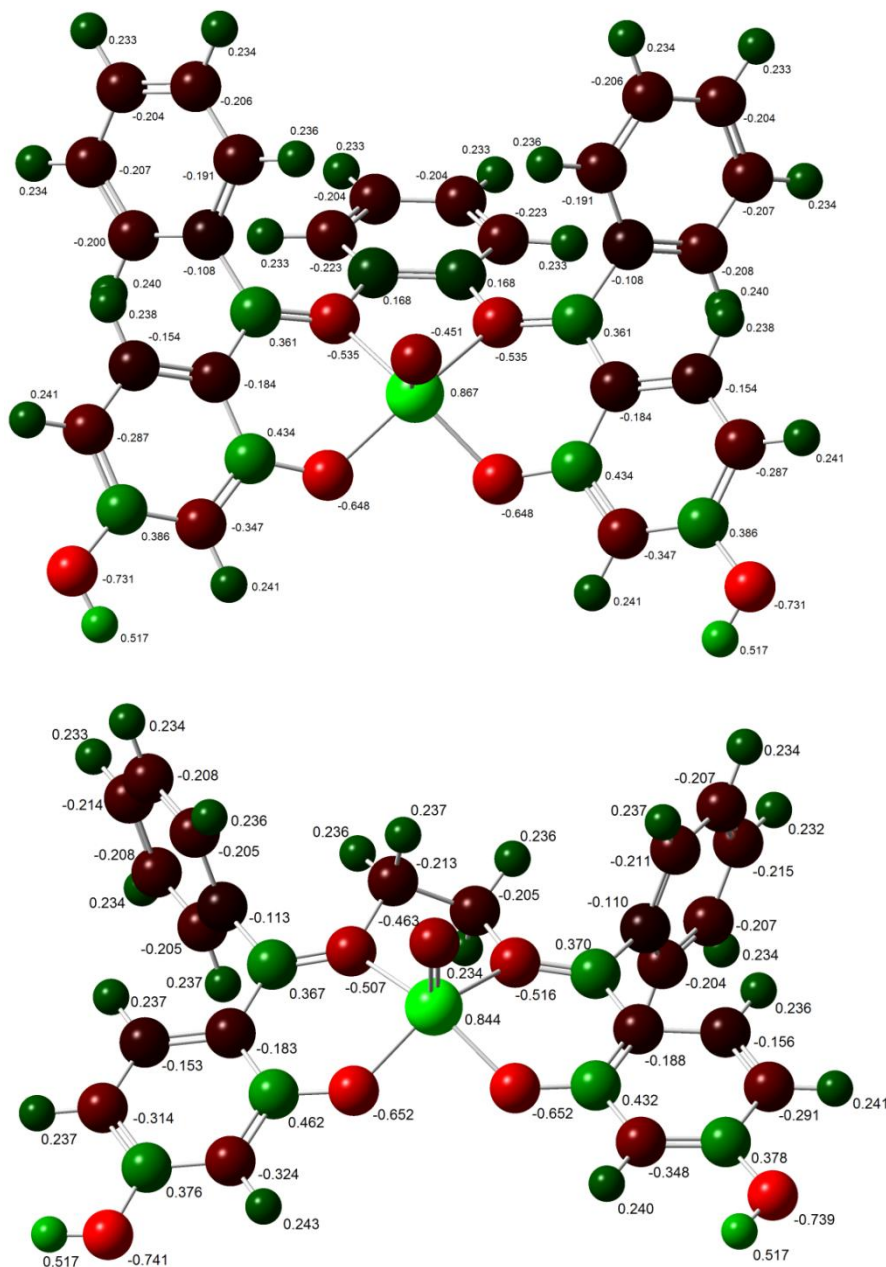
For the alkyl-bridged complexes, the slight differences in positive charge on the vanadium atoms can only be caused by the alkyl bridges, as all other regions between the complexes are conserved. Furthermore, the only regions of the ligands that interact with the vanadium are the donor atoms, *viz.* the imine N atoms, and the phenoxide O atoms. It can be seen from Table 6.8, that the charge distribution over the phenoxide donors is relatively the same. It is the N atoms that show the most difference between charge distribution. The values between them are too small, however, to determine a definite trend between the donor and vanadium charge distribution.

For [VO(L1)], with its aromatic bridging group, the positive charge on the vanadium is higher than for the other complexes. Also, the negative charge predicted to be localised on the imine N atoms is higher as well. Bonding is therefore calculated to be stronger for this fully aromatic complex than for the alkyl-derivatives. The higher positive charge on vanadium for this complex also implies a superior ability to coordinate nucleophiles to the vacant, axial position.

The most negatively charged atoms are the phenol O atoms, except for [VO(L4)], where the most negatively charged atom is the hydroxyl O atom. However, for the latter, the phenol O atoms are also very strongly, negatively charged. Considering the already well-known, weakly acidic nature of aromatic alcohols, these phenol groups would most likely be readily deprotonated in the presence of a suitable base.

Table 6.8: Selected calculated values for charge distribution in the oxovanadium complexes.

Compound	Highest positive charge		Highest negative charge		Average charge for:	
	Value	Assignment	Value	Assignment	Phenoxides	Imine N
[VO(L1)]	0.867	V	-0.731	Ar-OH	-0.648	-0.535
[VO(L2)]	0.844	V	-0.741	Ar-OH	-0.652	-0.512
[VO(L3)]	0.843	V	-0.742	Ar-OH	-0.652	-0.510
[VO(L4)]	0.845	V	-0.825	Alkyl-OH	-0.650	-0.520
[VO(L5)]	0.848	V	-0.741	Ar-OH	-0.651	-0.512

**Figure 6.20:** Atomic charge distribution for the complexes [VO(L1)] (top) and [VO(L2)] (bottom). Charge is displayed fractionally, and correlated to colour – green being positive and red, negative.

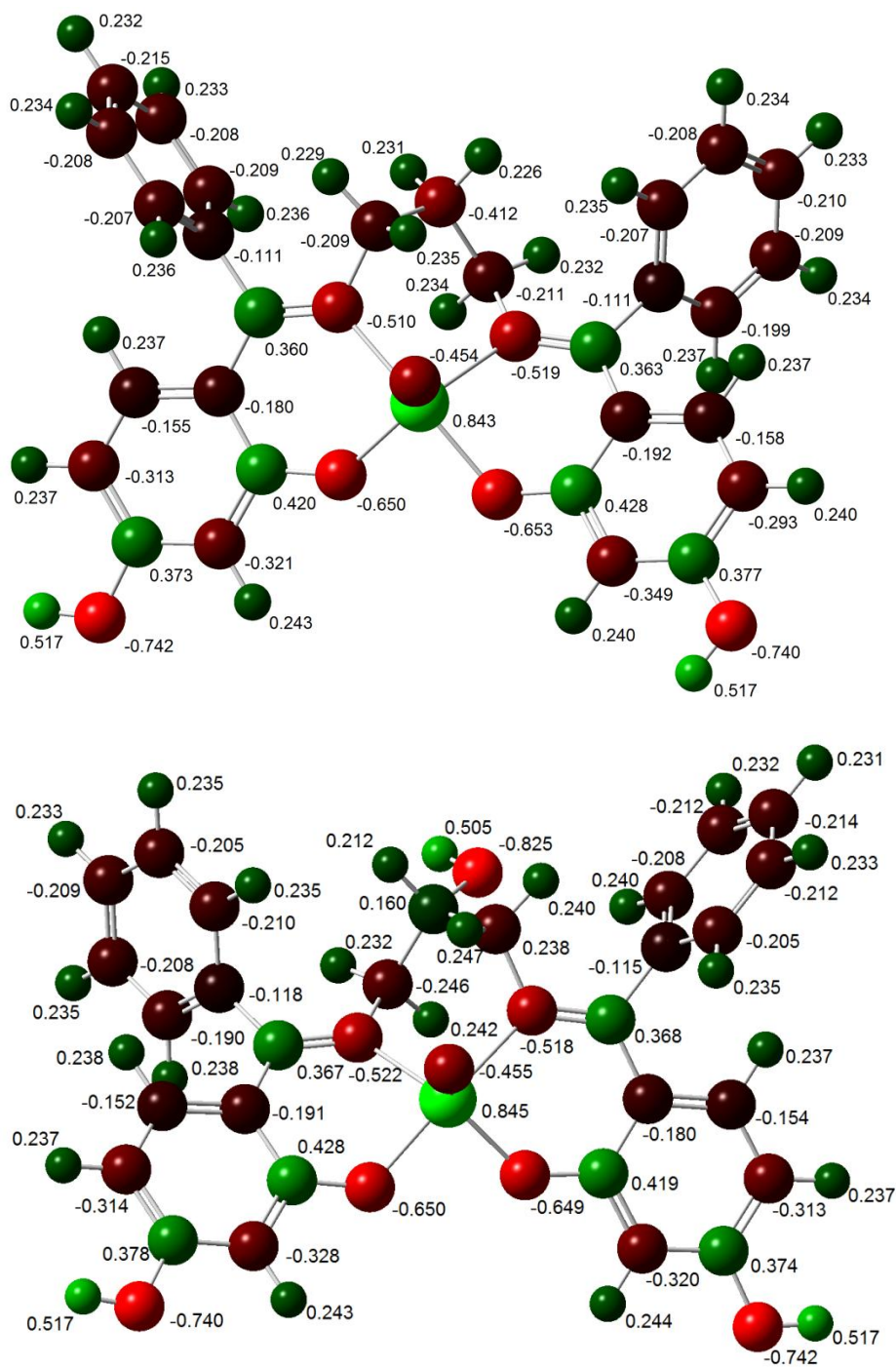


Figure 6.21: Natural atomic distribution over the complexes $[VO(L3)]$ (top) and $[VO(L4)]$ (bottom). Values shown for the charge are fractions, rather than integers, and the charge is correlated to colour – green being positive and red, negative.

stretching frequency. The percentage difference was calculated for each pair of experimental and calculated data; the results of which are presented in Table 6.9. The least amount of discord between theory and experiment are for the imine vibrations, as their percentage differences* are very low; never exceeding -2.5%. The average deviation for all three of the groups used as markers is -1.5%, -8.5% and -8.6% for the C=N, Ar-OH and V=O vibrational frequencies, respectively. Thus, the DFT-calculations gave frequencies that were in almost every instance higher than actually observed, and thus over-estimated the energy, or strength, of the selected bonds. The overlay of the theoretical and experimental spectra for each complex is given in Appendix C.

Table 6.9: Selected calculated and experimental vibrational frequencies for the oxovanadium(IV) Schiff base complexes, and the percentage difference* between the two values.

Vibrational Group	[VO(L1)]			[VO(L2)]		
	exp.	calc.	% Diff.	exp.	calc.	% Diff.
C=N	1515	1538	-1.52	1526	1563	-2.42
Ar-OH	3417	3661	-7.14	3377	3704	-9.68
V=O	962	1058	-9.98	981	1063	-8.36
Vibrational Group	[VO(L3)]			[VO(L4)]		
	exp.	calc.	% Diff.	exp.	calc.	% Diff.
C=N	1568	1566	0.13	1537	1563	-1.69
Ar-OH	3416	3701	-8.34	3394	3706	-9.19
V=O	979	1061	-8.38	982	1060	-7.94
Vibrational Group	[VO(L5)]					
	exp.	calc.	% Diff.			
C=N	1534	1572	-2.48			
Ar-OH	3419	3702	-8.28			
V=O	976	1057	-8.30			

*Percentage difference (% Diff.) calculated as $\% Diff. = \left(\frac{Exp - Calc.}{Exp.} \right) \times 100\%$.

There is very little reference to the vibrational frequency results of DFT calculations for vanadyl complexes in most publications, where they are generally used only to check the geometry optimisation results. However, vibrational frequency results, when given, have been reported to correlate very well with the experimentally determined IR spectra at the B3LYP/6-31G and LANL2DZ level of theory (here, the 6-31G basis set is applied to the ligand, and the LANL2DZ basis set is applied to the vanadium atom). The correlation coefficient was as high as 0.991 for certain groups.¹⁴⁵

6.4.4 Electronic transition calculations for the vanadium(IV) complexes

Electronic absorption spectra were simulated for the V(IV) complexes, not so much as a means to predict their spectra, but rather to gain insight into which orbitals were involved in the transitions. Calculations were performed using the TD-SCF method solving for twelve excited states. The level of theory used was the same as for the geometry optimisations, namely, the B3LYP/LANL2DZ level of theory. The fact that the LANL2DZ basis set simplifies calculations by using an effective core potential for the core electrons should not affect the results, as these electrons are not involved in electronic transitions.

*Percentage differences represent the amount by which a calculated value is over- or under-estimated from the experimentally determined one.

The results obtained *in silico* were compared to the experimentally determined UV-vis spectra of the complexes; the calculated and experimental data for selected peaks for all the complexes are summarized in Table 6.10. In general, there was good agreement in the line shape of the spectra between the calculated and experimental absorption envelopes. Each peak in the spectrum is the result of several electronic transitions arising from different molecular orbitals with similar transition energies. These orbitals may have either π or σ character. However, of all the transitions calculated, all of the major transitions were of the $\pi \rightarrow \pi^*$ nature. This reflects the highly conjugated nature of the complexes, which involves ligand π orbitals, which appear to be delocalised over the vanadium's d orbitals as well. The HOMO and LUMO for each complex is shown in Figure 6.23 and 6.24; although the transitions are not only between these MOs, they do show the same character, and similar distribution to the other orbitals involved in the transitions.

Table 6.10: Selected calculated and experimentally determined electronic absorption peaks for the oxovanadium(IV) Schiff base complexes. The orbitals most responsible for this transition, their hybridisation character and oscillator strength are also given.

Complex	Absorption wavelength / nm		Molecular orbitals of strongest transition	Character	Oscillator Strength
	Exp.	Calc.			
[VO(L1)]	289	397	HOMO-4 \rightarrow LUMO+1	$\pi \rightarrow \pi^*$	0.0917
		405	HOMO \rightarrow LUMO+1	$\pi \rightarrow \pi^*$	0.1174
	324	459	HOMO-2 \rightarrow LUMO	$\pi \rightarrow \pi^*$	0.2751
[VO(L2)]	302	347	HOMO-4 \rightarrow LUMO	$\pi \rightarrow \pi^*$	0.1242
		351	HOMO-2 \rightarrow LUMO	$\pi \rightarrow \pi^*$	0.0474
	322	381	HOMO-3 \rightarrow LUMO	$\pi \rightarrow \pi^*$	0.0307
[VO(L3)]	283	354	HOMO-2 \rightarrow LUMO	$\pi \rightarrow \pi^*$	0.0485
		369	HOMO-4 \rightarrow LUMO	$\pi \rightarrow \pi^*$	0.0352
	308	357	HOMO-4 \rightarrow LUMO	$\pi \rightarrow \pi^*$	0.0275
[VO(L4)]	320	356	HOMO-3 \rightarrow LUMO	$\pi \rightarrow \pi^*$	0.0542
		372	HOMO-4 \rightarrow LUMO+1	$\pi \rightarrow \pi^*$	0.0284
[VO(L5)]	270	356	HOMO-4 \rightarrow LUMO+1	$\pi \rightarrow \pi^*$	0.0587
		374	HOMO-2 \rightarrow LUMO+2	$\pi \rightarrow \pi^*$	0.0333
	324	365	HOMO-4 \rightarrow LUMO	$\pi \rightarrow \pi^*$	0.0244

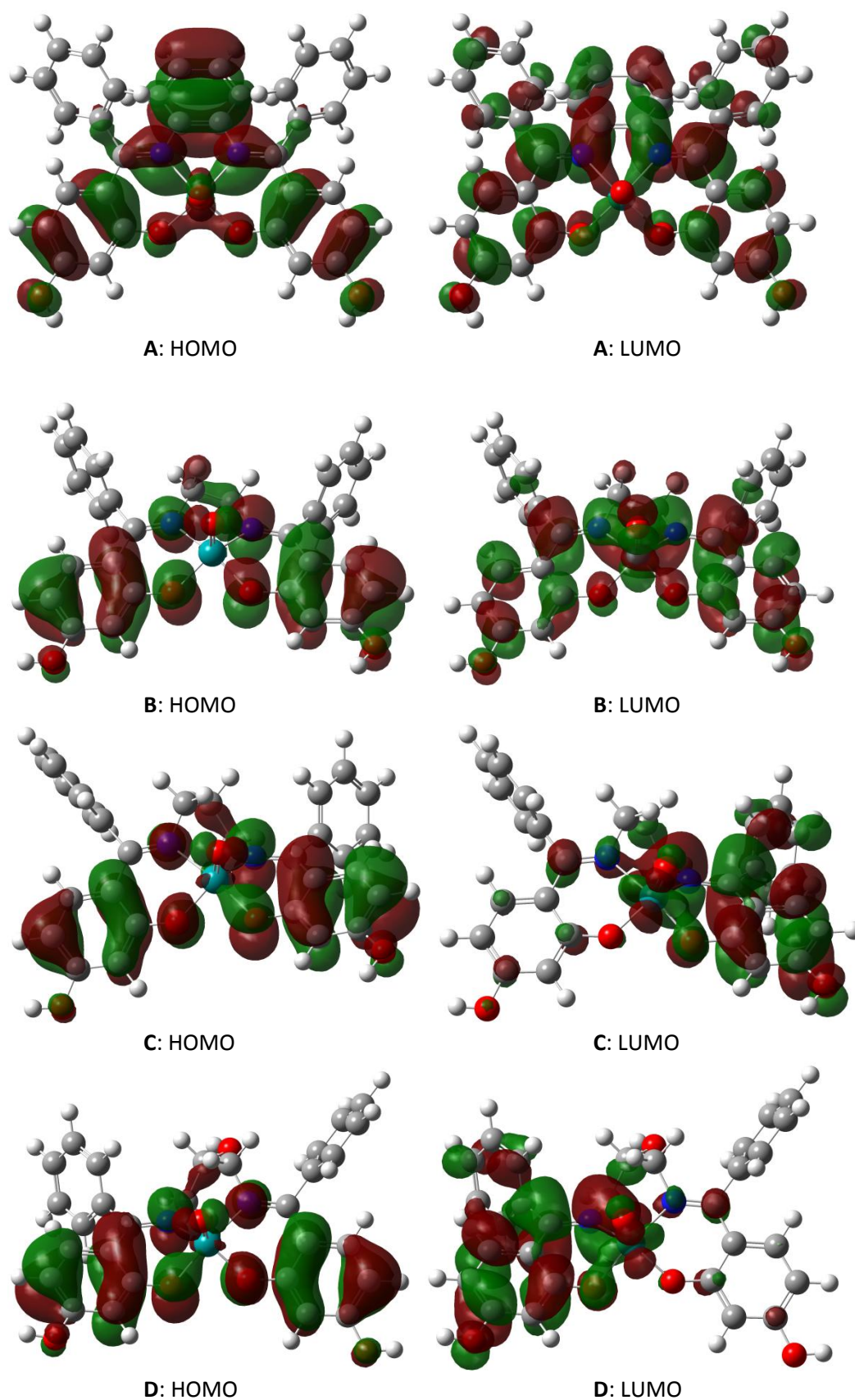


Figure 6.23: DFT calculated HOMO and LUMO for the complexes: **A**, ([VO(L1)]); **B**, ([VO(L2)]); **C**, ([VO(L3)]) and **D**, ([VO(L4)]) The extensive, conjugated π character on each complex can be clearly seen in these diagrams.

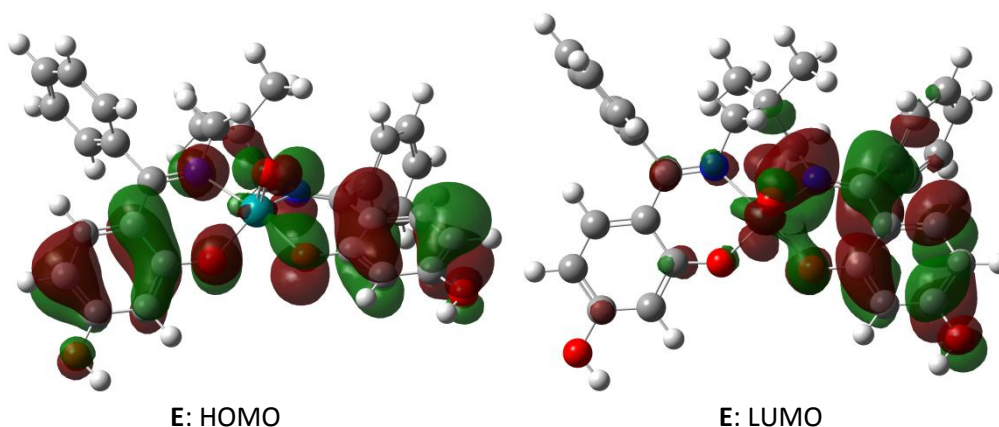


Figure 6.24: DFT calculated HOMO and LUMO for the oxovanadium(IV) complex [VO(L5)], (E). The conjugated system responsible for the strong $\pi \rightarrow \pi^*$ transitions can be clearly seen in this diagram.

As mentioned, the line shape of the predicted spectra matches that of the experimental spectra reasonably well. An overlay of the predicted and experimental spectra for [VO(L2)] is shown in Figure 6.25 as an example of the typical result. What can also be seen in the overlay of the spectra is that, although the line shape has been well-predicted, the energy of these peaks has been underestimated in every instance. Furthermore, the minor bands present as shoulders on the experimental absorption envelope are absent from the calculated spectrum. From the point of view of consistency, these results are very good, as other DFT studies using the B3LYP/6-31G and LANL2DZ levels of theory have predicted spectra where transitions are both over and underestimated for the same complex.¹⁴⁵

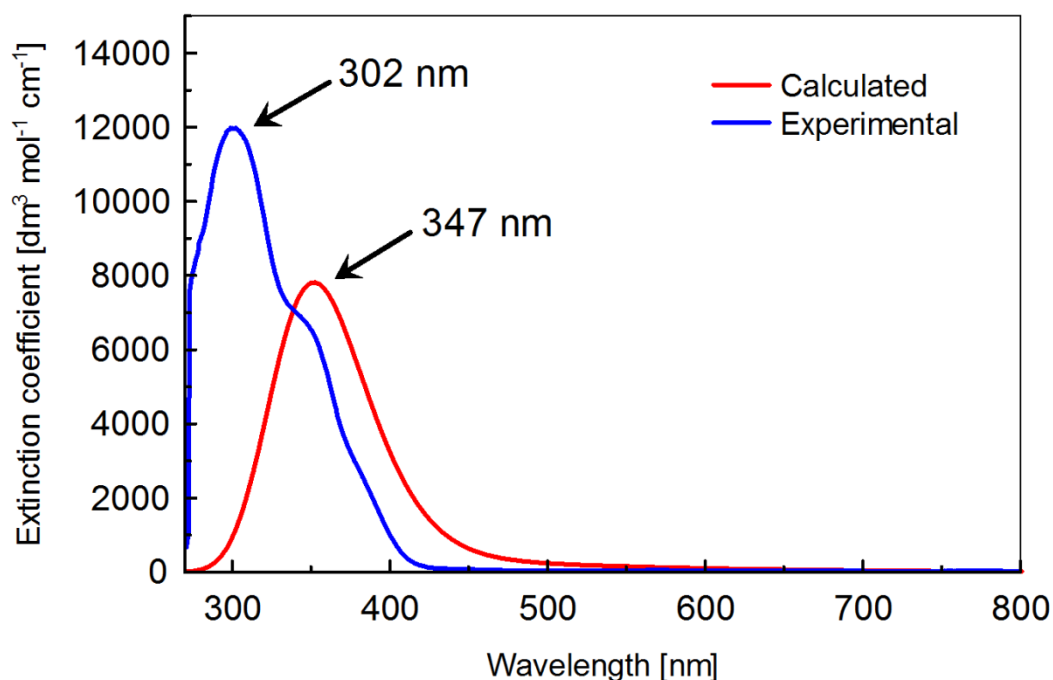


Figure 6.25: Overlay of the simulated and experimentally determined UV-Visible spectra for [VO(L2)] to show similarities in line shape, and differences in predicted absorption peaks.

6.5 Summary and Conclusions

Geometry optimisations at the B3LYP/6-311G (d,p) level of theory for the ligands, whose structures had not been solved by XRD, displayed similar geometry to **H₂L5**, whose structure had been solved by XRD. The reasonable agreement between the experimental and computational structures for **H₂L5** and the similarity between the calculated ligand structures, suggests the structures predicted are approximately the same as would be found experimentally. The optimised geometries for the complexes at the B3LYP/LANL2DZ predicted the vanadium centres to have a pseudo-square-pyramidal coordination geometry. This is typical for vanadium-salen type complexes, and is most likely correct here.¹¹⁴

Natural bond orbital analysis showed that the most negatively charged atoms for the ligands were the iminium N and phenoxide O atoms. This suggests that they are suitable for binding strongly to a positively charged metal centre. For the complexes, the vanadium atom was always the most positively charged. The vanadium is thus suitably electrophilic to undergo attack from a nucleophile, like peroxide.

The predicted IR spectra compared well in line shape to the experimentally determined ones. Correlation for the ligands was poor, though, for the prominent heteroatom-H stretching frequencies, being largely overestimated. It is likely that this occurs because H-bonding has not been taken into account. H-bonding would definitely be occurring in the solid state, and would result in the bond strength being significantly lowered. Correlation between theory and experiment was much better for the complexes.

Electronic transitions calculated *via* TD-SCF DFT calculations correctly predicted the line shape, and number of major transitions; however the wavelength was always overestimated. For the ligands, the overestimation was from as little as 2 to 90 nm, while for the complexes, the deviation ranged from 36 to 135 nm. Additionally, the intensity was overestimated for the ligands and generally underestimated for the complexes – sometimes severely so. Transitions could be ascribed to $\pi \rightarrow \pi^*$ molecular orbitals for all complexes and metal-free Schiff bases. All compounds showed extensive conjugation of the π orbitals over their structures, and for the complexes, involved mixing of the metal and ligand orbitals.

Chemical shifts calculated for the ligands showed generally poor correlation to the experimental spectra, although the ¹³C shifts were significantly better than the ¹H shifts. This most likely has more to do with the choice of protons and carbon atoms used to compare the results though. The far, up-field shift of the iminium H⁺ was correctly predicted, however, and provides further support that this zwitterionic species exists in solution as well as in the solid state.

Chapter 7 | *In Vitro* anticancer activity

7.1 Cell lines used

In the previous chapters, various physical, chemical and spectroscopic properties of the complexes were studied to assess their potential as therapeutic agents for cancer. In particular, establishing that the complexes could bind peroxide was seen as favourable grounds to proceed with biological testing, as this is often perceived as crucial to a vanadium compound's biological efficacy.

It is important, when evaluating a compound's anticancer activity, to screen the compound against as wide a range of cell lines as possible. For these initial trials, four cancer cell lines were used, *viz.*: A549, HT29, TK-10 and U251. A549 is a non-small lung cancerous cell line, and a cancer stem cell (CSC).¹⁴⁶ In addition to their CSC nature, they have increased tumour-initiation ability, and therefore pose a serious threat to cancer relapse. HT29 is a human colon adenocarcinoma cell line, and is also a CSC. Like A549, it has increased tumour-initiation ability, but also possesses increased invasion ability.¹⁴⁶ TK-10 is a human renal adenocarcinoma cell line, and U251 is a central nervous system cancerous cell line. This small selection of cells, therefore, offers a broad representation of different cancer cell-lines.

The cytotoxic effect of a compound is measured in terms of its IC_{50} value. The term IC_{50} is an acronym for the inhibitory concentration 50 %, or in other words, the concentration of compound required to inhibit the growth of 50 % of the cell culture in question. A graphical representation of the IC_{50} value is shown in Figure 7.1. Therefore, the lower this value, the more effective the compound is in preventing cell growth, through whatever mechanism it may be acting. Very often, these values are presented as negative logarithms of the actual values. This simplifies presentation and interpretation of data, as compounds with higher $-\log(IC_{50})$ values, have a higher activity. The magnitude of their effectiveness can also be readily compared. All data pertaining to the compounds evaluated, and the agents to which they are compared, are presented as $-\log(IC_{50})$ values.

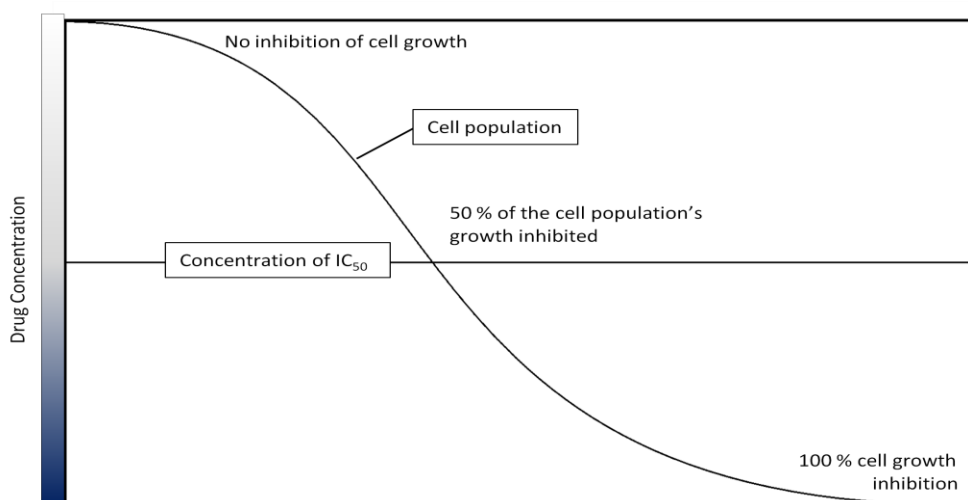


Figure 7.1: Typical growth/inhibition curve for determining the IC_{50} value of a compound. Concentration is plotted against the total cell population relative to a control population. The concentration at which 50 % of the cell population has been prevented from growing is determined to be the IC_{50} value of the compound in question.

7.2 Cell culture and drug assay method

Screening of the vanadyl complexes was performed by the Advanced Materials Division of Mintek, South Africa. Tumour cells were trypsinised on the first day and distributed in a flat-bottomed, 96 well plate, where they were left to adhere overnight. The final concentration of cells was 2×10^5 cells mL^{-1} . On the second day, solutions containing the vanadyl complexes were administered at a final concentration of 50 μM per well, with subsequent serial dilutions to give a total of eight different concentrations of compound per cell line. After incubating for 72 hours after compound administration, MTS (Celltiter One Solution, Promega, USA) was added, and a reading taken after a strong colour change was observed. Each concentration of compound administered was done in triplicate, and the experiment was repeated four times. Sigmoidal curves were fitted to the results using Origin 6.1 software, and the IC_{50} values were determined from these fitted curves.

7.3 Results and discussion

7.3.1 Activity of oxovanadium(IV) Schiff base complexes

The *in vitro* anticancer properties of the oxovanadium(IV) Schiff base complexes, as well as the contrasting agent $\text{Au}(\text{dppe})_2\text{Cl}$, are given in Table 7.1; results for cisplatin obtained from the National Cancer Institute (NCI) are supplied for comparison as well.¹⁴⁷ From these results, it can be seen that the oxovanadium complexes show generally high activity against the cancerous cell lines A549, TK-10 and U251. However, for the cell line HT29, most of the compounds showed a negligible impact on cell growth. The only exception to this was $[\text{VO}(\text{L1})]$, which demonstrated activity comparable to many other standard chemotherapeutic agents (comparable compounds are given in Section 7.3.2). The effects of the compounds on the A549, TK-10 and U251 cell lines will be considered further. A graphic representation of the activities of the oxovanadium(IV) complexes, $[\text{Au}(\text{dppe})_2]\text{Cl}$ and cisplatin is given in Figure 7.2.

For the A549 cell line, all vanadium compounds tested showed very high activity, comparable to, and in the case of $[\text{VO}(\text{L4})]$, exceeding the activity of cisplatin. The compounds $[\text{VO}(\text{L2})]$ and $[\text{VO}(\text{L3})]$ displayed very similar activities to each other, which were both slightly lower than that seen for cisplatin. $[\text{VO}(\text{L5})]$ and $[\text{VO}(\text{L1})]$ had the lowest and second lowest $-\log(\text{IC}_{50})$ values of all the vanadium complexes tested against the A549 cell line respectively. Nevertheless, they were still more effective than many standard agents currently employed in the treatment of cancer.

For the renal adenocarcinoma cell line TK-10, the only compound that displayed negligible activity was $[\text{VO}(\text{L5})]$. All others tested showed excellent inhibitory activity, although none were as effective as cisplatin; $[\text{VO}(\text{L4})]$ did however come close to this activity, with a $-\log(\text{IC}_{50})$ value of 5.499 compared to 5.602 for cisplatin. $[\text{VO}(\text{L4})]$'s activity is almost a full order of magnitude greater than that of the compounds $[\text{VO}(\text{L1})]$ and $[\text{VO}(\text{L2})]$, and about half an order of magnitude greater than that of $[\text{VO}(\text{L3})]$.

The vanadium compounds had a significant effect on the central-nervous system cell line U251, although on average it was slightly lower than the activity displayed against the A549 and TK-10 cell lines. Yet again, the agent with the most potent activity was $[\text{VO}(\text{L4})]$, which showed a $-\log(\text{IC}_{50})$ value only slightly lower than that of cisplatin. There is a remarkable consistency between the vanadium complexes, all of them having $-\log(\text{IC}_{50})$ values of approximately 4.5. Even though a higher

concentration of drug is needed for the latter complexes, their activity is still comparable, or superior, to that of many standard anticancer agents.

The compounds tested then, all show very good anticancer activity in general for the cell lines A549, TK-10 and U251. The complex [VO(L4)] was the most effective one tested against these cell lines. The lack of activity shown against the HT29 cell line suggests potential mechanistic differences between the [VO(L1)] and the other compounds, which, given its unique structure compared to the other complexes, is a likely option. Further testing of these complexes against additional cancerous cell lines is necessary to accurately determine if this is the case though. The lack of activity against HT29 for the other complexes is encouraging though, because it is preferable that a drug administered has an effect only on the diseased cells. This would limit the potential side-effects associated with chemotherapy. The fact that HT29 is a colon cancer cell line suggests that the compounds may have no detrimental effect on intestinal cells in general, potentially opening the door to orally administered chemotherapy. Of course, these are only preliminary results, and many further tests would be necessary to determine if this is a viable option at all.

It is important to note that only the complexes have so far been screened, and not the free ligands. Whether or not the above activity is due solely, or at least partially, to the presence of the vanadyl unit cannot be stated with certainty until the ligands are screened by themselves. Only the A549 cell line has been screened previously with VO_4 , which did show very low inhibitory effects.¹⁴⁸ The assay performed here then, was only a preliminary one to assess the cytotoxic potential of the complexes; hence the apparent omission of the ligands. However, because the complexes show such promising anticancer potential, further assays including the ligands and free metal salts are now justifiable.

Table 7.1: Negative logarithms of the IC_{50} (M) values for the oxovanadium(IV) complexes and the contrasting agents $[\text{Au}(\text{dppe})_2]\text{Cl}$ and cisplatin, on the cancerous cell lines A549, HT29, TK-10 and U251. (NA = not active).

Compound	$-\log(\text{IC}_{50})$ [M] (std.dev.)	
	A549	HT29
[VO(L1)]	4.949	4.459
[VO(L2)]	5.216	NA
[VO(L3)]	5.272	NA
[VO(L4)]	5.971	NA
[VO(L5)]	4.876	NA
$[\text{Au}(\text{dppe})_2]\text{Cl}$	6.504	5.42
cisplatin	5.602	5.602

Compound	$-\log(\text{IC}_{50})$ [M] (std.dev.)	
	TK-10	U251
[VO(L1)]	4.495	4.603
[VO(L2)]	4.565	4.458
[VO(L3)]	4.906	4.448
[VO(L4)]	5.499	5.232
[VO(L5)]	NA	4.499
$[\text{Au}(\text{dppe})_2]\text{Cl}$	6.241	6.606
cisplatin	5.602	5.602

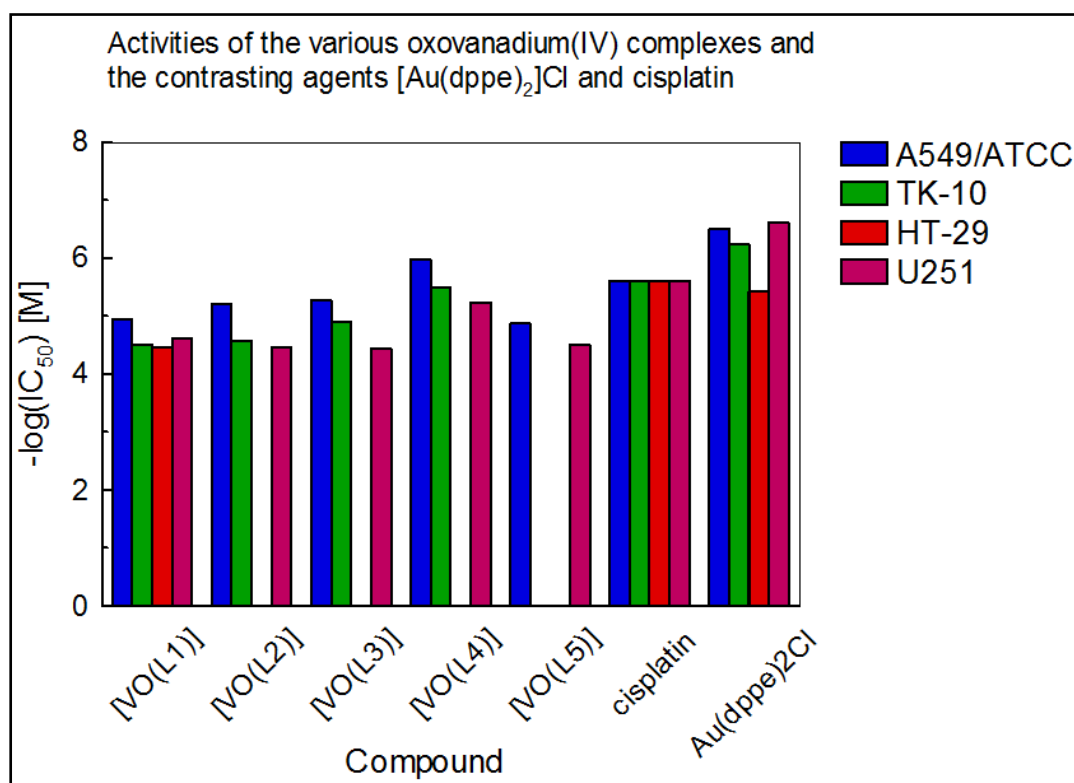


Figure 7.2: Bar graph of the tested compounds and their contrasting agents showing the negative logarithm of the concentration of the compounds required to inhibit 50 % of the cell population's growth for the cancer cell lines A549 (blue), TK-10 (green), HT29 (red) and U251 (purple).

7.3.2 Comparable compounds

The vanadyl complexes all showed generally good anticancer activity against the cell lines tested, with $-\log(\text{IC}_{50})$ values of approximately 4.5 to 5.5. Prior to elucidating their mode of action through various assays or experiments, it is preferable to compare their anticancer activity with other anticancer compounds whose modes of action are known. Therefore, a comparison of all listed compounds of the NCI's "standard agents" list¹⁴⁵ was made for compounds having similar activity towards the cell lines tested, when administered at a final concentration of ca. 50 μM .

Of a total of seven compounds with comparable activity to the vanadyl compounds, five are derivatives of doxorubicin; the other two are bisantrene hydrochloride and methotrexate. Structures of these compounds are shown in Table 7.2, while their activities against the cell lines A549, HT29, TK-10 and U251 are shown graphically in Figure 7.3. Although the similarities in activities between the vanadyl complexes and these standard agents (SAs) could be simply a coincidence, it is interesting that the SAs are largely from the same family, or share similar modes-of-action. Interestingly, bisantrene hydrochloride, although not from the doxorubicin family, operates by the same mode-of-action as these doxorubicin derivatives.

The doxorubicin-family of compounds exerts their cytotoxic effects by intercalation of the DNA molecule, and inhibition of the enzyme Topoisomerase II (Topo II). Inhibition of Topo II occurs after the enzyme has created a single strand break in the DNA. Thus, DNA replication is prevented, along with cell growth. The aromatic anthracycline group of these compounds is responsible for the actual

intercalation between the DNA base-pairs, while the sugar groups interact with adjacent base pairs in the minor groove.

Although the vanadyl complexes may not be intercalating DNA or inhibiting Topo II, there is good reason to believe that they are interacting with DNA and causing breaks in the DNA chain – the same effect the doxorubicin compounds have. It has been shown that vanadyl complexes of hydroxyl-salen derivatives are capable of interacting with DNA and causing strand cleavage.⁴³ The cleavage of DNA occurred *via* a vanadium-mediated redox process, with a radical mechanism and H_2O_2 as a substrate. The pathway involved oxidation of a DNA base, deglycosylation and elimination of phosphate, to produce strand breaks predominantly at the guanosine-containing regions. It was this result that prompted the inclusion of hydroxyl groups on the vanadyl complexes of this study, in order to facilitate interaction with DNA; hence, it would not be surprising if the cytotoxic properties of the vanadyl compounds were due to their interactions with DNA.

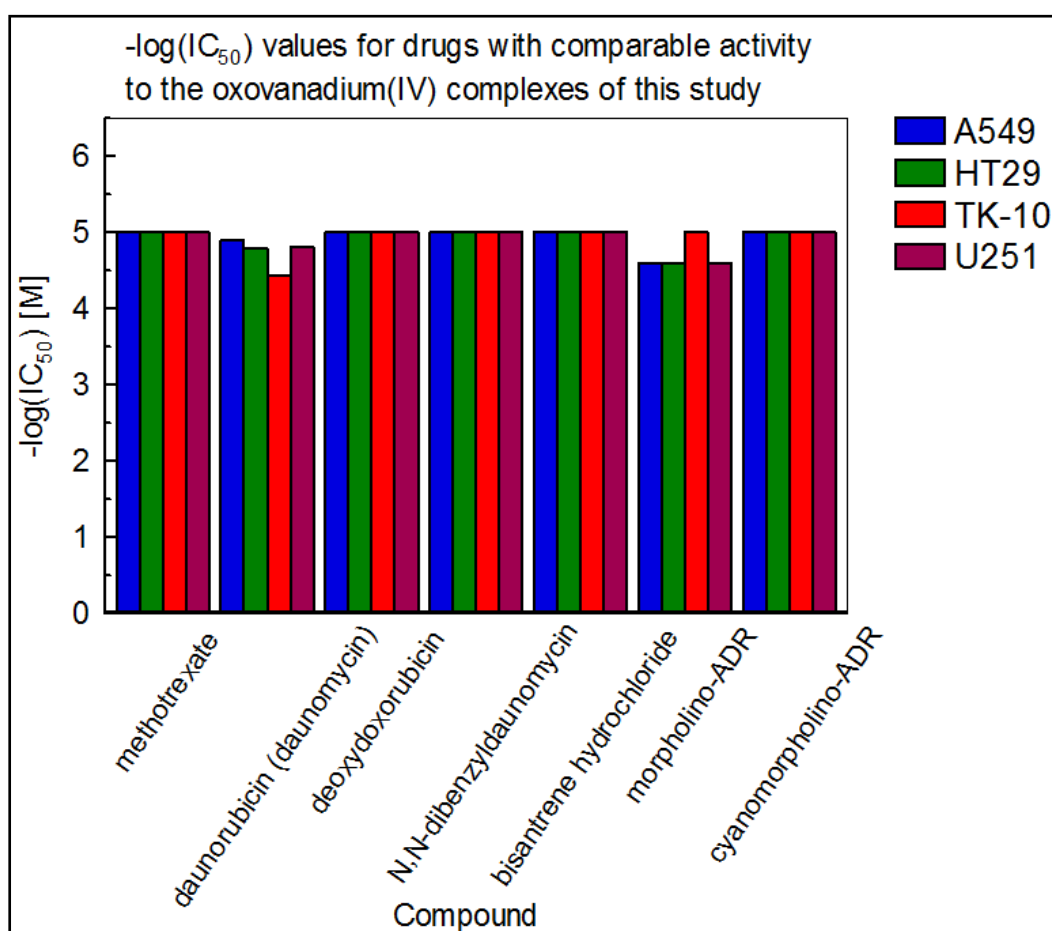
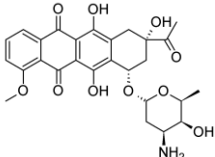
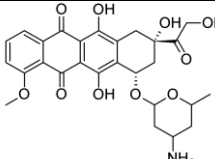
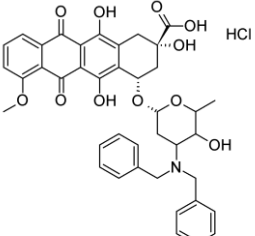
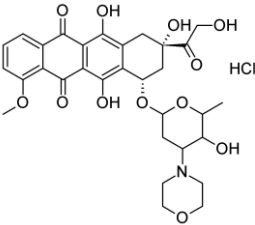
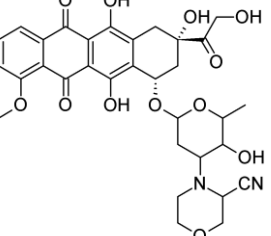
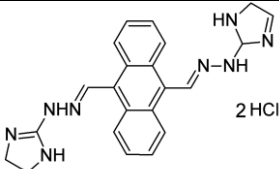
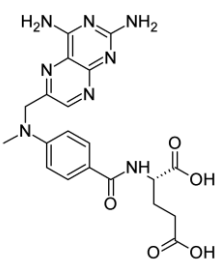


Figure 7.3: $-\log(IC_{50})$ values for selected standard agents for the cancerous cell lines A549, HT29, TK-10 and U251. Agents shown are those that displayed cytotoxicity comparable to the oxovanadium(IV) complexes at a final concentration of *ca* 50 μ M.

Table 7.2: Standard anticancer agents that had comparable activity to the vanadyl complexes for the tumour cell lines A549, HT29, TK-10 and U251. The structure of each, and their mode of cytotoxicity are shown (continued on following page).

		<u>Daunorubicin</u>		
Cytotoxicity ($-\log(\text{IC}_{50})$)		Structure		Mode of Action
A549	4.903			Intercalator: Topoisomerase II inhibitor
HT29	4.792			
TK-10	4.439			
U251	4.807			
		<u>Deoxydoxorubicin</u>		
Cytotoxicity ($-\log(\text{IC}_{50})$)		Structure		Mode of Action
A549	5			Intercalator: Topoisomerase II inhibitor
HT29	5			
TK-10	5			
U251	5			
		<u>N,N-dibenzyl-daunomycin</u>		
Cytotoxicity ($-\log(\text{IC}_{50})$)		Structure		Mode of Action
A549	5			Intercalator: Topoisomerase II inhibitor
HT29	5			
TK-10	5			
U251	5			
		<u>Morpholino-ADR</u>		
Cytotoxicity ($-\log(\text{IC}_{50})$)		Structure		Mode of Action
A549	4.602			Intercalator: Topoisomerase II inhibitor
HT29	4.602			
TK-10	5			
U251	4.602			
		<u>Cyanomorpholino-ADR</u>		
Cytotoxicity ($-\log(\text{IC}_{50})$)		Structure		Mode of Action
A549	5			Intercalator: Topoisomerase II inhibitor
HT29	5			
TK-10	5			
U251	5			

		<u>Bisantrene hydrochloride</u>		
Cytotoxicity ($-\log(\text{IC}_{50})$)		Structure		Mode of Action
A549	5			Intercalator: Topoisomerase II inhibitor
HT29	5			
TK-10	5			
U251	5			
		<u>Methotrexate</u>		
Cytotoxicity ($-\log(\text{IC}_{50})$)		Structure		Mode of Action
A549	5			Competitive inhibitor: Folic acid metabolism
HT29	5			
TK-10	5			
U251	5			

7.4 Conclusions

The oxovanadium(IV) Schiff base complexes [VO(L1)], [VO(L2)], [VO(L3)], [VO(L4)] and [VO(L5)] were screened against the tumour cell lines A549, HT29, TK-10 and U251. The cytotoxic effect of the complexes was highly dependent on the cell line screened. For the A549 cell line, all complexes exhibited a high level of potency, with $-\log(\text{IC}_{50})$ values ranging from *ca* 4.8 up to 5.9. HT29, conversely, was resistant to all vanadyl compounds, except for [VO(L1)], which had an $-\log(\text{IC}_{50})$ value of *ca* 4.5. All compounds, except for [VO(L5)], were active against TK-10; their $-\log(\text{IC}_{50})$ values were between 4.5 and 5.5, approximately. The U251 cell line was sensitive to all compounds tested, although not as strongly as were A549 and TK-10 cell lines. $-\log(\text{IC}_{50})$ values for this line were between *ca* 4.5 and 5.2. The complex [VO(L4)] was the most cytotoxic species in all instances, except for the HT29 tumour cells, where it was inactive. The relatively high $-\log(\text{IC}_{50})$ values justify the screening of the free ligands to assess whether or not the cytotoxic effect is due to the presence of the vanadyl unit.

Comparison of the activities of the vanadyl complexes to that of standard anticancer agents showed similarity between them and the doxorubicin class of compounds, as well as bisantrene hydrochloride and methotrexate. Apart from methotrexate, all the comparable standard agents are intercalators that disrupt the DNA double helix and inhibit Topoisomerase II to produce single-stranded breaks in the DNA. Given this coincidence, it is speculated that the complexes interact with the DNA to induce strand cleavage. The most likely mechanism for this process is a vanadium-centred radical process, using H_2O_2 as a substrate. However, further screening against different cell lines, as well as tests to determine their biological targets are required to fully determine their mode of action.

Chapter 8 | *Conclusions and Future Work*

8.1 Conclusions

The main objectives of this study, namely, the synthesis of novel Schiff-base ligands and their oxovanadium(IV) chelates, and their characterisation through various physical and spectroscopic means was accomplished. Additionally, their ability to coordinate H₂O₂ was successfully evaluated. This work culminated in preliminary studies of their cytotoxic properties against a small selection of human cancer cell lines.

Synthesis for most ligands was readily achieved by refluxing the starting materials in the appropriate molar ratio; the desired products were sparingly soluble in methanol, and could be filtered off from the mother liquor in high purity. No further purification was required. The ligands are very robust; all of them having high decomposition temperatures above 200 – 300 °C. The crystal structure of the ligand **H₂L5** was solved using X-ray diffraction, and showed the somewhat unusual property of being a zwitterion. The chemical shift for the iminium proton is located very far up-field, at *ca* 15 ppm. The other ligands also show a single proton shift at *ca* 15 ppm, and it therefore plausible that the other ligands are also zwitterions.

Chelation of vanadium by the ligands was complicated by the ligands' poor solubility, which required the use of high-boiling point solvents, such as DMSO. The result of this was poor yields. However, an extremely facile synthesis was possible by controlling the pH of an aqueous solution. This afforded the rapid chelation of vanadium (5-10 minutes) in a room temperature solution, with the added advantage of being able to isolate the products in good yields and high purity by simple filtration. The use of water as the only solvent, with the only by-product being sodium hydroxide, means that this chelation can be considered as an environmentally friendly, or "green", chemical reaction.

From the powder EPR spectroscopic results, it was apparent that the complexes possessed axial symmetry. The amount of distortion from the ideal square-pyramidal geometry increased as the length and bulk of the bridging group increased, although by how much the geometry was distorted could not be determined, as the contribution to the A_{\parallel} value from the novel iminium donors is unknown. Isotropic hyperfine coupling constants for the complexes shows the same trend in donor strength as for the anisotropic, powder spectra, however the amount of electron donation from the ligand is less than expected compared to similar vanadyl complexes. This is believed to be a result of the bulky benzyl substituents on the iminium carbon atoms that distort the ligand structure, thus preventing ideal overlap of the atomic orbitals. The g_0 value is higher than that of the free electron value for all complexes investigated, which indicates that the electron is coupling to nearby electrons – possibly those of a solvent molecule. Finally, it was found that deprotonation of the substituent hydroxyl group greatly increased the electron donating strength of the complexes. This phenomenon was explained by induction of additional electron density into the aromatic system by the negatively charged, oxide.

Electronic absorption spectra were dominated by the strong $\pi \rightarrow \pi^*$ bands of the aromatic system. The intensity and energy of these bands was decreased by metal binding. The fully conjugated system showed the least amount of decrease in energy of its $\pi \rightarrow \pi^*$ bands following chelation, compared to those with only partial conjugation, as the aromatic bridging group could contribute the more electron density to the donor atom's aromatic system. The low intensity, energy transfer

reaction occurring at *ca* 550 nm was ascribed to a MLCT process involved the unpaired electron and anti-bonding orbitals on the tetradentate, or oxide, ligands. There were large changes in the energy of these MLCT bands, which was attributed to the ligand field strength of the tetradentate ligand, and the extent of solvent coordination to the vanadium(IV) ion. A larger degree of solvent coordination is believed to cause a lowering of the energy of the MLCT bands. The compound [VO(L4)] appears to coordinate solvent more strongly than the other vanadyl complexes.

NMR spectroscopy was employed to monitor the oxidation of $^{51}\text{V(IV)}$ to $^{51}\text{V(V)}$, and to assess the nature of the vanadium species that were being formed in solution. Despite being paramagnetic, the $^{51}\text{V(IV)}$ nuclei could be observed, albeit poorly, by NMR spectroscopy. This allowed for further confirmation of the amount of electron density being donated to the vanadium centre by each ligand based on how far down-field each $^{51}\text{V(IV)}$ signal was observed. The trend observed for the anisotropic EPR spectra was seen again for the NMR spectra, except for [VO(L5)], which could not be observed by NMR spectroscopy, i.e. the amount of electron donation decreased as the length and bulk of the alkyl bridging group increased, and the aromatic bridging group being superior electron donor compared to the aliphatic one.

In the NMR spectra of a DMSO-d6 solution of the vanadyl complexes, titration with H_2O_2 (6 % w/w) caused the decrease of the original V(IV) peak, and the emergence of two new, unequal V(V) peaks. These new peaks were in the region typically expected for an oxoperoxovanadium(V) compound, and were separated by *ca* 40 ppm. This magnitude of this separation lead to the identification of these two peaks belonging to the protonated and unprotonated forms of the oxoperoxovanadium(V) species. The magnitude of the change in chemical shift from the $^{51}\text{V(IV)}$ to the $^{51}\text{V(V)}$ species gave an indication of the increase in electron donation to the vanadium centre. Interestingly, it was found that the weaker the initial complex was, the greater the gains in covalent character for the vanadium were, with [VO(L4)] showing the greatest increase in covalent character.

A modification of the Evans method for determining bulk magnetic susceptibility by NMR spectroscopy was used to determine if a change in the oxidation state of the vanadium was occurring. A significant shift relative to an internal reference sample was observed for the addition of H_2O_2 to a DMSO-d6 solution of vanadyl complex. The same experiment was performed using NaOH, a known oxidising agent of vanadyl complexes, which gave almost identical results to that of the previous experiment with H_2O_2 , validating the fact that a change in the oxidation state of vanadium for +4 to +5 was responsible for the change in bulk magnetic susceptibility.

To ensure that an oxoperoxovanadium(V) species had formed rather than the peroxide having simply dissociated to form hydroxide, which had oxidised the vanadium(IV), a titration using NaOH was performed for each complex, and monitored by ^{51}V NMR spectroscopy. As for the hydrogen peroxide titration, the small $^{51}\text{V(IV)}$ peak was replaced by a large, sharp peak as NaOH was added, however the chemical shift of this new ^{51}V peak was much further down-field relative to that formed by the addition of H_2O_2 to the same compound.

Density Functional Theory was used to calculate models for a number of features of both the free ligands and the complexes. For the Schiff-base ligands, calculations were performed at the B3LYP/6-311G(d,p) level of theory. The geometry optimisation for **H₂L5** could be compared to the crystallographically solved XRD structure. The RMSD value was not as small as could be desired, however, the general structural features were predicted to within reasonable limits. The geometry

for the remaining ligands was thus optimised at the same level of theory. Analysis of the bond lengths for those atoms involved in intramolecular hydrogen-bonding showed that a zwitterionic conformation was predicted, rather than a keto-amine tautomeric form. Vibrational frequency calculations were run on all the optimised structures, and they yielded no negative eigenvalues; this showed that a true energy minimum had been achieved. The IR spectra predicted by these frequency calculations all had a line-shape that was in close agreement to that observed experimentally, however the energy of the stretching frequencies for the hetero-atoms was very poorly predicted, being largely overestimated. In the solid state, there should be a large amount of hydrogen bonding that would lower the energy of the observed stretching frequencies, which would explain the overestimated energy for the isolated compounds.

A natural bond orbital (NBO) analysis showed that the most negative atoms for each ligand were the nitrogen and oxygen atoms. Their high negative charge suggests that they are the most likely atoms to behave as donors to a positively charged metal centre.

TD-DFT calculations of the electronic transitions predicted UV-Vis absorption spectra with a line shape in good agreement with the experimental ones. The major transitions giving rise to the spectra were ascribed to $\pi \rightarrow \pi^*$ transitions of the aromatic system; the molecular orbitals of which were distributed over large portions of the compounds.

NMR spectra were, in general, poorly predicted, although the ^{13}C NMR spectra showed closer agreement to their experimental counterparts than the ^1H NMR spectra. The iminium proton was, however, very well predicted; having a chemical shift located down-field at *ca* 15 ppm for all compounds. This is good support for the zwitterionic nature of the Schiff-bases.

For the complexes, calculations were performed at the B3LYP/LANL2DZ level theory. Optimised geometries for the complexes predicted a square-pyramidal coordination geometry about the vanadium atom. The amount of distortion increased when moving from a two-carbon, to a three-carbon long bridge, i.e. a change from a 6-5-6 chelate ring conformation to a 6-6-6 one. An increased amount of bulk on the propyl chain also increased the distortion.

NBO analysis showed that the most positively charged atom in each complex was the vanadium atom. This has implications for the peroxide binding, as the nucleophilic peroxide species is most likely to attack the electrophilic vanadium atom.

Vibrational frequency calculations returned no negative eigenvalues, confirming the lowest energy state had been achieved for each of the structurally optimised complexes. The line-shape of the simulated IR spectra showed a good correlation to those determined experimentally.

TD-DFT calculations of the electronic transitions predicted the major transitions as being due to $\pi \rightarrow \pi^*$ excitations. Extensive mixing of the ligand π orbitals with the metal orbitals was also predicted. Overall, the line-shape of the simulated spectra matched closely those observed.

Very promising preliminary results were obtained when screening the compounds against the human carcinoma cell lines A549, HT29, TK-10 and U251, which represented a diverse range of cancer cell lines. A549 was the most sensitive cell line to the inhibitory effects of the compounds, while HT29 was resistant to all vanadyl complexes except for [VO(L1)]. The growth of TK-10 cells, while resistant to the inhibitory effects of [VO(L5)], was inhibited by all other compounds

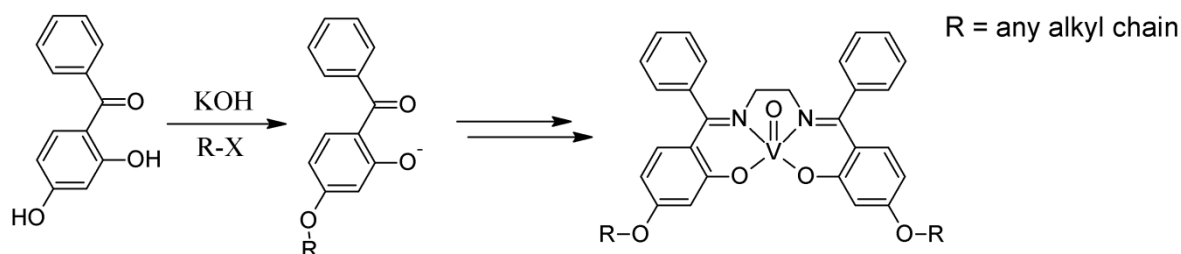
significantly. U251, like A549, was susceptible to all vanadyl complexes tested, although not to the same extent. Of all compounds tested, [VO(L4)] was, in general, the most effective, with a $-\log(\text{IC}_{50})$ between 4.5 and 4.8, which is comparable to, or better than, cisplatin for the cell lines it was screened against. These compounds therefore warrant further investigation as anti-cancer agents.

8.2 Future work

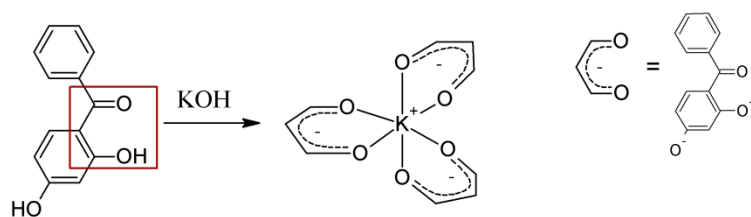
8.2.1 Improving solubility

Perhaps one of the greatest shortcomings of the vanadyl complexes is their limited solubility. This would obviously affect their ability to function in biological environments, where both water solubility and the ability to cross lipid membranes is required. Future synthetic work will focus on making water and/or lipid soluble derivatives of the vanadyl complexes. One way by which this could be readily done is presented here.

Firstly, the mildly acidic hydroxyl group that is not already involved in chelating the vanadium could be alkylated (Scheme 8.1). Using the starting material 2,4-dihydroxybenzophenone, an alkyl chain could be attached by deprotonating at this position with a suitable base, such as KOH, and then adding an alkyl halide.¹⁴⁰ The KOH will deprotonate both alcohols, however the potassium ion would be coordinated by the keto group and oxide at position 2 of the benzyl ring; effectively protecting them from electrophilic attack (Scheme 8.2).



Scheme 8.1: Alkylation of the hydroxyl group at position 4 of 2,4-dihydroxybenzophenone using potassium hydroxide and an alkyl halide to produce a vanadyl complex with enhanced solubility.



Scheme 8.2: Assumed mode of protection for the oxide at position 2 of the substituted benzyl ring is *via* coordination to potassium.

The incorporation of alkyl chains onto the complexes should improve their solubility in organic solvents, and hence their lipid membrane permeability. To test this, the partition coefficient of these complexes for an octanol/water mixture will be determined.

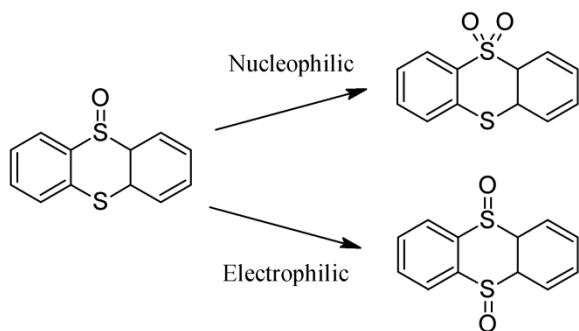
8.2.2 Exploring H_2O_2 -mediated reactions

It was shown how the complexes bound peroxide to form oxoperoxovanadium(V) complexes. The reactivity of this species is yet to be determined, and will be the subject of future research.

Firstly, the reversible nature of the peroxide mediated oxidation and reduction will be monitored by ^{51}V NMR and EPR spectroscopy. This will involve using hydrogen peroxide to oxidise a vanadyl compound, and then using a reducing agent, such as glutathione, to attempt to revert the vanadium(V) species to vanadium(IV). If successful, then the process will be repeated to determine the potential turn-over number of the compound.

Following this, a rhodamine-B assay will be performed to determine whether or not hydroxyl radicals are being formed by the oxidation/reduction process.¹⁴⁹ This is done by monitoring the degradation of the rhodamine-B dye with time in a solution containing peroxide, the vanadyl complex and a reducing agent. Degradation of the dye should be impeded by the addition of mannitol, a hydroxyl radical scavenger, if free OH^\bullet radicals are being produced. This is necessary as, although the complexes have been shown to bind peroxide, they must be able to generate reactive oxygen species, as this is considered the main mode-of-action for vanadium compounds.¹⁵⁰

Finally, the reactant thianthrene-5-oxide can be used to determine the mechanism of the peroxide addition to a substrate, *viz.* nucleophilic or electrophilic.¹²¹ For an electrophilic reaction mechanism, a peroxide oxygen is electrophilic in nature, and attacks a nucleophilic substrate, whereas in a nucleophilic reaction mechanism, it is the peroxide oxygen that is attacked by an electrophile. Thianthrene-5-oxide has two sulphurs, one nucleophilic and one electrophilic; reaction of this compound with a peroxy-vanadium complex will therefore lead to two different products, depending on the reaction mechanism (Scheme 8.3).



Scheme 8.3: The reactant thianthrene-5-oxide and the two products it can form with a peroxy-metal complex depending on the reaction mechanism.

8.2.3 Enhancing understanding of EPR spectra

If further complexes are to be made, being able to interpret their EPR spectra according to the additivity rule would afford a quick means to assessing their coordination geometry in solution. In order to do this, the contribution of an iminium donor the parallel hyperfine coupling constant needs to be known. This requires the synthesis of ligands possessing either only iminium donors, or coordinating a single iminium to vanadium along with other, already well understood ligands. At the same time, the crystal structure needs to be determined for as many compounds as possible.

Knowing the solid state structures for the complexes will give information regarding their distortion from the ideal square-pyramidal geometry.

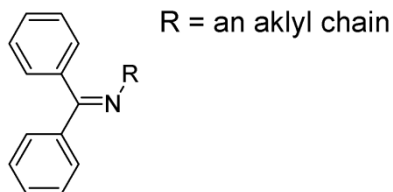


Figure 8.1: A ligand that should have an electron donating ability similar to the iminium donors of the Schiff base ligands studied in this body of work.

8.2.4 Further evaluation of biological activity

The vanadyl compounds displayed excellent anticancer activity in their initial 5-dose screening. However, these results will be more meaningful if it can be confirmed that the inhibitory effects on the cancer cells were the result of the intact oxovanadium(IV) complex, and not just the ligand, vanadium salt, or other possible decomposition product. Therefore, the same 5-dose study on the same cell lines needs to be performed with the free ligand, vanadyl sulphate and solvent used, i.e. DMSO. Once this is done, the true efficacy of the vanadyl compounds will be known, and their screening against additional cell lines will be validated.

References

1. M.E. Weeks and H.M. Leicester, 'Discovery of the Elements', Easton, PA, 1956.
2. S.J. Briggs, *Met. Technol.* 1983, **10**, 150.
3. R. Bonnett and P. Brewer, *Tetrahedron Lett.*, 1970, **30**, 2579.
4. 'CRC Handbook of Chemistry and Physics', 74th ed., Ed. D.R. Lide, CRC press, Boca, Raton, 1994.
5. N.D. Chasteen, *Struct. Bonding*, 1983, **53**, 105.
6. D. Reher, A Survey of ⁵¹V NMR Spectroscopy, *Bulletin of Magnetic Resonance*, **4**, 33–83.
7. M. Thirumavalavan, A.M. Martins, Direct synthesis of macrocyclic VO²⁺ complex from cyclam (1,4,8,11-tetraazacyclotetradecane) with amino–amido groups and ESR studies, *Inorg. Chem. Comm.*, 2006, **9**, 497–499.
8. R.J.H. Clark, 'The Chemistry of Titanium and Vanadium', Elsevier, Amsterdam, 1968.
9. H. Sinn and W. Kaminsky, *Adv. Organomet. Chem.*, 1980, **18**, 129.
10. R.J. Kinney, W.O. Jones and R.G. Bergman, *Journal of the American Chemical Society*, 1978, **107**, 7902.
11. A.M. Evangelou, Vanadium in cancer treatment, *Critical Reviews in Oncology/Hematology*, 2002, **42**, 249–265.
12. R.N. Pau in: "Biology and Biochemistry in Nitrogen Fixation," ed. M.J. Dilworth and A.R. Glenn, Elsevier, Amsterdam, 1991, Chapter 3, 41.
13. F.A. Cotton, G. Wilkinson and P.L. Gaus, *Basic Inorganic Chemistry 3rd ed.*, John Wiley & Sons, New York, 1995, pg. 555.
14. L.V. Vilas Boas and J. Costa Pessoa, In: 'Comprehensive Coordination Chemistry', Eds. G. Wilkinson, R.D. Gillard and J.A. Mcleverty, Pergamon, New York, 1987, **3**, p. 453.
15. R.L. Richards, 'Vanadium: Inorganic & Coordination Chemistry', In: 'Encyclopedia of Inorganic Chemistry', 2nd ed., Ed. R.B. King, 2005.
16. E.M. Page and S.A. Wass, 'Vanadium: Inorganic & Coordination Chemistry', In: 'Encyclopedia of Inorganic Chemistry', 1st ed., Ed. R.B. King, Wiley, 1994.
17. S. Di Bella, G. Lanza, A. Guilino and I. Fragala, *Inorg. Chem.*, 1996, **35**, 3885.
18. P.B. Chatterjee, N. Kundu, S. Bhattacharya, K.-Y. Choi, A. Endo and M. Chaudhury, Targeted Synthesis of μ -Oxo Divanadium(V) Compounds with Asymmetry in Coordination Environments, *Inorg. Chem.*, 2007, **46**, 5483–5485.
19. A. Hills, D.L. Hughes, G. Jeffery Leigh and J. Roger Sanders, Crystal and Molecular Structure of the Compound [(salen)VOVO(salen)] [I₅].MeCN [salen = N,N'-ethylenebis(salicylideneimine)] and the Preparation of Similar Complexes with Other Schiff-base Ligands, *J. Chem. Soc. Dalton Trans.*, 1991, 61–64.
20. T.S. Smith, R. LoBrutto, V.L. Pecoraro, Paramagnetic spectroscopy of vanadyl complexes and its application to biological systems, *Coord. Chem. Rev.*, 2002, **228**, 1–18.
21. S.N. Poddar, and K. Dey, Complex Compounds of SCHIFF's Bases of 3-Aldehydosalicylic acid Iron, Manganese and Vanadium Complexes. *Z. Anorg. Allg. Chem.*, 1964, **327**, 104–109.
22. C.R. Cornman, K.M. Geiser-Bush, S.P. Rowley and P.D. Boyle, Structural and Electron Paramagnetic Resonance Studies of the Square Pyramidal to Trigonal Bipyramidal Distortion of Vanadyl Complexes Containing Sterically Crowded Schiff Base Ligands, *Inorg. Chem.*, 1997, **36**, 6401–6408.

23. C. Slebodnick, B.J. Hamstra and V.L. Pecoraro, Modeling the biological chemistry of vanadium: Structural and reactivity studies elucidating biological function, *Struct. Bonding*, 1997, **89**, 51.
24. D. Rehder, In: 'Multinuclear N.M.R.', ed. J. Mason, Plenum, 1987. Chap. 19.
25. H.L. Krauss and G. Gnatz, *Chem. Ber.* 1962, **95**, 1023.
26. C. Kimblin, X. Bu and A. Butler, Modeling the Catalytic Site of Vanadium Bromoperoxidase: Synthesis and Structural Characterisation of Intramolecularly H-bonded Vanadium(V) Oxoperoxo Complexes, $[\text{VO}(\text{O}_2)(^{\text{NH}_2}\text{pyg}_2)]\text{K}$ and $[\text{VO}(\text{O}_2)(^{\text{BrNH}_2}\text{pyg}_2)]\text{K}$, *Inorg. Chem.*, 2002, **41**, 161–163.
27. D. Fenske, A.-F. Shihada, H. Schwab, and K. Dehnicke, Dioxodichlorovanadat $[\text{VO}_2\text{Cl}_2]^-$; Darstellung, Schwingungsspektrum und Kristallstruktur von $[\text{Ph}_3\text{PMe}][\text{VO}_2\text{Cl}_2]$, *Z. Anorg. Allg. Chem.*, 1980, **471**, 140–146.
28. L.L. Hopkins, Jr. and H.E. Mohr in: 'The Bioessentiality of Vanadium, Newer Trace Elements in Nutrition', eds. W. Morte and W.E. Cornatzer, Dekker, New York, 1971.
29. D.C. Crans, J.J. Smees, E. Gaidamauskas and L. Yang, The Chemistry and Biochemistry of Vanadium and the Biological Activities Exerted by Vanadium Compounds, *Chem. Rev.*, 2004, **104**, 849–902.
30. K. Kanamori, Structures and properties of multinuclear vanadium(III) complexes: seeking a clue to understand the role of vanadium(III) in ascidians, *Coord. Chem. Rev.*, 2003, **237**, 147–161. H. Michibata, N. Yamaguchi, T. Uyama and T. Ueki, Molecular biological approaches to the accumulation and reduction of vanadium by ascidians, *Coord. Chem. Rev.*, 2003, **237**, 41–51.
31. <http://www.aboututila.com/PhotoGallery/PGSeaCreatures03.htm> (11/12/2012).
32. T. Ueki, N. Kawakami, M. Toshishige, K. Matsuo, K. Gekko and H. Michibata, Characterization of vanadium-binding sites of the vanadium-binding protein Vanabin2 by site-directed mutagenesis, *Biochimica et Biophysica Acta*, 2009, **1790**, 1327–1333.
33. D. Rehder, Vanadium nitrogenase, *J. Inorg. Biochem.*, 2000, **80**, 133–136. A. Butler and M. Sandy, Mechanistic considerations of halogenating enzymes, *Nature*, 2009, **460**, 848–854; A. Butler, Mechanistic considerations of the vanadium haloperoxidases, *Coord. Chem. Rev.*, 1999, **187**, 17–35.
34. K.H. Thompson, J.H. McNeill and C. Orvig, Vanadium Compounds as Insulin Mimics, *Chem. Rev.*, 1999, **99**, 2561–2571.
35. D.C. Crans, L. Yang, J.A. Alfano, L. ai-Har Chi, W. Jin, M. Mahroof-Tahir, K. Robbins, M.M. Toloue, L.K. Chan, A.J. Plante, R.Z. Grayson and G.R. Willsky, (4-Hydroxypyridine-2,6-dicarboxylato)oxovanadate(V)—a new insulin-like compound: chemistry, effects on myoblast and yeast cell growth and effects on hyperglycemia in rats with STZ-induced diabetes, *Coord. Chem. Rev.*, 2003, **237**, 13–22.
36. D. Gambino, Potentiality of vanadium compounds as anti-parasitic agents, *Coord. Chem. Rev.*, 2011, **255**, 2193–2203.
37. A. Meshkini and R. Yazdanparast, Chemosensitization of human leukemia K562 cells to taxol by a Vanadium-salen complex, *Experimental and Molecular Pathology*, 2010, **89**, 334–342.
38. U. Hanauske, A.R. Hanauske, M.H. Marshal, V.A. Muggia and D.D. Von Hoff, Biphasic effects of vanadium salts on in vitro tumor colony growth. *Int. J. Cell Cloning*, 1987, **5**, 170–178.
39. R. Faure, M. Vincent, M. Dufour, A. Shaver and B.I. Posner, Arrest of the G2/M transition of the cell cycle by protein tyrosine phosphatase inhibition: studies on a neuronal and a glial cell line. *J. Cell Biochem*, 1995, 389–401.

40. A. Morinville, D. Maysinger and A. Shaver, From Vanadis to Atropos: vanadium compounds as pharmacological tools in cell death signalling. *TIPS*, 1998, **19**, 452–460.
41. I. Jaspers, J.M. Samet, S. Erzurum and W. Reed, Vanadium-induced κ B dependent transcription depends upon peroxide-induced activation of p38 mitogen-activated protein kinase. *Am. J. Respir. Cell Mol. Biol.*, 2000, **23**, 95–102.
42. G. Verquin, G. Fontaine, M. Bria, E. Zhilinskaya, E. Abi-Aad, A. Aboukais, B. Baldeyrou, C. Bailly and J.L. Bernier, DNA modification by oxovanadium(IV) complexes of salen derivatives, *J. Biol. Inorg. Chem.*, 2004, **9**, 345–353.
43. Y.L. Kuo, A.H. Liu and T.J. Marks, Metallocene interactions with DNA and DNA-processing enzymes. In: Siegel H, Siegel A, editors. *Metal ions in biological systems*. New York: Marcel Dekker, 1995, 53–85.
44. Manning FCR, Patierno SR. Apoptosis: inhibitor or instigator of carcinogenesis? *Cancer Invest.* 1996, **14**, 455–465.
45. G.L. Schieven, A.F. Wahl, S. Mydra, L. Grosmaire and J.A. Ladbetter, Lineage-specific induction of B cell apoptosis and altered signal transduction by the phosphotyrosine inhibitor bis(maltolato) oxovanadium (IV), *J. Biol. Chem.*, 1995, **270**, 20824–20831.
46. V.C. Salice, A.M. Cortizo, C.L. Gomez Dumm and S.B. Etchevery, Tyrosine phosphorylation and morphological transformation induced by four vanadium compounds on MC3T3E1 cells. *Mol. Cell. Biochem.* 1999, **198**, 119–128.
47. D.R. Green and J.C. Reed, Mitochondria and apoptosis, *Science*, 1998, **281**, 1309–1312.
48. K. Takenaga, Suppression of metastatic potential of high-metastatic Lewis lung sarcoma cells by vanadate, an inhibitor of tyrosine phosphatase, through inhibiting cell-substrate adhesion. *Invasion Metastasis*, 1996, **16**, 97–106.
49. S. Dharwan, S. Singh and B.B. Aggarwal, Induction of endothelial cell surface adhesion molecules by tumor necrosis factor is blocked by protein tyrosine phosphatase inhibitors: role of nuclear transcription factor NF- κ B. *Eur. Immunol.*, 1997, **27**, 2172–2179.
50. N. Matsuyoshi, M. Hamagushi, S. Tanigushi, A. Nagafuchi, S. Tsukita and M. Tackeishi, Cadherin-mediated cell-cell adhesion is perturbed by the v-src tyrosine phosphorylation in metastatic fibroblasts, *J. Cell. Biol.*, 1992, **118**, 703–714.
51. R.L. Shepard, M.A. Winter, S.C. Hsaio, H.L. Pearce, W.T. Beck and A.H. Dantzig, Effects of modulators on the ATPase activity and vanadate nucleotide trapping of human P-glycoprotein, *Biochem. Pharmacol.*, 1998, **56**, 719–727.
52. M. Valko, C.J. Rhodes, J. Moncol, M. Izakovic and M. Mazur, Free radicals, metals and antioxidants in oxidative stress-induced cancer, *Chemico-Biological Interactions*, 2006, **160**, 1–40.
53. H. Sakurai, Vanadium distribution in rats and DNA cleavage by vanadyl complex: Implication for vanadium toxicity and biological effects, *Envir. Health Perspect.*, 1994, **3**, 35–36.
54. X. Shi, D.C. Flynn, K. Liu and N. Dalal, Vanadium (IV) formation in the reduction of vanadate by glutathione reductase/NADPH and the role of molecular oxygen. *Ann. Clin. Lab. Sci.*, 1997, **27**, 422–427.
55. J.Z. Byckowski and A.P. Kulkarni, Vanadium redox cycling, lipid peroxidation and coxygenation of benzo(α)pyrene,7,8-dihydrodiol, *Biochim. Biophys. Acta*, 1991, **1125**, 136–141.
56. D. Beyersmann and A. Hartwig, Carcinogenic metal compounds: recent insight into molecular and cellular mechanisms. *Arch. Toxicol.*, 2008, **82**, 493–512.

57. A. Goc, Biological activity of vanadium compounds, *Central European Journal of Biology*, 2006, **314**, 314–332.
58. I. Fridovich, Biological effects of the superoxide radical, *Arch. Biochem. Biophys.*, 1986, **247**, 1–11.
59. C. Michiels, M. Raes, O. Toussaint and J. Remacle, Importance of Se-glutathione peroxidase, catalase, and Cu/Zn-SOD for cell survival against oxidative stress, *Free Rad. Biol. Med.* 1994, **17**, 235–248.
60. S.I. Liochev and I. Fridovich, The role of O_2^- in the production of OH^\bullet — *in-vitro* and *in-vivo*, *Free Rad. Biol. Med.* 1994, **16**, 29–33.
61. S.I. Liochev and I. Fridovich, The Haber-Weiss cycle — 70 years later: an alternative view, *Redox report*, 2002, **7**, 55–57.
62. H. Diehl and C.C. Hach, {Bis[*N,N'*-bis(*o*-hydroxybenzylidene)ethylenediamine]- μ -aquadocobalt(II)} *Inorganic Syntheses*, 1950, **3**, 196–201.
63. D.M. Boghaei and S. Mohebi, Synthesis, characterisation and study of vanadyl tetradentate Schiff base complexes as catalyst in aerobic selective oxidation of olefins, *J. Mol. Cat. A: Chem.*, 2002, **179**, 41–51. K.H. Thompson and C. Orvig, Coordination chemistry of vanadium in metallopharmaceutical candidate compounds, *Coord. Chem. Rev.*, 2001, **219-221**, 1033–1053.
64. N. Deligönül and M. Tümer, Synthesis, characterisation, catalytic, electrochemical and thermal properties of tetradentate Schiff base complexes, *Trans. Met. Chem.*, 2006, **31**, 920–929.
65. M. Kojima, H. Taguchi, M. Tsuchimoto and K. Nakajima, Tetradentate Schiff base–oxovanadium(IV) complexes: structures and reactivities in the solid state, *Coord. Chem. Rev.* 2003, **237**, 183–196.
66. K. Oyaizu, E.L. Dewi and E. Tsuchida, Coordination of BF_4^- to Oxovanadium(V) Complexes, Evidenced by the Redox Potential of Oxovanadium(IV/V) Couples in CH_2Cl_2 , *Inorg. Chem.*, 2003, **42**, 1070–1075.
67. B. Cashin, D. Cunningham, J.F. Gallagher, P. McArdle and T. Higgins, A Vanadyl Donor Bond to Tin in a Heterobimetallic Complex: the Crystal Structure of $SnPh_3Cl-VO(\text{salpren})$ ($H_2\text{salpren} = N,N'-1,2\text{-propylenebis-salicylideneamine}$), *J. Chem. Soc., Chem. Commun.*, 1989, 1445–1446.
68. B. Cashin, D. Cunningham, P. Daly, P. McArdle, M. Munroe and N. Chonchubhair, Donor Properties of the Vanadyl Ion: Reactions of Vanadyl Salicylaldimine β -Ketimine and Acetylacetonato Complexes with Group 14 and 15 Lewis Acids, *Inorg. Chem.*, 2002, **41**, 773–782.
69. M. Kirihara, Aerobic oxidation of organic compounds catalyzed by vanadium compounds, *Coord. Chem. Rev.*, 2011, **255**, 2281–2302.
70. A. Horn Jr., C.A.L. Filgueiras, J.L. Wardell, M.H. Herbst, N.V. Vugman, P.S. Santos, J. G.S. Lopes and R. A. Howie, A fresh look into VO(salen) chemistry: synthesis, spectroscopy, electrochemistry and crystal structure of $[VO(\text{salen})(H_2O)]Br \cdot 0.5CH_3CN$, *Inorg. Chim. Acta*, 2004, **357**, 4240–4246.
71. N. Choudhary, P.B. Hitchcock and G.J. Leigh, Six-coordinate vanadyl tetradentate Schiff base complexes with methanol, methoxide, water or fluoride as the sixth ligand, *Inorg. Chim. Acta*, 2000, **310**, 10–20.
72. P.B. Chatterjee, N. Kundu, S. Bhattacharya, K.-Y. Choi, A. Endo and M. Chaudhury, Targeted Synthesis of μ -Oxo Divanadium(V) Compounds with Asymmetry in Coordination Environments, *Inorg. Chem.*, 2007, **46**, 5483–5485.

73. P.B. Chatterjee, D. Mandal, A. Audhya, K.Y. Choi, A. Endo and M. Chaudhury, Reporting a New Class of Divanadium(V) Compounds Connected by an Unsupported Hydroxo Bridge, *Inorg. Chem.*, 2008, **47**, 3709–3718.
74. P.B. Chatterjee, S. Bhattacharya, A. Audhya, K.Y. Choi, A. Endo and M. Chaudhury, Coordination Asymmetry in Divanadium(V) Compounds Containing a V_2O_3 Core: Synthesis, Characterisation, and Redox Properties, *Inorg. Chem.*, 2008, **47**, 4891–4902.
75. P.B. Chatterjee, S.M.T. Abtab, K. Bhattacharya, A. Endo, E.J. Simon, J. Teat and M. Chaudhury, Hetero-Bimetallic Complexes Involving Vanadium(V) and Rhenium(VII) Centers, Connected by Unsupported μ -Oxido Bridge: Synthesis, Characterisation, and Redox Study, *Inorg. Chem.*, 2008, **47**, 8830–8838.
76. J.A.L. da Silva, J.J.R. Fraústo da Silva and A.J.L. Pombeiro, Oxovanadium complexes in catalytic oxidations, *Coord. Chem. Rev.*, 2011, **255**, 2232–2248.
77. V. Conte, A. Coletti, B. Floris, G. Licini and C. Zonta, Mechanistic aspects of vanadium catalysed oxidations with peroxides, *Coord. Chem. Rev.* 2011, **255**, 2165–2177.
78. A. Butler, M.J. Clague and G.E. Meister, Vanadium Peroxide Complexes, *Chem. Rev.* 1994, **94**, 625–638.
79. M. Mohammadi and R. Yazdanparast, Radical scavenging abilities and hepatoprotective effect of [N.N'-Bis(salicylidene)ethane-1,2-diaminato] oxovanadium(IV) complex in CCl_4 -treated rats, *Experimental and Toxicologic Pathology*, 2010, **62**, 533–538.
80. A. Meshkini and R. Yazdanparast, Chemosensitization of human leukemia K562 cells to taxol by a Vanadium-salen complex, *Experimental and Molecular Pathology*, 2010, **89**, 334–342.
81. M.B. Smith and J. March, March's Advanced Organic Chemistry, reactions, mechanisms and structure, 5th ed., J. Wiley & Sons, USA, pg. 1186.
82. K. Lippe, D. Gerlach, E. Kroke and J. Wagler, Hypercoordinate Organosilicon Complexes of an ONN'O' Chelating Ligand: Regio- and Diastereoselectivity of Rearrangement Reactions in Si–Salphen Systems, *Organomet.* 2009, **28**, 621–629.
83. J. Dupont, R.F. de Souza and P.A.Z. Suarez, Ionic Liquid (Molten Salt) Phase Organometallic Catalysis, *Chem. Rev.*, 2002, **102**, 3667–3692.
84. M.M. Fickling, A. Fischer, B.R. Mann, J. Packer and J. Vaughan, Hammett Substituent Constants for Electron-withdrawing Substituents: Dissociation of Phenols, Anilinium Ions and Dimethylanilinium Ions, *J. Am. Chem. Soc.*, 1959, **17**, 4226–4230.
85. G.D. Triantafillou, E.I. Tolis, A. Terzis, Y. Deligiannakis, C.P. Raptopoulou, M.P. Sigalas and T.A. Kabanos, Monomeric Oxovanadium(IV) Compounds of the General Formula $cis-[V^{IV}(=O)(X)(L_{NN})_2]^{+/0}$ {X = OH^- , Cl^- , SO_4^{2-} and L_{NN} = 2,2'-Bipyridine (Bipy) or 4,4'-Disubstituted Bipy}, *Inorg. Chem.*, 2004, **43**, 79–91.
86. M. Sutradhar, G. Mukherjee, M.G.B. Drew and S. Ghosh, Synthesis, Reactivity, and X-ray Crystal Structure of Some Mixed-Ligand Oxovanadium(V) Complexes: First Report of Binuclear Oxovanadium(V) Complexes Containing 4,4'-Bipyridine Type Bridge, *Inorg. Chem.*, 2006, **45**, 5150–5161.
87. K.I. Smith, L.L. Borer and M.M. Olmstead, Vanadium(IV) and Vanadium(V) Complexes of Salicyladimine Ligands, *Inorg. Chem.*, 2003, **42**, 7410–7415.
88. H. Karabiyik, B. Guzel, M. Aygun, G. Boga and O. Buyukgungor, 1-((E)-{(IR,2R)-2-[(E)-(2-Hydroxy-1-naphthyl)methyleneamino]cyclohexyl}iminiomethyl)naphthalen-2-olate: a Schiff base compounds having both OH and NH character, *Acta Cryst.*, 2007, **C63**, o215–o218.
89. K. Ogawa and J. Harada, *J. Mol. Struct.*, 2003, **647**, 211–216.

90. H. Karabiyik, B. Guzel, M. Aygun, G. Boga, and O. Buyukgungor, *Acta Cryst.*, 2007, **C63**, o215-o218.
91. G.M. Sheldrick, *SADABS*, 1996, University of Göttingen, Germany; Bruker, *SAINT*, 2007, Bruker AXS Inc., Madison, Wisconsin, USA.
92. F.H. Allen, O. Kennard, D.G. Watson, L. Brammer, A.G. Orpen, and R. Taylor, *J. Chem. Soc. Perkin Trans.*, 1987, **2**, S1-19. K. Ha, 4,4'-Dinitro-2,2'-[propane-1,3-diylbis(iminiumylmethanylylidene)]diphenolate, *Acta Cryst.*, 2012, **E68**, o1399.
93. M. Nishio, *CrystEngComm*, 2004, **6**, 130-158.
94. J. Selbin, The Chemistry of Oxovanadium(IV), *Chem. Rev.*, 1965, **65**, 153–175.
95. T. Mukherjee, J.C. Pessoa, A. Kumar and A.R. Sarkar, Oxidovanadium(IV) Schiff Base Complex Derived from Vitamin B₆: Synthesis, Characterisation, and Insulin Enhancing Properties, *Inorg. Chem.*, 2011, **50**, 4349–4361.
96. D.M. Murphy, in: EPR (Electron Paramagnetic Resonance) Spectroscopy of Polycrystalline Oxide Systems,
97. M. Thirumavalavan and A.M. Martins, Direct Synthesis of macrocyclic VO²⁺ complex from cyclam (1,4,8,11-tetraazacyclotetradecane) with amino–amido groups and ESR studies, *Inorg. Chem. Comm.*, 2006, **9**, 497–499.
98. N.D. Chasteen, in: L.J. Berliner, J. Reuben (Eds.), Biological Magnetic Resonance, vol. 3, Plenum Press, New York, 1981, pp. 53–119.
99. T.S. Smith, C.A. Root, J.W. Kampf, O.G. Rasmussen and V.L. Pecoraro, *J. Am. Chem. Soc.*, 2000, **122**, 767.
100. A.J. Tasiopoulos, A.N. Troganis, A. Evangelou, C.P. Raptopoulou, A. Terzis, Y. Deligiannakis and T.A. Kabanos, *Chem. Eur. J.*, 1999, **5**, 910.
101. B.H. Hamstra, A.L.P. Houseman, G.J. Colpas, J.W. Kampf, R. LoBrutto, W.D. Frasch and V.L. Pecoraro, *Inorg. Chem.*, 1997, **36**, 4866.
102. A.L.P. Houseman, R. LoBrutto and W.D. Frasch, *Biochemistry*, 1995, **34**, 3277.
103. C.R. Cornman, E.P. Zovinka, Y.D. Boyajian, K.M. Geiser-Bush, P.D. Boyle and P. Singh, *Inorg. Chem.* 1995, **34**, 4213.
104. A.C. Saladino and S.C. Larsen, Computational Study of the Effect of the Imidazole Ring Orientation on the EPR Parameters for Vanadyl–Imidazole Complexes, *J. Phys. Chem. A.*, 2002, **106**, 10444–10451.
105. L.J. Boucher and T.F. Yen, Spectral Properties of Oxovanadium(IV) Complexes. III. Salicyldimines, *Inorg. Chem.* 1969, **8**, 689–692.
106. L.J. Boucher, E.C. Tynan and T.F. Yen, Spectral Properties of Oxovanadium(IV) Complexes. I. β -Ketimines, *Inorg. Chem.*, 1968, **7**, 731–736.
107. J.E. Drake, J. Vekris and J.S. Wood, The Crystal and Molecular Structure and the Electronic Spectrum of Bis(trimethylamine)oxovanadium(IV) Dichloride, *Inorg. Phys. Theor.*, 1968, **A**, 1000–1005.
108. H. Hagen, C. Bezemer, J. Boersma, H. Kooijman, M. Lutz, A.L. Spek and G. van Koten, Vanadium(IV) and -(V) Complexes with O,N-Chelating Aminophenolate and Pyridylalkoxide Ligands, *Inorg. Chem.*, 2000, **39**, 3970–3977.
109. J. Clayden, N. Greeves, S. Warren and P. Wothers, 'Organic Chemistry', Oxford University Press, 2001.
110. International patent number (Internationale Veröffentlichungsnummer): WO 2012/156109 A2.

111. H.A. Kuska and J.A. Ryan, Use of Electron Spin Resonance Data to Assist in the Assignment of Vanadyl Optical Transitions, *Inorg. Chem.*, 1976, **15**, 3184–3185.
112. M. Wojdyr, *J. Appl. Cryst.*, 2010, **43**, 1126.
113. M.R. Maurya, Development of the coordination chemistry of vanadium through bis(acetylacetonato)oxovanadium(IV): synthesis, reactivity and structural aspects, *Coord. Chem. Rev.*, 2003, **237**, 163–181.
114. S. Sarmah, D. Kalita, P. Hazarika, R. Borah and N.S. Islam, Synthesis of new dinuclear and mononuclear peroxovanadium(V) complexes containing biogenic co-ligands: a comparative study of some of their properties, *Polyhedron*, 2004, **23**, 1097–1107.
115. S. Sarmah, P. Hazarika, N.S. Islam, A.V.S. Rao and Y. Ramasarma, Peroxo-bridged divanadate as selective bromide oxidant in bromoperoxidation, *Mol. and Cell. Biochem.*, 2002, **236**, 95–105.
116. H. Mimoun, L. Saussine, E. daire, M. Postel, J. Fischer and R. Weiss, Vanadium(V) Peroxo Complexes. New Versatile Biomimetic Reagents for Epoxidation of Olefins and Hydroxylation of Alkanes and Aromatic Hydrocarbons, *J. Am. Chem. Soc.*, 1983, **105**, 3101–3110.
117. S. Funahashi, Y. Ito, M. Tanaka, *J. Coord. Chem.* 1973, **3**, 125-130.
118. A.J. Carmichael, *Free Rad. Res. Commun.*, 1990, **10**, 37-45.
119. L. Pettersson, I. Andersson and A. Gorzas, Speciation in Peroxovanadate systems, *Coord. Chem. Rev.*, 2003, **237**, 77–87.
120. A.G.J. Ligtenbarg, R. Hage and B.L. Feringa, Catalytic oxidations by vanadium complexes, *Coord. Chem. Rev.*, 2003, **237**, 89–101.
121. C. Bolm, Vanadium-catalyzed asymmetric oxidations, *Coord. Chem. Rev.*, 2003, **237**, 245–256.
122. N. Pooransingh, E. Pomerantseva, M. Ebel, S. Jantzen, D. Rehder and T. Polenova, ⁵¹V Solid-State Magic Angle Spinning NMR Spectroscopy and DFT Studies of Oxovanadium(V) Complexes Mimicking the Active Site of Vanadium Haloperoxidases, *Inorg. Chem.*, 2003, **42**, 1256–1266.
123. G. Asgedom, A. Sreedhara, J. Kivikoski, J. Valkonen and C.P. Rao, Mononuclear *cis*-Dioxovanadium(V) Anionic Complexes [VO₂L][−] {H₂L = [1+1] Schiff Base derived from Salicylaldehyde (or Substituted Derivatives) and 2-Amino-2-methylpropan-1-ol}: Synthesis, Structure, Spectroscopy, Electrochemistry and Reactivity Studies, *J. Chem. Soc. Dalton Trans.*, 1995, 2459–2466.
124. D.F. Evans, The Determination of the Paramagnetic Susceptibility of Substances by Nuclear Magnetic Resonance, *J. Chem. Soc.*, 1959, 2003–2005.
125. J.L. Deutsch and S.M. Poling, The Determination of Paramagnetic Susceptibility by NMR: A physical chemistry experiment, *J. Chem. Ed.*, 1969, **46**, 167–168.
126. D. Otsfeld and I.A. Cohen, A Cautionary Note on the Use of the Evans Method for Magnetic Measurements, *J. Chem. Ed.* 1972, **49**, 829.
127. K.G. Orrell and V. Sik, Correction to Static Tube Nuclear Magnetic Resonance Method for Determination of Magnetic Susceptibilities of Solutes in Solution, *Anal. Chem.*, 1980, **52**, 567–569.
128. E.M. Schubert, Utilizing the Evans Method with a Superconducting NMR Spectrometer in the Undergraduate Laboratory, *J. Chem. Ed.*, 1992, **69**, 62.
129. N.F. Choudhary, N.G. Connelly, P.B. Hitchcock and G.J. Leigh, New compounds of tetradentate Schiff bases with vanadium(IV) and vanadium(V), *J. Chem. Soc., Dalton Trans.*, 1999, 4431–4446.

130. G.H. Grant and W.G. Richards, Computational Chemistry, *Oxford Science Publishers*, Oxford, 1996.
131. F. Jensen, *Introduction to Computational Chemistry*, 2nd ed., Wiley, West Sussex, 2007.
132. C.J. Cramer and D.G. Truhlar, Density functional theory for transition metals and transition metal chemistry, *Physical Chemistry Chemical Physics*, 2009, **11**, 10757–10816.
133. P.J. Stephens, F.J. Devlin, C.F. Chabalowski and M.J. Frisch *J. Phys. Chem.*, 1994, **98**, 11623.
134. Gaussian NEWS Vol. 5(2), Gaussian Inc., Pittsburgh, PA, 1994, 2.
135. a) A.D. McLean and G.S. Chandler, Contracted Gaussian-basis sets for molecular calculations. 1. 2nd row atoms, Z=11-18, *J. Chem. Phys.*, 1980, **72**, 5639–5648. b) K. Raghavachari, J.S. Binkley, R. Seeger and J.A. Pople, Self-consistent Molecular Orbital Methods. 20. Basis set for correlated wave-functions, *J. Phys. Chem.*, 1980, **72**, 650–654.
136. a) W.R. Wadt and P.J. Hay, *J. Chem. Phys.*, 1985, **82**, 270; b) W.R. Wadt and P.J. Hay, *J. Chem. Phys.*, 1985, **82**, 284; c) W.R. Wadt and P.J. Hay, *J. Chem. Phys.*, 1985, **82**, 299.
137. M.L. Munzarova and M. Kaupp, A Density Functional Study of EPR Parameters for Vanadyl Complexes Containing Schiff Base Ligands, *J. Phys. Chem. B*, 2001, **105**, 12644–12652.
138. N. Matsuoka, M. Tsuchimoto and N. Yoshioka, Theoretical Study of Magnetic Properties of Oxovanadium(IV) Complex Self-Assemblies with Tetradentate Schiff Base Ligands, *J. Phys. Chem. B*, 2011, **115**, 8465–8473.
139. Y. Abe, A. Iyoda, K. Seto, A. Morlguchl, T. Tanase and H. Yokoyama, Synthesis, Structures and Ion-Association Properties of a Series of Schiff Base Oxidovanadium(V) Complexes with 4-Substituted Long Alkoxy Chains, *Eur. J. Inorg. Chem.*, 2008, 2148–2157.
140. H. Eshtiagh-Hosseini, M.R. Housaindokht, S.A. Beyramabadi, S.H.M. Tabatabaei, A.A. Esmaili and M.J. Khoshkholgh, Synthesis, experimental and theoretical characterisation of N,N'-dipyridoxyl(1,4-butanediamine) Schiff-base ligand and its Cu(II) complex, *Spectrochimica Acta Part A*, 2011, **78**, 1046–1050.
141. G.-D. Tang, J.-Y. Zhao, R.-Q. Li, Y.-Cao, Z.-C. Zhang, Synthesis, characteristic and theoretical investigation of the structure, electronic properties and second-order nonlinearity of salicylaldehyde Schiff base and their derivatives, *Spectrochimica Acta Part A*, 2011, **78**, 449–457.
142. C.R. Bhattacharjee, C. Datta, G. Das and P. Mondal, Oxovanadium(IV) complexes of bidentate [N,O] donor Schiff-base ligands: synthesis and mesomorphism, *Phase Transitions*, 2012, **85**, 956–972.
143. K. Kurzak, K. Ejsmont and K. Koprek, X-ray and DFT-calculated structures of a vanadyl Schiff base complex: (methanol- κO)[2-methoxy-6-({2-[(2-oxido-3-methoxybenzylidene)amino]-benzyl}iminomethyl)phenolato- $\kappa^4 O^1, N, N, O^1$]oxidovanadium(IV) monohydrate, *Acta Cryst.*, 2012, **C68**, m161–m165.
144. H.S. Monfared, S. Alavi, R. Bikas, M. Vahedpour and P. Mayer, Vanadiumoxo-aryylhydrazone complexes: Synthesis, structure and DFT calculations, *Polyhedron*, 2010, **29**, 3355–3362.
145. I. Chiodi, C. Belgiovine, F. Donà, A.I. Scovassi and C. Mondello, Drug Treatment of Cancer Cell Lines: A Way to Select for Cancer Stem Cells?, *Cancers*, 2011, **3**, 1111–1128.
146. URL for NCI database/homepage
147. Z. Chi, L. Zhu and X. Lu, Comparison of two binuclear vanadium-catecholate complexes: Synthesis, X-ray structure and effects in cancer cells, *Journal of Molecular Structure*, 2011, **1001**, 111–117.

148. J. Van Steveninck, J. Van Der Zee and T.M.A.R. Dubbelman, Site-specific and bulk-phase generation of hydroxyl radicals in the presence of cupric ions and thiol compounds, *Biochem. J.*, 1985, **232**, 309–311.
149. R. Huang, A. Wallqvist and D.G. Covell, Anticancer metal compounds in NCI's tumour-screening database: putative mode of action, *Biochemical Pharmacology*, 2005, **69**, 1009–1039.

Appendix A | IR, UV-vis, NMR and EPR Spectra

Appendix A.1 IR spectra

A.1.1 Ligands

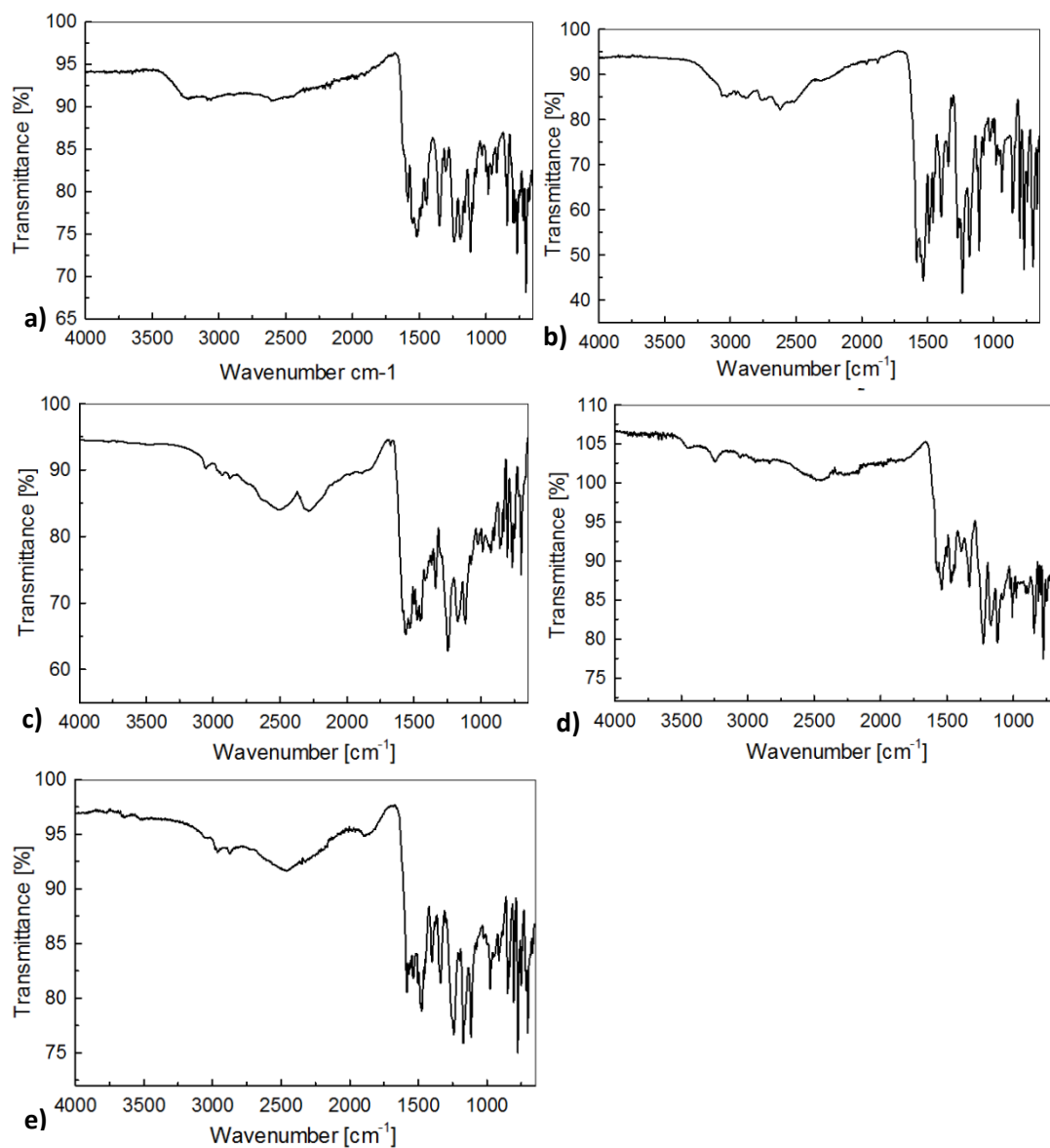


Figure A-1.1: FT-IR spectrum for powder of: a) H₂L1; b) H₂L2; c) H₂L3; d) H₂L4 and e) H₂L5.

A.1.2 Complexes

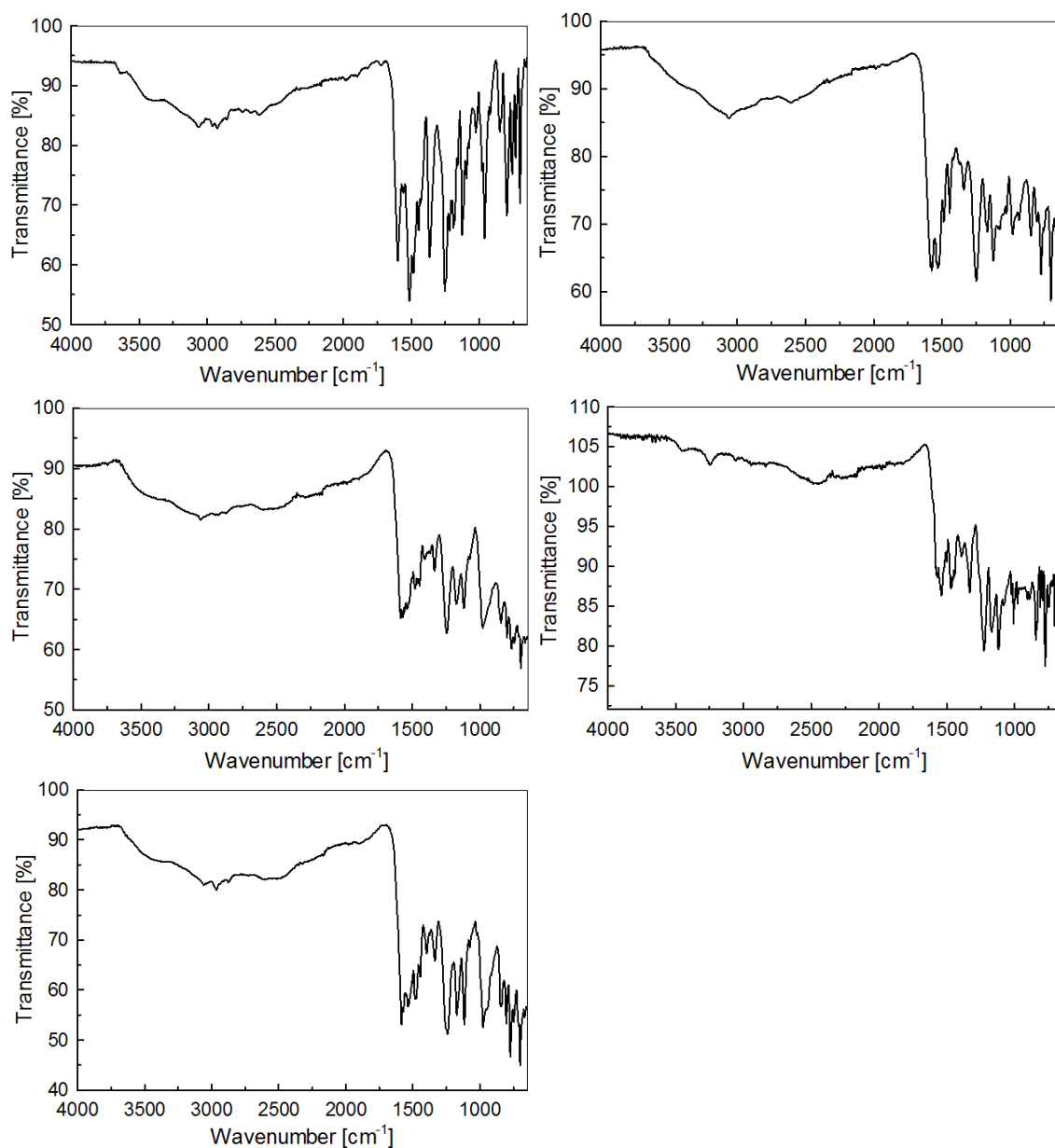


Figure A.1.2: FTIR spectrum for FT-IR spectrum for powder of: a) [VO(L1)]; b) [VO(L2)]; c) [VO(L3)]; d) [VO(L4)] and e) [VO(L5)].

A.2 UV-vis spectra

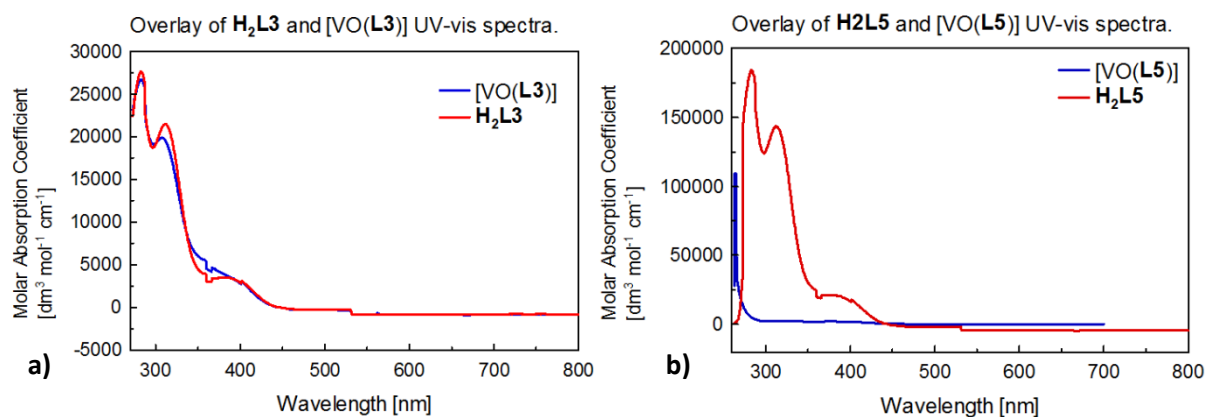


Figure A.2.1: Overlays of the UV-vis spectra for the complexes [VO(L3)] and [VO(L5)], each with their respective ligand.

A.3 NMR spectra

A.3.1 ¹H NMR spectra

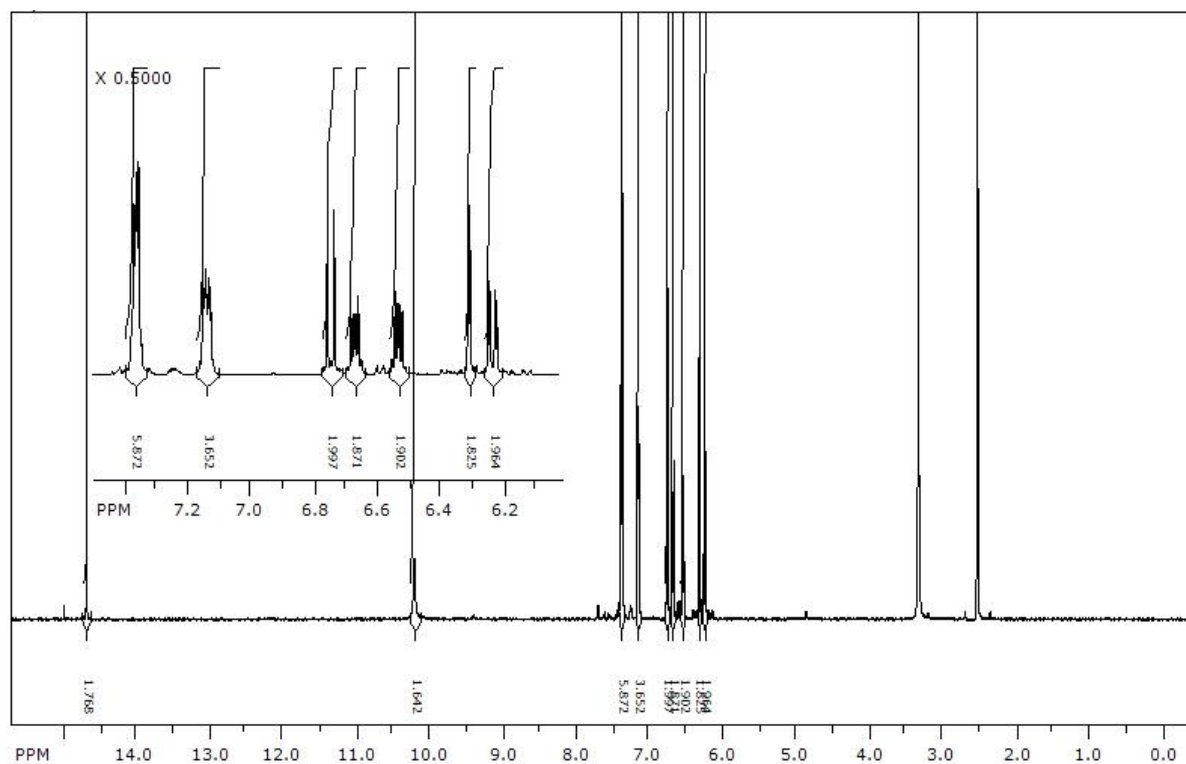


Figure A.3.1: ¹H NMR spectrum of H₂L1 in a room temperature solution of DMSO-d₆.

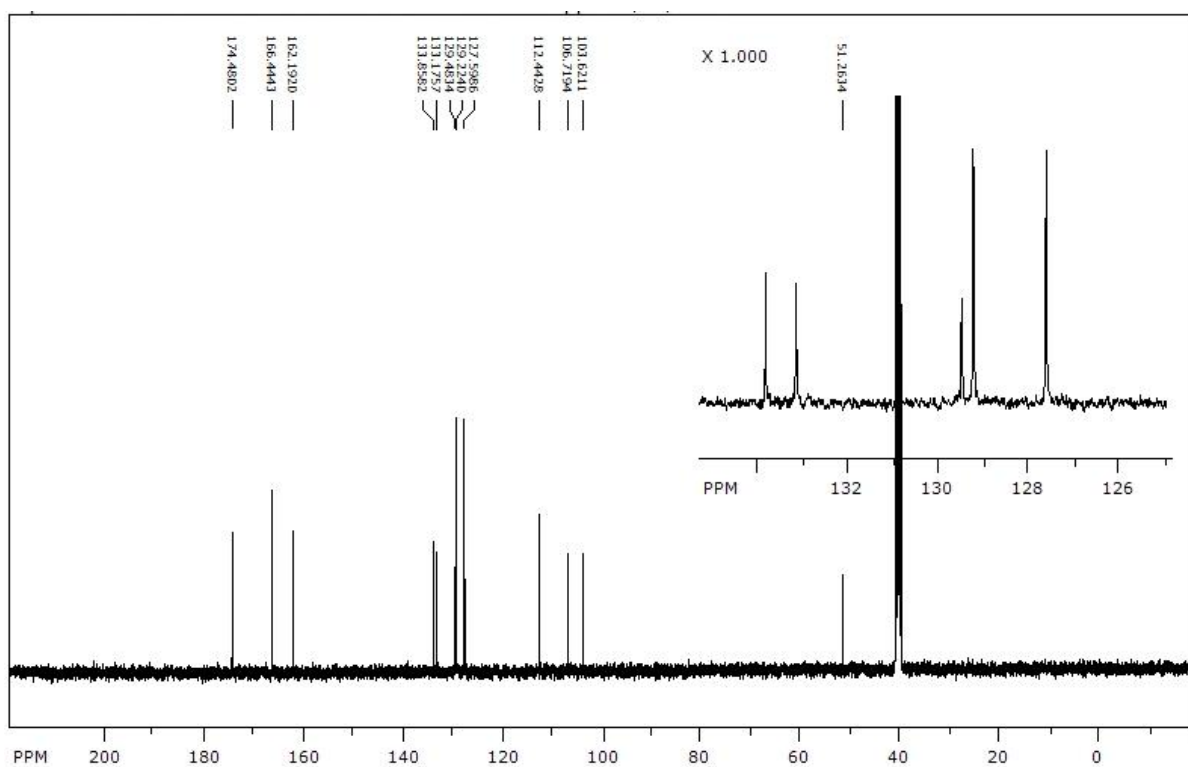


Figure A.3.2: ^1H NMR spectrum of H_2L_2 in a room temperature solution of DMSO-d_6 .

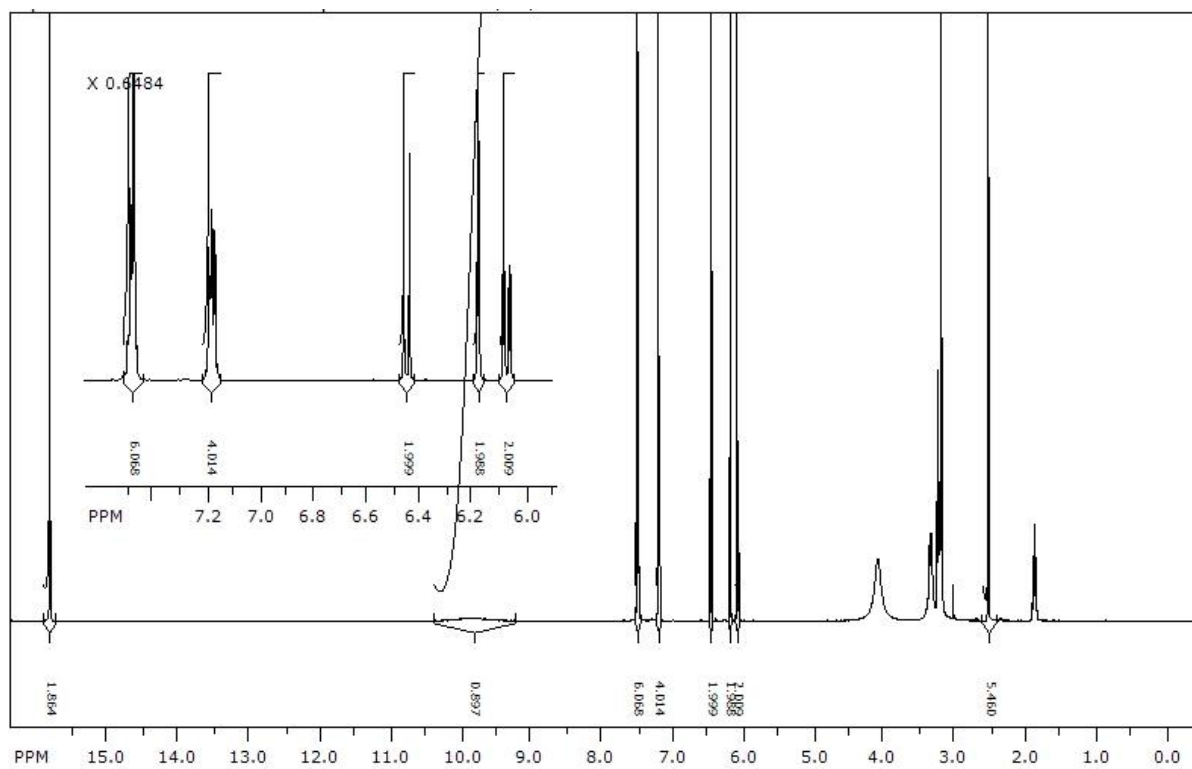


Figure A.3.3: ^1H NMR spectrum of H_2L_3 in a DMSO-d_6 solution at 298 K.

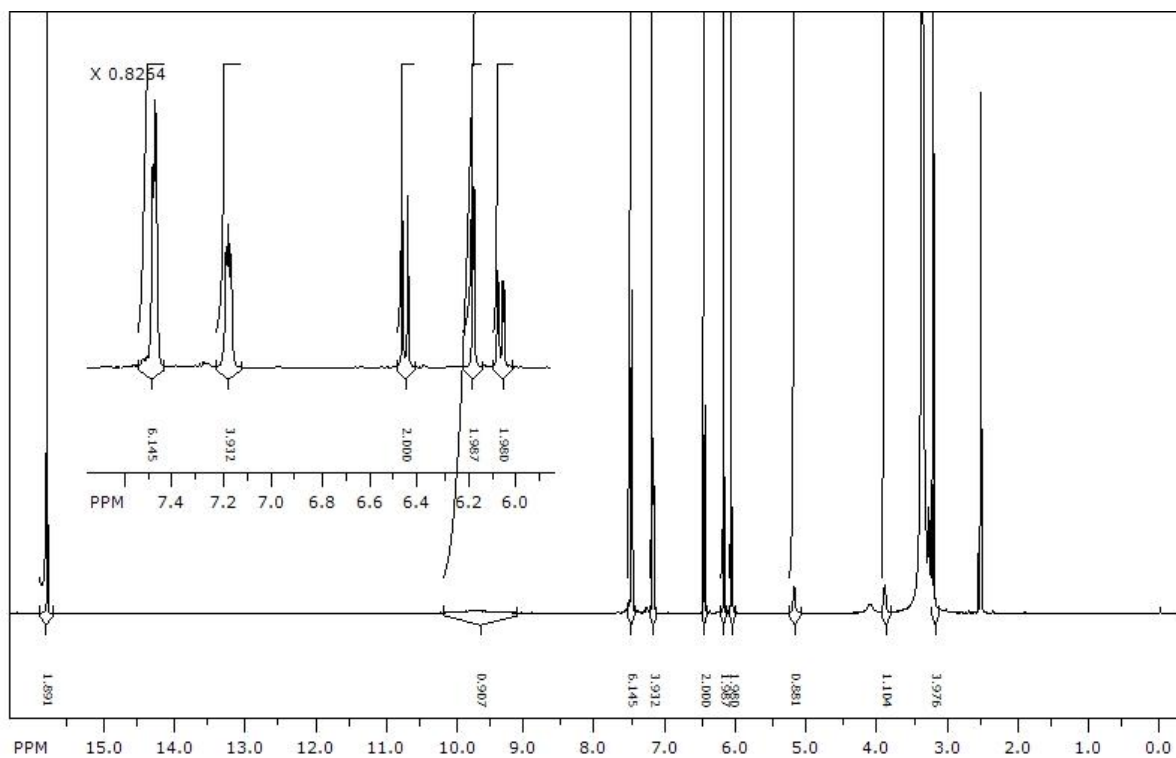


Figure A.3.4: ^1H NMR of $\text{H}_2\text{L4}$ in a DMSO-d_6 solution at 298 K.

A.3.2 ^{13}C NMR spectra

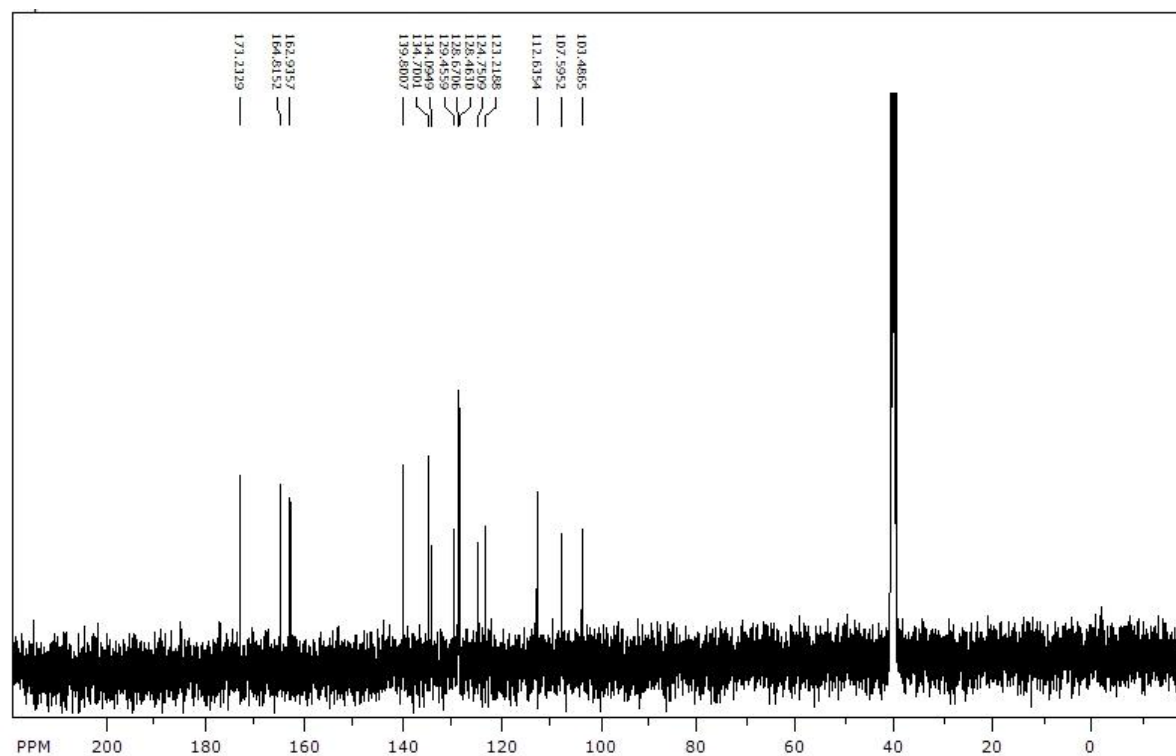


Figure A.3.5: ^{13}C NMR spectrum of $\text{H}_2\text{L1}$ in a DMSO-d_6 solution at 298 K.

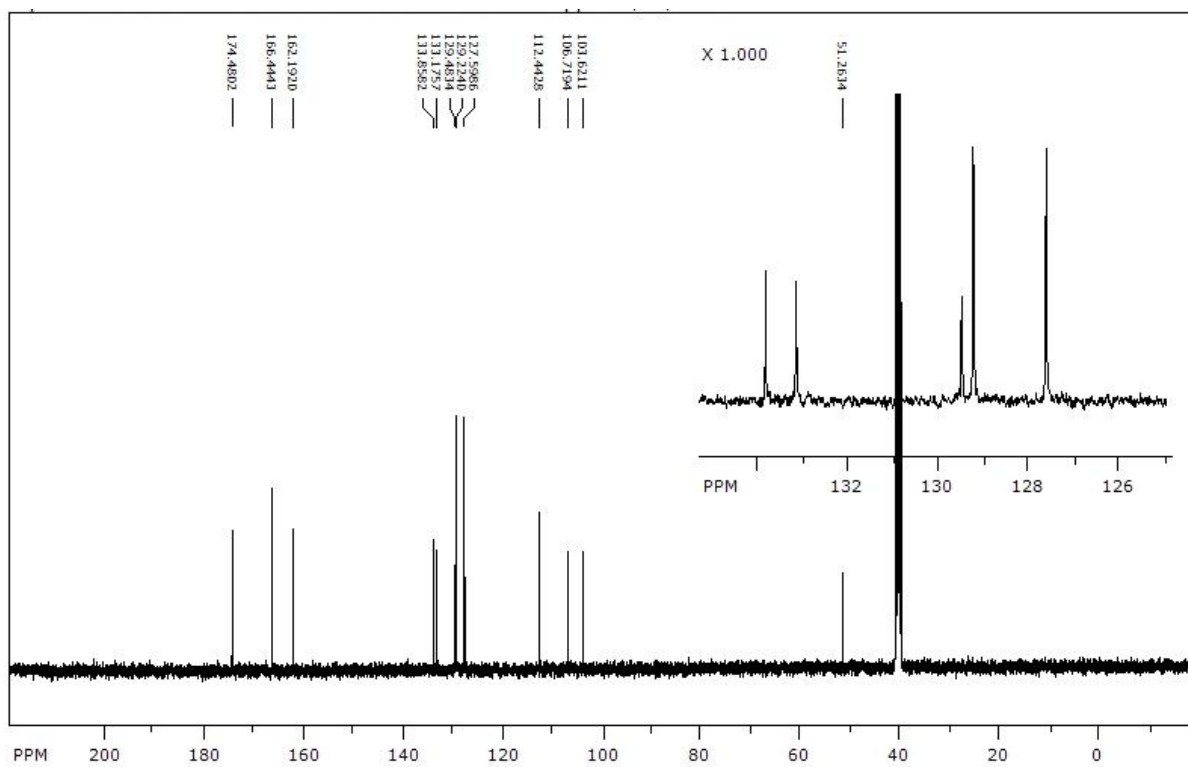


Figure A.3.6: ^{13}C NMR spectrum of H_2L_2 in DMSO-d_6 at 298 K.

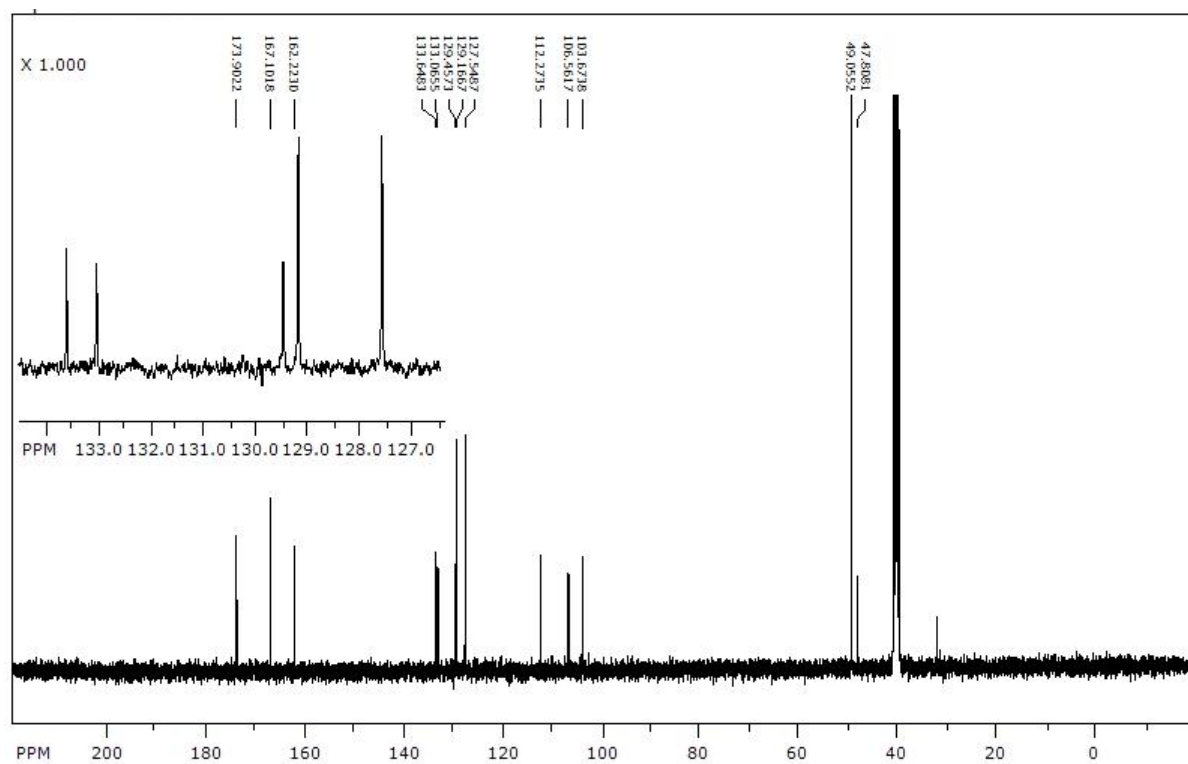


Figure A.3.7: ^{13}C NMR spectrum of H_2L_3 in DMSO-d_6 at 298 K.

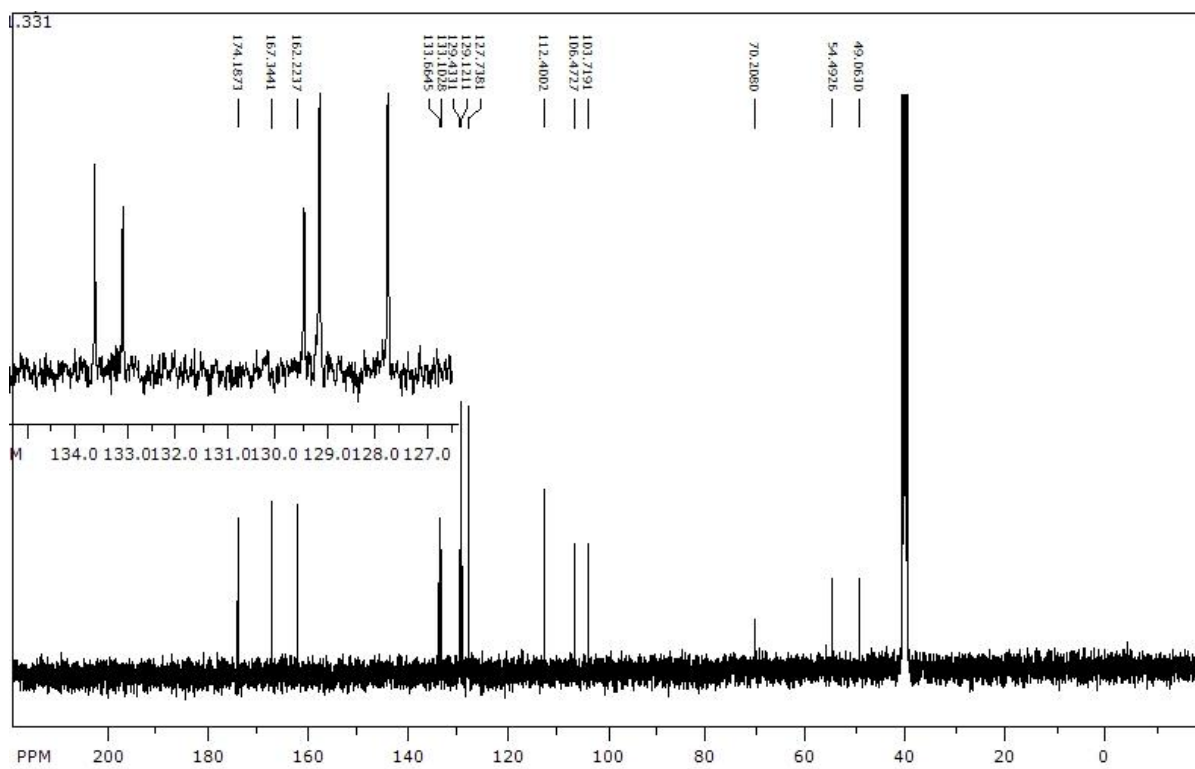


Figure A.3.8: ^{13}C NMR spectrum of $\text{H}_2\text{L4}$ in DMSO-d_6 at 298 K.

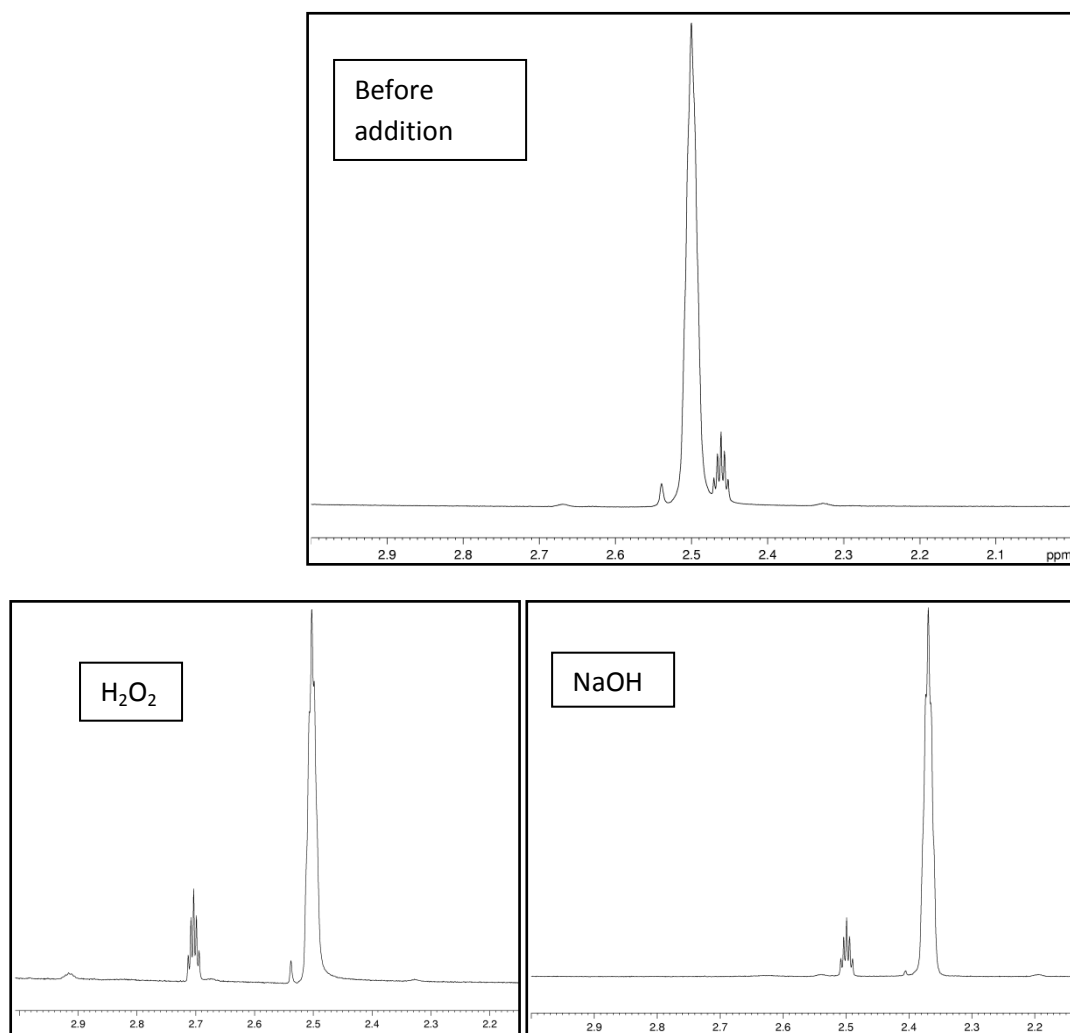
A.3.3 ^{51}V NMR spectra

Figure A.3.9: Changes observed in the chemical shift of an internal reference sample of DMSO-d₆ upon addition of H₂O₂ or NaOH caused by changes in the bulk magnetic susceptibility for [VO(L₂)].

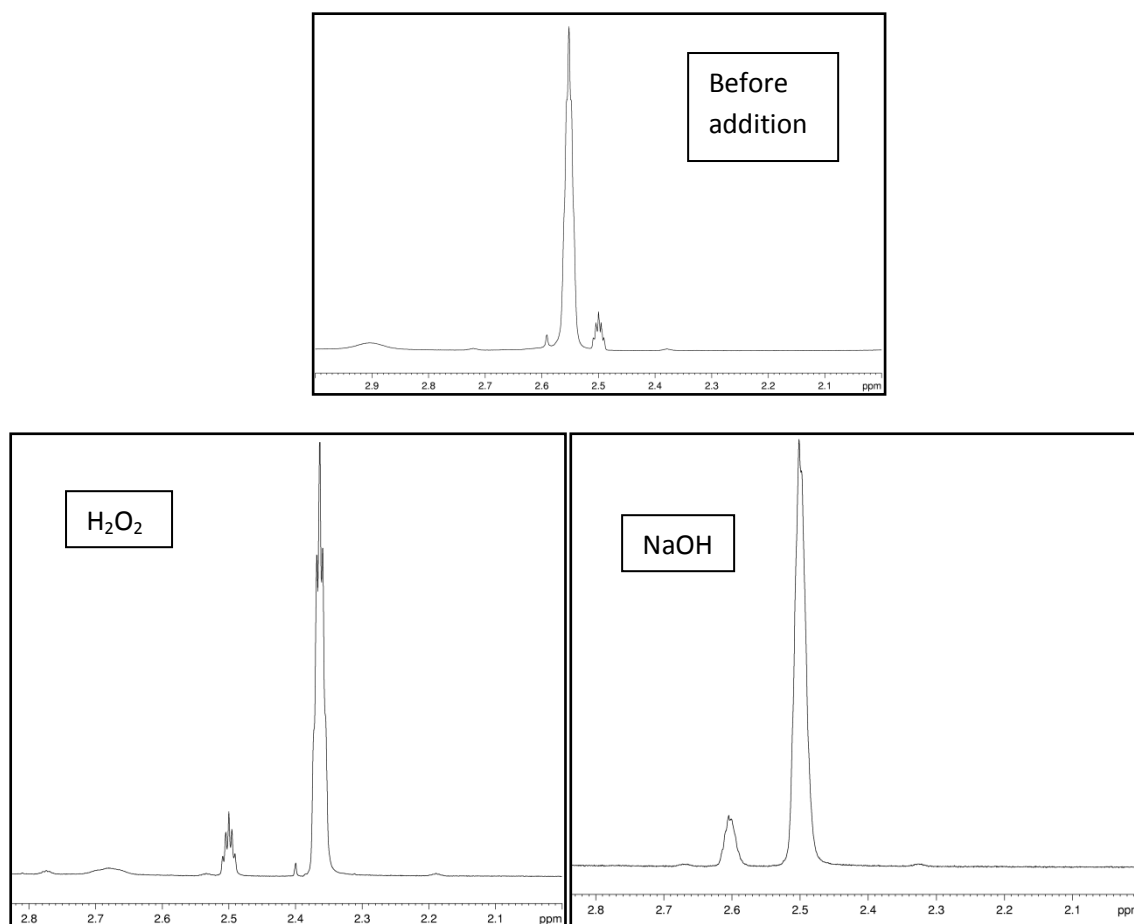


Figure A.3.10: Changes observed in the chemical shift of an internal reference sample of DMSO- d_6 upon addition of H_2O_2 or NaOH caused by changes in the bulk magnetic susceptibility for $[\text{VO}(\mathbf{L3})]$.

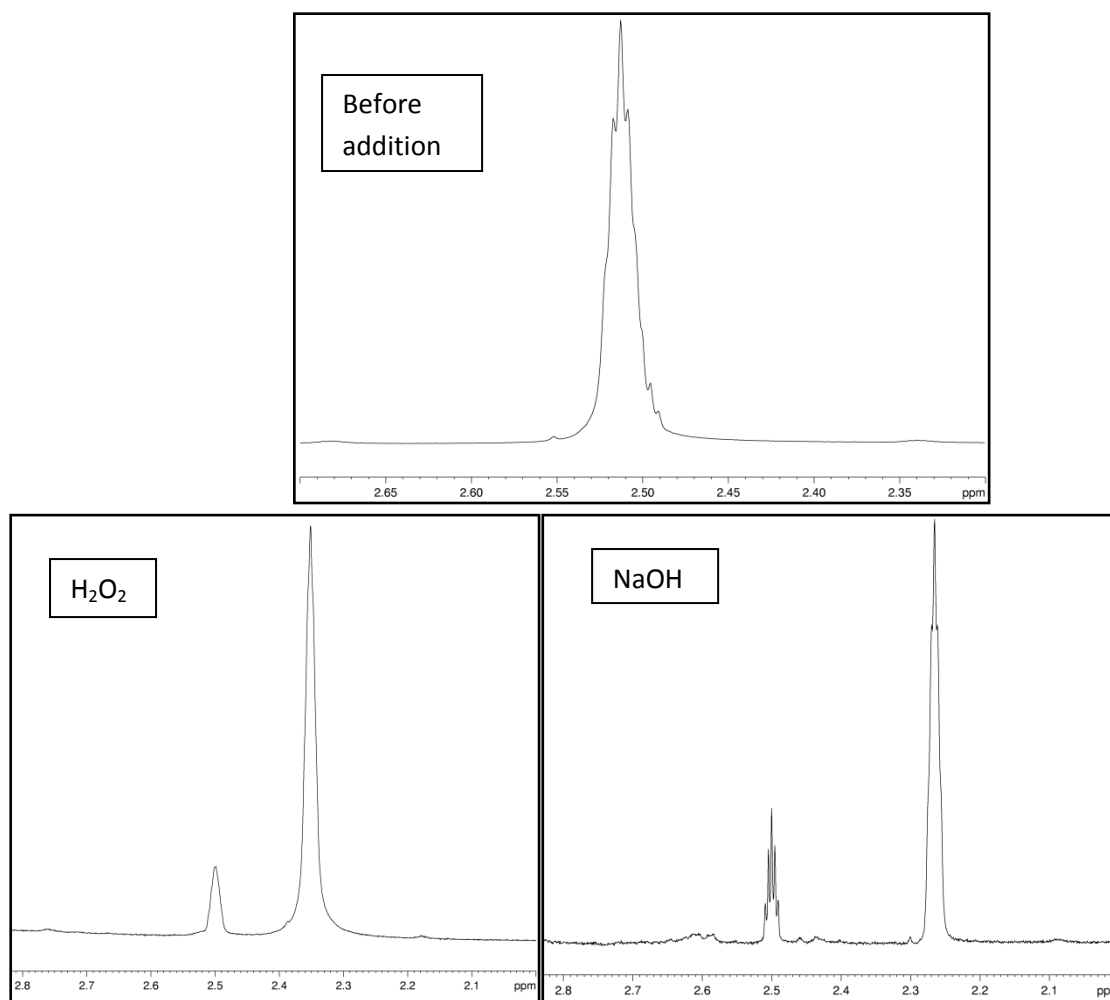


Figure A.3.11: Changes observed in the chemical shift of an internal reference sample of DMSO-d₆ upon addition of H₂O₂ or NaOH caused by changes in the bulk magnetic susceptibility for [VO(L4)].

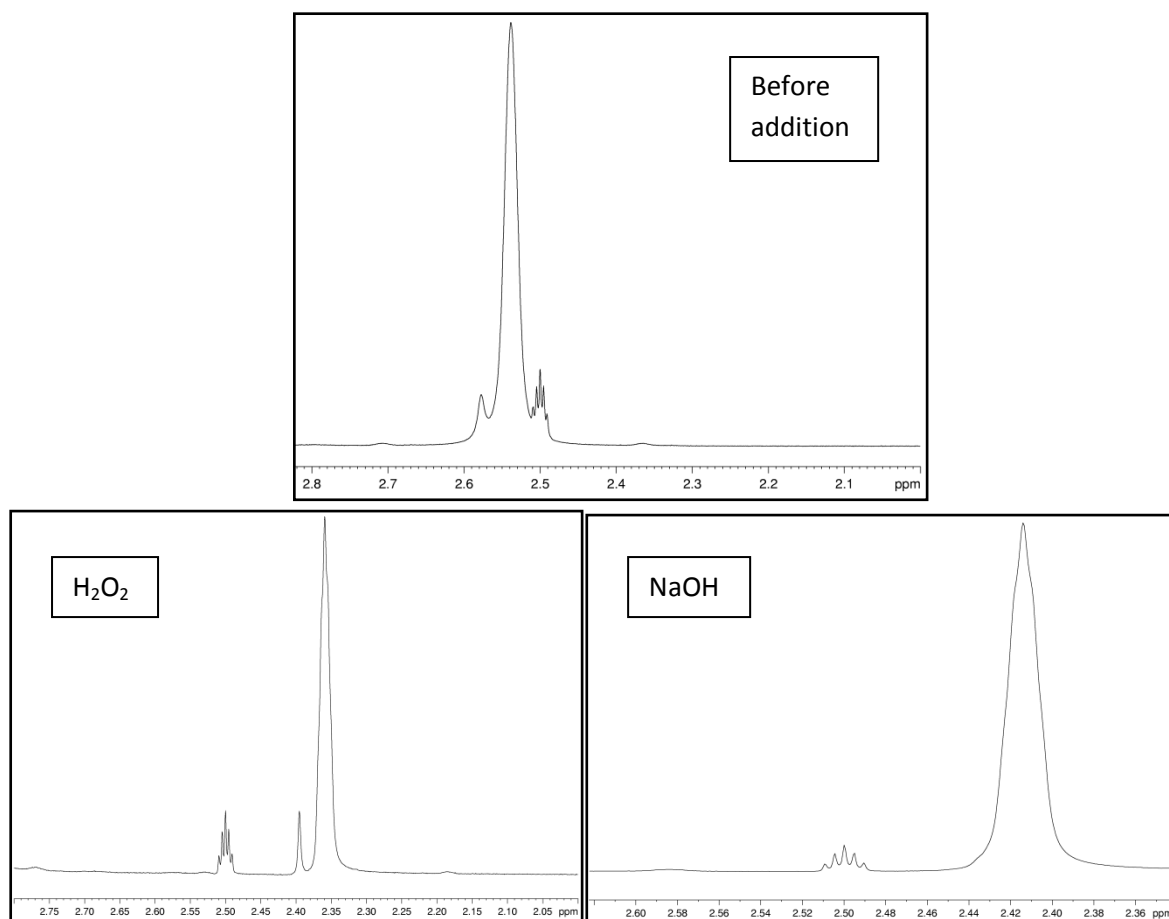


Figure A.3.12: Changes observed in the chemical shift of an internal reference sample of DMSO-d₆ upon addition of H₂O₂ or NaOH caused by changes in the bulk magnetic susceptibility for [VO(L5)].

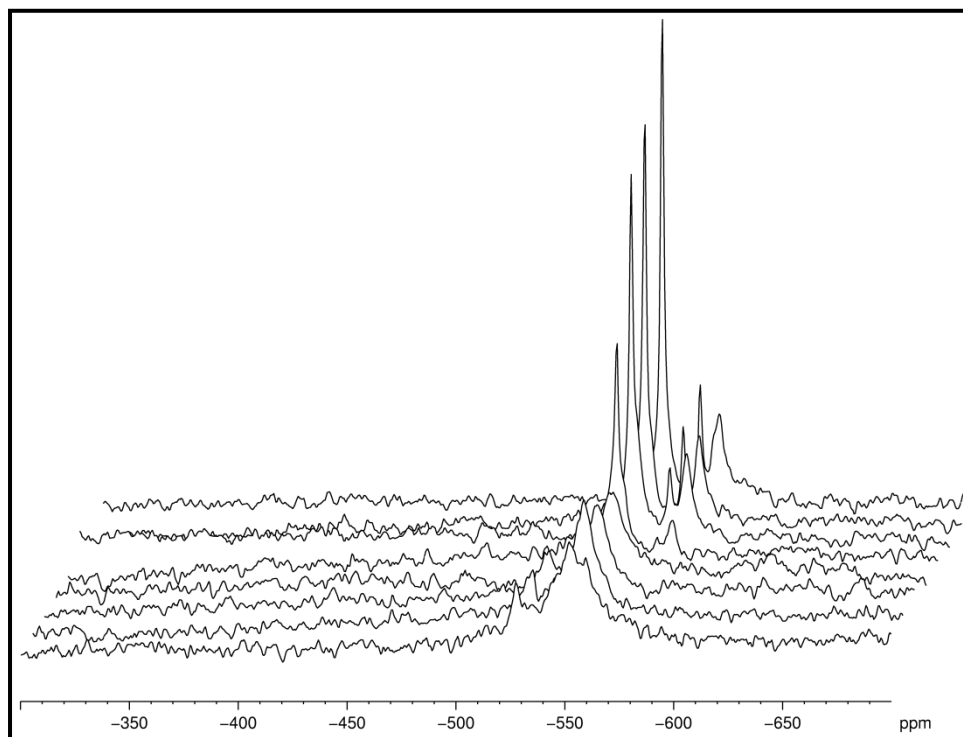


Figure A.3.13: Spectral overlay for the addition of NaOH to a DMSO-d₆ solution of [VO(L2)].

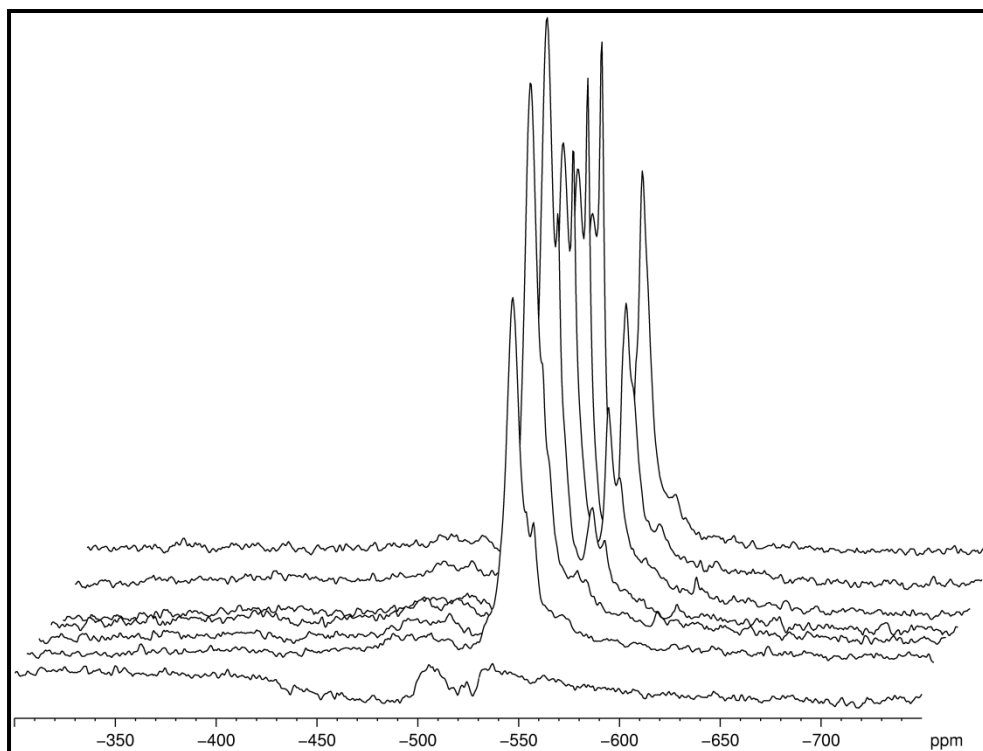


Figure A.3.14: Spectral overlay for the addition of NaOH to a DMSO-d6 solution of [VO(L3)].

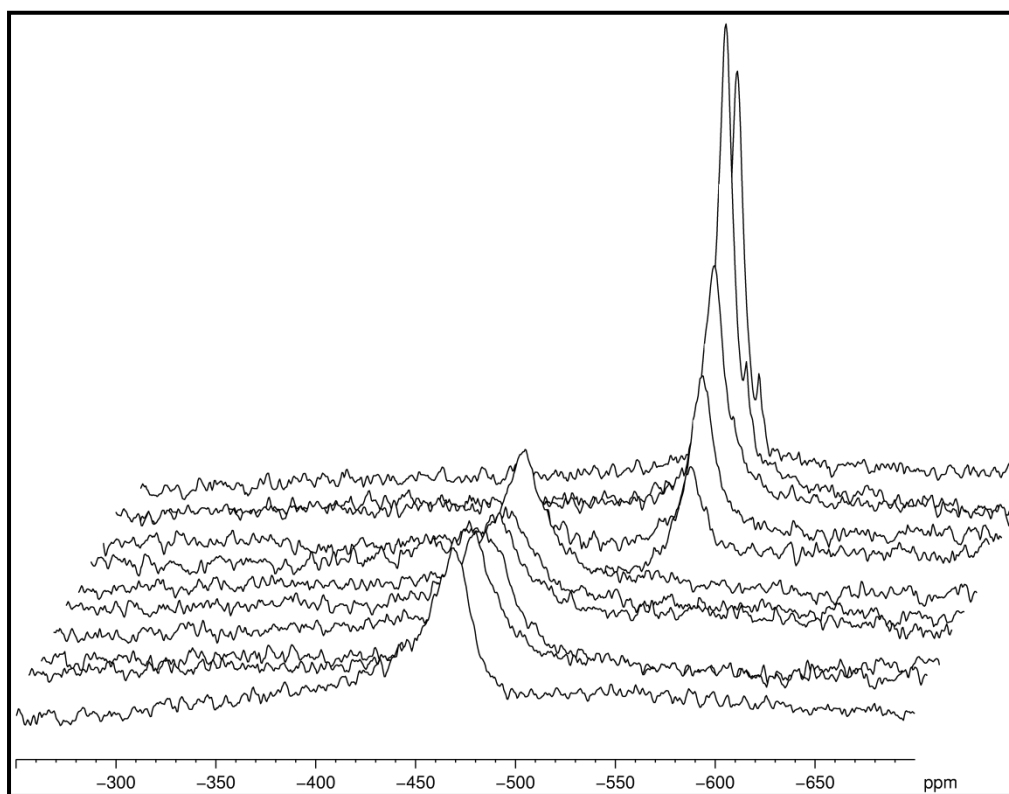


Figure A.3.15: Spectral overlay for the addition of NaOH to a DMSO-d6 solution of [VO(L4)].

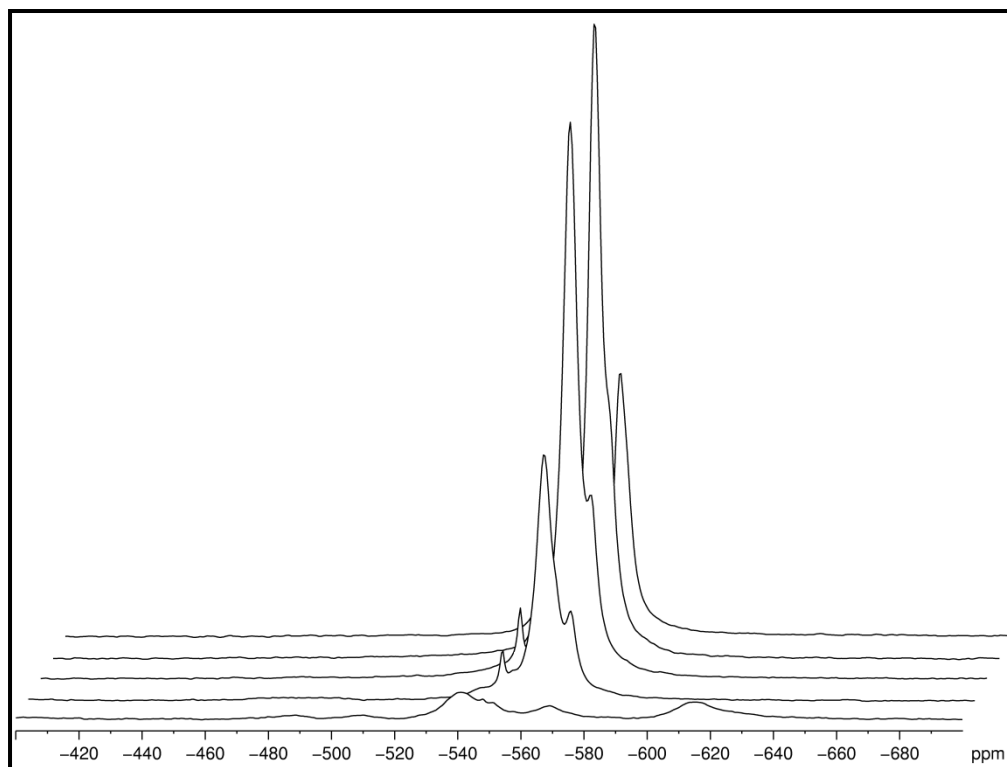


Figure A.3.16: Spectral overlay for the addition of NaOH to a DMSO-d6 solution of [VO(L5)].

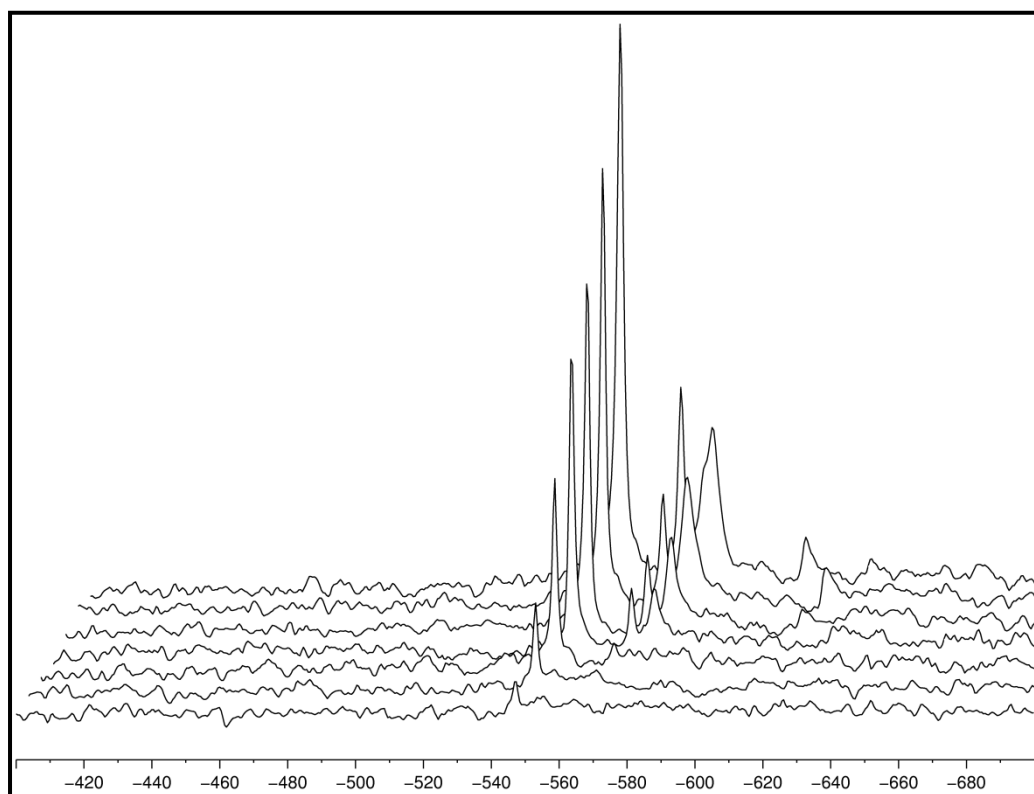


Figure A.3.17: Spectral overlay for the addition of NaOH to a DMSO-d6 solution of [VO(salen)].

Appendix B | *Crystallographic Data Tables***B.1: Crystallographic data tables for H₂L5****Table B.1.1:** Crystal data and structure refinement for **H₂L5**.

Empirical formula	C ₃₁ H ₃₀ N ₂ O ₄	
Formula weight	494.57 amu	
Temperature	100 K	
Wavelength	0.71073 Å	
Crystal system	Monoclinic	
Space group	<i>P</i> 2 ₁ / <i>c</i>	
Unit cell dimensions	<i>a</i> = 9.0766 (7) Å	$\alpha = 90^\circ$
	<i>b</i> = 21.5777 (19) Å	$\beta = 104.782 (5)^\circ$
	<i>c</i> = 14.1584 (12) Å	$\gamma = 90^\circ$
Volume	2681.2 (4) Å ³	
Z	4	
Density (calculated)	1.225 Mg m ⁻³	
Absorption coefficient	0.08 mm ⁻¹	
<i>F</i> (000)	1048	
Crystal size	0.40 × 0.10 × 0.10 mm	
Theta range for data collection	1.8–28.4°	
Index ranges	-11 ≤ <i>h</i> ≤ 12, -25 ≤ <i>k</i> ≤ 28, -18 ≤ <i>l</i> ≤ 18	
Reflections collected	4261	
Independent reflections	6563 [R(int) = 0.052]	
Completeness to theta = 25.00°	99.9%	
Absorption correction	multi-scan	
Max. And min. transmission	0.968 and 0.992	
Refinement method	Least squares matrix: full	
Data / restraints / parameter	6563 / 0 / 346	
Goodness-of-fit on <i>F</i> ²	1.13	
Final <i>R</i> indices [<i>I</i> > 2σ (<i>I</i>)]	R1 = 0.063, wR2 = 0.204	
<i>R</i> indices (all data)	R1 = , wR2 =	
Largest diff. peak and hole	0.39 and -0.26 e Å ⁻³	

Table B.1.2: Fractional atomic coordinates and isotropic or equivalent isotropic displacement parameters (\AA^2).

	<i>x</i>	<i>y</i>	<i>z</i>	$U_{\text{iso}}^*/U_{\text{eq}}$
C1	0.2498 (2)	0.52652 (9)	-0.17555 (15)	0.0363 (4)
C2	0.2937 (2)	0.56806 (10)	-0.23997 (15)	0.0398 (5)
C3	0.2602 (3)	0.55691 (10)	-0.33917 (16)	0.0446 (5)
C4	0.1770 (3)	0.50352 (10)	-0.37927 (16)	0.0467 (5)
C5	0.1290 (2)	0.46344 (10)	-0.31900 (16)	0.0423 (5)
C6	0.1602 (2)	0.47370 (9)	-0.21671 (14)	0.0341 (4)
C7	0.0997 (2)	0.43226 (9)	-0.15724 (15)	0.0353 (4)
C8	-0.0029 (2)	0.37983 (10)	-0.20080 (14)	0.0389 (5)
C9	0.0433 (3)	0.31867 (10)	-0.17762 (16)	0.0438 (5)
C10	-0.0543 (3)	0.27007 (11)	-0.21553 (18)	0.0555 (7)
C11	-0.1933 (3)	0.28173 (13)	-0.2782 (2)	0.0612 (7)
C12	-0.2376 (3)	0.34222 (13)	-0.3024 (2)	0.0597 (7)
C13	-0.1423 (3)	0.39097 (12)	-0.26376 (18)	0.0502 (6)
C14	0.0595 (2)	0.41245 (10)	0.00660 (15)	0.0393 (5)
C15	0.1711 (2)	0.38799 (10)	0.09946 (15)	0.0399 (5)
C16	0.2628 (2)	0.33497 (10)	0.06939 (15)	0.0418 (5)
C17	0.3510 (2)	0.24231 (9)	0.17200 (14)	0.0348 (4)
C18	0.4351 (2)	0.21884 (9)	0.26506 (14)	0.0329 (4)
C19	0.5238 (2)	0.25949 (9)	0.33775 (15)	0.0383 (5)
C20	0.6063 (3)	0.23453 (10)	0.42621 (15)	0.0422 (5)
C21	0.6000 (2)	0.17169 (10)	0.44585 (15)	0.0402 (5)
C22	0.5134 (2)	0.13146 (9)	0.37539 (15)	0.0395 (5)
C23	0.4339 (2)	0.15490 (9)	0.28686 (14)	0.0357 (4)
C24	0.2644 (2)	0.20115 (9)	0.09249 (14)	0.0359 (4)
C25	0.1111 (3)	0.18982 (12)	0.08005 (17)	0.0492 (6)
C26	0.0305 (3)	0.15382 (13)	0.00298 (17)	0.0596 (7)
C27	0.1059 (4)	0.12823 (12)	-0.06095 (18)	0.0596 (7)
C28	0.2564 (3)	0.14071 (14)	-0.05059 (18)	0.0640 (7)
C29	0.3350 (3)	0.17709 (13)	0.02446 (18)	0.0546 (6)
C30	0.0731 (3)	0.36366 (13)	0.16547 (17)	0.0559 (6)
C31	0.2751 (3)	0.43990 (11)	0.15118 (17)	0.0567 (6)
N1	0.1343 (2)	0.44070 (8)	-0.06241 (12)	0.0375 (4)
N2	0.3526 (2)	0.30225 (8)	0.15561 (13)	0.0406 (4)
O1	0.28732 (18)	0.53636 (7)	-0.08171 (10)	0.0442 (4)
O2	0.3015 (2)	0.59485 (8)	-0.40315 (11)	0.0594 (5)
O3	0.52735 (19)	0.31919 (6)	0.32061 (11)	0.0500 (4)
O4	0.6803 (2)	0.15227 (7)	0.53444 (11)	0.0572 (5)

Table B.1.3: IUCR CIF check report for H₂L5.**checkCIF/PLATON (standard)****Datablock: red1**

Bond precision: C-C = 0.0032 Å Wavelength=0.71073
 Cell: a=9.0766(7) b=21.5777(19) c=14.1584(12)
 alpha=90 beta=104.782(5) gamma=90
 Temperature: 100 K

	Calculated	Reported
Volume	2681.2(4)	2681.2(4)
Space group	P 21/c	P 21/c
Hall group	-P 2ybc	-P 2ybc
Moiety formula	C31 H30 N2 O4	C31 H30 N2 O4
Sum formula	C31 H30 N2 O4	C31 H30 N2 O4
Mr	494.57	494.57
Dx, g cm ⁻³	1.225	1.225
Z	4	4
Mu (mm ⁻¹)	0.081	0.081
F000	1048.0	1048.0
F000'	1048.47	
h, k, lmax	12, 28, 18	12, 28, 18
Nref	6716	6563
Tmin, Tmax	0.990, 0.992	0.968, 0.992
Tmin'	0.968	

Correction method= MULTI-SCAN
 Data completeness= 0.977 Theta(max)= 28.370
 R(reflections)= 0.0634(4261) wR2(reflections)= 0.2041(6563)
 S = 1.130 Npar= 346

The following ALERTS were generated. Each ALERT has the format

test-name_ALERT_alert-type_alert-level.

Click on the hyperlinks for more details of the test.

● Alert level C

[PLAT230 ALERT 2 C](#) Hirshfeld Test Diff for C5
 -- C6 .. 5.9 su
[PLAT309 ALERT 2 C](#) Single Bonded Oxygen (C-O
 .GT. 1.3 Ang) O1
[PLAT309 ALERT 2 C](#) Single Bonded Oxygen (C-O
 .GT. 1.3 Ang) O3
[PLAT601 ALERT 2 C](#) Structure Contains Solvent
 Accessible VOIDS of . 90 A**3
[PLAT755 ALERT 4 C](#) D-H Calc 0.84000, Rep
 0.840(10) Senseless su
 O4 -H41 1.555 1.555
 # 70
[PLAT756 ALERT 4 C](#) H...A Calc 1.78000, Rep
 1.780(10) Senseless su
 H41 -O1 1.555 2.645
 # 70

● Alert level G

[FORMU01 ALERT 1 G](#) There is a discrepancy between the atom counts in the

_chemical_formula_sum and
_chemical_formula_moiety. This is
usually due to the moiety formula being in
the wrong format.

Atom count from
_chemical_formula_sum: C31 H30 N2 O4

Atom count from
_chemical_formula_moiety:H90 N6 O12

[PLAT005 ALERT 5 G](#) No

_iucr_refine_instructions_details in the CIF

?

[PLAT007 ALERT 5 G](#) Note: Number of Unrefined

D-H Atoms 2

0 **ALERT level A** = Most likely a serious
problem - resolve or explain

0 **ALERT level B** = A potentially serious
problem, consider carefully

6 **ALERT level C** = Check. Ensure it is not
caused by an omission or oversight

3 **ALERT level G** = General information/check it
is not something unexpected

1 ALERT type 1 CIF construction/syntax error,
inconsistent or missing data

4 ALERT type 2 Indicator that the structure
model may be wrong or deficient

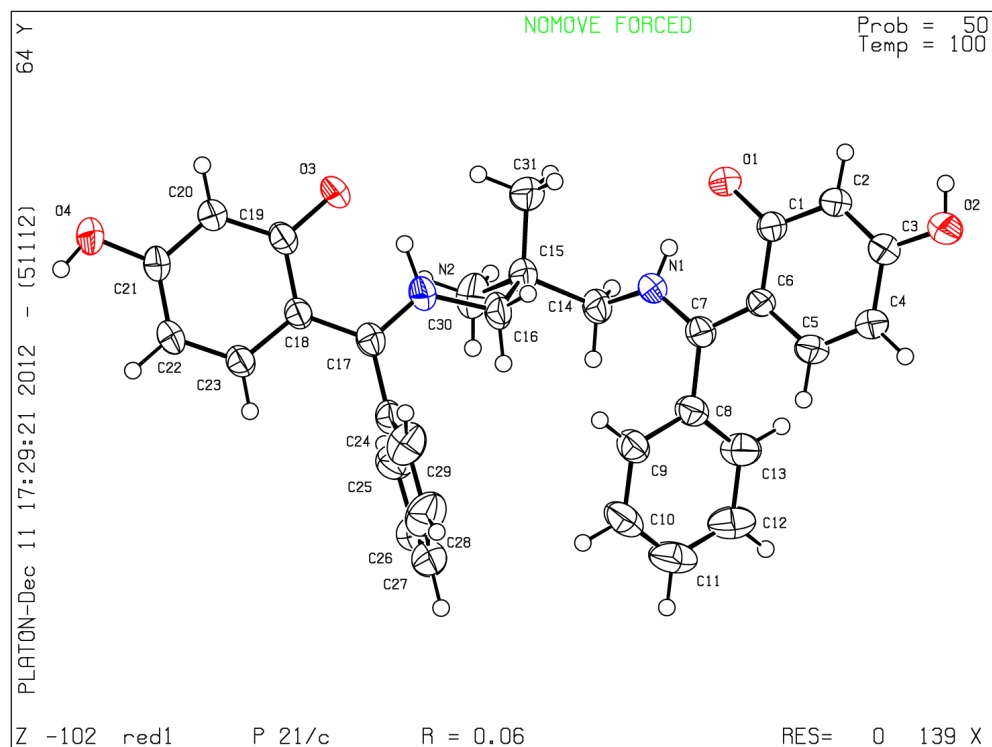
0 ALERT type 3 Indicator that the structure
quality may be low

2 ALERT type 4 Improvement, methodology,
query or suggestion

2 ALERT type 5 Informative message, check

PLATON version of 05/11/2012; check.def file version of 05/11/2012

Datablock red1 - ellipsoid plot



Appendix C | Comparisons of Experimental and DFT-calculated Spectra

C.1 UV-vis spectral overlays

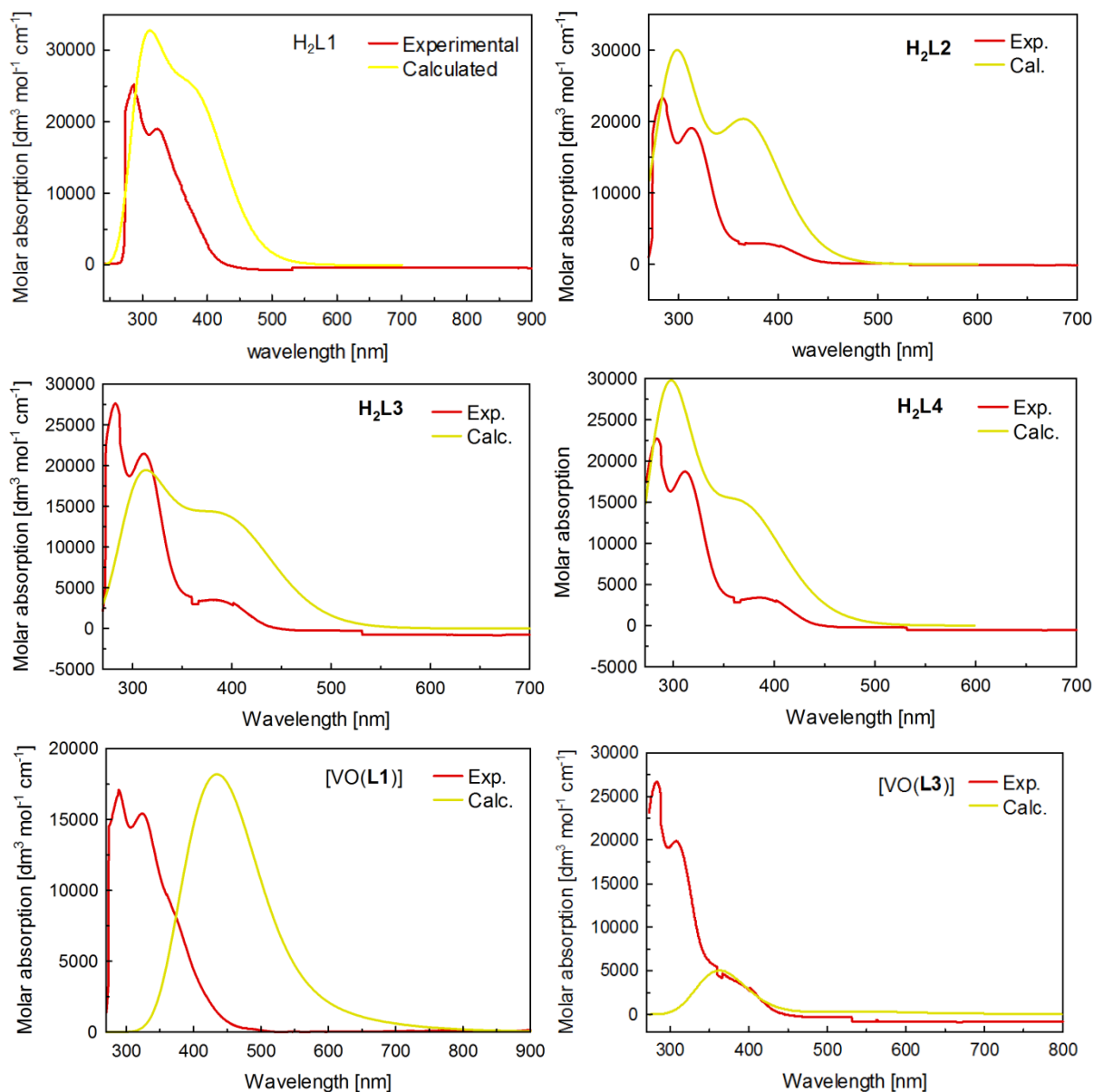


Figure C.1: Spectral overlays of DFT-calculated and experimentally determined UV-vis spectra for the oxovanadium(IV) Schiff base complexes and their ligands.

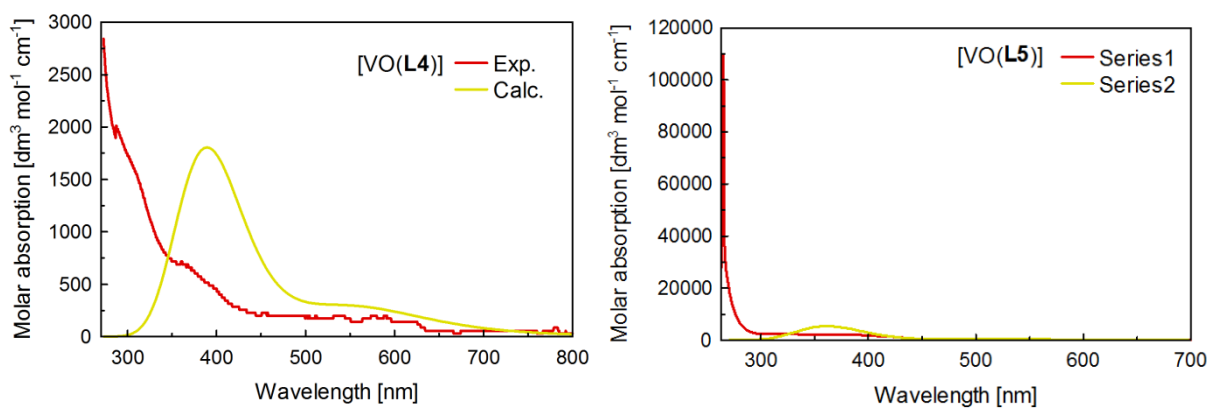


Figure C.2: Spectral overlays of DFT-calculated and experimentally determined UV-vis spectra for the oxovanadium(IV) Schiff base complexes and their ligands.

C.2 IR spectral overlays

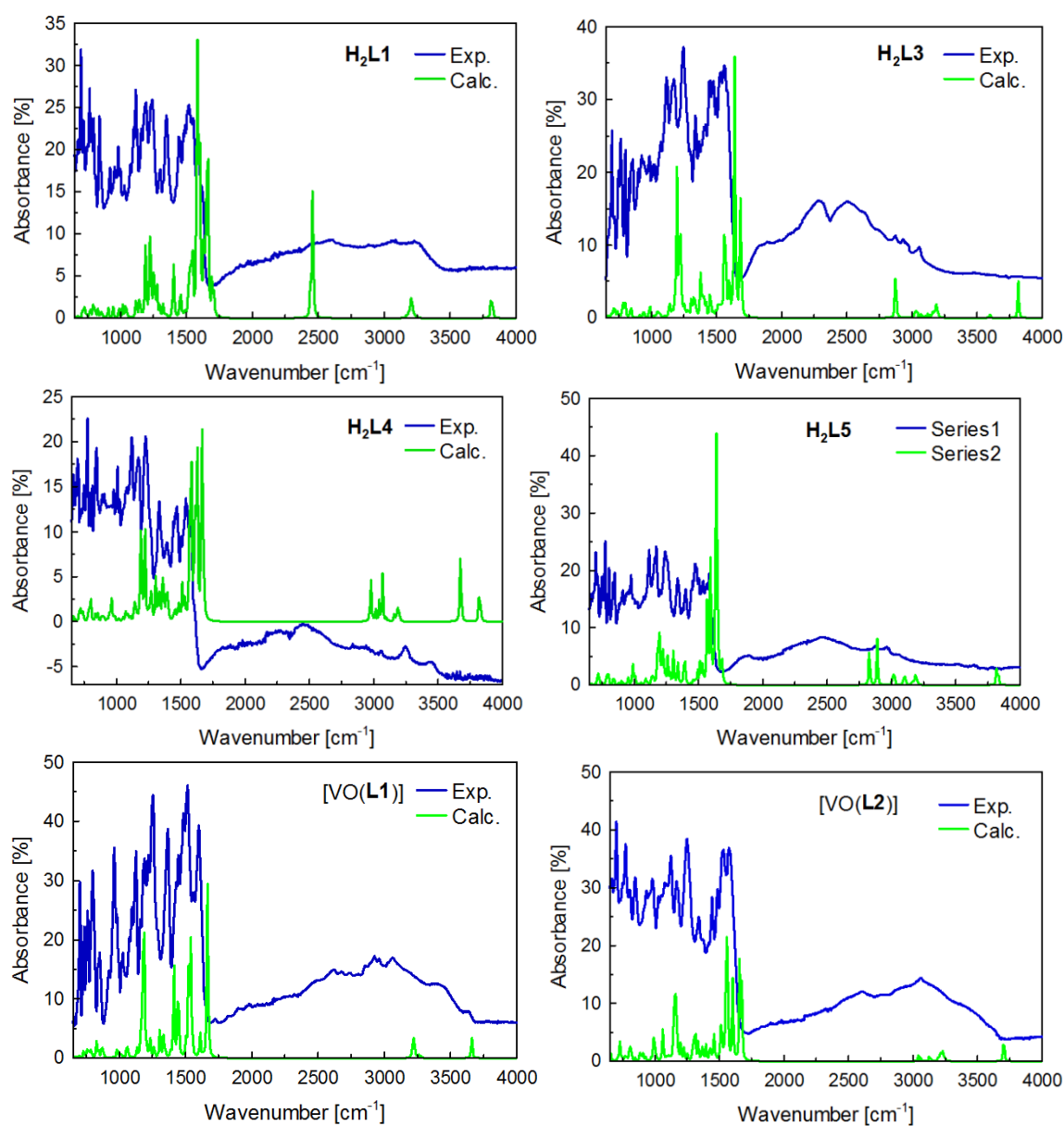


Figure C.3: Spectral overlays of experimental and DFT-calculated IR spectra for the ligands and complexes.

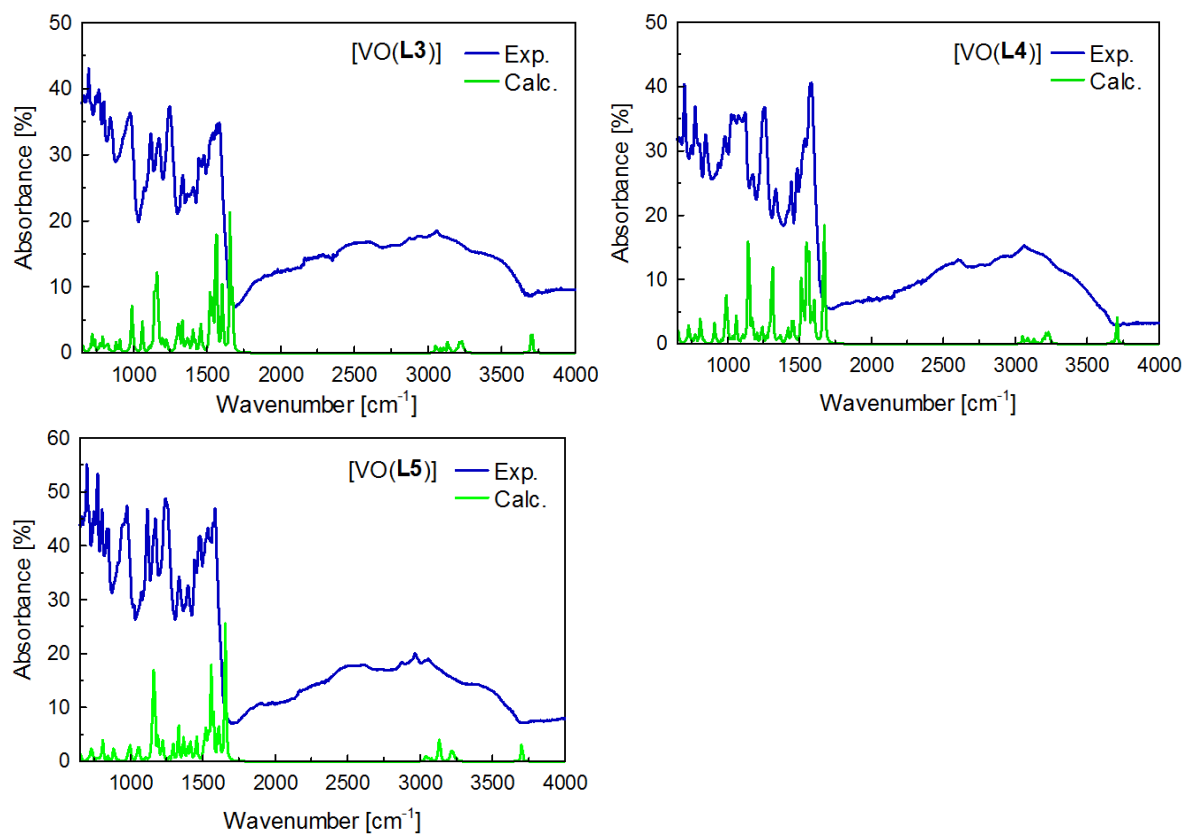


Figure C.4: Spectral overlays of experimental and DFT-calculated IR spectra for the ligands and complexes.